Karlsruhe Institute of Technology

Supersymmetry in the Light of Dark Matter and a 125 GeV Higgs Boson

Conny Beskidt

Zur Erlangung des akademischen Grades eines
DOKTORS DER NATURWISSENSCHAFTEN
an der Fakultät für Physik des Karlsruhe Instituts für Technologie (KIT)

genehmigte

DISSERTATION

von

Dipl. Phys. Conny Renate Beskidt
aus Oberwischau

Tag der mündlichen Prüfung: 14. November 2014

Referent:	Prof. Dr. Wim de Boer Institut für Experimentelle Kernphysik (IEKP)
Korreferent:	Prof. Dr. Günter Quast Institut für Experimentelle Kernphysik (IEKP)

KIT – University of the State of Baden-Wuerttemberg and National Research Center of the Helmholtz Association

www.kit.edu

I declare that I have developed and written the enclosed thesis completely by myself, and have not used sources or means without declaration in the text.

Karlsruhe, 27. Oktober 2014

.....

(**Conny Beskidt**)

Contents

1. Introduction **1**

2. Elementary Particles and Their Interactions **3**
2.1. The Standard Model of Elementary Particle Physics 3
2.1.1. The Higgs Mechanism 5
2.1.1.1. The Fermion masses and their Weak Interaction 7
2.1.1.2. The Higgs masses and its Couplings 8
2.1.2. Testing the Standard Model at the Large Hadron Collider 9

3. Supersymmetry - a Theory Beyond the Standard Model **13**
3.1. Introduction to Supersymmetry 14
3.1.1. Electroweak Symmetry Breaking 17
3.2. The μ-problem and the Next-To-Minimal Supersymmetric Standard Model 20
3.2.1. The Higgs Sector in the Next-To-Minimal Supersymmetric Standard Model 21
3.3. Constrained Supersymmetric Models 23
3.4. Sparticle Masses 25

4. Methods and Tools to Study the Supersymmetric Parameter Space **29**
4.1. Concept of Parameter Estimation Using the Method of Least Squares . . . 29
4.1.1. Maximizing the Likelihood Function 29
4.1.2. Confidence Intervals 31
4.2. Constraining the Supersymmetric Parameter Space with Experimental Data 34
4.2.1. Software Tools 37
4.3. Multi-Step Fitting Approach 38

5. Favored Parameter Space for Single Experimental Constraints **41**
5.1. The Relic Density 41
5.2. Standard Model Higgs Boson 48
5.3. Branching Ratios from B-Physics 52
5.3.1. Rare Decay of a B_S Meson: $B_s^0 \to \mu^+\mu^-$ 52
5.3.2. Leptonic Decay of the B Meson: $B \to \tau\nu_\tau$ 55
5.3.3. Radiative penguin $b \to s\gamma$ 57
5.4. Mass Limits on Squarks and Gluinos 59
5.5. Mass Limit on the pseudo-scalar Higgs Boson 62
5.6. Elastic WIMP-Nucleon Scattering 64
5.6.1. Spin-Dependent Cross Section 64
5.6.2. Spin-Independent Cross Section 66
5.7. Anomalous Magnetic Moment of the Muon 69

6. Combination of All Constraints in the CMSSM and NMSSM **73**
6.1. Determination of the Allowed Parameter Space . . . 74
6.1.1. Higgs Sector Parameters . . . 74
6.2. Comparison of the Allowed Parameter Space . . . 75
6.2.1. Discussion on the NMSSM Parameter Space . . . 76
6.2.2. Discussion on the CMSSM Parameter Space . . . 78
6.2.2.1. Best-Fit Point in the CMSSM . . . 79
6.2.3. Influence of g-2 . . . 81
6.2.4. Higgs Sector . . . 82
6.2.5. Neutralino Sector . . . 86
6.2.6. Elastic Scattering Cross Section . . . 89
6.3. Comparison to Other Analyses . . . 91
6.4. Prospects of Future Searches Including Extrapolated Sensitivities for SUSY 94

7. Summary and Outlook **97**
7.1. Higgs Sector . . . 98
7.2. Dark Matter Sector . . . 98
7.3. Outlook . . . 99

Bibliography **101**

Appendix **113**
A. Probability Density Function . . . 113
A.1. χ^2 distribution . . . 113
B. Parametrization of the Experimental Limits . . . 114
B.1. Limit on the Pseudo-Scalar Higgs Boson Mass . . . 114
B.2. Mass Limits on Squarks and Gluinos . . . 117
B.3. Standard Model-like Higgs Boson . . . 120
B.4. Elastic Scattering Cross Section . . . 121
C. Implementation of the χ^2 function . . . 124
D. Strong and Electroweak Diagrams . . . 125
E. Scalar Form-Factors . . . 125
F. Allowed 68% C.L. Regions . . . 125
G. Optimized tanβ values in the m_0-$m_{1/2}$ plane . . . 126
H. Impact of the Theoretical Error on the Higgs mass . . . 127
I. Mass spectrum and χ^2 contributions for the CMSSM benchmark points . . 128
J. Running of the masses in the CMSSM . . . 130
K. Mass spectrum for the NMSSM Benchmark Points . . . 131
L. Branching Ratios for the NMSSM Benchmark Points II and III . . . 131
M. Neutralino Mixing Matrix for BMP I and III . . . 132
N. Comparison of Allowed 68% C.L. Regions . . . 132
O. Extrapolation of XENON100 . . . 134
P. Additional SUSY Searches at the LHC . . . 134

List of Figures

2.1. The potential $V(\phi)$ of a simple scalar real field ϕ for a positive and negative value of μ^2. . . . 6
2.2. Integrated luminosity versus day delivered and recorded by CMS during the stable beams for p-p collisions at 8 TeV in 2012. . . . 9
2.3. The di-muon invariant mass spectrum including $\mathcal{L}_{int} = 40\text{pb}^{-1}$. . . . 10
2.4. Comparison of theoretical and experimental measured total SM production cross section. . . . 11

3.1. Evolution of the inverse of the coupling constants within the SM and the supersymmetric extension of the SM. . . . 15
3.2. Dominant one loop diagrams from the stop and the top quark contributing to the lightest Higgs boson mass in the MSSM. . . . 20

4.1. Illustration of the construction of the confidence interval limits. . . . 31
4.2. Effect of the quantile Φ^{-1} on a standard Gaussian pdf for a central and one-sided confidence interval. . . . 32

5.1. Rotation curve of a spiral galaxy. . . . 42
5.2. The co-moving WIMP number density in the early universe. . . . 42
5.3. Selected dominant annihilation diagrams contributing to the dark matter relic abundance within the co-annihilation, the focus point and m_A resonance region. . . . 43
5.4. Running of $m^2_{H_u}$ and $m^2_{H_d}$ from the GUT to the low energy scale. . . . 45
5.5. Dependence of the relic density on $\tan\beta$ for varying SUSY masses and trilinear couplings A_0. . . . 45
5.6. The relic density within the m_0-$m_{1/2}$ plane for optimized values of $\tan\beta$ and A_0. . . . 46
5.7. Fraction of the stau self annihilation to the relic density leading to a lower minimum for increasing neutralino mass. . . . 47
5.8. Dependence of the light Higgs mass on the CMSSM parameters. . . . 48
5.9. Dependence of the light Higgs mass on X_t for the constrained and general MSSM. . . . 49
5.10. Normalized couplings to up- and down-type fermions for the light and heavy scalar Higgs bosons. . . . 50
5.11. The lightest Higgs mass as function of $\tan\beta$ for a fixed mass point and varying values of λ. . . . 51
5.12. Dominant diagrams for $B^0_s \to \mu^+\mu^-$ in the SM and MSSM. . . . 53
5.13. $BR(B^0_s \to \mu^+\mu^-)$ plotted versus $\tan\beta$ for varying SUSY masses and trilinear couplings. . . . 54
5.14. $BR(B^0_s \to \mu^+\mu^-)$ and $\sin(2\theta_{\tilde{t}})$ plotted in the $\tan\beta$-A_0 plane for a fixed mass point. . . . 54

5.15. The leptonic decay of a $B^{\pm}$ meson mediated by the annihilation into a charged Higgs $H^{\pm}$ and a virtual $W^{\pm}$ boson. 55
5.16. The ratio of the SUSY and SM branching ratio of $B \to \tau\nu_{\tau}$ and the corresponding charged Higgs mass distribution plotted versus tanβ. 56
5.17. Charged Higgs mass distribution and the resulting ratio $R_{B\to\tau\nu_{\tau}}$ plotted versus the trilinear coupling A_0. 56
5.18. Sample diagrams to the electromagnetic radiative decay $B \to X_s\gamma$ within the SM and SUSY. 58
5.19. $BR(B \to X_s\gamma)$ and the corresponding chargino and charged Higgs mass distribution plotted versus tanβ for different values of the remaining CMSSM parameters. 59
5.20. Diagrams contributing to the strong production at the LHC. 60
5.21. Cross section distribution for the strong production at the LHC translated into the m_0-$m_{1/2}$ plane. 61
5.22. Dependence of the stop mass on A_0 and tanβ and the corresponding cross section contribution σ_{stop} to the total hadronic cross section. 62
5.23. The dominant diagrams contributing to the production of a Higgs boson at the LHC in the SM and MSSM. 63
5.24. Comparison of the 95% C.L. exclusion contours on the pseudo-scalar Higgs boson mass for the different benchmark scenarios m_h^{max}, m_h^{mod+} and m_h^{mod+}. 63
5.25. Diagrams contributing to the spin-dependent elastic scattering of neutralinos from quarks. 65
5.26. Spin-dependent WIMP-neutron cross section and the corresponding Higgsino component within the tanβ-A_0 plane for a fixed mass point. 65
5.27. Diagrams contributing to the spin-independent WIMP-nucleon cross section. 66
5.28. χ^2 contribution of the spin-independent WIMP-nucleon cross section and the corresponding mass distribution of the heavy scalar Higgs H within the tanβ-A_0 plane. 67
5.29. χ^2 contribution of the spin-independent WIMP-nucleon cross section and the corresponding Higgsino component within the tanβ-A_0 plane for a fixed mass point within the focus point region. 67
5.30. Relative difference between the cross section using the averaged and lowest form-factors for the spin-independent cross section calculation as a function of the neutralino mass. 68
5.31. Diagrams contributing to a_{μ} in the SM and SUSY. 69
5.32. Dependence of Δa_{μ} on tanβ for different mass points. 70

6.1. Diagrams associated with the DM annihilation, DM-nucleon scattering and DM production at a collider. 74
6.2. The strong correlation of the CMSSM parameters is demonstrated for a fixed mass point including the Ωh^2 and $B_s^0 \to \mu^+\mu^-$ constraint. 75
6.3. The correlation of the NMSSM parameters including the Ωh^2 and m_h constraint in the $\lambda - \kappa$ plane. 76
6.4. The allowed parameter space for the CMSSM and NMSSM in the m_0-$m_{1/2}$ plane. 77
6.5. The allowed parameter space for the CMSSM and NMSSM translated into the gluino-squark mass plane. 77
6.6. The running of the soft masses from the high to the low scale for the best-fit point in the CMSSM. 80
6.7. Comparison of the running of the Higgs soft masses from the high to the low scale in the CMSSM and NMSSM. 80

6.8. The g-2 favored region of the CMSSM parameter space translated into the m_0-$m_{1/2}$ plane for quadratic and linear addition of the errors. 81
6.9. The Higgs boson mass plotted as function of $m_{1/2}$ within the CMSSM and NMSSM. 82
6.10. The m_A dependence of the three eigenvalues of the Higgs mass matrix and the singlet component for the benchmark scenarios in the NMSSM. 84
6.11. Relic density and the lightest Higgs mass plotted as a function of A_κ. . . . 86
6.12. The neutralino mass matrix elements squared for the benchmark points in the CMSSM and NMSSM. 87
6.13. The allowed parameter space within the spin-independent WIMP-nucleon cross section versus WIMP mass plane for the CMSSM and NMSSM. . . . 88
6.14. The Higgs masses m_A, $m_{H_{1(2)}}$ and the spin-independent WIMP-nucleon cross section as a function of the trilinear couplings A_λ. 89
6.15. Comparison of the 95% C.L. contour line of Ref. [168] and the corresponding contour line resulting from the allowed 95% C.L. region of this analysis. . . 92
6.16. Comparison of the 95% C.L. contour lines of the results of Ref. [171] and [172] and the allowed 95% C.L. region resulting from this analysis. 93
6.17. Comparison of the 95% C.L. contour line of Ref. [173] and the contour line for the NMSSM resulting from this analysis. 93
6.18. The extrapolated sensitivity of LHC at 14 TeV and $3000 fb^{-1}$ within the m_0-$m_{1/2}$ and gluino-squark mass plane. 95
6.19. Same allowed parameter space as in Fig. 6.13 but including the expected sensitivities for LHC-14 and XENON1T for the CMSSM and NMSSM. . . . 95

7.1. Mass limits for the gluino, first and second generation squarks, the Higgs bosons and the lightest neutralino in the CMSSM and NMSSM. 99

B.1. Comparison of the published 95% C.L. contour and their parametrization needed for the contribution $\chi^2_{m_A}$. 115
B.2. Comparison of the model independent published 95% C.L. contour and their parametrization needed for the contribution $\chi^2_{m_\phi}$. 116
B.3. Comparison of the published and parameterized 95% C.L. contour for the contribution χ^2_{ATLAS}. 118
B.4. Upper limit on the cross section of the stop contribution and corresponding exclusion contour in the m_0-$m_{1/2}$ plane. 119
B.5. Comparison between the published 95% C.L. contour from LEP and the parametrization for χ^2_{LEP}. 121
B.6. Comparison of the published and parameterized 90% C.L. contour of the WIMP-nucleon cross section from the spin-independent elastic scattering cross section. 122
B.7. Comparison of the published and parameterized 90% C.L. contour for the χ^2 contribution resulting from the spin-dependent WIMP-proton cross section. 123
B.8. Comparison of the published and parameterized 90% C.L. contour for the spin-dependent WIMP-neutron cross section. 123
B.9. Additional diagrams contributing to strong production at the LHC. 124
F.10. The allowed 68%(a) and 95% C.L. (b) regions for the CMSSM within the m_0-$m_{1/2}$ plane. 126
F.11. The allowed 68%(a) and 95% C.L. (b) regions for the NMSSM within the m_0-$m_{1/2}$ plane. 126
G.12. The optimized $\tan\beta$ values for the CMSSM and NMSSM within the m_0-$m_{1/2}$ plane. 127

H.13. Impact of the theoretical error of the Higgs mass on the 68% and 95% C.L. region within the CMSSM. 127
J.14. The running of the soft masses from the high to the low scale for the CMSSM points II and III. 130
M.15. The neutralino mass matrix elements squared for the benchmark points BMP I and III in the NMSSM. 132
N.16. Comparison of the 68% C.L. contour lines of Ref. [168] and the allowed 68% C.L. region resulting from this analysis. 133
N.17. Comparison of the 68% C.L. contour lines of the result of Ref. [171] and [172] and the allowed 68% C.L. region of this analysis. 133
P.18. Diagrams contributing to the electroweak production at the LHC. 135
P.19. Cross section distribution for the electroweak production at the LHC translated into the m_0-$m_{1/2}$ plane. 135

List of Tables

2.1. Summary of the electric charge Q_f, the third component of the weak isospin I_f^3 and the corresponding weak hypercharge Y_f of the first generation fermions. 5

3.1. Summary of the chiral and gauge supermultiplet fields representing the particle content of the minimal supersymmetric standard model. 16
3.2. Couplings from the neutral Higgs bosons $\phi = h^0, H^0, A^0$ to up-/down-type fermions and gauge bosons normalized to the SM Higgs coupling. 19
3.3. Summary of the input parameters for the corresponding constrained and non-universal Higgs mass SUSY models. 25

4.1. Confidence level for different values of the quantile Φ^{-1} and vice versa, for the central and one-sided confidence interval. 33
4.2. Quantile Q_γ given for different values of the confidence level for a confidence region for n fitted parameters. 34
4.3. List of experimental measurements used to constrain the supersymmetric parameter space. 35
4.4. List of limits used for the global fits to constrain the supersymmetric parameter space. 36
4.5. List of the standard model input parameter used for the global fits. 38

6.1. Parameter set and sparticle masses for the benchmark points in the CMSSM. 79
6.2. Parameter set for the benchmark points in the NMSSM referring to different Higgs boson scenarios. 83
6.3. Reduced couplings from the Higgs boson to up-/down-type fermions and gauge boson and the corresponding Higgs mixing elements for the benchmark points in the NMSSM. 83
6.4. Summary of the branching ratios for the Higgs bosons into SM particles, neutralinos and charginos for the benchmark points. 85

B.1. The hadronic cross section $\sigma_{tot}(pp \to \tilde{g}\tilde{g}, \tilde{g}\tilde{q}, \tilde{q}\tilde{q})$ given on the published 95% C.L. contour line for the χ^2 contribution χ^2_{ATLAS}. 117
B.2. The hadronic cross section $\sigma_{tot}^{(w/o)}(pp \to \tilde{g}\tilde{g}, \tilde{g}\tilde{q}, \tilde{q}\tilde{q})$ without the stop contribution is given on the published 95% C.L. contour line for the χ^2 contribution $\chi^2_{ATLAS_1}$. 119
E.3. Summary of the default and the lowest scalar form-factors. 125
I.4. Theoretical prediction for selected constraints for the parameter points in Table 6.1. 128
I.5. χ^2 contributions for each constraint for the parameter points in Table 6.1. . 128
I.6. Mass spectrum at low scale for the parameter points in Table 6.1. 129
K.7. Mass spectrum at low scale for the parameter points in Table 6.2. 131
L.8. Branching ratios for BMP II and III in the NMSSM. 132

List of Abbreviations

ATLAS	A Toroidal LHC Apparatus
BMP	Benchmark Point
C.L.	Confidence Level
CMSSM	Constrained Minimal Supersymmetric Standard Model
CMS	Compact Muon Solenoid
DDMS	Direct Dark Matter Search
DM	Dark Matter
EW	Electroweak
FCNC	Flavor Changing Neutral Current
GUT	Grand Unified Theory
GWS	Glashow-Weinberg-Salam
LHCb	Large Hadron collider beauty experiment
LHC	Large Hadron Collider
LS	Least Squares
MCMC	Markov-Chain-Monte-Carlo
ML	Maximum Likelihood
MSSM	Minimal Supersymmetric Standard Model
mSUGRA	Minimal Supergravity
NLO	Next-To-Leading Order
NLSP	Next-To-Lightest Particle
NMSSM	Next-To-Minimal Supersymmetric Standard Model
NNLO	Next-To-Next-To-Leading Order
NUH	Non-Universal Higgs

pdf	Probability Density Function
PDG	Particle Data Book
PQ	Peccei-Quinn
QCD	Quantum Chromodynamics
QED	Quantum Electrodynamics
SD	Spin-Dependent
SI	Spin-Independent
SM	Standard Model
SUSY	Supersymmetry
vev	Vacuum Expectation Value
WIMP	Weakly Interacting Massive Particle

1. Introduction

The standard model of particle physics (SM), a theory describing all known elementary particles and their interactions, is a successful theory. It has been extensively tested over the past forty years. After the precision measurements at the LEP e^+e^- collider, yielding limits for the top quark and Higgs boson mass, the Nobel Prize in Physics was awarded in 1999 jointly to Gerardus 't Hooft and Martinus J.G. Veltman "for elucidating the quantum structure of electroweak interactions in physics" [1].
In July 2012 the last missing particle, the so-called Higgs boson, has been discovered at the Large Hadron Collider (LHC) at CERN in Geneva by two independent experiments [2, 3]. It was predicted by the Higgs mechanism, a mechanism incorporated into the SM to give the massive particles their mass. In the last two years, it became clear that the discovered scalar particle is in fact SM-like, since the measured quantum numbers and the decay rates are in agreement with the prediction of the SM. However, this last missing piece of the SM does not close the theory, but the discovery raises new questions.
Although the SM predicts a Higgs boson, its mass could have been anywhere between the GeV[1] and TeV scale. In addition, the corrections to the Higgs boson mass include quadratic terms of a parameter, which is associated with the scale up to which the SM is supposed to be valid [4]. The physical mass of the Higgs boson results from the sum of the bare mass, which enters the Lagrangian, and the corresponding radiative corrections. If the Planck scale is assumed to be the scale to which the SM is valid, an incredible fine-tuning of the masses is needed, since a cancellation from $\sim (10^{19}\ \text{GeV})^2$ to $\sim (10^2\ \text{GeV})^2$ is requested [5]. Less fine-tuning would require new physics at the TeV scale. Beside the fine-tuning problem, the cosmological observations point towards the existence of dark matter (DM), which cannot be explained within the SM [6]. It becomes apparent that if a 125 GeV Higgs boson and a dark matter particle are considered an extension of the SM is required.

Supersymmetry (SUSY), a theory beyond the SM, solves the fine-tuning problem, since it provides a symmetry between fermions and bosons: for each fermion a supersymmetric bosonic partner exists and vice versa [7–11]. The corrections to the Higgs boson mass naturally cancel since the fermions and bosons contribute with opposite signs to the radiative corrections. So a light Higgs boson and the validity of the theory up to high energy scales is maintained. In fact, a light Higgs boson with a mass below 135 GeV is predicted within SUSY [12]. Therefore the discovered Higgs boson strongly supports SUSY despite

[1] Using the mass-energy equivalence the mass can be expressed in units of eV/c^2 with the speed of light in vacuum c. The convention of natural units $c = \hbar = 1$ is used throughout this thesis.

of the fact that no supersymmetric particle has been found so far. The enriched particle spectrum also includes a perfect dark matter candidate. Assuming R-parity conversation, which is required to preserve the proton stability [13], the lightest supersymmetric particle is stable and provides the right amount of dark matter. Within the minimal supersymmetric extension of the SM, the so-called minimal supersymmetric SM (MSSM), many experimental observations can be simultaneously described. However the parameter space which is associated to a 125 GeV Higgs boson favors rather high masses of the supersymmetric partner. Again this can lead to a fine-tuning problem, since the corrections to the Higgs boson mass include the mass difference of the SM and their SUSY partners. A minimal extension of the MSSM can solve this fine-tuning problem.
Within the so-called next-to-minimal supersymmetric SM (NMSSM) an additional Higgs singlet is introduced. In this way, the Higgs sector is modified due to mixing effects, which provides a 125 GeV Higgs boson for moderate and light SUSY masses leading to less fine-tuning. This model is particularly interesting for experimental searches for SUSY, since it leads to a lighter supersymmetric particle spectrum which is in reach of the LHC. The enriched Higgs sector also extends the possibilities for search strategies, which so far have mostly considered the minimal supersymmetric SM.

The goal of this thesis is twofold: first, the supersymmetric parameter space allowed by accelerator and cosmological constraints is determined for both supersymmetric models, the constrained MSSM and NMSSM. The second aspect is the comparison of the Higgs and dark matter sector of the two SUSY models which lead to phenomenological different scenarios. In particular their differences are important to distinguish the two SUSY models and to estimate the discovery reach for current SUSY searches and for the next run of future experiments, like the LHC at 14 TeV and future experiments for the direct search for dark matter. A further reason to study the dark matter and the Higgs sector is due to their connection: the nine orders of magnitude between the DM annihilation and DM scattering cross section on nuclei is most easily explained if the interaction happens via exchange of a Higgs boson, since the latter hardly interacts with the almost massless quarks inside the nuclei. Since a weak neutral interaction can also be mediated by a Z^0 boson, the corresponding coupling has to be suppressed. These non-trivial requirements are easily accomplished within the minimal and next-to-minimal supersymmetric SM, which further motivates their study.

In chapter 2 the SM is briefly reviewed to give an introduction of the theoretical concepts. The theoretical framework of Supersymmetry as well as the studied models are introduced in chapter 3. The tools and methods which have been applied are described in chapter 4. For a comprehensive understanding of the results of the combination of all constraints, the favored region of each constraint in the parameter space has to be investigated first. so in chapter 5 the results for the single observables are given. The results of the combination of all constraints are presented subsequent in chapter 6. In addition, the differences of the allowed parameter space of the two SUSY models are highlighted with respect to a 125 GeV Higgs and dark matter. The results are further compared to other analyses and prospects for the sensitivities of future searches are given. Finally a short summary and concluding remarks are given in chapter 7.

2. Elementary Particles and Their Interactions

The fundamental constituents of matter and their interactions are studied within particle physics, while the kind of particles regarded as fundamental changed with time during the 20th century. The standard model (SM) of elementary particle physics is currently the established theory and includes all elementary particles and the fundamental forces of nature. It was developed in the latter of the 20th century and finalized in the mid 1970s. The SM is a successful theory, which has been extensively tested over the past forty years. It includes an enormous theoretical framework, thus only a brief introduction is given in this thesis. More details can be found in reviews or textbooks, see e.g. [14–16] and [17–21]. The section starts with a short introduction of the SM, which is mainly derived from Ref. [4] and includes only the relevant aspects referred to this thesis. At the end its experimental confirmation by the current largest and most powerful particle collider is presented.

2.1. The Standard Model of Elementary Particle Physics

The SM describes the building blocks of matter, the fermions namely quarks and leptons, and their interactions. It contains the electromagnetic, weak and strong force mediated by the corresponding gauge bosons, the photon, the $W^{\pm}$ and Z^0 bosons and the gluons. The theoretical framework of the SM is based on the combination of the electroweak theory, also known as the Glashow-Weinberg-Salam (GWS) theory [22], and quantum chromodynamics (QCD), the theory of the strong force. The GWS theory evolved from Glashow's model to unify the weak and electromagnetic interaction in the framework of $SU(2) \times U(1)$ symmetry. The Higgs mechanism [23] was added by Weinberg and Salam [24, 25] to generate masses for the gauge particles and fermions. The proof of renormalizability, i.e. being a self-consistent mathematical theory, was given by t'Hooft [26, 27]. QCD is based on the idea that the color charge is the source of the strong interaction between quarks [28, 29]. QCD, a gauge theory including color $SU(3)$ symmetry, was established to be the theory of the strong force through the discovery of asymptotic freedom by Gross, Politzer and Wilczek [30–32]. Efforts to unify the strong and electroweak theory within a grand unified theory (GUT) is yet not possible in the SM, since the corresponding couplings do not unify [33]. As will be discussed in the next section, gauge coupling unification works in the supersymmetric extension of the SM.

The SM is described in the mathematical framework of the gauge field theory with the local symmetry group

$$SU(3)_C \times SU(2)_L \times U(1)_Y, \tag{2.1}$$

The subgroups $SU(3)_C$ and $SU(2)_L \times U(1)_Y$ correspond to the symmetry group of the QCD and electroweak (EW) interaction. The model involves two kind of fields: matter and gauge fields. The matter fields consist of three generations of left- and right-handed chiral quarks and leptons $f_{L,R}$, which fulfill $f_{L,R} = \frac{1}{2}(1 \mp \gamma_5)f$, where γ_5 is the chirality operator and f represents a dirac fermion. The left(right)-handed leptons and quarks are arranged in weak isospin doublets(singlets):

$$\begin{aligned}
L_1 &= \begin{pmatrix}\nu_e\\ e^-\end{pmatrix}_L, \quad e_{R_1} = e^-_R, \quad Q_1 = \begin{pmatrix}u\\ d\end{pmatrix}_L, \quad u_{R_1} = u_R, \quad d_{R_1} = d_R,\\
L_2 &= \begin{pmatrix}\nu_\mu\\ \mu^-\end{pmatrix}_L, \quad e_{R_2} = \mu^-_R, \quad Q_2 = \begin{pmatrix}c\\ s\end{pmatrix}_L, \quad u_{R_2} = c_R, \quad d_{R_2} = s_R,\\
L_3 &= \begin{pmatrix}\nu_\tau\\ \tau^-\end{pmatrix}_L, \quad e_{R_3} = \tau^-_R, \quad Q_3 = \begin{pmatrix}t\\ b\end{pmatrix}_L, \quad u_{R_3} = t_R, \quad d_{R_3} = b_R.
\end{aligned} \tag{2.2}$$

Leptons consist of the electron, the muon, the tau lepton and their corresponding neutrinos. The quarks are furthermore denoted according to their flavor as up-, down-, charm-, strange-, top- and bottom quark. For each particle the corresponding anti-particle exist. The weak hypercharge Y_f of the fermions is defined via the so-called Gell-Mann-Nishijima relation in terms of the third component of the weak isospin I^3_f and the electric charge Q_f in units of the elementary charge e:

$$Q_f = I^3_f + \frac{1}{2}Y_f. \tag{2.3}$$

In Table 2.1 a summery of the quantum numbers of the first generation fermions is shown. The quantum numbers resemble for the second and third generation. The quarks transform as triplets of $SU(3)_C$, whereas the colorless leptons are color singlets. The relation

$$\sum_f Y_f = \sum_f Q_f = 0 \tag{2.4}$$

ensures the cancellation of the chiral anomalies [34, 35] within each generation. In addition it preserves the renormalizability of the EW theory [36].
The gauge fields correspond to the spin one bosons, which are associated with the generators of the corresponding algebra of the group:

$$\begin{array}{ccccc}
SU(3)_C & \times & SU(2)_L & \times & U(1)_Y.\\
\downarrow & & \downarrow & & \downarrow\\
G^\alpha_\mu & & W^a_\mu & & B_\mu\\
\alpha = 1, ..., 8 & & a = 1, 2, 3 & &
\end{array}$$

The field B_μ represents the generator Y of the $U(1)_Y$ group. The three fields W^a_μ correspond to the generators T^a_L of the $SU(2)_L$ group, which can be written as $T^a_L = \frac{1}{2}\tau^a$, where τ^a denotes the 2×2 Pauli matrices. The eight generators T^a_C of the $SU(3)_C$ group lead to an octet of gluon fields G^b_μ and can be written in terms of the Gell-Mann matrices λ^a: $T^a_C = \frac{1}{2}\lambda^a$. The SM Lagrangian

Table 2.1.: Summary of the electric charge Q_f, the third component of the weak isospin I_f^3 and the corresponding weak hypercharge Y_f of the first generation fermions.

	e_L^-	ν_e	e_R^-	d_L	u_L	d_R	u_R
Q_f	-1	0	-1	$-\frac{1}{3}$	$+\frac{2}{3}$	$-\frac{1}{3}$	$+\frac{2}{3}$
I_f^3	$-\frac{1}{2}$	$+\frac{1}{2}$	0	$-\frac{1}{2}$	$+\frac{1}{2}$	0	0
Y_f	-1	-1	-2	$+\frac{1}{3}$	$\frac{1}{3}$	$-\frac{2}{3}$	$+\frac{4}{3}$

$$\begin{aligned}\mathcal{L}_{SM} = &-\frac{1}{4}G^a_{\mu\nu}G_a^{\mu\nu} - \frac{1}{4}W^a_{\mu\nu}W_a^{\mu\nu} - \frac{1}{4}B_{\mu\nu}B^{\mu\nu} \\ &+ \bar{L}_i i D_\mu \gamma^\mu L_i + \bar{e}_{R_i} i D_\mu \gamma^\mu e_{R_i} \\ &+ \bar{Q}_i i D_\mu \gamma^\mu Q_i + \bar{u}_{R_i} i D_\mu \gamma^\mu u_{R_i} + \bar{d}_{R_i} i D_\mu \gamma^\mu d_{R_i}.\end{aligned} \tag{2.5}$$

is invariant under local $SU(3)_C \times SU(2)_L \times U(1)_Y$ gauge transformation using the covariant derivative D_μ, which reads

$$D_\mu \psi \quad = \quad \left(\partial_\mu - i g_s T_a G^a_\mu - i g_2 T_a W^a_\mu - i g_1 \frac{Y_q}{2} B_\mu\right)\psi. \tag{2.6}$$

Here g_1, g_2 and g_s represent the coupling constants of the $U(1)_Y$, $SU(2)_L$ and $SU(3)_C$ group. The first line in Eq. 2.5 describes the kinetic term of the gauge bosons. It includes the corresponding field strengths, which are given by

$$\begin{aligned} G^a_{\mu\nu} &= \partial_\mu G^a_\nu - \partial_\nu G^a_\mu + g_s f^{abc} G^b_\mu G^c_\nu, \\ W^a_{\mu\nu} &= \partial_\mu W^a_\nu - \partial_\nu W^a_\mu + g_2 \epsilon^{abc} W^b_\mu G^c_\nu, \\ B_{\mu\nu} &= \partial_\mu B_\nu - \partial_\nu B_\mu. \end{aligned} \tag{2.7}$$

ϵ^{abc} denotes the antisymmetric tensor, while the tensor f^{abc} corresponds to the structure constants of the $SU(3)_C$ group. This non-abelian nature of the $SU(2)$ and $SU(3)$ groups give rise to self-interaction terms leading to triple and quadric gauge couplings between the gauge fields. The interaction of the matter fields Ψ with the gauge fields as well as their kinetic terms are included via the covariant derivative D_μ.
So far, the fermion and gauge fields are massless although experimentally proved to be massive. The explicit integration of mass terms for gauge bosons $\frac{1}{2}M_V^2 W_\mu W^\mu$ violates local $SU(2)_L \times U(1)_Y$ gauge invariance while explicit mass terms for fermions $-m_f \bar{\psi}_f \psi_f$ breaks chiral symmetry.

2.1.1. The Higgs Mechanism

The way to generate masses for the gauge bosons and fermions without violating gauge invariance and preserving renormalizability is accomplished through the concept of spontaneous symmetry breaking via the Higgs mechanism[1]. Here the lowest energy state, identified as the vacuum, does not respect gauge symmetry, so effective masses for propagating particles are induced. The Higgs mechanism, i.e. the spontaneous breakdown of the

[1]The mechanism was developed in 1960s by three independent groups: by Robert Brout and Francois Englert [37], by Peter Higgs [23] and by Gerald Guralnik, C.R. Hagen and Tom Kibble [38]. However, the short naming of the mechanism prevailed ignoring the other contributing names.

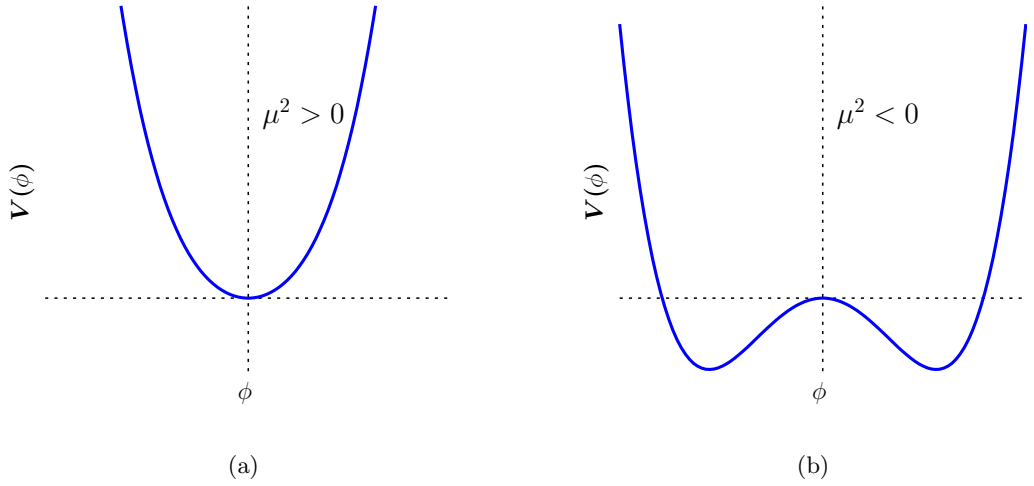

Figure 2.1.: The potential $V(\phi)$ of a simple scalar real field ϕ for positive (a) and negative (b) μ^2 illustrating the development of a non-zero vev.

gauge symmetry and the associated mass generation of the gauge bosons, will be briefly discussed for the SM in this section. The summary is mainly derived from Ref. [4].
The symmetry group of the SM has to be broken as $SU(2)_L \times U(1)_Y \rightarrow U(1)_{\text{em}}$ to get massive $W^{\pm}$ and Z^0 gauge bosons. The exact symmetry of quantum electrodynamics (QED)has to be preserved at the same time. This implies the conservation of the electric charge, i.e. the sub-group $U(1)_{\text{em}}$ remains a symmetry of the vacuum after the spontaneous symmetry breaking. The simplest option is a complex $SU(2)$ doublet of scalar fields ϕ with the hypercharge $Y_\Phi = +1$:

$$\Phi = \begin{pmatrix} \phi^+ \\ \phi^0 \end{pmatrix}. \tag{2.8}$$

The corresponding Lagrangian including the invariant terms of the scalar field reads

$$\mathcal{L}_{scalar} = (D^\mu \Phi)^\dagger (D_\mu \Phi) - V(\Phi^\dagger \Phi), \tag{2.9}$$

where the potential V is given by

$$V(\Phi^\dagger \Phi) = \mu^2 \Phi^\dagger \Phi + \lambda (\Phi^\dagger \Phi)^2. \tag{2.10}$$

Since the Higgs complex $SU(2)$ doublet is a color singlet with respect to $SU(3)_C$, the covariant derivative D_μ in Eq. 2.9 includes only the interactions generators of the $SU(2)_L$ and $U(1)_Y$ group. Since the vacuum is not charged, the neutral component of the doublet field Φ will develop a non-zero vacuum expectation value (vev) for $\mu^2 < 0$, which can be chosen to be at

$$\langle \Phi \rangle_0 \equiv \langle 0|\Phi|0\rangle = \begin{pmatrix} 0 \\ \frac{v}{\sqrt{2}} \end{pmatrix} \quad \text{with} \quad v = \left(-\frac{\mu^2}{\lambda}\right)^{1/2} \tag{2.11}$$

by using a $SU(2)_L$ gauge transformation. The minimum for the potential V of a simple scalar real field ϕ is illustrated for positive(negative) μ^2 in Fig. 2.1(a)(Fig. 2.1(b)).

The field Φ can be expanded around the minimum and written at first order in terms of the four fields $\theta_{1,2,3}(x)$ and $H(x)$

$$\Phi(x) = \begin{pmatrix} \theta_2 + i\theta_1 \\ \frac{1}{\sqrt{2}}(v+H) - i\theta_3 \end{pmatrix} = e^{i\theta_a(x)\tau^a(x)/v} \cdot \begin{pmatrix} 0 \\ \frac{1}{\sqrt{2}}(v+H(x)) \end{pmatrix}, \tag{2.12}$$

while $\theta_{1,2,3}(x)$ corresponds to the massless goldstone bosons. Using a $SU(2)_L$ gauge transformation to move to the unitarity gauge leads to the new field

$$\Phi(x) \quad \rightarrow \quad e^{-i\theta_a(x)\tau^a(x)}\Phi(x) = \frac{1}{\sqrt{2}} \begin{pmatrix} 0 \\ v + H(x) \end{pmatrix}. \tag{2.13}$$

The first term of the scalar Lagrangian of Eq. 2.9 can be written in terms of this new field

$$\begin{aligned} |D_\mu \Phi|^2 &= \left| \left(\partial_\mu - ig_2 \frac{\tau_a}{2} W_\mu^a - ig_1 \frac{1}{2} B_\mu \right) \Phi \right|^2 \\ &= \frac{1}{2} \left| \begin{pmatrix} \partial_\mu - \frac{i}{2}(g_2 W_\mu^3 + g_1 B_\mu) & -\frac{ig_2}{2}(W_\mu^1 - iW_\mu^2) \\ -\frac{ig_2}{2}(W_\mu^1 + iW_\mu^2) & \partial + \frac{i}{2}(g_2 W_\mu^3 - g_1 B_\mu) \end{pmatrix} \begin{pmatrix} 0 \\ v+H \end{pmatrix} \right|^2 \\ &= \frac{1}{2}(\partial_\mu H)^2 + \frac{1}{8} g_2^2 (v+H)^2 \left| W_\mu^1 + iW_\mu^2 \right|^2 + \frac{1}{8}(v+H)^2 \left| g_2 W_\mu^3 - g_1 B_\mu \right|. \end{aligned} \tag{2.14}$$

From Eq. 2.14 new physical fields $W_\mu^\pm$, Z_μ and A_μ, the orthogonal field to Z_μ, are derived

$$W^\pm = \frac{1}{\sqrt{2}}(W_\mu^1 \mp iW_\mu^2), \quad Z_\mu = \frac{g_2 W_\mu^3 - g_1 B_\mu}{\sqrt{g_2^2 + g_1^2}}, \quad A_\mu = \frac{g_2 W_\mu^3 + g_1 B_\mu}{\sqrt{g_2^2 + g_1^2}}. \tag{2.15}$$

If the mass terms $M_W^2 W_\mu^+ W_\mu^- + \frac{1}{2} M_Z^2 Z_\mu Z^\mu + \frac{1}{2} M_A^2 A_\mu A^\mu$ are compared with the quadratic terms of the vector fields, the acquired masses for the $W^\pm$ and Z^0 bosons can be identified

$$M_W = \frac{1}{2} v g_2, \quad M_Z = \frac{1}{2} v \sqrt{g_2^2 + g_1^2}, \quad M_A = 0. \tag{2.16}$$

The photon is still massless and the vev[2] v is fixed in terms of the $W^\pm$ boson mass $M_W = \frac{1}{2} g_2 v \ \rightarrow \ v \approx 246$ GeV. The $W^\pm$ bosons mediate the charged currents, which changes the flavor of a single quark. The exchange of a Z^0 boson is related to the neutral current.

2.1.1.1. The Fermion masses and their Weak Interaction

The same scalar field Φ can be used to generate the fermion masses by introducing the isodoublet $\tilde{\Phi} = i\tau_2 \Phi^*$ and the corresponding $SU(2)_L \times U(1)_Y$ invariant Yukawa Lagrangian:

$$\mathcal{L}_F = -\lambda_e \bar{L} \Phi e_R - \lambda_d \bar{Q} \Phi d_R - \lambda_u \bar{Q} \tilde{\Phi} u_R + h.c.. \tag{2.17}$$

After spontaneous symmetry breaking the Lagrangian can be re-written in terms of the new field in Eq. 2.13. After diagonalization of the mass matrices, i.e. by transforming the weak to the physical states, the constant terms in front of $\bar{f}f = (\bar{f}_L f_R + \bar{f}_R f_L)$ are identified with the fermion masses, e.g.

[2] In case the Higgs field is not normalized by $1/\sqrt{2}$ the vev v is accordingly $v \approx 174$GeV.

$$m_e = \frac{\lambda_e v}{\sqrt{2}}, \quad m_u = \frac{\lambda_u v}{\sqrt{2}}, \quad m_d = \frac{\lambda_d v}{\sqrt{2}}. \tag{2.18}$$

The fermionic part of the SM Lagrangian from Eq. 2.5 describes the interaction of the fermions with the gauge bosons. The fermionic interaction can be written in terms of the new physical fields after EWSB and the weak eigenstates can be transform to the physical states, which diagonalize the mass matrices. For the quarks all interactions take the same form in the physical basis except for the weak charged currents. As a result the charged current $W^{\pm}$ interactions couples to the physical quarks eigenstates via

$$\begin{aligned} -\frac{g_2}{\sqrt{2}}(\bar{u}_L, \bar{c}_L, \bar{t}_L)\gamma^\mu W^+_\mu V_{CKM} \begin{pmatrix} d_L \\ s_L \\ b_L \end{pmatrix} + h.c. \\ V_{CKM} \equiv V_L^u V_L^{d\dagger} = \begin{pmatrix} V_{ud} & V_{us} & V_{ub} \\ V_{cd} & V_{cs} & V_{cb} \\ V_{tb} & V_{ts} & V_{tb} \end{pmatrix}, \end{aligned} \tag{2.19}$$

where V_{CKM} is the 3×3 unitary Cabibbo-Kobayashi-Maskawa matrix [39, 40]. The unitary of V ensures the absence of flavor changing neutral currents (FCNC) at tree level. The mass and weak eigenstates for leptons contribution in charged currents resemble since the neutrinos are supposed to be massless within the SM, even though there are experimental evidence suggesting massive neutrinos, e.g. from neutralino oscillation.

2.1.1.2. The Higgs masses and its Couplings

Combining the scalar potential 2.10 and Eq. 2.13 derives the following Lagrangian for the Higgs Field H, which includes the kinetic part of the Higgs field $\frac{1}{2}(\partial_\mu H)^2$ from the covariant derivative as well as the mass and the self-interaction parts of the Higgs field from the scalar potential

$$\begin{aligned} \mathcal{L}_H &= \frac{1}{2}(\partial_\mu H)\partial^\mu H - V \\ &= \frac{1}{2}(\partial^\mu H)^2 - \lambda v^2 H^2 - \lambda v H^3 - \frac{\lambda}{4}H^4. \end{aligned} \tag{2.20}$$

From Eq. 2.20 the mass term of the Higgs boson is identified

$$M_H^2 = 2\lambda v^2 = -2\mu^2. \tag{2.21}$$

The mass of the Higgs boson is a free parameter and has been determined experimentally to be around 125 GeV. The couplings of the Higgs boson to the gauge and fermions can be obtained from the Lagrangian:

$$\begin{aligned} g_{Hff} = i\frac{m_f}{v}, \quad g_{HVV} = -2i\frac{M_V^2}{v}, \quad g_{HHVV} = -2i\frac{M_V^2}{v^2}, \\ g_{HHH} = 3i\frac{M_H^2}{v}, \quad g_{HHHH} = 3i\frac{M_H^2}{v^2}. \end{aligned} \tag{2.22}$$

A complete overview of the Higgs couplings can be found in Ref. [41].

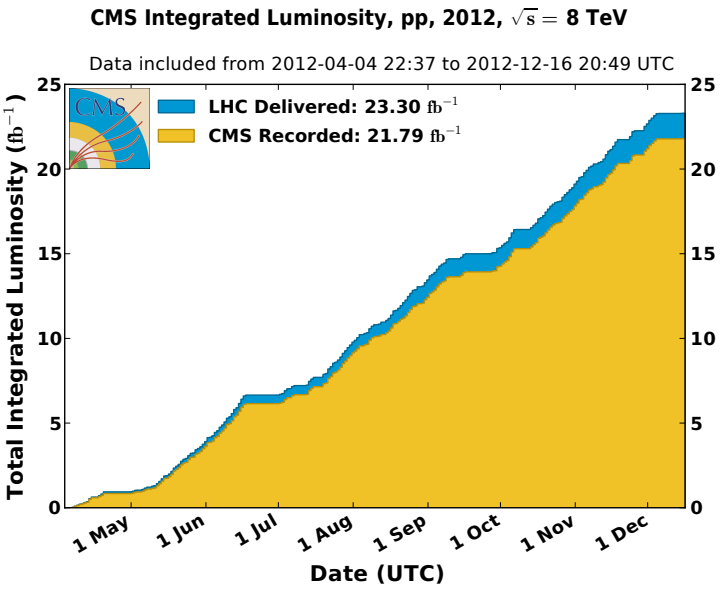

Figure 2.2.: Integrated luminosity versus day delivered (blue) and recorded by CMS (orange) during the stable beams for p-p collisions at 8 TeV centre-of-mass energy in 2012. The figure has been taken from [43].

2.1.2. Testing the Standard Model at the Large Hadron Collider

The complementary progress of theory and experiment plays an important role in particle physics. Besides the development of the theoretical framework, the gain of knowledge about elementary particles is coming from accelerating particles to very high energies in collider experiments. Detecting the collision products allows to test the predictions of the SM.

Todays world's largest and highest energy particle accelerator is the Large Hadron Collider (LHC) [42] based at CERN, the European Organization for Nuclear Research, near Geneva in Switzerland. It is located in a 27 km circular tunnel around 100 m beneath the Swiss/French border. Seven experiments are located within the ring structure. The LHC is designed to collide counter-rotating proton beams with energies up to 7 TeV per nucleon to study the conditions in the very early universe. To bend the proton along the ring 1232 dipole magnets are installed and able to generate a 8.3 T magnetic field. Before the particles reach their high energies in the LHC, they have to pass through a pre-acceleration chain to be injected with an energy of 450 GeV. At the design energy the protons are arranged in up to 2808 bunches per beam with $1.15 \cdot 10^{11}$ protons per bunch. A design bunch spacing of 25 ns and a frequency of 40 MHz leads to 600 million particle collisions per second. After a electronic pre-selection only 1% of the events are further selected for the analysis leading to several petabytes of collision data per year, which is analyzed by a grid-based computer network infrastructure. The design luminosity of the LHC is 10^{34} cm^{-2}s^{-1} for proton collisions. The luminosity $\mathcal{L} = \dot{N}/\sigma$ describes the relation of the number of events per second $\dot{N}$ for a process with a given cross section σ. $\mathcal{L}$ is determined by the machine parameter, e.g. high-intensity beams with small transverse beam areas. The integrated luminosity $\mathcal{L}_{int}$ is therefore a measure for the total number of events via the relation $N = \int \mathcal{L}\sigma dt = \mathcal{L}_{int}\sigma$. The integrated luminosity delivered over time by the LHC and recorded by the CMS experiment is shown in Fig. 2.2 to demonstrate the excellent performance of the LHC. This qunatity is needed for rare processes, since rare events are limited by the production cross section. In spite of the low production cross section, the number of events can be increased with higher luminosity.

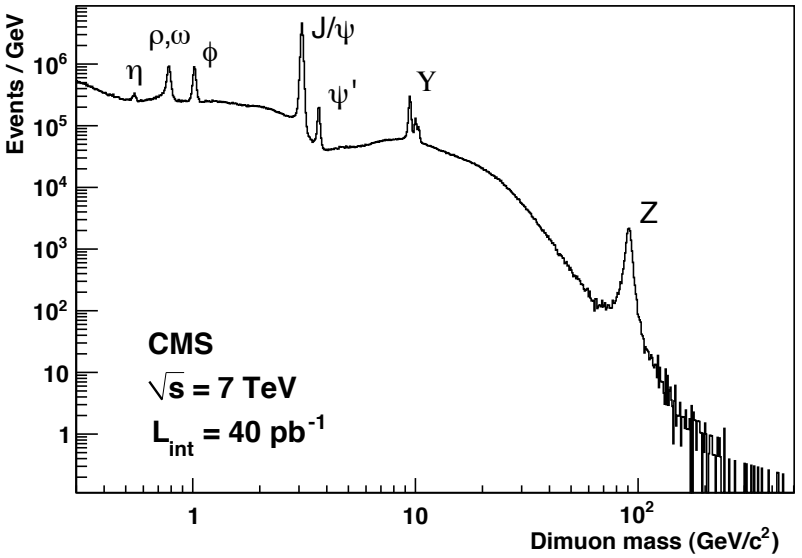

Figure 2.3.: The invariant mass spectrum of opposite-sign muon pairs taken from Ref. [47] including $\mathcal{L}_{int} = 40\text{pb}^{-1}$.

At four intersection points the main detectors[3] are located. The results of the following main detectors have been relevant for this thesis:

- CMS ("Compact Muon Solenoid") [44] and ATLAS ("A Toroidal LHC Apparatus") [45] represent the general purpose detectors. Their aim is to investigate a wide range of physics starting from the detection of the Higgs boson, which succeeded in July 2012, to the discovery of evidences for new physics beyond the SM. The characteristic design of the two detectors are slightly different. However, both experiments feature the typical detector structure consisting of several layers of sub detectors: the inner detector arranged around the collision center consists of a tracking system, which is integrated into a magnetic field. The momentum of the particles is measured by the deflection within the magntic fiels. The tracking system is surrounded by the electromagnetic and hadronic calorimeter, where the deposited energy of the particles is measured. By combining the energy and momentum measurement, the particles can be identified. Unlike the other particles, muons can cross the whole detector. They are detected within the muon spectrometer which is the last layer of the detector.
- LHCb ("Large Hadron Collider beauty Experiment") [46] is designed to investigate heavy flavor, EW and QCD physics by performing precision measurements of the decay of B-mesons. Studying for example the parameters of CP violation will help to explain matter-antimatter asymmetry of the universe.

In march 2010 the LHC started its operation at the highest center of mass energy ever reached. Ever since the first proton-proton collision at 7 TeV, it operated successfully so in 2012 the energy per beam could be increased to 4 TeV. All experimental measurements preformed up to now by the LHC are in excellent agreement with the predictions of the SM. Fig. 2.3 shows the measurement of the mass spectrum for opposite sign muon pairs, which reveals the structure of the bound states produced in hadron collisions decaying into pairs of muons. The first di-muon spectrum has already been recorded only within

[3] In total seven detectors have been installed at the LHC, but the four experiments TOTEM ("Total Elastic and diffractive cross section measurement"), MoEDAL ("Monopole and Exotics Detector At the LHC") and LHCf ("Large Hadron Collider forward") and ALICE ("A Large Ion Collider Experiment") are much smaller and more specialized.

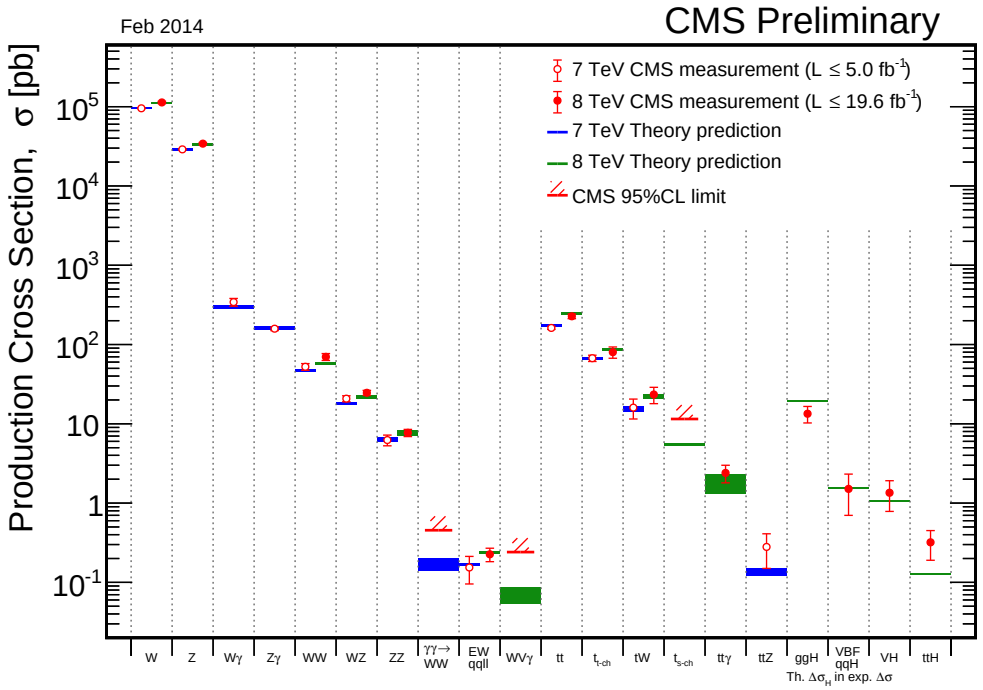

Figure 2.4.: Comparison of a subset of SM total production cross section measurements and the corresponding theoretical expectations at NLO and NNLO taken from Ref. [48].

the first short rediscover phase of data taking recapitulated high energy physics of the last fifty years. The fast re-discovery of the SM is impressive but it is also required to discover new phenomena, since SM processes are used to calibrate the detectors and to understand the background processes. The excellent performance of the LHC became apparent by the discovery of the Higgs boson. On 4th July 2012, its detection by the ATLAS and CMS experiment was announced. The first elementary scalar particle in nature was discoverd, while in 2013 the predicted positive parity and zero spin were confirmed.
In addition to the Higgs discovery, the first observation of a rare decay of a B_S meson in two muons has been recorded by LHCb and CMS. The collected data have been used to perform measurements of many SM processes within a wide cross section range covering many orders of magnitude. Only a short summary of cross section measurement of CMS is shown in Fig. 2.4 together with the theoretical predictions including calcualtions at next-to leading order (NLO) and next-to-next-to-leading order (NNLO) of perturbation theory. It shows an excellent agreement within the uncertainties representing a remarkable achievement of the SM and the LHC.
After two months of heavy ion collisions in 2013 the LHC went into a shutdown for magnet and detector upgrades. For 2015 it is planned to start running at 13-14 TeV. In addition to the collision energy also a luminosity upgrade of the LHC has been proposed for 2020.

3. Supersymmetry - a Theory Beyond the Standard Model

The SM is an extremely successful theory. Its high prescision predictions have been extensively tested over the past forty years . However, a number of fundamental questions are left unanswered, which leads to the believe that the SM is incomplete and should be regarded as an effective theory describing particle physics at the experimentally probed energy scale. Extended theories beyond the SM are required, which include the SM as a low energy limit. Physics beyond the SM can be motivated by the naturalness problem of the SM, which occurs by calculating radiative corrections. Since it gives a hint of the scale of new physics, the naturalness problem is shortly discussed in the following.
Divergent calculations of loop integrals are handled in the SM by regularization e.g. using a Lorentz invariant cut-off Λ, so the leading divergency in any quantity is logarithmic $\delta m \propto m \ln \frac{\Lambda}{m}$. This leads to small radiative corrections even up to the Planck scale[1] $\Lambda \sim M_P \approx 10^{19}$GeV. The divergence is absorbed in a field strength renormalization constant and is associated with the running of the coupling constant. However, this is not valid for a scalar field within the SM, e.g. the Higgs field. The calculation of the radiative correction turns out to be quadratically divergent

$$m_{SM}^2(\text{phys}) \simeq m_{SM}^2 - \frac{c}{16\pi^2}\Lambda^2, \tag{3.1}$$

where m_{SM}^2 corresponds to the Higgs mass parameter squared from the Lagrangian. The second term includes the leading contribution in the cut-off Λ with a numerical coefficient c. The cut-off parameter Λ can be interpreted as the scale up to which the SM is supposed to be valid. If the validity of the SM is assumed to reach the Planck scale given the physical Higgs mass, the Lagrangian mass has to be incredibly fine tuned to provide the needed cancellation from $\sim (10^{19}\ \text{GeV})^2$ to $\sim (10^2\ \text{GeV})^2$. This cancellation is often referred to as the fine-tuning problem in the context of the naturalness of a theory. A reasonable and natural scale for Λ would be the TeV scale. Then new degrees of freedom coming with new physics have to appear at the TeV scale to cancel the quadratic divergencies at all orders of perturbation theory. Since the fermion and boson loops contribute with different signs to the Higgs mass, the cancellation can be managed if the couplings of fermions and bosons are related via a symmetry.
The symmetry which relates the properties of bosons and fermions is called Supersymmetry

[1] The Planck scale corresponds to the energy scale at which quantum effects of gravity become essential.

(SUSY), which will be discussed in more detail in section 3.1. SUSY solves the fine-tuning problem and is able to answer numerous fundamental questions of the SM, which motivates its examination:

- The **hierarchy problem** describes the mismatch of the observed and natural value of the electroweak scale due to radiative corrections. In contrast to the SM, the tiny scale ratio of the EW and the Planck scale is not destabilized by radiative corrections within SUSY.
- The spontaneous **electroweak symmetry breaking** has to be introduced ad hoc within the SM by choosing the negative sign of the mass parameter μ without any explanation for this choice. EWSB occurs naturally within SUSY, since renormalization effects drive the Higgs boson squared mass parameter negative.
- The **mass of the Higgs boson** was measured to be 125 GeV. However, it could have been as heavy as 1 TeV within the SM[2]. The Higgs mass range was only constrained experimentally from precision fits to electroweak data [50]. Unlike the SM, a light Higgs boson below 135 GeV [12] is predicted within the minimal supersymmetric extension of the SM.
- Attempts to embed the SM in a larger gauge symmetry leading to one single force and one unified coupling failed, since the requested unification of the gauge couplings to higher energies is not possible using the SM RGEs, see Fig. 3.1(a). The **unification of the gauge couplings** tends to work well if the couplings are extrapolated using the supersymmetric evolution equations, see Fig. 3.1(b), which was first examined in Ref. [33].
- **Gravitation** although being a fundamental force, is not included in the SM and described separately in general relativity. Local symmetry described by supergravity within SUSY could incorporate general relativity, although remaining non-renormalizable.
- Cosmological observations show that a large fraction of the matter in the universe consists of **dark matter** (DM), which is indicated only by its gravitational effect on visible matter. In contrast to SM particles, the lightest supersymmetric particle is an excellent candidate for cold dark matter, since it provides all needed properties and the correct amount of dark matter.

3.1. Introduction to Supersymmetry

Supersymmetry was evolved in the late 1960s and early 1970s. The first concepts arose in the context of string theory [51–53] until in 1974 Wess and Zumino wrote down the first four-dimensional supersymmetric quantum field theory [54–56]. Many phenomenological studies of SUSY followed [13, 57–59], while the interest in SUSY has grown after recognizing that SUSY provides a solution of the fine-tuning problem. The simplest supersymmetric version of the SM, the Minimal Supersymmetric SM (MSSM) was developed in the early 1980s [7–10] and is ever since of interest of phenomenological and experimental studies [13, 58, 59]. The following short introduction to SUSY and in particular the MSSM is derived from Ref. [10]. More details can be found in reviews or textbooks, see e.g. [7–11, 60] and [12, 49, 61–63].
Within SUSY a bosonic state is turned into a fermionic state and vice versa by a transformation generated by the operator Q which respects

[2] Arguments of the unitarity of the S-matrix, which results from the conservation of probabilities at the quantum level, leads to an upper limit of about 780 GeV [49] on the Higgs boson mass.

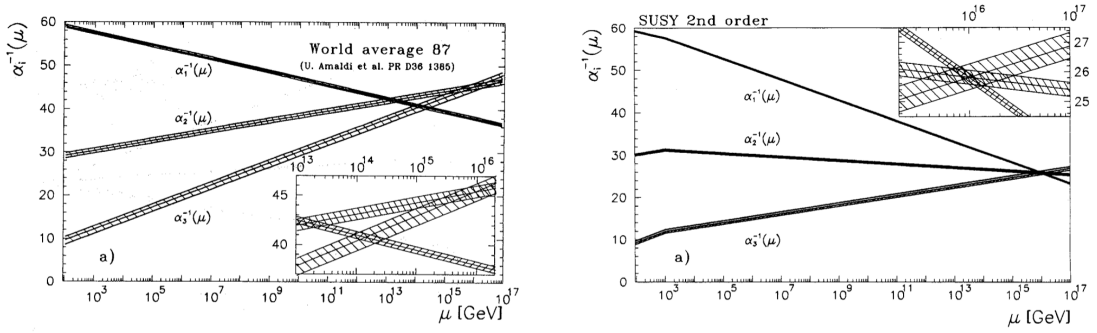

(a) (b)

Figure 3.1.: Evolution of the inverse of the coupling constants within the SM (a) and the supersymmetric extension of the SM (b) taken from [33]. The unification of the couplings is only obtained in the latter case.

$$Q\,|\text{boson}\rangle = |\text{fermion}\rangle\,, \quad Q\,|\text{fermion}\rangle = |\text{boson}\rangle\,. \tag{3.2}$$

The generator Q and the hermitian conjugated $Q^\dagger$ are fermionic operators, i.e. they carry spin angular momentum 1/2. Since SUSY is a space-time symmetry, the generators Q and $Q^\dagger$ must satisfy an algebra with

$$\begin{aligned} \{Q, Q^\dagger\} &= P^\mu, \\ \{Q, Q\} &= \{Q^\dagger, Q^\dagger\} = 0, \\ [P^\mu, Q] &= [P^\mu, Q^\dagger] = 0, \end{aligned} \tag{3.3}$$

where P^μ is the four momentum generator of space-time translations. The irreducible representation of the SUSY algebra, called supermultiplets, contain both fermion and boson states, which are superpartners of each other. The particles in the same supermultiplet have the same representation of the gauge group with the same corresponding quantum numbers, except for the spin.
There are two possible types of supermultiplets: scalar (chiral) and vector (gauge) supermultiplets. Scalar supermultiplets consist of a single Weyl fermion with two spin helicity states and two real scalars, which can be assembled into a complex scalar field. Vector supermultiplets contain a massless spin 1 gauge boson with two helicity states and their fermionic superpartners. In the supersymmetric extension of the SM the known fundamental particles of the SM are organized in supermultiplets along with their superpartners whose spin differ by 1/2 unit. The SM fermions have spin 0 partners named squarks and sleptons[3]. Squarks and sleptons are denoted as left and right-handed which refer to the helicity of the superpartners. The Higgs scalar boson is arranged in a chiral supermultiplet with the spin 1/2 superpartner, the Higgsino[4]. Two Higgs chiral supermultiplets are needed for the MSSM to be a consistent quantum field theory. Only one Higgs supermultiplet would lead to a gauge anomaly. Furthermore, no anti-chiral superfields can be involved into the Lagrangian, so two Higgs supermultiplets with $Y = \pm 1$ are necessary to have Yukawa couplings both to the up- and down-type fermions. The fields are denoted accordingly as H_u and H_d, with an electric charged and neutral component according to

[3]The scalar superpartners to the SM fermions are denoted by prepending an "s". The symbols for the sfermions differ by a tilde from the corresponding SM particles.

[4]The nomenclature for the spin 1/2 superpartners to the SM bosons is to append "ino" to the corresponding SM name. The symbols are marked with an additional tilde.

Table 3.1.: Summary of the chiral and gauge supermultiplet fields representing the particle content of the MSSM taken from Ref. [12]. The particles are classified according to the transformation properties under the SM gauge group.

Names		spin 0	spin 1/2	$SU(3)_C$	$SU(2)_L$	$U(1)_Y$
squarks, quarks	Q	$(\tilde{u}_L, \tilde{d}_L)$	(u_L, d_L)	**3**	**2**	1/3
	$\bar{u}$	$\tilde{\bar{u}}_L = \tilde{u}_R^\dagger$	$\bar{u}_L = (u_R)^c$	$\bar{\mathbf{3}}$	**2**	-4/3
	$\bar{d}$	$\tilde{\bar{d}}_L = \tilde{d}_R^\dagger$	$\bar{d}_L = (d_R)^c$	$\bar{\mathbf{3}}$	**2**	2/3
sleptons, leptons	L	$(\tilde{\nu}_{eL}, \tilde{e}_L)$	(ν_{eL}, e_L)	**1**	**2**	-1
	$\bar{e}$	$\tilde{\bar{e}}_L = \tilde{e}_R^\dagger$	$\bar{e}_L = (e_R)^c$	**1**	**1**	2
Higgs, Higgsinos	H_u	(H_u^+, H_u^0)	$(\tilde{H}_u^+, \tilde{H}_u^0)$	**1**	**2**	1
	H_d	(H_d^0, H_d^-)	$(\tilde{H}_d^0, \tilde{H}_d^-)$	**1**	**2**	-1

Names	spin 1/2	spin 1	$SU(3)_C$	$SU(2)_L$	$U(1)_Y$
gluinos, gluons	$\tilde{g}$	g	**8**	**1**	0
winos, W bosons	$\tilde{W}^\pm, \tilde{W}^0$	$W^\pm, W^0$	**1**	**3**	0
bino, B boson	$\tilde{B}$	B	**1**	**1**	0

the weak isospin component. The SM bosons and their superpartners, the gauginos, are described in gauge supermultiplets. Combining all supermultiplets the number of particles within the MSSM is essentially doubled compared to the SM. The particle content of the MSSM is summarized in Table 3.1. The particles are classified according to their transformation properties under the SM gauge group. The chiral supermultiplets are defined in terms of left-handed Weyl spinors, so the right-handed particle fields can be accommodated within the left-type convention by regarding them as the charge conjugated of the left-type anti-particles fields which appear in Table 3.1. A generation index can be added to the particle fields according to the three fermion generations.

If SUSY would be exact, the masses of the summarized superpartners in Table 3.1 would be equal. Since no superpartners have been discovered so far, SUSY has to be broken. In order to still provide the cancellation of the quadratic divergencies in scalar squared masses to all orders in perturbation theory, a so-called soft breaking of SUSY is required. This is maintained since the dimensionless couplings λ are related by introducing additional scalar fields to the SM fermions. But the breaking of SUSY still leads to logarithmic corrections of the order of $\lambda(m_H^2 - m_f^2)\ln\Lambda$. Since the mass splitting of the SM particles and their superpartners determines the size of the logarithmic correction, the superpartners cannot be too heavy, otherwise the corrections would be again unnaturally large. Especially the stop and sbottoms as well as the winos and binos give large contributions to $\delta m_{H_u}^2$ and $\delta m_{H_d}^2$. Assuming $\Lambda \approx M_p$ and $\lambda \approx 1$ the lightest superpartner should not be much heavier than the TeV scale to avoid again a fine-tuning problem.
The corresponding effective Lagrangian of the MSSM can be divided into two parts:

$$\mathcal{L} = \mathcal{L}_{\text{SUSY}} + \mathcal{L}_{\text{soft}}. \tag{3.4}$$

The first term is the SUSY generalization of the SM, which contains all gauge and Yukawa interactions $\mathcal{L}_{\text{SUSY}} = \mathcal{L}_{\text{gauge}} + \mathcal{L}_{\text{yukawa}}$ and preserves SUSY invariance. The interactions and particle masses in $\mathcal{L}_{\text{SUSY}}$ are determined by their gauge transformation properties and by the superpotential W. W is incorporated into $\mathcal{L}_{\text{yukawa}}$ and its form is restricted by the requirement of gauge invariance. The MSSM superpotential reads [11]

$$W = \epsilon_{ij}(\mathbf{y^u}_{ab} Q_a^j \bar{u}_b H_u^i + \mathbf{y^d}_{ab} Q_a^j \bar{d}_b H_d^i + \mathbf{y^L}_{ab} L_a^j \bar{e}_b H_d^i + \mu H_u^i H_d^j), \tag{3.5}$$

where $i, j = 1, 2$ are the $SU(2)$ and $a, b, d = 1, 2, 3$ the generation indices. The color indices are suppressed for simplicity but can be added as a further index. The dimensionless Yukawa parameters $\mathbf{y^u}, \mathbf{y^d}, \mathbf{y^d}$ are 3×3 matrices in family space.
The superpotential resembles Eq. 2.17 after exchanging the SM fields with the superfields listed in Table 3.1 except for the last term since the Higgs mixing is absent in the SM. In fact further terms in addition to those in Eq. 3.5 exist which violate either baryon (B) or lepton (L) number. The non observation of proton decay and many other processes give strong constraints on the baryon or lepton number violation, e.g. [64, 65], thus such terms must either be suppressed or excluded in nature. To preserve B- and L-conservation a new global $U(1)_R$ symmetry, called R-symmetry, is added to the MSSM, which eliminates only $B - L$ violating terms in the renormalizable superpotential. The corresponding multiplicatively conserved quantum number, the R-Parity, is defined by

$$R = (-1)^{3(B-L)+2S}. \tag{3.6}$$

According to Eq. 3.6, SM particles have a R-parity of $+1$ while SUSY particles carry $R = -1$. If R-Parity is conserved sparticles can only be produced in pairs and heavy sparticle will decay eventually in the stable lightest supersymmetric particle.

The second term in the Lagrangian of Eq. 3.4 includes the SUSY violating soft breaking terms. The construction of these soft breaking terms is described in [10] for the MSSM and leads to

$$\begin{aligned}
\mathcal{L}_{\text{soft}} = &-\frac{1}{2}\left(M_3 \tilde{g}\tilde{g} + M_2 \tilde{W}\tilde{W} + M_1 \tilde{B}\tilde{B} + h.c.\right) \\
&- \left(\tilde{\bar{u}}_L \mathbf{a_u} \tilde{Q} H_u - \tilde{\bar{d}}_L \mathbf{a_d} \tilde{Q} H_d - \tilde{\bar{e}}_L \mathbf{a_e} \tilde{L} H_d + h.c.\right) \\
&- \tilde{Q}^\dagger \mathbf{m_Q^2} \tilde{Q} - \tilde{L}^\dagger \mathbf{m_L^2} \tilde{L} - \tilde{\bar{u}}_L^\dagger \mathbf{m_{\bar{u}}^2} \tilde{\bar{u}}_L - \tilde{\bar{d}}_L^\dagger \mathbf{m_{\bar{d}}^2} \tilde{\bar{d}}_L - \tilde{\bar{e}}_L^\dagger \mathbf{m_{\bar{e}}^2} \tilde{\bar{e}}_L \\
&- m_{H_u}^2 H_u^\dagger \cdot H_u - m_{H_d}^2 H_d^\dagger \cdot H_d - (b H_u \cdot H_d + h.c.).
\end{aligned} \tag{3.7}$$

M_1, M_2, M_3 represent the gaugino mass terms, while $(\mathbf{m_Q^2}, \mathbf{m_{\bar{u}}^2}, \mathbf{m_{\bar{d}}^2}, \mathbf{m_L^2}, \mathbf{m_{\bar{e}}^2})$ are 3×3 matrices in family space and correspond to the squark and slepton mass terms. The triple scalar couplings are described by the complex 3×3 dimensional matrices $\mathbf{a_u}, \mathbf{a_d}, \mathbf{a_e}$. The last line contains the supersymmetric breaking contribution to the Higgs potential with the squared mass terms $m_{H_u}^2$, $m_{H_d}^2$ and b. $\mathcal{L}_{\text{soft}}$ leads the required soft breaking, i.e. the cancellation of the quadratic divergencies in the radiative correction of all scalar masses to all orders in perturbation theory. Such terms are independent of the breaking mechanism. Even though different breaking mechanisms lead to common results for the soft breaking terms, the supersymmetric models which are further discussed refer to the supergravity mechanism of SUSY breaking (minimal supergravity, mSUGRA). This breaking mechanism leads to a simplification of the soft terms using unified boundary conditions for masses and couplings at the GUT scale. This will be further discussed in section 3.3. All mass relations calculated at low scale by the RGEs apply these mSUGRA/GUT boundary conditions. For more details on different SUSY breaking mechanism see Refs. [10, 11].

3.1.1. Electroweak Symmetry Breaking

The minimum of the Higgs potential in the supersymmetric extension of the SM should break electroweak symmetry down to electromagnetism $SU(2)_L \times U(1)_Y \to U(1)_{\text{em}}$, as

already described in section 2.1.1.2 for the SM. The mechanism has to be applied to the extended Higgs sector in the MSSM which consits of the two complex Higgs doublets

$$H_u = \begin{pmatrix} H_u^+ \\ H_u^0 \end{pmatrix} \quad \text{and} \quad H_d = \begin{pmatrix} H_d^0 \\ H_0^- \end{pmatrix}. \tag{3.8}$$

Possible vevs for the charged components of the Higgs scalar are rotated away by using a $SU(2)_L$ gauge transformation, which assures unbroken electromagnetism at the minimum of the potential. Using these simplifications the corresponding Higgs potential includes only the neutral component and reads

$$\begin{aligned} V =& (|\mu|^2 + m_{H_u}^2)|H_u^0|^2 + (|\mu|^2 + m_{H_d}^2)|H_d^0|^2 - (bH_u^0 H_d^0 + h.c.) \\ &+ \frac{1}{8}(g_1^2 + g_2^2)(|H_u^0|^2 - |H_d^0|^2)^2. \end{aligned} \tag{3.9}$$

In order to allow for real positive solutions and a potential which is bounded from below, the following inequalities are required

$$\begin{aligned} &2b < 2|\mu|^2 + m_{H_u}^2 + m_{H_d}^2, \\ &b^2 > (|\mu|^2 + m_{H_u}^2)(|\mu|^2 + m_{H_d}^2). \end{aligned} \tag{3.10}$$

Both inequalities can only be fulfilled simultaneously, if at least one of the Higgs mass squared is negative, which is not applicable at the GUT scale due to the boundary conditions. However, for a lower energy scale a negative mass squared naturally occurs for $m_{H_u}^2$, because of the large top Yukawa coupling contribution in the RGE. In this way the top mass was predicted to be heavy well before its discovery [66]. This mechanism is referred to as radiative electroweak symmetry breaking. The vevs of the doublets

$$\langle H_u^0 \rangle = \frac{1}{\sqrt{2}} v_u \quad \text{and} \quad \langle H_d^0 \rangle = \frac{1}{\sqrt{2}} v_d \tag{3.11}$$

are related to the Z^0 boson mass and the electroweak gauge couplings via $v_u^2 + v_d^2 = v^2 = 4m_Z^2/(g_1^2 + g_2^2) \approx (256 \text{ GeV})^2$. Their ratio is defined as $\tan\beta \equiv v_u/v_d = \frac{v \sin\beta}{v \cos\beta}$, which varies within $0 < \beta < \pi/2$ for real and positive vevs[5]. The minimization condition $\partial V/\partial H_u^0 = \partial V/\partial H_d^0 = 0$ has to be satisfied, which leads to the following relations at tree level using $\tan\beta$ and the Z^0 boson mass m_Z:

$$\begin{aligned} \sin(2\beta) &= \frac{2b}{m_{H_u}^2 + m_{H_d}^2 + 2|\mu|^2}, \\ m_Z^2 &= \frac{|m_{H_d}^2 - m_{H_u}^2|}{\sqrt{1 - \sin^2(2\beta)}} - m_{H_u}^2 - m_{H_d}^2 - 2|\mu|^2. \end{aligned} \tag{3.12}$$

If the soft breaking mass terms of the Higgs fields $m_{H_u}^2$ and $m_{H_d}^2$ are known at the weak scale because of the RGEs, together with the knowledge of the Z^0 boson mass and $\tan\beta$, the values of b and μ are fixed due to EWSB, while the sign of μ is undetermined. The physical fields and their masses are obtained by expanding the two complex scalar fields H_u and H_d

[5] To avoid large non perturbatively top and bottom Yukawa couplings, $\tan\beta$ should be larger than ~ 1.2 and less than ~ 60, whereas the exact boundary values depend on the top quark mass.

Table 3.2.: Couplings from the neutral Higgs bosons $\phi = h^0, H^0, A^0$ to up-/down-type fermions and gauge bosons normalized to the SM Higgs couplings taken from [67].

ϕ	$g_{\phi dd}$	$g_{\phi uu}$	$g_{\phi VV}$
h^0	$-\frac{\sin\alpha}{\cos\beta}$	$\frac{\cos\alpha}{\sin\beta}$	$\sin(\beta-\alpha)$
H^0	$\frac{\cos\alpha}{\cos\beta}$	$\frac{\sin\alpha}{\sin\beta}$	$\cos(\beta-\alpha)$
A^0	$\tan\beta$	$\cot\beta$	0

around the vacuum into real and imaginary parts. The mass matrices are evaluated for the fields at the minimum and diagonalized, i.e. rotation matrices are chosen to get diagonal squared masses in terms of the mass eigenstates fields. Three of the eight real, scalar degrees of freedom of two complex $SU(2)_L$ Higgs doublets become the longitudinal modes of the massive Z^0 and $W^\pm$ bosons after EWSB. The remaining five Higgs scalar mass eigenstates consist of two CP-even neutral scalars h^0 and H^0, one CP-odd neutral scalar A^0 and two charged scalars $H^\pm$. The corresponding physical squared masses m_h^2, m_H^2, m_A^2 and $m_{H^\pm}^2$ at tree level read

$$\begin{aligned} m_A^2 &= 2b/\sin(2\beta) = 2|\mu|^2 + m_{H_u}^2 + m_{H_d}^2, \\ m_{h,H}^2 &= \frac{1}{2}\left(m_A^2 + m_Z^2 \mp \sqrt{(m_A^2 - m_Z^2)^2 + 4m_Z^2 m_A^2 \sin^2(2\beta)}\right), \\ m_{H^\pm}^2 &= m_A^2 + m_W^2. \end{aligned} \tag{3.13}$$

The mixing angle α fulfills

$$\frac{\sin 2\alpha}{\sin 2\beta} = -\left(\frac{m_H^2 + m_h^2}{m_H^2 - m_h^2}\right), \quad \frac{\tan 2\alpha}{\tan 2\beta} = \left(\frac{m_A^2 + m_Z^2}{m_A^2 - m_Z^2}\right) \tag{3.14}$$

and varies within $-\pi/2 < \alpha < 0$. The MSSM Higgs sector can be fully described by two free parameters, which are often chosen to be $\tan\beta$ and m_A^0. Table 3.2 shortly summarize the couplings of the neutral Higgs bosons to up-/down-type fermions and gauge bosons, which are determined by the two angles α and β, while a complete overview of the Higgs couplings can be found in [41].

The masses of the heavier Higgses A^0, H^0 and $H^\pm$ can be arbitrarily large, but the mass of the lightest Higgs boson h^0 is bound from above at tree level by the Z^0 boson mass $m_h < m_Z|\cos(2\beta)|$. However, the one-loop contributions to the light Higgs boson mass m_h shift the mass up to larger values. The main contributions are coming from the one-loop diagrams involving top quarks and squarks as shown in Fig. 3.2. The additional corrections are of the order of

$$\Delta(m_h^2) = \frac{3}{4\pi^2}\cos^2\alpha\ y_t^2 m_t^2\ \ln\left(m_{\tilde{t}_1} m_{\tilde{t}_2}/m_t^2\right), \tag{3.15}$$

including the stop mass eigenstates $m_{\tilde{t}_1}, m_{\tilde{t}_2}$ resulting from the mixing of the left- and right-handed stops. A major contribution even occurs for large stop mixing. Including the stop and other important corrections, see e.g. [68–71], the bound on the Higgs mass is weaker and around $m_h \lesssim 135$ GeV, if the sparticles contributing to the loops are assumed to have masses below 1 TeV. In the so-called decoupling limit, $m_A \gg m_Z$, the mass of the lightest Higgs boson saturates the upper bound and the heavier Higgs masses m_H and m_A are nearly degenerated. The corresponding mixing angle α approximates $\beta - \pi/2$. This leads to SM Higgs couplings to quarks, leptons and electroweak gauge bosons for the lightest Higgs boson, as can be extracted from Table 3.2.

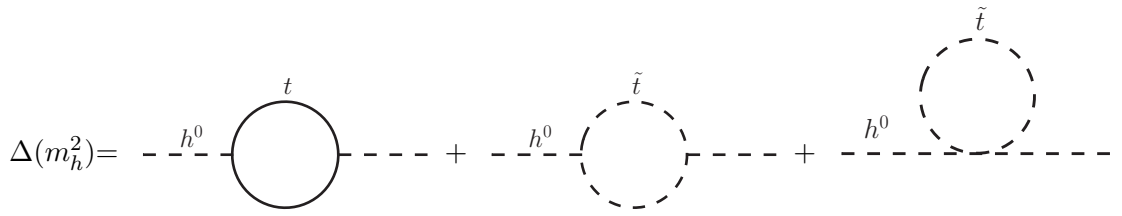

Figure 3.2.: Dominant one loop diagrams from stop and top contributing to the lightest Higgs boson mass in the MSSM. A large positive correction is coming from the incomplete cancellation due to the soft breaking terms.

3.2. The μ-problem and the Next-To-Minimal Supersymmetric Standard Model

Radiative electroweak symmetry breaking occurs naturally in the MSSM in contrast to the SM, but a problem still persist. It refers to the naturalness of the μ parameter, which is illustrated by expanding Eq. 3.12 for large $\tan\beta$:

$$m_Z^2 = -2(m_{H_u}^2 + |\mu|^2) + \frac{2}{\tan^2\beta}(m_{H_d}^2 - m_{H_u}^2) + \mathcal{O}(1/\tan^4\beta). \tag{3.16}$$

μ is a SUSY respecting parameter appearing in the superpotential, while the other masses are SUSY breaking parameters. Although being unrelated they have to cancel within one order of magnitude to get a Higgs vev of the order of $\mathcal{O}(10^2)$ as shown in Eq. 3.16. There is no reason for μ to be of the order of m_{soft}, so small compared to M_P. Several extensions of the MSSM have been proposed to solve this so-called μ-problem [72]. One possibility is the next-to-minimal supersymmetric SM (NMSSM), whose main features will shortly be discussed in this section mainly derived from Ref. [73] and [74]. For more details see e.g. Refs. [73–78].

Within the NMSSM the Higgs sector is further extended by introducing a new, additional Higgs singlet field S. This opens the possibility of new contributions to the superpotential e.g. an interaction term $\lambda S H_u H_d$ of the Higgs singlet with the two doublets. The μ term present in the MSSM is absent at tree-level before symmetry breaking and arises if the scalar field S acquires a non-zero expectation values. An effective μ_{eff} term is generated, which is expected to be naturally of the order of the electroweak scale $\mu_{eff} = \lambda\langle S\rangle$, since μ_{eff} is dynamically linked to the vev of the singlet. However, this minimal extended scenario possesses a global $U(1)$ Peccei-Quinn (PQ) symmetry [79]. The spontaneous breaking of this symmetry at electroweak scale, leads to a phenomenologically excluded axion [80, 81]. To remove the unwanted PQ symmetry a cubic self coupling $\frac{1}{3}\kappa S^3$ is added to the superpotential, which leads to a discrete Z_3 symmetry $\Psi \to e^{2\pi i/3}\Psi$, whose breaking gives rise to cosmological weak scale domain walls [82]. This would lead to unacceptable large anisotropies in the cosmic microwave background [83]. The breaking of the Z_3 symmetry itself causes divergent tadpole contributions, which destabilize the mass hierarchy [84]. More details about the breaking can be found in [77, 78], where scenarios are introduced enabling an adequate Z_3 symmetry breaking, i.e. the surviving tadpole terms are sufficiently suppressed to not upset the mass hierarchy but to be large enough to prevent the domain walls.
The resulting superpotential for the NMSSM is described by

$$W_{NMSSM} = W_{MSSM} + \lambda S H_u H_d + \frac{1}{3}\kappa S^3, \tag{3.17}$$

where W_{MSSM} denotes the first three terms in Eq. 3.5. λ and κ are dimensionless couplings, while S represents the chiral supermultiplet, which contains a real scalar and pseudo-scalar boson and a Weyl fermion, the singlino. These fields have no gauge couplings to their own, so the can only interact with SM particles by mixing with the neutral MSSM fields with the same spin and charge. The two additional bosons mix with the scalar and pseudo-scalar Higgs bosons, which leads in total to seven Higgs bosons: H_1, H_2, H_3, A_1, A_2 and $H^{\pm}$. The singlino mixes with the four MSSM neutralinos inducing overall five neutralinos: $\chi_1^0, \chi_2^0, \chi_3^0, \chi_4^0$ and χ_5^0. The modified Higgs sector is discussed in the next section, whereas the modified neutralino sector will summarized in section 3.4.

3.2.1. The Higgs Sector in the Next-To-Minimal Supersymmetric Standard Model

The NMSSM superpotential combined with the corresponding soft breaking terms lead to the following tree level Higgs potential for the two Higgs doublets and the singlet S [75]:

$$\begin{aligned} V =& |\lambda S|^2(|H_u|^2 + |H_d|^2) + |\lambda H_u H_d + \kappa S^2|^2 \\ &+ \frac{g_1^2 + g_2^2}{8}(|H_d|^2 - |H_u|^2)^2 + \frac{g_2^2}{2}|H_u^\dagger H_d|^2 \\ &+ m_{H_u}^2|H_u|^2 + m_{H_d}^2|H_d|^2 + m_S^2|S|^2 + (\lambda A_\lambda S H_u H_d + \frac{1}{3}\kappa A_\kappa S^3 + h.c.). \end{aligned} \tag{3.18}$$

Here the notation $H_u H_d \equiv \epsilon_{\alpha\beta}(H_u)^\alpha (H_d)^\beta = H_u^+ H_d^- - H_u^0 H_d^0$ is used. The last line in Eq. 3.18 results from the soft SUSY breaking terms and includes dimensionful coefficients and soft mass terms for the fields. Additional parameters A_λ, A_κ and m_S are introduced to the MSSM soft mass terms m_{H_u} and m_{H_d}. The convention of a real combination of $\lambda\kappa^*$ is adopted to avoid CP violation at tree level in the Higgs sector. The Higgs singlet field decouples in the MSSM limit, which is reached if the couplings λ and κ vanish for fixed A_λ and A_κ. EWSB can be applied for the modified Higgs potential in Eq. 3.18 analogous to the MSSM. The vevs are described by

$$\langle H_d \rangle = \frac{1}{\sqrt{2}} v_d, \quad \langle H_u \rangle = \frac{1}{\sqrt{2}} v_u \quad \text{and} \quad \langle S \rangle = \frac{1}{\sqrt{2}} v_s, \tag{3.19}$$

where v_u and v_d resemble the MSSM relation $v_u^2 + v_d^2 = v^2 = 4m_Z^2/(g_1^2 + g_2^2) \approx (246\ \text{GeV})^2$. Adopting the vevs into the potential, the following three minimization conditions[6] are obtained which connect the soft mass terms to the vevs of the Higgs fields:

$$\begin{aligned} m_{H_d}^2 &= \frac{g_1^2 + g_2^2}{8}(v_u^2 - v_d^2) - \frac{1}{2}\lambda^2 v_u^2 + \frac{1}{2}(\sqrt{2}A_\lambda + \kappa v_s)\lambda v_s \frac{v_u}{v_d} - \frac{1}{2}\lambda^2 v_s^2, \\ m_{H_u}^2 &= \frac{g_1^2 + g_2^2}{8}(v_d^2 - v_u^2) - \frac{1}{2}\lambda^2 v_d^2 + \frac{1}{2}(\sqrt{2}A_\lambda + \kappa v_s)\lambda v_s \frac{v_d}{v_u} - \frac{1}{2}\lambda^2 v_s^2, \\ m_S^2 &= -\kappa^2 v_s^2 - \frac{1}{2}\lambda^2 v^2 + \kappa\lambda v_u v_d + \frac{1}{\sqrt{2}}\lambda A_\lambda \frac{v_u v_d}{v_s} - \frac{1}{\sqrt{2}}\kappa A_\kappa v_s. \end{aligned} \tag{3.20}$$

The values of λ,κ and $\mu_{eff} = \lambda\langle s \rangle$ are fixed, if the soft breaking mass terms of the Higgs fields and the trilinear couplings are known at the weak scale from the RGEs together with the Z^0 boson mass and tanβ. The sign of μ_{eff} stays undetermined. The tree level Higgs matrices can be extracted after expanding the full scalar potential around the vevs.

[6] A general analysis of the local minima of the superpotential is given in Ref. [74].

The potential provides the following non zero mass terms after applying a rotation to the Higgs fields:

$$M_{H^\pm}^2 H^+ H^- + \frac{1}{2}\begin{pmatrix} P_1 & P_2 \end{pmatrix} \mathcal{M}_-^2 \begin{pmatrix} P_1 \\ P_2 \end{pmatrix} + \frac{1}{2}\begin{pmatrix} S_1 & S_2 & S_3 \end{pmatrix} \mathcal{M}_+^2 \begin{pmatrix} S_1 \\ S_2 \\ S_2 \end{pmatrix}. \tag{3.21}$$

The charged fields correspond already to the physical mass eigenstates with the tree level masses of the charged fields $H^\pm$ of

$$M_{H^\pm}^2 = M_A^2 + M_W^2 - \frac{1}{2}(\lambda v)^2, \tag{3.22}$$

which includes

$$M_A^2 = \frac{\lambda v_s}{\sin 2\beta}(\sqrt{2}A_\lambda + \kappa v_s). \tag{3.23}$$

In contrast to the charged Higgs fields the CP-odd matrix $\mathcal{M}_-^2$ of the pseudo-scalar fields $P_i (i = 1, 2)$ and the CP-even matrix $\mathcal{M}_+^2$ of the scalar fields $S_i (i = 1, 2, 3)$ have to be further rotated to get the physical mass eigenstates. The matrix elements of the pseudo-scalar mass matrix $\mathcal{M}_-^2$ read

$$\begin{aligned} \mathcal{M}_{-11}^2 &= M_A^2, \\ \mathcal{M}_{-12}^2 &= \frac{1}{2}(M_A^2 \sin 2\beta - 3\lambda\kappa v_s^2)\frac{v}{v_s}, \\ \mathcal{M}_{-22}^2 &= \frac{1}{4}(M_A^2 \sin 2\beta + 3\lambda\kappa v_s^2)\frac{v^2}{v_s^2} - 3\kappa v_s A_\kappa/\sqrt{2}. \end{aligned} \tag{3.24}$$

The top left entry of the CP-odd squared mass matrix is defined to be M_A^2, which is equal to the pseudo-scalar Higgs boson mass in the MSSM limit. The 3×3 scalar mass matrix $\mathcal{M}_+^2$ contains the following elements

$$\begin{aligned} \mathcal{M}_{+11}^2 &= M_A^2 + (M_Z^2 - \frac{1}{2}(\lambda v)^2)\sin^2 2\beta, \\ \mathcal{M}_{+12}^2 &= -\frac{1}{2}(M_Z^2 - \frac{1}{2}(\lambda v)^2)\sin 4\beta, \\ \mathcal{M}_{+13}^2 &= -\frac{1}{2}(M_A^2 \sin 2\beta + \lambda\kappa v_s^2)\frac{v}{v_s}\cos 2\beta, \\ \mathcal{M}_{+22}^2 &= M_Z^2 \cos^2 2\beta + \frac{1}{2}(\lambda v)^2 \sin^2 2\beta, \\ \mathcal{M}_{+23}^2 &= \frac{1}{2}(2\lambda^2 v_s^2 - M_A^2 \sin^2 2\beta - \lambda\kappa v_s^2 \sin 2\beta)\frac{v}{v_s}, \\ \mathcal{M}_{+33}^2 &= \frac{1}{4}M_A^2 \sin^2 2\beta \frac{v^2}{v_s^2} + 2\kappa^2 v_s^2 + \kappa v_s A_\kappa/\sqrt{2} - \frac{1}{4}\lambda\kappa v^2 \sin 2\beta. \end{aligned} \tag{3.25}$$

The Higgs masses are sorted according to their mass after the diagonalization of $\mathcal{M}_-^2$ and $\mathcal{M}_+^2$, which gives in total three scalar Higgs bosons H_1, H_2, H_3 and two pseudo-scalar Higgs bosons A_1, A_2. While in the MSSM the Higgs sector is defined by two free parameters, six free parameters are needed to describe the Higgs sector in the NMSSM:

$$\lambda,\ \kappa,\ A_\kappa,\ A_\lambda,\ \tan\beta \text{ and } \mu_{eff}.$$

A simple analytic solution of the eigenvalues for a 3×3 matrix does not exist so only approximate solutions for the scalar Higgs bosons are available. For large values of $\tan\beta$ and m_A the masses of the two lightest Higgs bosons read [73]

$$\begin{aligned} M^2_{H_{1/2}} \approx \frac{1}{2}\Bigg\{ & M_Z^2 + \frac{1}{2}\kappa v_s(4\kappa v_s + \sqrt{2}A_\kappa) \\ & \mp\sqrt{[M_Z^2 - \frac{1}{2}\kappa v_s(4\kappa v_s + \sqrt{2}A_\kappa)]^2 + \frac{v^2}{v_s^2}[2\lambda^2 v_s^2 - M_A^2 \sin^2 2\beta]^2}\Bigg\}. \end{aligned} \tag{3.26}$$

Two features of the NMSSM Higgs sector can be derived from Eq. 3.26:

- Given the sum rule $M^2_{H_1} + M^2_{H_2} \approx M_Z^2 + \frac{1}{2}\kappa v_s(4\kappa v_s + \sqrt{2}A_\kappa)$, the second lightest scalar Higgs boson mass is maximized if the lightest one approaches zero.
- M_A is restricted to a narrow allowed range around $M_A \approx \sqrt{2}\lambda v_s / \sin 2\beta$ to respect a positive light Higgs mass squared.

Like in the MSSM, higher order corrections dominated by top and stop loops affect the tree level Higgs masses. The lightest Higgs boson can be approximated to

$$\begin{aligned} M^2_{SM} \simeq\ & M_Z^2 \cos^2 2\beta + \lambda^2 v^2 \sin^2 2\beta - \frac{\lambda^2}{\kappa^2} v^2 (\lambda - \kappa \sin 2\beta)^2 \\ & + \frac{3 m_t^4}{4\pi^2 v^2}\left(\ln\left(\frac{m_{\tilde{t}}^2}{m_t^2}\right) + \frac{A_t^2}{m_{\tilde{t}}^2}\left(1 - \frac{A_t^2}{12 m_{\tilde{t}}^2}\right)\right). \end{aligned} \tag{3.27}$$

Here the soft SUSY breaking stop mass squared are assumed to satisfy $m_{\tilde{t}}^2 \sim m_{Q_3}^2 \gg m_t^2$ [74]. The couplings of the Higgs bosons to quarks and fermions are modified according to the mixing matrix. A large fraction of the singlet component for a Higgs boson indicates a reduction of the MSSM-like couplings due to the sum rule of the mixing matrix elements. A summary of all tree level couplings can be found in [74].

3.3. Constrained Supersymmetric Models

The minimal supersymmetric extension of the SM, although called minimal, introduces many free parameters in addition to the SM parameters, which arises from the soft SUSY breaking as already discussed in section 3.1. Counting all free parameters describing masses, couplings and mixing angles in the soft SUSY breaking terms, leads in total to 105 free additional parameters [85]. In the most general form the MSSM contains new sources of CP violation and FCNC due to off-diagonal elements of the squark and slepton mixing matrices. However, a large amount of the parameter space could already be excluded experimentally [86] and will not further be considered. Within the framework of minimal supergravity [87–89], which includes the gravity mediated breaking of SUSY, such off-diagonal terms are naturally suppressed. As a result the soft breaking parameters at high energy, e.g. the GUT scale, take the following simple form for the MSSM[7]:

[7] These equations can be extended according to the additional parameters in the NMSSM.

$$\begin{aligned} \mathbf{m_Q^2} = \mathbf{m_{\bar{u}}^2} = \mathbf{m_{\bar{d}}^2} = \mathbf{m_L^2} = \mathbf{m_{\bar{e}}^2} &= m_0^2\mathbf{1}, \\ M_1 = M_2 = M_3 &= m_{1/2}, \\ m_{H_u}^2 = m_{H_d}^2 &= m_0^2, \\ \mathbf{a_u} = A_0\mathbf{y_u}, \mathbf{a_d} = A_0\mathbf{y_d}, \mathbf{a_e} &= A_0\mathbf{y_e}, \\ b &= B_0\mu. \end{aligned} \tag{3.28}$$

The RGEs are used to compute the low energy values of the parameters according to the unified boundary conditions for the SUSY masses and couplings at the GUT scale. The spectrum of the simplest SUSY model, the so-called constrained MSSM (CMSSM)[8], is determined by five free parameter

$$m_0,\ m_{1/2},\ A_0,\ \tan\beta \text{ and } \mathrm{sgn}(\mu).$$

The unification of the Higgs and the scalar sector at high energies has no theoretical motivation, so the universality of the scalar masses can be relaxed, which decouples the squared masses of the Higgs boson and squark/sleptons. Such SUSY models are denoted as non-universal Higgs (NUH) mass models. The free Higgs mass squared $m_{H_u}^2$ and $m_{H_d}^2$ at the GUT scale introduce two additional free parameters at the high energy scale, which can be easily replaced by two equivalent parameters at a low scale e.g. m_A and μ. In total the NUH-CMSSM is determined by six free parameters:

$$m_0,\ m_{1/2},\ A_0,\ \tan\beta,\ m_A \text{ and } \mu.$$

The constrained and non-universal Higgs model can be adopted to the NMSSM: the most common choice for the free parameters of the constrained NMSSM (CNMSSM) are the following six parameters [90]:

$$m_0,\ m_{1/2},\ A_0,\ \tan\beta,\ \mathrm{sgn}(\mu) \text{ and } \lambda.$$

The singlet mass squared, the singlet vev and κ are determined by the minimization equations of the scalar potential according to the input parameters, while the sign of μ_{eff} is free. The non-universal Higgs model within the NMSSM, also known as semi-constrained NMSSM, allows the soft mass terms and the trilinear couplings involving the Higgs singlet to differ from the unified scalar masses and couplings. The SUSY spectrum is determined by the following set of free parameters [91, 92]:

$$m_0,\ m_{1/2},\ A_0,\ \tan\beta,\ \lambda,\ \kappa,\ A_\lambda,\ A_\kappa \text{ and } \mu_{eff}.$$

The sign convention, see Ref. [93], fixes λ and $\tan\beta$ to be positive whereas $\kappa, A_\lambda, A_\kappa$ and μ_{eff} can have both.

Table 3.3 summarizes the input parameters indicated by a cross for each analyzed SUSY model. The overview of the parameters and the corresponding multi-dimensional parameter space of the constrained SUSY models refer to the available options in the applied software package calculating the SUSY mass spectrum. Note that the free parameters can be replaced by each other according to the minimization conditions and mass relations. The common masses m_0 and $m_{1/2}$ as well as the trilinear couplings A_0, A_κ, A_κ are defined at the GUT scale. $\tan\beta$ is given at M_Z, while the couplings λ, κ and the Higgs mixing parameter μ_{eff} are specified at the SUSY scale. For the NUH-CMSSM m_A and μ_{eff} are defined at the EWSB scale.

[8] mSUGRA is not equal to the CMSSM, since mSUGRA implies a further assumption for the gravitino mass $m_{3/2} = m_0$, which is independent in the CMSSM.

Table 3.3.: Summary of the parameters for the corresponding constrained and non-universal Higgs mass SUSY models. The crosses mark the input parameters for the corresponding SUSY model.

	CMSSM	NUH-CMSSM	CNMSSM	NUH-CNMSSM
m_0	x	x	x	x
$m_{1/2}$	x	x	x	x
A_0	x	x	x	x
$\tan\beta$	x	x	x	x
$\text{sign}(\mu)$	x		x	
λ			x	x
κ				x
m_A/A_λ		x		x
A_κ				x
μ/μ_{eff}		x		x

3.4. Sparticle Masses

The SUSY mass spectrum at low energy is given by the evolution of the masses and couplings from the high to the low energy scale using the RGEs. A summary of the one and two loop RGEs can be found in [10] and [74] for the MSSM and NMSSM, respectively. Some relevant aspects of the sparticle masses are shortly discussed in this section.

The gluino, a color octet, cannot mix with any other particle in the MSSM. Using GUT boundary conditions for the MSSM and NMSSM, the gluino mass parameter M_3 is proportional to the common spin 1/2 mass $m_{1/2}$ and related to the other two gaugino mass parameters M_1 and M_2 via [9]

$$M_3 \approx M_{\tilde{g}} \approx 2.7 m_{1/2},\ M_2 \approx 0.8 m_{1/2},\ M_1 \approx 0.4 m_{1/2}. \tag{3.29}$$

At the TEV scale this implies roughly the predicted mass relation $M_1 : M_2 : M_3 \approx 1 : 2 : 6$. The gluino gets a positive contribution to the mass including one-loop corrections to the gluino propagator due to gluon and quark-squark loops. In the constrained SUSY models the gluino is therefore always slightly heavier compared to the first and second generation squarks.

The first and second generation squarks and sleptons have negligible Yukawa couplings, which leads to nearly degenerate unmixed pairs. The third generation squarks and sleptons can have very different masses compared to the first and second-family sparticles, because of the effects of large Yukawa and soft couplings, leading to $m^2_{U_3} < m^2_{Q_3}$. The third generation squarks are therefor significantly smaller then the other two generation squark squared masses. The off-diagonal terms of the mixing matrix lead to a significant mixing, which predicts the lightest squark to be the lightest stop $\tilde{t}_1$ in many models, which is predominantly the right-handed stop $\tilde{t}_R$. The requirement of positive squared masses for third family squarks and slepton leads to a bound on A_0 for large $\tan\beta$, which is typically within $-2m_0 < A_0 < 3m_0$. This range can vary depending on the particular parameter space.

The charged Higgsinos and gauginos mix to form the charged mass eigenstates of the supersymmetric partners of the gauge bosons, the so-called charginos. The charginos are denoted by $\tilde{\chi}^\pm_j$ with $j = 1, 2$ according to the convention $m_{\tilde{\chi}^\pm_1} < m_{\tilde{\chi}^\pm_2}$. The mass term in the Lagrangian for the gauge-eigenstate basis $\psi^\pm = (\tilde{W}^+, \tilde{H}^+_u, \tilde{W}^-, \tilde{H}^-_d)$ reads

$$\mathcal{L}_{\tilde{\chi}^{\pm}} = -\frac{1}{2}(\psi^{\pm})^T \mathcal{M}_{\tilde{\chi}^{\pm}} \psi^{\pm} + h.c.. \tag{3.30}$$

The 2×2 block mass matrix

$$\mathcal{M}_{\tilde{\chi}^{\pm}} = -\begin{pmatrix} \mathbf{0} & \mathbf{X^T} \\ \mathbf{X} & \mathbf{0} \end{pmatrix} \tag{3.31}$$

includes

$$\mathbf{X} = -\begin{pmatrix} M_2 & gv_u \\ gv_d & \mu \end{pmatrix}. \tag{3.32}$$

The mass eigenstates are related to the 2×2 matrices and can be explicitly solved, which leads to the following tree level masses:

$$\begin{aligned} m^2_{\tilde{\chi}^{\pm}_{1/2}} = \frac{1}{2}[&|M_2|^2 + |\mu|^2 + 2m_W^2 \\ &\mp \sqrt{(|M_2|^2 + |\mu|^2 + 2m_W^2)^2 - 4|\mu M_2 - m_W^2 sin2\beta|^2}]\end{aligned}. \tag{3.33}$$

In the limit of GUT boundary conditions the charginos consist of a wino-like and Higgsino-like chargino.

The neutral gauginos and Higgsinos mix to mass eigenstates as well, the so-called neutralinos. The neutralino sector within the MSSM and NMSSM is quite different because of the additional Higgs singlet. The corresponding Higgsino, the singlino, enters the mass matrix which leads to an additional neutralino component in the NMSSM. The neutralinos are denoted by $\tilde{\chi}^0_i$ with $i = 1, 2, ..., 5$ according to the convention $m_{\tilde{\chi}^0_1} < m_{\tilde{\chi}^0_2} < ... < m_{\tilde{\chi}^0_5}$. Within the gauge eigenstate basis $\Psi = (\tilde{B}, \tilde{W}^0, \tilde{H}^0_d, \tilde{H}^0_u, \tilde{S})$, the neutralino mass term of the Lagrangian reads

$$\mathcal{L}_{\tilde{\chi}^0} = -\frac{1}{2}(\psi^0)^T \mathcal{M}_{\tilde{\chi}^0} \psi^0 + h.c.. \tag{3.34}$$

It includes the neutralino mass matrix

$$\mathcal{M}_{\tilde{\chi}^0} = \begin{pmatrix} M_1 & 0 & -g_1 v_d/\sqrt{2} & g_1 v_u/\sqrt{2} & 0 \\ 0 & M_2 & g_2 v_d/\sqrt{2} & -g_2 v_u/sqrt2 & 0 \\ -g_1 v_d/\sqrt{2} & g_2 v_d/\sqrt{2} & 0 & -\mu_{eff} & -\lambda v_u \\ g_1 v_u/\sqrt{2} & -g_2 v_u/\sqrt{2} & -\mu_{eff} & 0 & -\lambda v_d \\ 0 & 0 & -\lambda v_u & -\lambda v_d & \sqrt{2}\kappa v_s \end{pmatrix}, \tag{3.35}$$

The first 4×4 elements in Eq. 3.35 resemble the neutralino mass matrix in the MSSM. The mass eigenstates are obtained by the diagonalization of $\mathcal{M}_{\tilde{\chi}^0}$. Usually the diagonal terms dominate over the off-diagonal terms, so the neutralino masses are approximately of the order of M_1, M_2, μ in the MSSM and in case of the NMSSM of M_1, M_2, μ_{eff} and $\sqrt{2}\kappa v_s$. For small v/v_s and $\lambda v/\kappa v_s$ the mixing effects with the singlino are small. This leads to a nearly decoupled singlino, so the remaining neutralinos are almost indistinguishable from the MSSM neutralinos. The value of μ is determined by electroweak symmetry breaking, so it is usually of the order of the SUSY breaking scale in the MSSM. Since M_1 and M_2 are related via the RGE, see Eq. 3.29, the ratio $M_1 < M_2 << |\mu|$ is fulfilled, so the mass

matrix indicates a nearly bino like lightest neutralino within the MSSM. In the NMSSM, μ_{eff} is related to the vev of the Higgs singlet S, which is of the order of the electroweak scale, so typically the last diagonal element is the lightest one, which leads to a lightest, singlino-like neutralino in the NMSSM.

4. Methods and Tools to Study the Supersymmetric Parameter Space

Whether a parameter set within the parameter space of a supersymmetric model is allowed or excluded is related to the agreement of the theoretical predictions to the experimental data. Global fits are preformed to distinguish the allowed from the excluded part of the parameter space, i.e. the allowed values of all free parameters of the supersymmetric models are determined under the consideration of selected experimental results.
In this section, the statistical methods and analysis tools to perform the global fits are introduced as well as the selected set of experimental measurements and their application to the fit.

4.1. Concept of Parameter Estimation Using the Method of Least Squares

The parameter space of the supersymmetric models consists of physical regions of interest and regions, where the parameters lead either to unphysical or already excluded models. Within the interesting parameter space, statistical tests are used to state how well the observed data is in agreement with the predicted observables. Therefore, the region of interest has to be identified first by using the method of least squares (LS), which is related to the method of maximum likelihood (ML). The discussion about these statistical data analysis methods has been mainly derived from Ref. [94].

4.1.1. Maximizing the Likelihood Function

The method of ML is a technique to estimate the values of the parameters for a finite data sample. Assuming a set of independent measurements $y_1, ..., y_n$ which are distributed according to the probability density function (pdf) $f(y_i; \theta)$. The value of at least one parameter θ (or parameters $\boldsymbol{\theta} = (\theta_1, ..., \theta_m)$) is not known. The joint pdf for y_i, called the likelihood function $L(\theta)$,

$$L(\theta) = \prod_{i=1}^{n} f(y_i; \theta), \tag{4.1}$$

yields high values for the true parameter, whereas a parameter far away from the true value should give a low joint probability. The maximum likelihood estimator defines the

parameter $\hat{\theta}$ (or $\hat{\boldsymbol{\theta}} = (\hat{\theta}_1, ..., \hat{\theta}_m)$), which maximizes the likelihood function and therefore is close to the true parameter. It is usually more convenient to use the logarithm of $L(\theta)$, since the logarithm leads to a numerically manageable quantity. The parameter value which maximizes $L(\theta)$ will also maximize $\log L(\theta)$.

The method of LS results from maximizing the log-likelihood function $\log L(\theta)$ of the joint pdf of Gaussian random variables. A set of N independent Gaussian random variables $y_i, i = 1, ..., N$ related to another variable x_i are assumed. The measurements y_i have a corresponding mean λ_i and a known variance σ_i^2. The true value is given as a function of x_i, which depends on the m unknown parameters $\boldsymbol{\theta} = (\theta_1, ..., \theta_m)$. The N measurements of y_i can be perceived as a single measurement of a N-dimensional random vector, so its joint pdf is the product of N Gaussians. To estimate the unknown parameters $\boldsymbol{\theta}$, the log-likelihood function of the joint pdf has to be maximized:

$$\log L(\boldsymbol{\theta}) = -\frac{1}{2} \sum_{i=1}^{N} \frac{(y_i - \lambda(x_i; \boldsymbol{\theta}))^2}{\sigma_i^2}, \tag{4.2}$$

which resembles minimizing the quantity

$$\chi^2(\boldsymbol{\theta}) = \sum_{i=1}^{N} \frac{(y_i - \lambda(x_i; \boldsymbol{\theta}))^2}{\sigma_i^2}. \tag{4.3}$$

The quantity χ^2 represents the quadratic sum of the difference between the measured and the hypothesized values, weighted by the inverse of the variance. This principle is known as the method of LS and can be used if the measurements are independent even in case they are non-Gaussian. The quantity $(y_i - \lambda(x_i; \boldsymbol{\theta}))^2/\sigma_i^2$ in Eq. 4.3 is a measure of the deviation between the measurements and the hypothesis. It is used to test the goodness of the fit, i.e. checking how likely it is to give the observed data assuming the hypothesis is true. The minimum value of χ^2 is distributed according to the χ^2-distribution with N-m degrees of freedom, see Appendix A.1, if the following aspects apply

1. $y_i, ..., y_N$ are independent Gaussian random variable with known variances σ_i^2,
2. the hypothesis $\lambda(x; \theta_1, ..., \theta_m)$ is linear in the parameter θ_i and
3. the functional form of the hypothesis is correct.

Since the expectation value of a random variable y from the χ^2-distribution is equal to the number of degrees of freedom n_d, the ratio χ^2/n_d is often quoted as a measure of the goodness-of-fit. Furthermore the p-value for a given χ^2 can be calculated. The p-value corresponds to the probability that the hypothesis would lead to a χ^2 value worse than the one actually observed and reads

$$P = \int_{\chi^2}^{\infty} f(y; n_d) dy, \tag{4.4}$$

where $f(y; n_d)$ is the χ^2-distribution for n_d degrees of freedom. If statement (1)-(3) are not applicable the concept of confidence intervals can be used to convey the agreement of data and hypothesis.

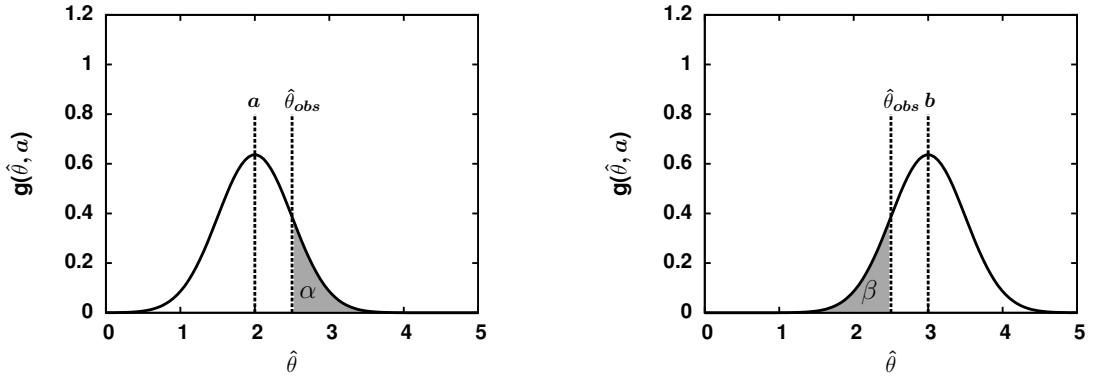

(a) (b)

Figure 4.1.: Illustration of the construction of the limits a and b of the confidence interval $[a, b]$ [94]. The pdf $g(\hat{\theta}; \theta)$ with $\theta = a$ (a) and $\theta = b$ (b) is shown. The shaded area corresponds to the probability α/β of the estimates $\hat{\theta}$ to be greater/less than $\hat{\theta}_{obs}$ if the true value is equal to be a/b.

4.1.2. Confidence Intervals

Confidence intervals allow to give a quantitative statement about the probability that a certain interval would contain the true value of the parameter. First an estimator $\hat{\theta}(x_1, ..., x_n)$ for a parameter θ from n observations of a random variable has to be evaluated which results in $\hat{\theta}_{obs}$. The pdf of $\hat{\theta}$ is known to be $g(\hat{\theta}; \theta)$, which contains the true value θ as a parameter. The limit a/b of a confidence interval is constructed to be the value for which a fraction α/β of the estimates would be higher/lower than $\hat{\theta}_{obs}$. This is illustrated in Fig. 4.1 whereas the corresponding probabilities read

$$\begin{aligned} \alpha &= \int_{\hat{\theta}_{obs}}^{\infty} g(\hat{\theta}; a) d\hat{\theta} = 1 - G(\hat{\theta}; a), \\ \beta &= \int_{-\infty}^{\hat{\theta}_{obs}} g(\hat{\theta}; b) d\hat{\theta} = G(\hat{\theta}; b). \end{aligned} \tag{4.5}$$

$G(\hat{\theta}; \theta)$ represents the cumulative distribution of the pdf $g(\hat{\theta}; \theta)$. The resulting interval $[a, b]$ is then called a confidence interval at a confidence level (C.L.) $1 - \alpha - \beta$. Usually the central confidence interval is used, where $\alpha = \beta = \gamma/2$ with the resulting probability $1 - \gamma$. If upper or lower limits are specified, one-sided confidence intervals are needed, so either a or b is given with the corresponding probability $1 - \alpha$ or $1 - \beta$. Since the pdf of the maximum likelihood estimator $\hat{\theta}$ for a parameter θ becomes Gaussian in the large sample limit, the confidence interval can be applied for a Gaussian distribution for $\hat{\theta}$ with the mean θ and the standard deviation $\sigma_{\hat{\theta}}$. $G(\hat{\theta}; \theta)$ in Eq. 4.5 becomes the cumulative distribution of a standard Gaussian $\Phi\left(\frac{\hat{\theta}-\theta}{\sigma_{\hat{\theta}}}\right)$:

$$\begin{aligned} \alpha &= 1 - G(\hat{\theta}; a, \sigma_{\hat{\theta}}) = 1 - \Phi\left(\frac{\hat{\theta}_{obs} - a}{\sigma_{\hat{\theta}}}\right), \\ \beta &= G(\hat{\theta}; b, \sigma_{\hat{\theta}}) = \Phi\left(\frac{\hat{\theta}_{obs} - b}{\sigma_{\hat{\theta}}}\right). \end{aligned} \tag{4.6}$$

which leads to

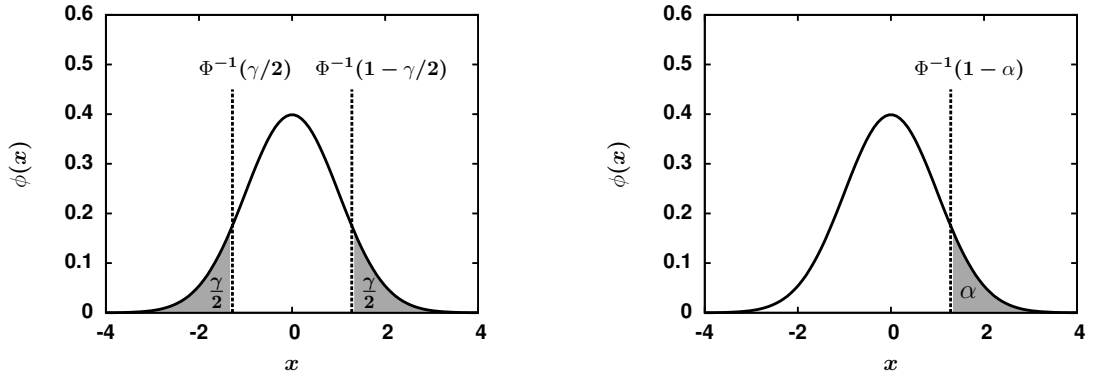

Figure 4.2.: The standard Gaussian pdf $\phi(x)$ is displayed to show the effect of the quantile Φ^{-1} for a central (a) and one-sided (b) confidence interval at a confidence level of $1-\gamma$ and $1-\alpha$, respectively, from Ref. [94].

$$\begin{aligned} a &= \hat{\theta}_{obs} - \sigma_{\hat{\theta}}\Phi^{-1}(1-\alpha), \\ b &= \hat{\theta}_{obs} - \sigma_{\hat{\theta}}\Phi^{-1}(\beta) = \hat{\theta}_{obs} + \sigma_{\hat{\theta}}\Phi^{-1}(1-\beta), \end{aligned} \tag{4.7}$$

The inverse function Φ^{-1} of the cumulative Gaussian distribution characterize the distance from the limit a, b to the estimator $\hat{\theta}_{obs}$ in units of the standard deviation $\sigma_{\hat{\theta}}$. This relation is illustrated in Fig. 4.2 for a central (a) and one-sided (b) confidence interval. Either the confidence level is chosen such that the quantile $\Phi^{-1}(1-\gamma/2)$ is an integer or a fixed confidence level is used to calculated the corresponding quantile. Both cases can be obtained for the central and one-sided confidence interval, see Table 4.1.

The confidence intervals can be applied for the ML and LS estimators by a simple prescription using the estimated variance. Considering the expansion of the log-likelihood function in a Taylors series around the ML estimate $\hat{\theta}$ and including $\log L(\hat{\theta}) = \log L_{max}$. The following simple equation can be derived, see Ref. [94]:

$$\log L(\hat{\theta} \pm N\sigma_{\hat{\theta}}) = \log L_{max} - \frac{N^2}{2}. \tag{4.8}$$

Eq. 4.8 indicates that changing the parameter θ by N standard deviations decreases the log-likelihood function by $N^2/2$. This translates into

$$\chi^2(\hat{\theta} \pm N\sigma_{\hat{\theta}}) = \chi^2_{min} + N^2. \tag{4.9}$$

using $\log L = -\chi^2/2$.

The confidence interval can be generalized to multidimensional confidence regions for n parameters, $\boldsymbol{\theta} = (\theta_1, ..., \theta_n)$. The joint pdf of $\hat{\boldsymbol{\theta}}$ becomes a multidimensional Gaussian

$$g(\hat{\boldsymbol{\theta}}|\boldsymbol{\theta}) = \frac{1}{(2\pi)^{n/2}|V|^{1/2}} \exp\left[-\frac{1}{2}Q(\hat{\boldsymbol{\theta}}, \boldsymbol{\theta})\right], \tag{4.10}$$

where Q is defined by

Table 4.1.: The upper rows show the value of the confidence level for different values of the quantile Φ^{-1} [94] for the central (left) and one-sided (right) interval. The lower rows show the opposite.

$\Phi^{-1}(1-\gamma/2)$	$1-\gamma$	$\Phi^{-1}(1-\alpha)$	$1-\alpha$
1	0.6827	1	0.8413
2	0.9544	2	9.772
3	0.9973	3	0.9987
$1-\gamma$	$\Phi^{-1}(1-\gamma/2)$	$1-\alpha$	$\Phi^{-1}(1-\alpha)$
0.90	1.645	0.90	1.282
0.95	1.960	0.95	1.645
0.99	2.576	0.99	2.326

$$Q(\hat{\boldsymbol{\theta}}, \boldsymbol{\theta}) = (\hat{\boldsymbol{\theta}} - \boldsymbol{\theta})^T V^{-1} (\hat{\boldsymbol{\theta}} - \boldsymbol{\theta}) \tag{4.11}$$

using the inverse of the covariance matrix V^{-1} and the transposed of the vector $(\hat{\boldsymbol{\theta}} - \boldsymbol{\theta})^T$. Constant $Q(\hat{\boldsymbol{\theta}}, \boldsymbol{\theta})$ represents contours of constant joint pdf $g(\hat{\boldsymbol{\theta}}|\boldsymbol{\theta})$. The corresponding likelihood function, a Gaussian centered around the ML estimator $\hat{\boldsymbol{\theta}}$, reads

$$L(\boldsymbol{\theta}) = L_{max} \exp\left[-\frac{1}{2} Q(\hat{\boldsymbol{\theta}}, \boldsymbol{\theta})\right]. \tag{4.12}$$

If the estimate is within a certain distance to the true value $\boldsymbol{\theta}$, e.g. $Q(\hat{\boldsymbol{\theta}}, \boldsymbol{\theta}) \leq Q_\gamma$, the probability can be described by

$$P(Q(\hat{\boldsymbol{\theta}}, \boldsymbol{\theta}) \leq Q_\gamma) = \int_0^{Q_\gamma} f(y; n) dy = 1 - \gamma. \tag{4.13}$$

The quantile Q_γ represents the inverse of the cumulative χ^2 distribution $F^{-1}(1-\gamma; n)$ and determines the confidence region at a confidence level $1-\gamma$. Different values of the quantile for n fitted parameters and various values of confidence levels are summarized in Table 4.2. Applying the confidence region to a LS fit resembles the relation shown in Eq. 4.9, while the quantile has to be replaced by the multidimensional equivalent

$$\chi^2(\boldsymbol{\theta}) = \chi^2_{min} + Q_\gamma. \tag{4.14}$$

The allowed parameter space is determined in this thesis by using a χ^2 minimization. The results of the global fits will be presented in a two parameter plane. In most cases the χ^2 distribution will be projected into the common m_0-$m_{1/2}$ mass plane, so the confidence regions for $n = 2$ parameter in Table 4.2 have to be adopted, i.e. a 95% C.L. interval would lead to $\Delta\chi^2 = \chi^2 - \chi^2_{min} = 5.99$.

The concept of confidence intervals is related to the test of goodness-of-fit. If $\hat{\theta}$ is used as a test statistic to test the hypothesis of $\theta = a$ and the region $\hat{\theta} \geq \hat{\theta}_{obs}$ has equal or less agreement with the hypothesis, then the resulting p-value of the test is α. For the confidence interval the probability is specified first and a is a random quantity, whereas for the goodness-of-fit a is specified first and the P-value is a random variable.

Table 4.2.: The quantile Q_γ is given for different values of the confidence level $1-\gamma$ for n fitted parameters [94].

$1-\gamma$	Q_γ				
	$n=1$	$n=2$	$n=3$	$n=4$	$n=5$
0.683	1.00	2.30	3.53	4.72	5.89
0.90	2.71	4.61	6.25	7.78	9.24
0.95	3.84	5.99	7.82	9.49	11.1
0.99	6.63	9.21	11.3	13.3	15.1

4.2. Constraining the Supersymmetric Parameter Space with Experimental Data

In this section the selected experimental data is summarized, which is included into the χ^2 function to determine the allowed region in the supersymmetric parameter space. The detailed discussion of each experimental constraint and the corresponding favored region in parameter space will be given in Chapter 5. The experimental constraints are summarized in Table 4.3 and 4.4. They are separated into results providing a actual measurement including a theoretical and experimental error and experimental limits including a 1σ error band. The constraints are further divided into

- direct constraints,
- indirect constraints
- and dark matter constraints.

The direct constraints include searches for SUSY particles, e.g. squarks, gluinos or additional Higgs bosons. Experimental results listed as indirect constraints represent observables, where SUSY particles appear indirect via loops, such as rare B-decays and the anomalous magnetic moment of the muon. Since SUSY provides a perfect dark matter candidate, dark matter observables are also included into the χ^2 function. The resulting χ^2 function including all constraints is defined by

$$\begin{aligned}\chi^2 &= \chi^2_{m_h} + \chi^2_{BR(B^0_s\to\mu^+\mu^-)} + \chi^2_{BR(B\to X_s\gamma)} + \chi^2_{R_{BR(B\to\tau\nu_\tau)}} + \chi^2_{\Delta a_\mu} + \chi^2_{\Omega h^2} + \chi^2_{m_A} \\ &\quad + \chi^2_{ATLAS} + \chi^2_{LEP} + \chi^2_{LUX} + \chi^2_{XENON100} + \chi^2_{COUPP}. \end{aligned} \tag{4.15}$$

Most of the χ^2 contributions associated with the constraints listed in Table 4.3 are defined in a straightforward way: the square of the difference between the experimental value given in Table 4.3 and the predicted value for a given SUSY parameter set, weighted by the inverse of the error squared. The error which is included into the χ^2 function corresponds to the total error σ, where σ results from the linear addition of the theoretical and experimental error. The linear addition is favored over the quadratic, since the quadratic addition can only be used if the summed errors are all Gaussian. The theoretical uncertainties are certainly non-Gaussian, since they correspond rather to intervals with constant probability, thus a linear addition of the errors is more conservative. This was checked by simply comparing the convolution of two Gaussian with a Gaussian and a flat top Gaussian, where the flat region represents the interval with a constant probability, which is more realistic for the theoretical errors. The latter one equals a Gaussian with an error closer to the linear addition of the individual errors, so the linear addition of the errors is applied [106].

The constraints which differ slightly from the previously mentioned, straightforward χ^2 contribution are briefly discussed:

Table 4.3.: List of experimental measurements used to constrain the supersymmetric parameter space. The references for the experimental data and the corresponding experimental and theoretical error are summarized in the last columns.

	Data	Exp. Error	Theo. Error	Refs.
Direct Constraint				
m_h in GeV	125.2	0.4	1.5	[2, 3, 95]
Indirect Constraint				
BR($B_s^0 \to \mu^+\mu^-$) $\times 10^{-9}$	2.9	0.7	0.23	[96–98]
BR($B \to X_s\gamma$) $\times 10^{-4}$	3.43	0.22	0.23	[99, 100]
BR($B \to \tau\nu_\tau$) $\times 10^{-4}$	0.96	0.26	0.14	[101, 102]
$\Delta a_\mu \times 10^{-12}$	28.70	6.33	4.94	[103, 104]
Dark Matter Constraint				
Ωh^2	0.1199	0.0027	0.01199	[6, 105]

- $\chi^2_{m_h}$: The CMS and the ATLAS experiment measured both a Higgs-like particle at a mass of about 125 GeV. The Higgs mass given in Table 4.3 corresponds to the mean of the two measurement. The experimental error results from a Gaussian error propagation of the two experimental errors given by CMS and ATLAS. Since no significant deviation of the coupling strengths compared to the SM was measured, the resulting reduced cross sections to fermions and gauge bosons should agree with the SM prediction within an error of 10%. This constraint and the resulting additional contribution $\chi^2_{\sigma_{red}}$ to the overall χ^2 in Eq. 4.15 is only relevant for the NMSSM, where the two light scalar Higgs bosons can have significant deviations to the SM couplings due to the mixing with the Higgs singlet. The corresponding χ^2 contribution $\chi^2_{\sigma_{red}}$ is defined in the straightforward way, while it includes the following decay modes as separate χ^2 contributions: $\gamma\gamma$, bb, $\tau\tau$ and ZZ/WW.
- $\chi^2_{R_{BR(B\to\tau\nu_\tau)}}$: The ratio $R_{BR(B\to\tau\nu_\tau)} = BR(B \to \tau\nu_\tau)_{SUSY}/BR(B \to \tau\nu_\tau)_{SM}$ of the SUSY and SM contribution to $BR(B \to \tau\nu_\tau)$ is used as a constraint for the χ^2 minimization. Therefore the χ^2 contribution includes the ratio of the experimental value $BR(B \to \tau\nu_\tau)_{EXP}$ and the SM prediction $BR(B \to \tau\nu_\tau)_{SM} = 0.74 \pm 0.14$ [102]. A Gaussian error propagation of the corresponding experimental and the theoretical error of the ratio is performed to get the total error on the ratio $R_{BR(B\to\tau\nu_\tau)} = BR(B \to \tau\nu_\tau)_{EXP}/BR(B \to \tau\nu_\tau)_{SM}$. In principle the branching ratio itself instead of the ratio can be included into the χ^2 function as it is the case for the other branching ratios. This would lead to similar allowed regions. Since the ratio is calculated within the applied software package, it is reasonable to use it as a constraint. By using the ratio of the SUSY and SM branching ratio, many SM parameters cancel, so the ratio suffers less from the uncertainties on the SM parameters. If the branching ratio is included into the χ^2 function, the uncertainties on the SM parameters have to be taken into account.

The χ^2 contributions for the experimental limits from Table 4.4, calculated from the non-observation of particular particles, differ to the straightforward calculation. The 90% and 95% C.L. limit contours given in the references listed in Table 4.4 have to be parameterized first and added as a one sided χ^2 contribution to the overall χ^2 function. Note the difference in the corresponding quantile Φ^{-1} for the central and one-sided confidence interval for the same confidence level shown in Table 4.1. Since the limits are interpreted as one-sided confidence interval the cut on χ^2_{min} is different compared to the central confidence

Table 4.4.: List of limits used for the global fits to constrain the supersymmetric parameter space. The corresponding references and confidence levels are given in the last columns.

	Parametrized Limit	C.L.	Refs.
	Direct Constraint		
m_A	in Appendix B.1	95	[107]
ATLAS	in Appendix B.2	95	[108, 109]
LEP	in Appendix B.3	95	[110]
	Dark Matter Constraint		
LUX	in Appendix B.4	90	[111]
XENON100	in Appendix B.4	90	[112]
COUPP	in Appendix B.4	90	[113]

intervals used for the measurements. In principle, the χ^2 contributions which correspond to the one-sided and central confidence intervals have to be treated separately since the cut with respect to χ^2_{min} is different. However, it is reasonable to use the simplified approach to apply the cut on the central confidence level given in Table 4.2 for the combination of all constraints. This is applicable, since the χ^2 distribution of the included limits show such a steep increase, the cut on the one-sided and central confidence interval with respect to χ^2_{min} resembles. The difference due to the cut on the χ^2 value translated into m_0 and $m_{1/2}$ is small compared to the used grid distance leading to the same exclusion contours independent of the treatment of the confidence intervals. In case the grid spacing is small compared to the translated χ^2 difference, the one-sided and central confidence intervals have to be treated separately. In the following the experimental limits used for the χ^2 function in Eq. 4.15 are discussed separately:

- $\chi^2_{m_A}$: The search for the neutral Higgs bosons A decaying into tau pairs in pp collisions at the LHC gives a 95% C.L. upper limit on the corresponding cross section which can be translated into a exclusion contour within the tanβ-m_A plane. For a given value of tanβ a certain mass of the pseudo-scalar Higgs boson is excluded and vice-versa. The corresponding χ^2 contribution is defined by $\chi^2_{m_A} = (\tan\beta^{th}(m_A) - \tan\beta^{95}(m_A))^2/\sigma^2_{\tan\beta^{95}}$, where $\sigma^2_{\tan\beta^{95}}$ is obtained from the 1σ error band around the 95% C.L. exclusion curve. For a given parameter set which includes tanβa specific pseudo-scalar Higgs mass m_A is predicted, while $\tan\beta^{th}(m_A)$ corresponds to the inverse pair of values. $\tan\beta^{95}(m_A)$ includes the experimental limit, where tanβ is parametrized as a function of m_A. The parameterization of $\tan\beta^{95}(m_A)$ is determined by the requirement that $\Delta\chi^2_{m_A}$ is 5.99 on the contour line, see Appendix B.1.

- χ^2_{ATLAS}: The direct searches for SUSY particles from the ATLAS experiment at the LHC give 95% C.L. limits on the hadronic cross section. It is used to excluded low SUSY masses, especially low gluinos and low first and second generation squarks because of their large cross section. In Ref. [108, 109] the 95% C.L. exclusion curves in the m_0-$m_{1/2}$ plane determines the limit on the hadronic cross sections into squarks and gluinos $\sigma_{tot}(pp \to \tilde{g}\tilde{g}, \tilde{g}\tilde{q}, \tilde{q}\tilde{q})$, which vary along the contour line due to varying efficiencies. By using Wilks' theorem, it can be demonstrated that the profile likelihood leads to a χ^2 distribution for the hadronic cross section, so the simplified assumption of an exclusion limit proportional to the hadronic SUSY cross section is reasonable. The corresponding χ^2 contribution is parametrized as follows: $\chi^2_{ATLAS} = \sigma^2_{tot}/\sigma^2_{ATLAS}$. Since the 95% C.L. contour is published, σ^2_{ATLAS} is determined as a function of m_0 requiring $\chi^2_{ATLAS} = 5.99$ on the contour line,

see Appendix B.2. In the NMSSM, the splitting in the stop sector can be large which leads to light stops. In this case the stop contribution to the total cross section has to be separately included into the χ^2 function, otherwise the parameter space referring to light stops is misleadingly excluded. The χ^2 contribution which includes the hadronic cross section without the stop contribution is determined in the same way as discussed above but the stop contribution is now parametrized as a function of the stop mass $m_{\tilde{t}}$. The corresponding stop contribution χ^2_{stop} is defined by $\chi^2_{stop} = (\sigma^{th}_{\tilde{t}}(m_{\tilde{t}}) - \sigma^{95}_{\tilde{t}}(m_{\tilde{t}}))^2/\sigma^2$. An estimated error of 15% on the cross section is used for σ. $\sigma^{th}_{\tilde{t}}(m_{\tilde{t}})$ represents the stop cross section $pp \to \tilde{t}\tilde{t}$ for a given stop mass $m_{\tilde{t}}$. The parameterization of $\sigma^{95}_{\tilde{t}}(m_{\tilde{t}})$ is determined by the requirement that $\Delta\chi^2_{stop}$ is 5.99 on the contour line, see Appendix B.2. The contour line is given by the stop cross section on the 95% C.L. exclusion contour from Ref. [108, 109] as a function of the corresponding stop mass.

- χ^2_{LEP}: The LEP collaboration established an upper bound on the HZZ coupling for a Higgs boson below 114.4 GeV at 95% C.L. from the collected e^+e^- collision data. χ^2_{LEP} is only relevant for the NMSSM, since two light Higgses exist which can provide non-SM couplings. A 95% C.L. upper bound on the ratio $\xi^2 = (g_{HZZ}/g^{SM}_{HZZ})^2$ is published in [110] as a function of the Higgs boson mass m_h, whose decays are predicted by the SM. The corresponding χ^2 contribution to the overall χ^2-function is defined by $\chi^2_{LEP} = (\xi^2_{th}(m_h) - \xi^2_{95}(m_h))^2/\sigma^2_{\xi^2_{95}}$. Here $\sigma_{\xi^2_{95}}$ can be obtained from the 1σ band given for the expected 95% C.L. exclusion curve. The function $\xi^2_{95}(m_h)$ is parameterized and determined by the requirement $\Delta\chi^2_{LEP} = 5.99$ on the contour line, see Appendix B.3. $\xi^2_{th}(m_h)$ corresponds to the normalized coupling for a parameter set which predicts m_h.

- χ^2_{LUX}, $\chi^2_{XENON100}$ and χ^2_{COUPP}: In elastic scattering experiments an upper 90% C.L. limit on the elastic WIMP-nucleon cross section is determined. Since the elastic scattering of a dark matter particle off a nuclei consist of a spin-dependent (SD) and spin-independent (SI) part both upper limits on the WIMP-nucleon cross section from the direct dark matter searches (DDMS) are considered. The XENON100, COUPP and the LUX experiment provide the current best limits on the SD and SI WIMP-nucleon cross section $\sigma_{\chi N}$. The contribution is defined by $\chi^2_{DDMS} = (\sigma^{th}_{\chi N}(m_\chi) - \sigma^{90}_{\chi N}(m_\chi))^2/\sigma^2_{\sigma^{90}_{\chi N}}$, where DDMS can be replaced by XENON100, COUPP or LUX, respectively. Since 90% C.L. upper limits are published, the excluded cross section $\sigma^{90}_{\chi N}(m_\chi)$ is determined by the requirement $\Delta\chi^2_{DDMS} = 4.61$ at the contour line, whereas the 1σ band in the corresponding references generates the weight $1/\sigma^2_{\sigma^{90}_{\chi N}}$, see Appendix B.4. $\sigma^{th}_{\chi N}(m_\chi)$ represents the predicted WIMP-nucleon cross section for a WIMP mass of m_χ.

4.2.1. Software Tools

All observables listed in Table 4.3 and 4.4 are calculated using the following software packages:

- micrOMEGAs [114] is a software package to compute dark matter observables. It is used to calculate the observables for the global fits within the MSSM for the constrained and the NUH model. It is linked to SuSpect [115] to calculate the supersymmetric spectrum including Higgs masses and mixing matrices. In addition it provides cross section calculations, the computation of several B-physics branching ratios and the anomalous magnetic moment of the muon. The version 3.6.9.2 has been used.

Table 4.5.: List of the standard model input parameters used for the global fits, taken from the PDG [86]. The masses are specified at the scale denoted in the brackets in $\overline{MS}$ scheme. All other masses corresponds to pole masses.

SM Parameter	PDG Value
m_t	$(173.07 \pm 0.52 \pm 0.72)$ GeV
$m_b(m_b)$	(4.18 ± 0.03) GeV
$\alpha_s(M_Z)$	0.1185(6)
M_Z	91.1876 ± 0.0021 GeV
$\alpha_{em}(M_Z)^{-1}$	127.944 ± 0.014
m_τ	(1776.82 ± 0.16) MeV
G_F	$1.1663787(6) \cdot 10^{-5}\text{GeV}^{-2}$

- NMSSMTools [116–118] is used to calculate the sparticle and Higgs masses within the NMSSM using the routine `NMSPEC` [117] for the constrained and NUH model. It is linked to micrOMEGAs to compute the remaining observables mentioned above. The version 4.3.0 has been used with the option 2 for the precision of the Higgs mass calculation.

Details about the implementation of the χ^2 function can be found in Appendix C.

4.3. Multi-Step Fitting Approach

The allowed parameter space can either be determined by minimizing a χ^2 function or using random sampling techniques. Random sampling techniques like Markov-Chain-Monte-Carlo (MCMC) methods are used to sample the probability distribution. This method is efficient for higher dimensional parameter space. The desired probability distribution is reached when the Markov Chain reached equilibrium. The probability distribution is constructed according to the state of the chain after a large number of steps. This characteristic is one of the problems using MCMC since it is difficult to determine how many steps are needed to converge to the stationary stage.

The free parameter of the supersymmetric models are highly correlated as will be shown in section 6.1. The correlation leads to spikes in χ^2 within the parameter space where the free parameters have to have specific correlated values. Although the χ^2 is very low in this narrow parameter region it can be easily missed in methods based on random stepping techniques since the convergence is extremely sensitive to the chosen step-size. To account for the strong correlations without knowing the correlation matrix, we use a multi-step fitting approach, which means that we fit the highly correlated parameters first for fixed other parameters. This allows to find the χ^2 spikes and not misleadingly exclude a allowed parameter set. The fixed parameters are the common SUSY masses m_0 and $m_{1/2}$. In this way it is possible to cope with the strong correlations and parallelize the minimization. A grid in m_0 and $m_{1/2}$ is defined in the range of 100 GeV to 5(3) TeV in $m_0(m_{1/2})$, which allows to independently minimize the χ^2 function defined in Eq. 4.15 for each m_0-$m_{1/2}$ pair with respect to all other parameters. The publicly available software tool MINUIT [119] is used to minimize the χ^2 function. MINUIT offers multiple minimization techniques out of which MIGRAD is used for this analysis. For each m_0-$m_{1/2}$ point the program is fast and quickly converge to the global minimum. For the global fit of the NUH model within the NMSSM additional minimizing steps are needed because of the enhanced number of free parameters compared to the minimization in the MSSM. In a last step all seven parameters can be varied at the same time to find the minimum for each m_0-$m_{1/2}$ pair.
After the optimization of the SUSY parameters, the SM parameters, like the top and

bottom mass and the strong coupling constant, should also be varied or be marginalized. The quark masses basically influence the running of the Higgs mass parameters, so different values of the SM parameters can be adjusted by slightly different values of the SUSY parameters which leads to a similar χ^2. It was checked that the allowed parameter space is hardly affected by the variation of the SM parameters. Thus an additional optimization of the SM parameters is not necessary. The SM parameter applied for the optimization are taken from the Particle Data Book (PDG) [86] and listed in Table 4.5.

5. Favored Parameter Space for Single Experimental Constraints

The allowed parameter space within the minimal and next-to-minimal supersymmetric SM is determined by using the multi-step fitting approach with respect to the experimental constraint listed in chapter 4. Each constraint and its favored region in the parameter space will be discussed separately. The knowledge of the favored region of a separate constraint is essential for the understanding of the favored region for the combination of all constraints.

5.1. The Relic Density

A large number of astronomical evidence indicate more matter than can be associated with the luminous matter in the galaxies. The first hint for dark matter was given in 1933 by Zwicky [120] by observing the Coma cluster. He calculated the gravitational mass of the galaxies using the virial theorem and obtained a value greater than expected from the luminous matter. Many other observations established the presence of DM in the universe as well, e.g. the observations of flat rotations curves of galaxies [121]. Fig. 5.1 shows the measured circular rotation velocities as function of the distance from the center of a spiral galaxy [122]. The flat distribution cannot be explained by the contribution from the observed disk and gas. An additional DM halo is needed to explain the large velocities outside the center of the galaxy. Besides the rotation curves, gravitational lensing [123] and the observed bullet cluster [124] fosters DM. Theoretical motivations for the existence of DM result from the structure formation of the universe [125], which can be brought in line with the results of N-body simulation [126] if cold DM is included into the calculations. Combined with limits on barionic matter from the primordial nucleosynthesis supports the existence of non-barionic, non-relativistic matter in the Universe.

Many candidates for dark matter exist nowadays, see e.g. Refs. [127, 128]. However, the leading hypothetical particle in particle physics is the so-called weakly interacting massive particle (WIMP) [129, 130]. The WIMPs are assumed to exist abundant in thermal equilibrium in the early universe, when the temperature exceeded the mass of the particle. The equilibrium abundance is maintained by the annihilation of the particle and its antiparticle into lighter particles and vice versa. By the time the temperature of the universe drops below the mass of the particle m_χ, the equilibrium abundance drops exponential according to the Boltzmann equation until the annihilation rate is below the expansion rate H of the

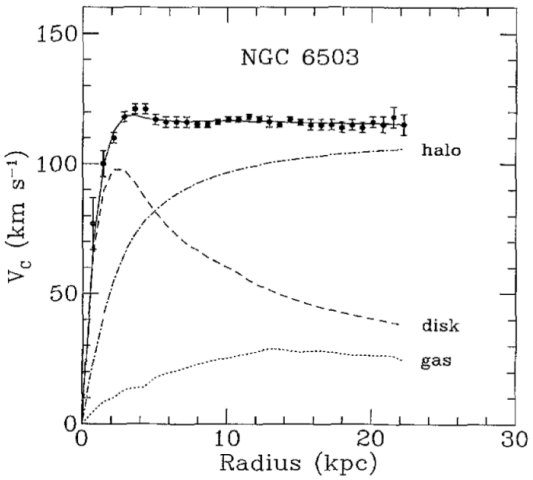

Figure 5.1.: Rotation curve of a spiral galaxy taken from Ref. [122]. The measured circular rotation velocities as function of the distance from the center of the galaxy cannot be explained by the contribution from the observed disk and gas. An additional DM halo is needed to explain the large velocities outside the center of the galaxy.

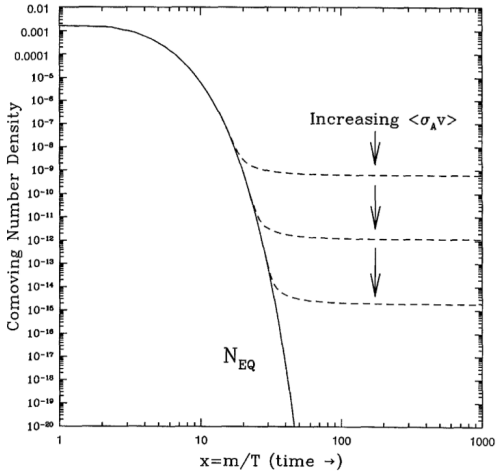

Figure 5.2.: Co-moving WIMP number density in the early universe as a function of time taken from Ref. [125]. The equilibrium abundance (solid line) freezes in and remains as relic abundance (dashed line) depending on the WIMP annihilation rate.

universe. At this freeze out point, which occurs typically for a temperature of $T \approx m_\chi/20$, the relic cosmological abundance freezes in, see Fig. 5.2.

The relic abundance can be determined by using thermodynamics and statistical mechanics to describe the particle production and reactions in the early universe. Assuming such a stable particle exist, the relic abundance, also denoted as the relic density, can be estimated to [127]

$$\Omega_\chi h^2 = m_\chi n_\chi/\rho_c \simeq 3 \cdot 10^{-27}\mathrm{cm}^3\mathrm{s}^{-1}/\langle\sigma_A v\rangle, \tag{5.1}$$

in units of the critical density ρ_c. The Hubble constant h is in units of 100 km s^{-1} Mpc^{-1}. $\langle\sigma_A v\rangle$ corresponds to the thermally averaged total annihilation cross section with the number density n_χ. The measured value of the relic density leads to an annihilation cross section right of the order of the electroweak interaction. Although such a interaction is expected for a stable particle associated with the weak scale interaction, the surprising

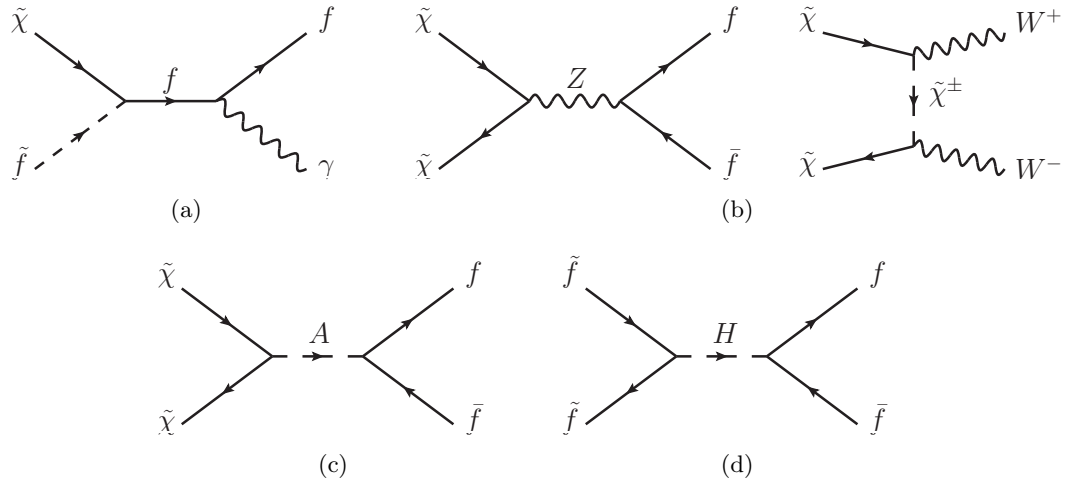

Figure 5.3.: Selected dominant annihilation diagrams contributing to the dark matter relic abundance within the co-annihilation (a), the focus point (b) and m_A resonance region (c). Since the neutralino is mainly a bino in most of the parameter space, the annihilation via the pseudo-scalar Higgs boson is preferred. The stau self annihilation diagram (d) becomes significant as well if the stau and the neutralino are degenerate in mass. Then they will freeze out in the early universe eventually at the same temperature and contribute to the time averaged annihilation cross section due to the large self annihilation cross section and the number density of the staus at the freeze-out temperature.

agreement is often referred to as the so-called WIMP miracle. The identity of the WIMP is still unknown though.

The lightest supersymmetric particle (LSP) is a perfect WIMP candidate in particular if the neutralino is the LSP. It is neutral, stable, massive and provides the right amount of DM in the universe. The parameter space where the LSP is represented by a charged or colored sparticle is not considered, since it disagrees with the experimental observations. The neutralino, a spin 1/2 majorana particle, can annihilate into SM particles via Higgses, gauge bosons, sfermions and gauginos. The corresponding annihilation channels determine the annihilation cross section and therefore the relic density. Since the neutralino is a superposition of the supersymmetric partners of the gauge bosons, its cross section can differ depending on the mixing. In addition its mass and the mass difference to the next-to-lightest particle (NLSP) determine the relic density.

Many different annihilation diagrams exist, see e.g. Ref. [127], leading to gauge boson and fermion final states. The selected diagrams shown in Fig. 5.3 correspond to the different regions in parameter space, which are separated roughly into three[1] relevant regions [10]:

- the co-annihilation region: co-annihilation occurs, if additional particles have the same quantum numbers and are within 10% of the LSP mass [131, 132]. It implies, that the extra particles are nearly as abundant as the relic species. Possible sparticle candidates are charginos, staus or light stops. The relic number density is determined by reaction of the type $\chi_i\chi_j \leftrightarrow XX'$,$\chi_iX \leftrightarrow \chi_jX'$ and $\chi_j \leftrightarrow \chi_iXX'$, where χ_i with $i = 1, ..., N$ and $i < j$ denote the sparticles and X, X' correspond to any SM particle. For similar annihilation cross sections for the LSP and NLSP the effect on the relic density is less than 5%. In case of colored NLSPs the cross sections are certainly not identical, which leads to a huge reduction of the relic density of the order of $\mathcal{O}(10^2)$ since the cross section difference is scaled with the ratio of the strong and electroweak coupling constant. For small values of m_0 and large $m_{1/2}$, the stau and

[1]The bulk region is only relevant for small squark masses, which is experimentally already disfavored.

the lightest neutralino are nearly degenerate in mass. Therefore they will freeze out in the early universe eventually at the same temperature leading to co-annihilation, which reduces the relic density.

- the m_A resonance region: the s-channel annihilation via a scalar Higgs boson is dominant for bino-like neutralinos. The correct relic density is reached close to the resonance, while on the resonance for $m_A = 2 \cdot m_\chi$ the cross section is too high leading to a too low relic density. For zero relative velocity the annihilation via a pseudo-scalar Higgs dominants over the scalar heavy Higgs due to CP conservation. The resonance region is also known as the funnel region, while its characteristic funnel only appears if $\tan\beta$ is fixed. This narrow funnel region vanishes and the whole m_0-$m_{1/2}$ plane opens up if $\tan\beta$ is varied, see e.g. Ref. [133].
- the focus point region: this region is associated with large values of m_0. Here the value of μ is small due to EWSB, which requires at least one Higgs soft mass to become negative at the electroweak scale. Since the Higgs mass at the GUT scale starts at $\sqrt{m_0^2 + \mu^2}$, small values of μ can compensate high values of m_0 to obtain EWSB by radiative corrections. Small values of μ lead to small chargino masses and a large Higgsino component for the lightest neutralino, so the coupling to gauge bosons and their superpartners are dominant in this region.

The annihilation and co-annihilation diagrams are often combined with a small contribution from the m_A resonance to obtain the correct relic density. However, in most of the parameter space, the neutralino is bino-like, so the annihilation via a pseudo-scalar Higgs boson is dominant. This leads to a strong dependence of the cross section on m_A and thus $\tan\beta$, which can be explained as follows: large Yukawa couplings can drive $m_{H_d}^2$ negative at the electroweak scale leading to EWSB as demonstrated in Fig. 5.4(a). Here the running of $m_{H_d}^2$ and $m_{H_u}^2$ from the GUT to the low energy scale for a fixed mass point $m_0 = 1000$ GeV and $m_{1/2} = 500$ GeV is shown using a small (Fig. 5.4(a)) and large (Fig. 5.4(b)) value of $\tan\beta$. For large values of $\tan\beta$, $m_{H_u}^2$ is driven close to zero as well or becomes even negative, see Fig. 5.4(b). The pseudo-scalar Higgs mass squared, which is at tree level given by the sum of $m_{H_u}^2$ and $m_{H_d}^2$ becomes light for large $\tan\beta$. Since the running of the soft masses is extremely sensitive to large values of $\tan\beta$, small changes in $\tan\beta$ in the range above 50 lead to strong variations of the pseudo-scalar Higgs mass m_A. The mass of the bino-like neutralino is related to $m_{1/2}$, so the pseudo-scalar Higgs mass shows the same proportionality $m_A \sim m_{1/2}$ due to the resonance requirement.

Since the relic density is proportional to m_A^{-4}, the dependencies on the CMSSM parameter are intensified for Ωh^2, which is demonstrated in Fig. 5.5(a). The relic density is plotted versus $\tan\beta$ for two mass points indicated by the corresponding m_0-$m_{1/2}$ values for $A_0 = 0$ GeV. The strong dependence on $\tan\beta$ is shown by the steep decrease for large $\tan\beta$. In Fig. 5.5(b) the same distribution is shown on a smaller scale to resolve the distribution of Ωh^2. A slight impact on the trilinear coupling for the pseudo-scalar Higgs mass is given due to one loop corrections to the Higgs mass squared, which are coming from squark mixing effects [134]. For a fixed value of A_0 there is only a specific value of $\tan\beta$, so by changing A_0, the preferred value of $\tan\beta$ can be shifted. This is indicated for the light SUSY mass by the dotted blue line in Fig. 5.5(a) which corresponds to $A_0 = -1500$ GeV. The dependence on A_0 is negligible compared to $\tan\beta$, but is crucial if the relic density is combined with other constraints. The red solid line in Fig. 5.5(a) corresponds to the relic density distribution for large SUSY masses, which require a larger pseudo-scalar Higgs mass due to the resonance requirement. This in turn narrows the resonance.
The correct value of the relic density can be obtained within almost the whole m_0 and $m_{1/2}$ plane by varying $\tan\beta$ and A_0, which is shown in Fig. 5.6. The color coding indicates the value of Ωh^2. Within the white upper left corner the stau represents the LSP. The red

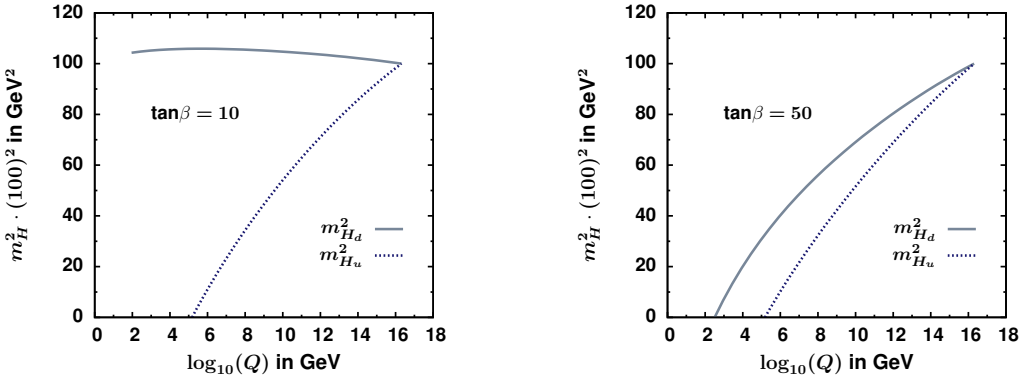

(a) (b)

Figure 5.4.: Running of $m^2_{H_u}$ and $m^2_{H_d}$ from the GUT to the low energy scale demonstrated for a fixed mass point $m_0 = 1000$ GeV, $m_{1/2} = 500$ GeV using $\tan\beta = 10$ (a) and $\tan\beta = 50$ (b). Large values of $\tan\beta$ drive both masses negative, which results in a small pseudo-scalar Higgs mass. The running of the soft masses is extremely sensitive to large values of $\tan\beta$, leading to strong variations in m_A.

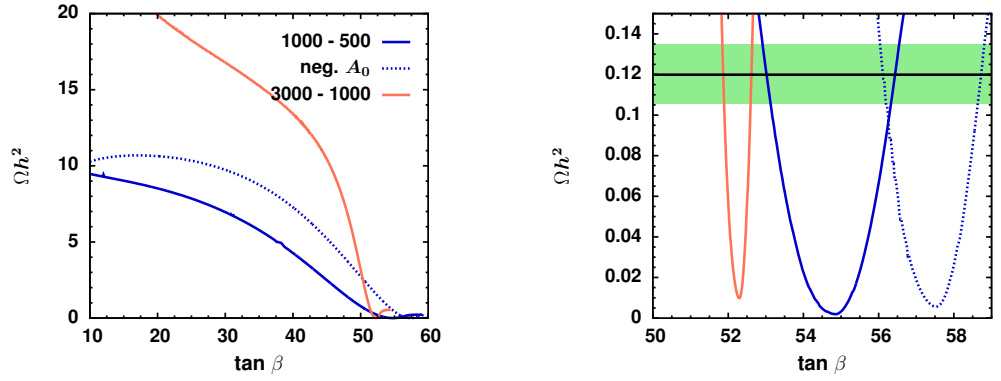

(a) (b)

Figure 5.5.: (a): Dependence of the relic density on $\tan\beta$ for varying SUSY masses indicated by the corresponding m_0-$m_{1/2}$ values for $A_0 = 0$ GeV. For a fixed value of A_0 a specific value of $\tan\beta$ exist. So varying A_0 leads to a shift in the preferred $\tan\beta$ value, as indicated for the light SUSY mass by the dotted blue line which corresponds to $A_0 = -1500$ GeV. The steep decrease of m_A for large values of $\tan\beta$ leads to a steep decrease of Ωh^2. The resonance is getting more narrow for larger SUSY masses as demonstrated by the red solid line. (b): Same distribution as in (a) but on a smaller scale to resolve the resonance. The horizontal line corresponds to the experimental measurement of Ωh^2, while the colored band represents the total error.

region in Fig. 5.6 next to the white region is excluded, since the relic density is too large. In this region the stau co-annihilation is not sufficient to reach the required annihilation cross section. An additional contribution from the m_A resonance is not possible because of the limited range of $\tan\beta$ and A_0 resulting from low m_0. Large values of $\tan\beta$ are again required to get the correct pseudo-scalar Higgs mass. For such large values of $\tan\beta$ the stau is the LSP in this parameter space, which is excluded. Almost the whole allowed region is dominated by the m_A resonance, except for the small focus point and stau co-annihilation region. The correct annihilation cross section is determined slightly off the resonance leading to a range of $m_A \approx 1.5 - 2.5 \cdot m_{\tilde{\chi}}$. The mass of the bino like neutralino is approximately $m_{\tilde{\chi}} \approx M_1 \approx 0.4 m_{1/2}$. To obtain a pseudo-scalar Higgs mass of the order of $m_{1/2}$, the relic density prefers large values of $\tan\beta$ around 50, as shown in Fig. 5.4. The

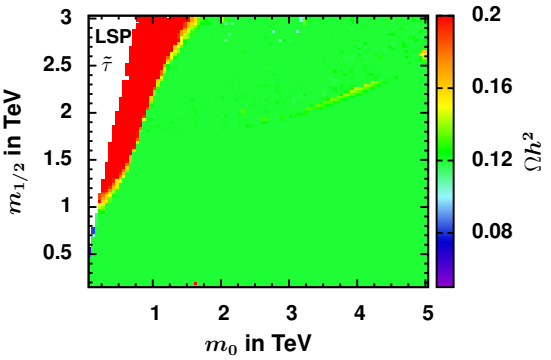

Figure 5.6.: The relic density is plotted within the m_0-$m_{1/2}$ plane for optimized tanβ and A_0 and is indicated by the color coding. The relic density can be fulfilled within almost the whole m_0-$m_{1/2}$ plane. The dominant annihilation via a pseudo scalar Higgs leads to $m_A \approx 1.5 - 2.5 \cdot m_\chi$, which requires tan$\beta \approx 50$ [133]. The white region in the top left corner is excluded since the stau represents the LSP. Within the red region the relic density is too large, since the stau co-annihilation is not sufficient to provide the required annihilation cross section.

pseudo-scalar Higgs boson decays predominantly into b-quark pairs for large tanβ. The corresponding annihilation cross section $\chi\chi \to A \to b\bar{b}$ is proportional to

$$\langle \sigma v \rangle \sim \frac{m_\chi^2 m_b^2 \tan^2\beta}{\sin^4 2\theta_W M_Z^2} \frac{(N_{31}\sin\beta - N_{41}\cos\beta)^2 (N_{21}\cos\theta_W - N_{11}\sin\theta_W)^2}{(4m_\chi^2 - m_A^2)^2 + m_A^2 \Gamma_A^2}. \tag{5.2}$$

The annihilation channel $\chi\chi \to A \to b\bar{b}$ is getting less significant for large SUSY masses. The large corresponding values of the neutralino mass above 1 TeV reduces the annihilation cross section. To still obtain the right amount of dark matter the dominant digram to $1/\Omega h^2$ is coming from the stau self annihilation via a scalar Higgs boson H. The corresponding diagram is shown in Fig. 5.3(d). If the stau is slightly above the neutralino mass, which occurs for large mixing in the stau sector $|A_0| \approx 3m_0$, the stau self annihilation can significantly contribute to the relic density. The large stau self annihilation cross section and the number density at the freeze-out temperature, which is hardly suppressed by the Boltzmann factor, gives a large contribution to $\langle \sigma v \rangle$, see Ref. [114, 127]. The fraction of the stau self annihilation into a $b\bar{b}$ pair is shown in Fig. 5.7(a) in the m_0-$m_{1/2}$ plane indicated by the color coding for optimized tanβ and A_0.

The stau contribution is only required for high neutralino masses as shown by the orange region in Fig. 5.7(a). Within the white region the annihilation via the pseudo-scalar Higgs boson still persist. The reason for the abrupt step in the contribution from the stau self annihilation for large neutralino masses is related to the minimization procedure. The χ^2 contribution is increasing for moderate A_0 for increasing $m_{1/2}$, so the minimization tool intend to search another lower minimum. It can be found in the stau self annihilation region, since the χ^2 value is much lower for the same SUSY mass point. This is demonstrated in Fig. 5.7(b), where Ωh^2 is plotted versus tanβ. The neutralino annihilation refers to moderate A_0 (blue lines), while the stau self annihilation is connected to large $|A_0|$ (red lines). The green line corresponds to the measured value of Ωh^2. The χ^2 contribution from the neutralino annihilation is higher compared to the self annihilation for increasing $m_{1/2}$. This leads to the abrupt step in A_0 shown in Fig. 5.7(a). Eliminating the stau annihilation channel leads to an exclusion of the corresponding parameter space. This parameter space has been checked not to be a software specific features. The same conclusions are obtained

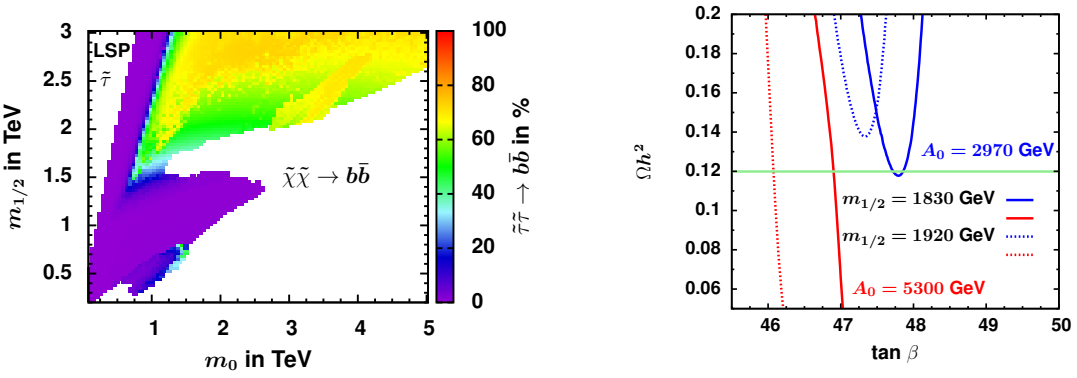

(a) (b)

Figure 5.7.: (a): The color coding corresponds to the fraction to the relic density, which is coming from stau self annihilation in %. Here the stau and the neutralino are degenerate in mass. The large stau self annihilation cross section and the number density at the freeze-out temperature gives a large contribution to the time averaged annihilation cross section, which is needed for large SUSY masses. For light SUSY masses, the annihilation via the pseudo scalar Higgs boson dominates. (b): The relic density $\Omega h^2$is plotted versus tanβ for two different neutralino masses indicated by the different values of $m_{1/2}$. The neutralino annihilation corresponds to the moderate A_0 (blue lines) and while the stau annihilation occurs for large A_0 (red lines). The measured value of the relic density indicated by the solid green line, can only be fulfilled for the stau self annihilation for increasing neutralino mass demonstrated by the dashed lines.

by using different combinations of additional spectrum calculator (SOFTSUSY [135]) and relic density calculation software (SuperIso Relic [136]).

Two additional allowed regions in the CMSSM parameter space are mentioned in the following, which are relevant if only Ωh^2 is considered but vanish if all constraints are combined:

- stop self annihilation: this annihilation channel can contribute to the relic density for large neutralino masses in the same way like the stau self annihilation. However, it requires small tanβ values of the order of 10 or less, which leads to light Higgs boson masses below 120 GeV. Such parameter sets vanish if the relic density is combined with the Higgs mass constraint.
- negative μ: the results shown so far correspond to a positive sign of μ. The relic density constraint can also be fulfilled for sgn(μ) $= -1$ but it prefers low values of tanβ leading again to a light Higgs mass. It was checked that the allowed parameter space is small compared to the results for sgn(μ) $= +1$, so only positive values of μ are considered for the CMSSM.

In the NUH-CMSSM the splitting of the soft SUSY breaking masses at the GUT scale and therefore the mass of the pseudo-scalar Higgs mass can be chosen independently of tanβ. The resonance condition has to be fulfilled though, leading to the similar combinations of tanβ and m_A for a fixed mass point. Only the co-annihilation region is affected by a slight extension. However, these extended regions are not compatible with a 125 GeV Higgs boson leading to a similar allowed region in the m_0-$m_{1/2}$ plane like in the CMSSM. It was checked that the results and conclusions of the CMSSM are mainly reproduced, so the NUH-CMSSM is not further considered.

In the CNMSSM, the GUT relations resemble the CMSSM boundary conditions but an additional coupling λ due to the extended Higgs sector has to be specified. λ tends to

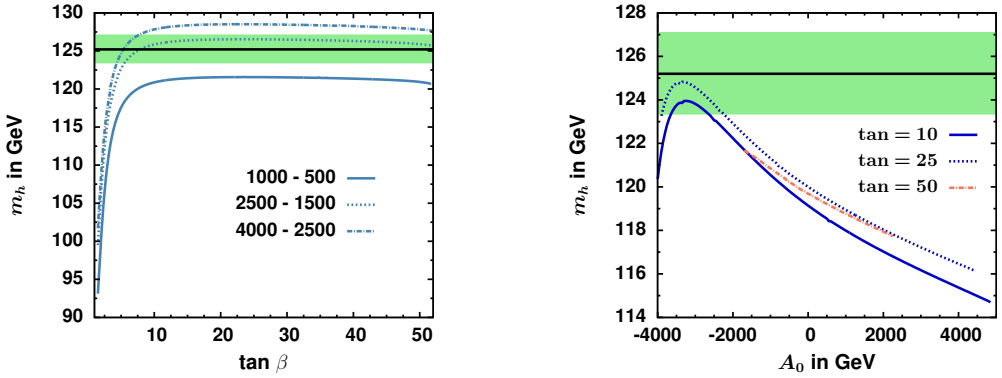

(a) (b)

Figure 5.8.: (a): The light Higgs mass m_h is plotted versus tanβ in the CMSSM for different mass points indicated by the m_0-$m_{1/2}$ values. The trilinear coupling A_0 is fixed, $A_0 = -2 \cdot m_0$. The horizontal line and the colored band correspond to the measured value and its total error. For large SUSY masses, the light Higgs mass can reach 125 GeV even for small values of tanβ. For large values tan$\beta \gtrsim 10$ the Higgs mass starts to saturate. (b): The Higgs mass is plotted versus A_0 for different values of tan$\beta = \{10, 25, 50\}$ for a fixed mass point $m_0 = 1000$ GeV $m_{1/2} = 1000$ GeV. The Higgs boson mass is maximized for moderate values of tanβ and large negative values of A_0 for a fixed mass point. The allowed range of A_0 is reduced for large values of tanβ, since positive sparticle mass squared are required.

vanish to fulfill the required Higgs mass constraint, which will be discussed in more detail in the next section. This leads to a decoupled singlet and therefore to a decoupled fifth neutralino $\tilde{\chi}_5^0$. This leads to the same conclusions as in the CMSSM, so they will not further be discussed. In the NUH-NMSSM the required Higgs mass leads to a strong mixing with the singlet, which impacts the neutralino sector. Many annihilation channels and corresponding diagrams become accessible. Due to the variety of the neutralino sector, only the relevant parameter space which is allowed by combing all constraints will discussed in section 6.2.5.

5.2. Standard Model Higgs Boson

In 2012 a Higgs-like boson was discovered at the LHC both in the ATLAS and the CMS experiment near a mass of 125 GeV. The measurements of CMS and ATLAS are compatible within errors including the combination of all discovery channels. The corresponding measured coupling strengths agree with the SM prediction within errors. The discovery of the Higgs boson completed the SM, but its mass could have been anywhere between the EW and GUT scale. Unlike the SM, within SUSY a light Higgs boson below 135 GeV is predicted, which strongly supports SUSY despite of the fact that no SUSY particle has been found so far. However, the predicted mass of the Higgs boson depends on the supersymmetric model.

The tree level mass of the Higgs boson is limited by the Z^0 boson mass within the MSSM, since $m_h \leq m_Z |\cos 2\beta|$ [67], as already mentioned in section 3.1.1. The light Higgs mass can be shifted to larger values by large loop corrections form stop and top loops. Such large contributions of the order of 35 GeV are accomplished by using large values of tanβ and large negative values of A_0 within the CMSSM. Such a parameter combination maximizes the splitting in the stop sector for fixed other values of CMSSM parameters. Fig. 5.8(a) shows the dependence of the light Higgs mass on tanβ for different mass points indicated by the corresponding m_0-$m_{1/2}$ values for $A_0 = -2 \cdot m_0$. The mass distribution saturates for high values of tanβ, since $\cos 2\beta \approx 1$. If the common SUSY masses are too low, the

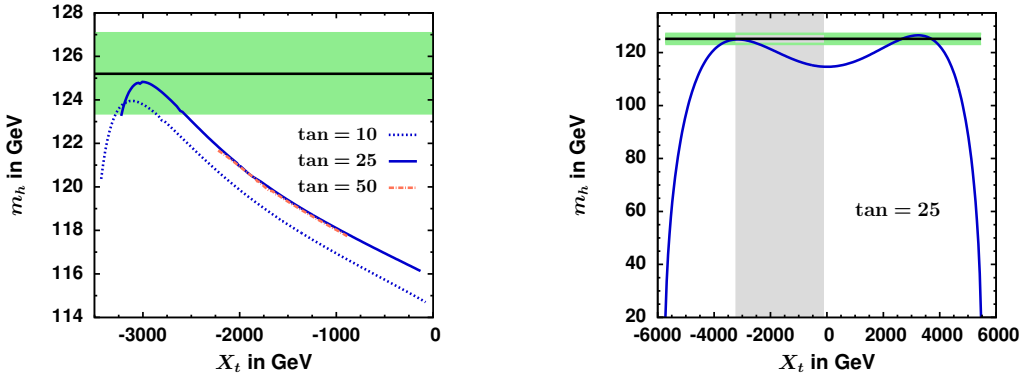

Figure 5.9.: (a): Higgs mass plotted versus the stop mixing parameter $X_t = A_t - \mu/\tan\beta$ for a fixed mass point $m_0 = 1000$ GeV $m_{1/2} = 1000$ GeV and different values of $\tan\beta = \{10, 25, 50\}$. The horizontal line corresponds to the experimental measurement while the colored band demonstrates the total error. The maximal Higgs boson mass is reached for large negative X_t combined with moderate to large values of $\tan\beta$. (b): m_h plotted versus X_t for the same mass point and $\tan\beta = 25$ using low energy input in the general MSSM, which is not restricted from any GUT scale relations. Only a limited range in X_t is available in the CMSSM indicated by the vertical colored band due to the fixed point solutions.

required Higgs mass cannot be reached even for a maximal mixing as demonstrated by the solid blue line in Fig. 5.8(a). For adequate SUSY masses a Higgs boson mass of 125 GeV is reached for $\tan\beta$ values above 10. The influence of A_0 due to the mixing is demonstrated in Fig. 5.8(b). Here the Higgs mass is plotted for a fixed mass point $m_0 = 1000$ GeV $m_{1/2} = 1000$ GeV and varying values of $\tan\beta = \{10, 25, 50\}$. For fixed CMSSM parameters the maximal Higgs mass is reached for large negative values of A_0. Since the range for A_0 is limited to $[-2 \cdot m_0, 3 \cdot m_0]$ for large $\tan\beta$ by the requirement of positive sparticle mass squared, the Higgs mass constraint prefers intermediate values of $\tan\beta$. The limited range on A_0 due to the fixed point solutions, see e.g Ref. [137], results in a limit on the stop mixing parameter $X_t = A_t - \mu/\tan\beta$. This is demonstrated in Fig. 5.9(a), which shows the same distribution as in Fig. 5.8(b), while A_0 is translated to X_t. The allowed range in the CMSSM corresponds only to a small range of the hypothetical X_t. In the general MSSM, which is not restricted by GUT boundary conditions, X_t can reach large positive values. In Fig. 5.9(b) the light Higgs mass is plotted versus X_t for the same mass point and $\tan\beta$=25 within the general MSSM. Here a large range of X_t is accessible, while only the vertical colored band is allowed within the CMSSM.

The required mass of about 125 GeV is reached almost in the whole m_0-$m_{1/2}$plane, except for small SUSY masses below $m_0 = 1000$ GeV $m_{1/2} = 500$ GeV. The lightest Higgs has SM like couplings, since the decoupling limit is fulfilled within the whole m_0-$m_{1/2}$ plane. Scenarios where the heavier scalar Higgs H corresponds to the 125 GeV SM Higgs are not possible within the CMSSM.
Such a light heavy Higgs is only accomplished if the squared soft mass $m^2_{H_u}$ is large and negative. So the running from the GUT to the low scale has to be very steep. This is fulfilled by large values of $\tan\beta$ but such large values are immediately connected to non-SM couplings. Fig. 5.10(b) and Fig. 5.10(d) shows the normalized couplings to up and down type fermions for the heavy Higgs as a function of m_A for different values of $\tan\beta = \{3, 30, 50\}$. It demonstrates that small $\tan\beta$ are favored to get compatible SM couplings especially for the down type fermions indicated by the dashed dotted blue lines, since it is proportional to $\sin\alpha/\cos\beta$. This is inconsistent with a small heavy Higgs mass

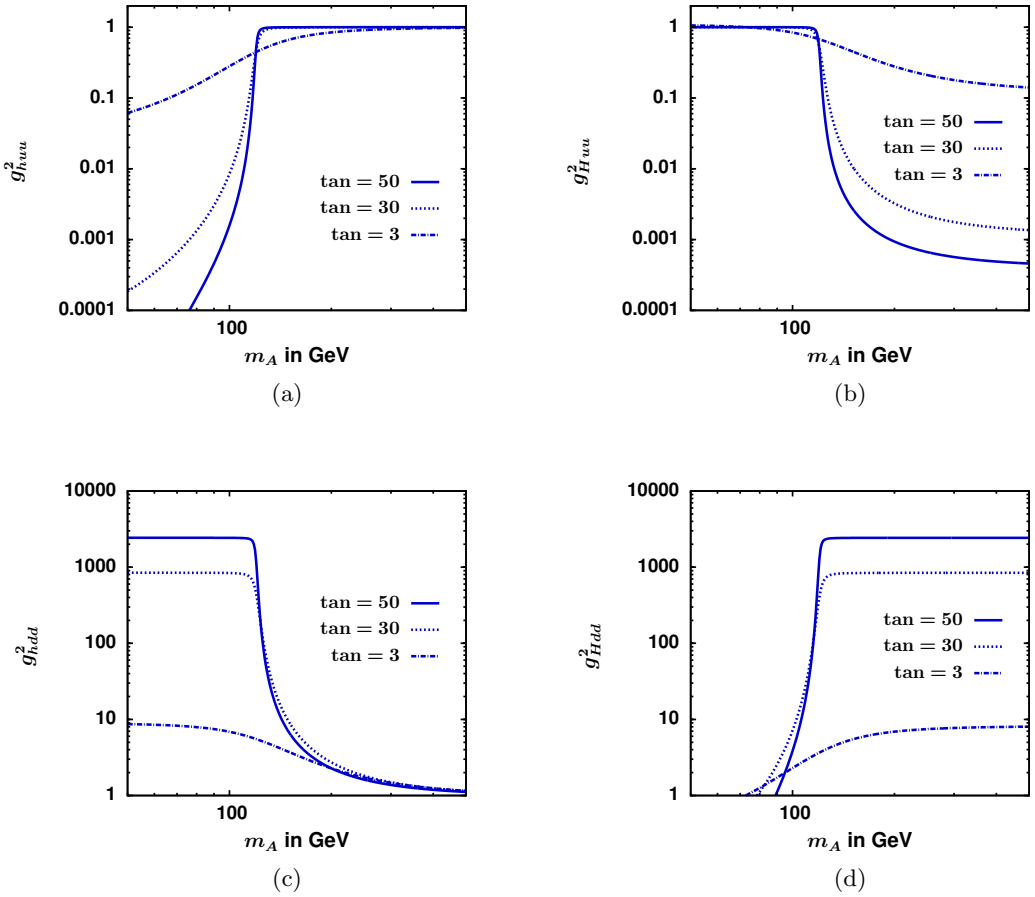

Figure 5.10.: Normalized couplings to up- and down-type fermions for the light and heavy scalar Higgs. Within the CMSSM, the heavy Higgs boson requires large values of tanβ above 50 to reach a low mass of about 125 GeV. This leads in turn to large non-SM couplings to down-type fermions as indicated by the solid blue lines in (d). In the NUH-CMSSM, where the pseudo-scalar Higgs mass and tanβ can be independently chosen, a light heavy Higgs boson with SM couplings is possible. However, the enhancement of down-type couplings for the light scalar Higgs below 125 GeV, indicated by the solid blue line in (c), is not compatible with the LEP bound on a light Higgs below 125 GeV.

using GUT boundary condition as indicated by the solid blue lines in Fig. 5.10. This is resolved, if tanβ and m_A are chosen independently as it is the case in the NUH-CMSSM. So a light scalar Higgs boson H with nearly SM couplings is possible. However even if the couplings to the heavier Higgs can be SM like, the couplings of the lightest Higgs below 125 GeV are certainly non SM-like. Fig. 5.10(a) and Fig. 5.10(c) shows the couplings to up- and down-type fermions for the light Higgs depending on m_A for different values of tan$\beta = \{3, 30, 50\}$. The coupling to down-type fermions is enhanced for light heavy Higgs bosons. This violates the LEP limit, which requires reduced couplings to SM particles for a Higgs below 114 GeV.
Furthermore, the combination with the relic density would lead to preferred large tanβ values, which is inconsistent with the constraints on the pseudo-scalar Higgs mass. Such scenarios are disfavored if all constraints are included. Even studies in a more larger parameter space called the phenomenological MSSM (pMSSM[2]), where all masses and couplings can be chosen independently at the low scale, such exotic scenarios emerge rare

[2]Within the phenomenological MSSM it is assumed that the first two sfermion generations are degenerate with negligible Yukawa couplings, which leads to 19 free parameters.

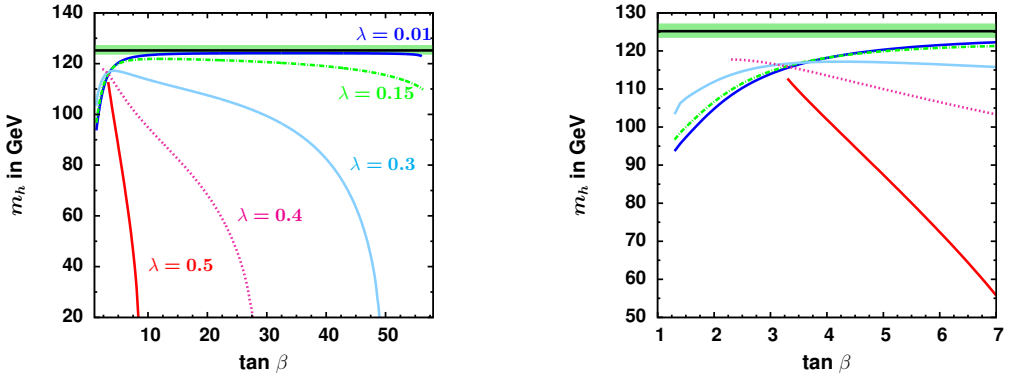

Figure 5.11.: (a): The lightest Higgs mass in the CNMSSM as function of tanβ for a fixed mass point $m_0 = 2500$ GeV $m_{1/2} = 1500$ GeV and varying values of $\lambda = \{0.01, 0.15, 0.3, 0.4, 0.5\}$. The lightest Higgs mass is enhanced for small values of tanβ combined with large values of λ as indicated by the solid yellow line. However, the required Higgs mass of 125 GeV is not reached, since the range of tanβ is limited. To obtain the Higgs mass of 125 GeV within the CNMSSM the MSSM limit $\lambda, \kappa \to 0$ is required as indicated by the blue dotted line. (b): The same distribution as in (a) is shown on a smaller scale to resolve the enhancement for low tanβ.

from the parameter scans [138]. This proposed light heavy Higgs scenarios [139], can only be discussed leaving out other constraints, e.g. flavor constraints see [140].

In the NMSSM, the SUSY Higgs sector is enriched compared to the MSSM by adding a further Higgs singlet. Due to the mixing with the additional Higgs singlet the lightest Higgs boson mass gets an additional term at tree level: $\lambda v|\sin 2\beta|$. This additional term leads to an significant enhancement for small values tanβ combined with large values of λ. Within the CNMSSM the range of λ and tanβ are correlated due to EWSB, which furthermore determines μ_{eff}. Due to the limited combinations of tanβ and λ, the enhancement is not sufficient to reach 125 GeV for small tanβ. This is shown in Fig. 5.11(a), where the lightest SM-like Higgs is plotted versus tanβ for different values of λ. Fig. 5.11(b) shows the same distribution on a smaller scale to resolve the enhancement. The enhancement is only valid for small tanβ around ~ 2 indicated by the solid yellow line. The distribution is limited for large values of λ above 0.4 as can be seen from the solid red line, so the required Higgs mass cannot be reached. Large values of tanβ combined with large values of λ leads to a reduced Higgs mass compared to the CMSSM. This results from another additional term which arise from the mixing with the Higgs singlet: $-\frac{\lambda^2}{\kappa^2} v^2 (\lambda - \kappa \sin 2\beta)^2$. For large tan$\beta$ the combination of the first and the second additional term leads in total to a negative contribution since the terms which include $\sin 2\beta$ vanish. The required mass of about 125 GeV is reached for small values of λ below 0.1 combined with moderate values of tanβ as indicated by the blue dotted line. For such small couplings, the second lightest Higgs corresponds to the heavy MSSM scalar Higgs while the additional singlet-like Higgs and singlino-like neutralino are completely decoupled. The resulting scenario thus reproduces the results from the CMSSM with slightly modified values of tanβ and A_0, which was checked by a combined global fit for the CNMSSM. The CNMSSM will therefore not further be considered.

Within the NUH-CMSSM the couplings can be chosen independently from each other while EWSB is still preserved. This opens a new window for small tan$\beta$and small values of μ_{eff} are now possible, leading to new solutions of the Higgs mixing matrix in addition to the results of the CNMSSM mentioned above. Among the three scalar Higgs bosons,

two relatively light scalar Higgs bosons are predicted within the NUH-NMSSM, so either the lightest or the second lightest Higgs boson can be the discovered Higgs boson at a mass of 125 GeV with the required SM couplings. The requirement of SM couplings for one of the light Higgs bosons leads immediately to reduced SM couplings for the remaining light Higgs boson according to the sum rule of the couplings. If the lightest Higgs is the SM like Higgs boson, a singlet like second-lightest Higgs boson with a slightly higher mass and reduced couplings to SM particles exist and vice versa. The third Higgs corresponds to the heavy scalar Higgs boson in the CMSSM. So far the couplings of the 125 GeV Higgs boson show no significant deviation from the SM. However, a possible modifications of the couplings can be easily obtained within the NUH-CNMSSM by a different mixing in the Higgs sector. A third singlet-like Higgs reproduces again the CMSSM scenario. The scenario where the third Higgs corresponds to the 125 GeV Higgs combined with two light Higgs boson below 125 GeV is not possible within the NUH-CMSSM. The sum rule of the Higgs couplings would lead non-SM couplings for one of the light Higgs boson inconsistent with the LEP limit. Within the NUH-CNMSSM there exist various scenarios, which can fulfill a SM-like 125 GeV Higgs boson, so only the relevant scenarios with respect to the combination with all constraints will be discussed in detail in section 6.2.4.

5.3. Branching Ratios from B-Physics

Indirect signals from SUSY can be found in processes that are rare or forbidden in the SM but have additional contributions from involving SUSY particles. The branching ratios from rare decays summarized in this section can be used to constrain the supersymmetric parameter space. In the last years the discrepancy between experimental measurements and theoretical predictions decreased, so large additional contributions from SUSY are not needed anymore.
In section 5.1 and 5.2, it was shown, that the NUH-CMSSM and CNMSSM, will not give further physical insight, and mainly reproduce the results from the CMSSM, so further discussions of the remaining constraints and the results of the combination of all constraints will only include the CMSSM and NUH-CNMSSM.
For clearness and to avoid lengthy expression the NUH-CNMSSM will be re-named to NMSSM from now on.

5.3.1. Rare Decay of a B_S Meson: $B_s^0 \to \mu^+\mu^-$

The decay of a B_S meson, a hadron composed of a s and $\bar{b}$ quark, into a pair of muons is highly suppressed in the SM, since it requires a transition forbidden at tree level of $b \to s$. This FCNC can only proceed via higher order diagrams at the one loop level, see SM diagrams in Fig. 5.12. The process receives an additional helicity suppression, which leads to a predicted branching fraction of $BR(B_s^0 \to \mu^+\mu^-)_{SM} = (3.65 \pm 0.23) \cdot 10^{-9}$ in the SM [98]. In 2012 the rare decay has been measured at the LHC independently by the LHCb [96] and the CMS [97] experiment which leads to the weighted average value of $BR(B_s^0 \to \mu^+\mu^-)_{EXP} = (2.9 \pm 0.7) \cdot 10^{-9}$ [141]. The measured value is slightly below the SM prediction but agrees within errors, so the contribution to the SM branching ratio from additional SUSY diagrams, shown in Fig. 5.12, should be small in order not to conflict with the measured value. $BR(B_s^0 \to \mu^+\mu^-)$ can be written in the form [142]

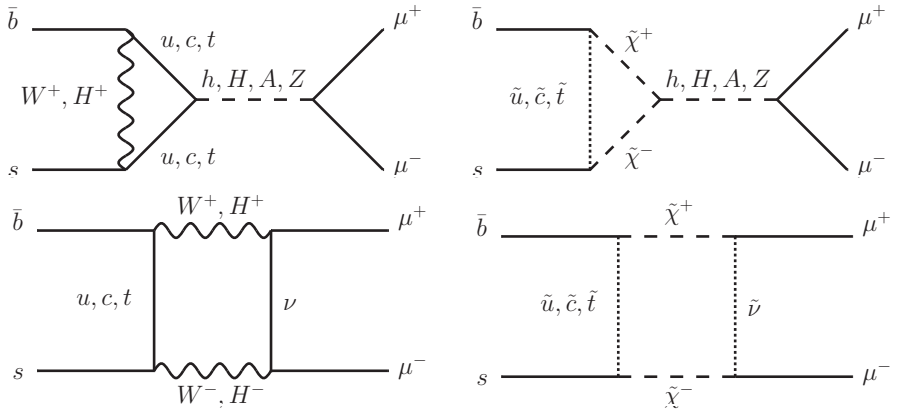

Figure 5.12.: Dominant diagrams for $B_s^0 \to \mu^+\mu^-$ in the SM and MSSM. The SUSY diagrams result from the SM diagrams by replacing the SM particles by the corresponding SUSY particles and additional Higgs bosons.

$$BR(B_s^0 \to \mu^+\mu^-) = \frac{2\tau_{B_s} M_{B_s}^5}{64\pi} f_{B_s}^2 \sqrt{1 - \frac{4m_\mu^2}{M_{B_s}^2}} \times \left[\left(1 - \frac{4m_\mu^2}{M_{B_s}^2}\right) \left| \frac{C_S - C_S'}{m_b + m_s} \right|^2 + \left| \frac{C_P - C_P'}{m_b + m_s} + 2\frac{m_\mu}{M_{B_s}^2}(C_A - C_A') \right|^2 \right], \tag{5.3}$$

where M_{B_s} is the B_s meson mass, τ_{B_s} its mean life and f_{B_s} the B_s decay constant. The coefficients $C_S^{(\prime)}, C_P^{(\prime)}$ and $C_A^{(\prime)}$ represent the scalar, pseudo-scalar and axial form-factors. The scalar and pseudo-scalar form-factors include the SUSY loop contribution coming from sparticles and Higgses. They give a large contribution to the SM branching ratio for large tanβ. Their dominant contribution to C_S is approximately [143]

$$C_S \simeq \frac{G_F \alpha}{\sqrt{2}\pi} V_{tb} V_{ts}^* \left(\frac{\tan^3 \beta}{4 \sin^2 \theta_W} \right) \left(\frac{m_b m_\mu m_t \mu}{M_W^2 M_A^2} \right) \frac{\sin 2\theta_{\tilde{t}}}{2} \left(\frac{m_{\tilde{t}_1}^2 \log\left[\frac{m_{\tilde{t}_1}^2}{\mu^2}\right]}{\mu^2 - m_{\tilde{t}_1}^2} - \frac{m_{\tilde{t}_2}^2 \log\left[\frac{m_{\tilde{t}_2}^2}{\mu^2}\right]}{\mu^2 - m_{\tilde{t}_2}^2} \right), \tag{5.4}$$

with the stop masses $m_{\tilde{t}_{1,2}}$ and the corresponding rotation angle $\theta_{\tilde{t}}$ to diagonalize the stop mass matrix. The other coefficients are given by $C_P = -C_S$, $C_S' = (m_s/m_b)C_S$ and $C_P' = -(m_s/m_b)C_P$. The $B_s^0 \to \mu^+\mu^-$ constraint can be fulfilled within the whole m_0-$m_{1/2}$ plane. It prefers low values of tanβ to be compatible with the SM predictions and therefore with the experimental measurement, since large values of tanβ lead to an enhancement of $\propto \tan^6 \beta$ as shown in Eq. 5.4. The steep increase of the branching ratio for large tanβ is demonstrated in Fig. 5.13(a). Here $BR(B_s^0 \to \mu^+\mu^-)$ is plotted versus tanβ for $A_0 = 0$ and different mass points in the CMSSM indicated by the corresponding m_0-$m_{1/2}$ values. The horizontal line corresponds to the experimental value while the colored band represents the total error. The slope of the distribution depends on the common SUSY masses m_0 and $m_{1/2}$, which determine the involved sparticles in the loops. The branching ratio starts to deviate from the SM value for moderate values of tanβ for light SUSY masses, as demonstrated by the solid dark blue line in Fig. 5.13(a). Heavy SUSY masses yield a small SUSY contribution, so a large range of tanβ is compatible with

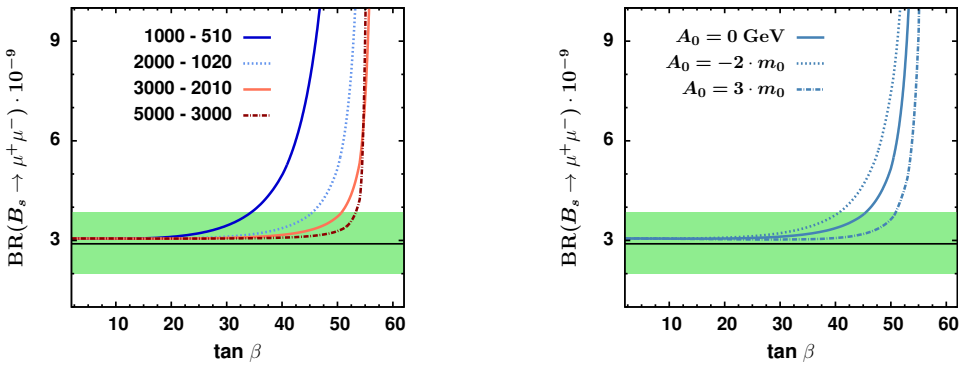

(a) (b)

Figure 5.13.: (a): $BR(B_s^0 \to \mu^+\mu^-)$ plotted versus tanβ for a fixed trilinear coupling $A_0 = 0$ GeV and varying SUSY masses indicated by the corresponding m_0-$m_{1/2}$ values. The SUSY contribution becomes small for increasing SUSY masses, which leads to a large allowed range for tanβ. (b): $BR(B_s^0 \to \mu^+\mu^-)$ plotted versus tanβ for a fixed mass point $m_0 = 2000$ GeV and $m_{1/2} = 1020$ GeV and varying trilinear coupling $A_0 = \{-2 \cdot m_0, 0, 3 \cdot m_0\}$. Large positive(negative) values of A_0 can reduce(enhance) the SUSY contribution for large tanβ due to a destructive interference coming from the stop sector. The horizontal line corresponds to the experimental measurement while the band represents its total error.

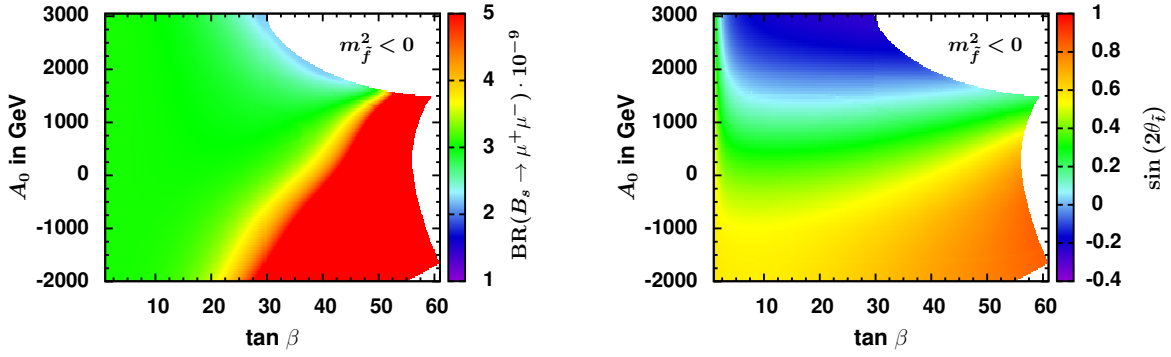

(a) (b)

Figure 5.14.: $BR(B_s^0 \to \mu^+\mu^-)$ (a) and the corresponding stop mixing angle $\sin(2\theta_{\tilde{t}})$ (b) plotted in the tanβ-A_0 plane and indicated by the color coding for a fixed mass point $m_0 = 1000$ GeV $m_{1/2} = 250$ GeV. The branching ratio drops below the SM prediction, as shown by the blue colored region in the top right corner of (a), if a small stop mixing and $\sin(2\theta_{\tilde{t}}) < 0$ coexist. Thus large values of $BR(B_s^0 \to \mu^+\mu^-)$ can be sufficiently suppressed by the stop mixing, see Ref. [144]. The white region is not allowed because of negative Higgs and/or sfermion mass squared.

the measured branching ratio up to tan$\beta \approx 50$, as shown by the red lines in Fig. 5.13(a). However, a huge enhancement for large tanβ still remains, since it is intensified by the decrease of the pseudo-scalar Higgs mass m_A as indicated in Eq. 5.4.
In the NMSSM small values of tanβ are required from the Higgs mass constraint, so the additional SUSY contribution to $BR(B_s^0 \to \mu^+\mu^-)$ is small and leads to a SM-like branching ratio. Within the CMSSM large values of tanβ are preferred by the relic density constraint. To fulfill all constraints simultaneously the enhancement of $BR(B_s^0 \to \mu^+\mu^-)$ from $\tan^6\beta/m_A^4$ has to be compensated by other parameters in Eq. 5.4. A reduction

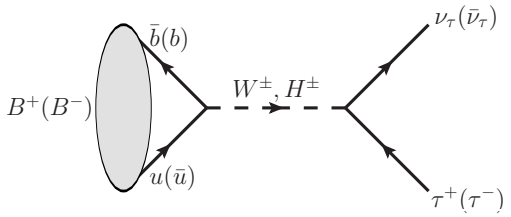

Figure 5.15.: The leptonic decay of a $B^\pm$ meson can be mediated within SUSY by the annihilation into a charged Higgs boson $H^\pm$ in addition to the SM annihilation into a virtual $W^\pm$ boson.

of the branching ratio for large tanβ is accomplished for large positive values of A_0 as demonstrated by the dashed-dotted line in Fig. 5.13(b). Here the dependence of $BR(B_s^0 \to \mu^+\mu^-)$ on tanβ for a fixed mass point and varying trilinear couplings is shown. The allowed range of tanβ can be enlarged(reduced) by large positive(negative) values of A_0 as shown by the dashed-dotted(dotted) line in Fig. 5.13(b). The impact of the trilinear coupling on the branching ratio is linked to the stop sector: Eq. 5.4 includes the stop mass difference of $\tilde{t}_1$ and $\tilde{t}_2$, so the branching ratio gets a strong suppression, if the stop masses are equal i.e. if the stop splitting is small, see Ref. [144]. The splitting is determined by the off-diagonal element, which is proportional to $(A_t - \mu \cdot \cot\beta)$. Large positive values of A_0 at the GUT scale yield small negative values of A_t at the low scale due to the fixed point solutions, see e.g Ref. [137], thus leading to a small stop mixing for large tanβ. An additional reduction from the stop sector is coming from the mixing angle $\sin(2\theta_{\tilde{t}})$. It changes its sign for increasing A_0, which eventually changes the sign of C_S and therefore C_P. The altering sign induces a destructive interference between C_P and C_A as derived from Eq. 5.3.
The dependence of $BR(B_s^0 \to \mu^+\mu^-)$ and the corresponding angle $\sin(2\theta_{\tilde{t}})$ on tanβ and A_0 for a fixed mass point are shown in Fig. 5.14(a) and Fig. 5.14(b). The color coding corresponds to the value of $BR(B_s^0 \to \mu^+\mu^-)$ and $\sin(2\theta_{\tilde{t}})$, respectively. The white region is excluded due to negative sfermion and/or Higgs mass squared. The enhancement of $BR(B_s^0 \to \mu^+\mu^-)$ for large tanβ is shown by the large red region in the bottom right corner of Fig. 5.14(a). The opposite is observed in the top right corner indicated by the blue colored region due to the destructive interference from the stop sector. The branching ratio drops below the SM prediction because of a small stop splitting and $\sin(2\theta_{\tilde{t}}) < 0$. The negative interference from the additional SUSY contribution is required to dissolve the small discrepancy between the measurement and the SM prediction of $BR(B_s^0 \to \mu^+\mu^-)$.

5.3.2. Leptonic Decay of the B Meson: $B \to \tau\nu_\tau$

The purely leptonic decay $B \to \tau\nu_\tau$ is sensitive to new physics, since the process can also be mediated by a charged Higgs boson $H^\pm$ in addition to a virtual $W^\pm$ boson, as shown in Fig. 5.15. The predicted branching ratio

$$BR(B \to \tau\nu_\tau)_{SM} = \frac{G_F^2 m_B m_\tau^2}{8\pi} f_B^2 |V_{ub}|^2 \left(1 - \frac{m_\tau^2}{m_B^2}\right)^2 \tag{5.5}$$

includes SM parameters like the CKM matrix element $|V_{ub}|$, which has to be determined experimentally. By studying the ratio of the SUSY and SM branching ratio all SM parameters cancel except for the well measured B meson mass, so the calculation of the SUSY contribution is less affected by uncertainties on the involved SM parameters. The BR ratio $R_{B\to\tau\nu_\tau}$ reads

$$R_{B\to\tau\nu_\tau} = BR(B \to \tau\nu_\tau)_{SUSY} / BR(B \to \tau\nu_\tau)_{SM} = \left(1 - \frac{\tan^2\beta}{1 + \tilde{\epsilon}_0 \tan\beta} \frac{m_B^2}{m_H^2}\right)^2, \tag{5.6}$$

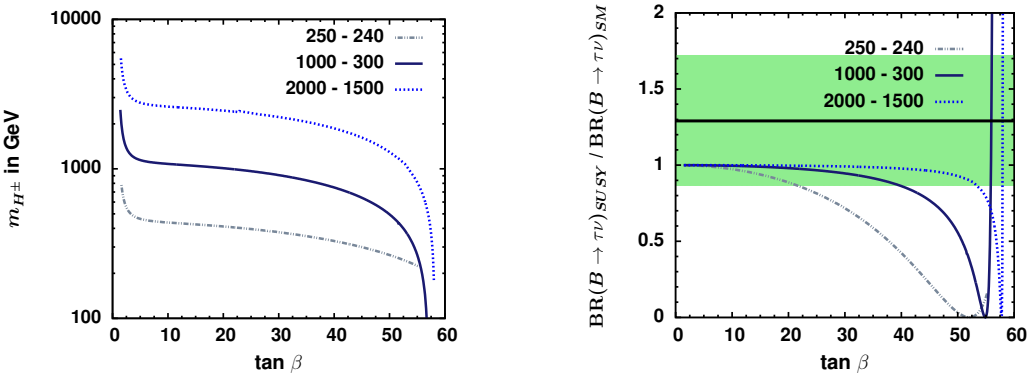

Figure 5.16.: The charged Higgs boson mass $m_{H^\pm}$ (a) and the corresponding BR ratio $R_{B\to\tau\nu_\tau} = BR_{SUSY}/BR_{SM}$ of the leptonic decay of the B meson (b) plotted versus tanβ for three different mass points denoted by the associated m_0-$m_{1/2}$ values. The horizontal line and the green band in (b) corresponds to $R_{B\to\tau\nu_\tau} = BR(B \to \tau\nu_\tau)_{EXP}/BR(B \to \tau\nu_\tau)_{SM}$ and its total error. The steep decrease of the charged Higgs mass for large tanβ shown in (a) leads to a positive SUSY contribution to $R_{B\to\tau\nu_\tau}$ in (b). $R_{B\to\tau\nu_\tau}$ stays close to the SM prediction for a large range of tanβ if $m_{H^\pm}$ is of the order of several TeV.

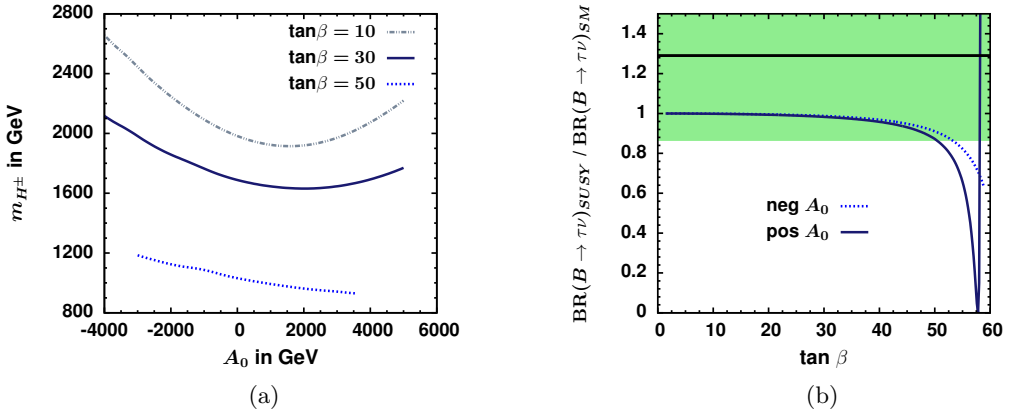

Figure 5.17.: (a): Dependence of the charged Higgs mass $m_{H^\pm}$ on the trilinear coupling A_0 for different values of tan$\beta = \{10, 30, 50\}$ for a fixed mass point $m_0 = 1500$ GeV $m_{1/2} = 1020$ GeV. The sensitivity of $m_{H^\pm}$ on A_0 is coming from one loop corrections including squark mixing effects. (b): The corresponding value of $R_{B\to\tau\nu_\tau}$ plotted versus tanβ for $A_0 = -2000(1500)$ GeV indicated by the solid(dotted) line. A positive SUSY contribution to $R_{B\to\tau\nu_\tau}$ is obtained for large values of tanβ combined with a large positive value of A_0.

where $\tilde{\epsilon}_0$ is a SUSY correction factor, which results mainly from one-loop QCD corrections including gluinos [145, 146] and is maximum of the order of 0.01 [147]. The theoretical and experimental uncertainties are combined to a total error on $R_{B\to\tau\nu_\tau}$ using a Gaussian error propagation. The experimental average of $BR(B \to \tau\nu_\tau)_{EXP} = (0.96 \pm 0.26) \cdot 10^{-4}$ [101] is in agreement with the SM prediction $BR(B \to \tau\nu_\tau)_{SM} = (0.74 \pm 0.14) \cdot 10^{-4}$ [102] within uncertainties, so its ratio $R_{B\to\tau\nu_\tau} = BR(B \to \tau\nu_\tau)_{EXP}/BR(B \to \tau\nu_\tau)_{SM} = (1.29 \pm 0.43)$ is compatible to one within 1σ. The $B \to \tau\nu_\tau$ constraint can be fulfilled in the whole m_0-$m_{1/2}$ plane, if the additional SUSY contribution is large and positive to reach the required value of $R_{B\to\tau\nu_\tau} = 1.29$. In case of a negative SUSY contribution it has to be small to stay within 1σ near the SM prediction. The latter one is easily fulfilled for small values of tanβ, as can be derived from Eq. 5.6. The SUSY contribution decreases the BR

ratio with respect to the corresponding charged Higgs mass, which depends on tanβ and the common SUSY masses m_0 and $m_{1/2}$. This is demonstrated in Fig. 5.16(a) and Fig. 5.16(b), which show the dependence of $m_{H^\pm}$ and the corresponding BR ratio $R_{B\to\tau\nu_\tau}$ on tanβ for three different SUSY mass points indicated by the m_0-$m_{1/2}$ values. High SUSY masses are correlated with large charged Higgs masses as shown by the lines in Fig. 5.16(a). The mass of the charged Higgs boson $m_{H^\pm}$ controls the slope of $R_{B\to\tau\nu_\tau}$, so the BR ratio stays close to one if $m_{H^\pm}$ is of the order of several TeV as can be seen from the dotted line in Fig. 5.16(b). If $m_{H^\pm}$ is small due to light SUSY masses, the ratio deviates from the SM prediction even for small values of tanβ demonstrated by the dashed line in Fig. 5.16(b). Small charged Higgs masses $m_{H^\pm} \approx 45 \cdot m_B \approx 200$ GeV, which arise from large tan$\beta \gtrsim 50$, lead to a compensation of the negative SUSY contribution. Even an additional positive SUSY contribution for $\tan\beta > \left(\tilde{\epsilon}_0 + \sqrt{\tilde{\epsilon}_0^2 + 2\frac{m_B^2}{m_H^2}}\right) / \frac{m_B^2}{m_H^2}$ is possible as shown by the dotted line in Fig. 5.16(b).

The trilinear coupling A_0 slightly modifies the charged Higgs mass via one loop corrections to the Higgs mass squared, which are coming from squark mixing effects [134]. The dependence of $m_{H^\pm}$ on the trilinear coupling for a fixed mass point and three different values of tanβ is shown in Fig. 5.17(a). The one loop correction to the Higgs mass squared include terms $\propto (\mu/\tan\beta)^2$, which follows approximately a quadratic function in A_0. The resulting dependence of the branching ratio on A_0 is shown in Fig. 5.17(b). The solid(dotted) line corresponds to $R_{B\to\tau\nu_\tau}$ for a positive(negative) value of A_0 plotted versus tanβ. If large positive A_0 are combined with a large value of tanβ $m_{H^\pm}$ is getting small and leads to a positive contribution to $R_{B\to\tau\nu_\tau}$ for a fixed mass point as shown in Fig. 5.17(b). However, in the CMSSM such parameter combinations are not compatible with the exclusion limit coming from the search for neutral MSSM Higgs bosons decaying into taus, see section 5.5. Within the NMSSM low values of tanβ are preferred, so $R_{B\to\tau\nu_\tau}$ is close to the SM prediction.

5.3.3. Radiative penguin $b \to s\gamma$

The decay $b \to s\gamma$ is suppressed in the SM since it represents a FCNC which only proceeds by higher order loops. A sample leading order diagram is shown in Fig. 5.18(a), where the transition $b \to s\gamma$ is possible via a penguin digram involving a W^- boson and a top quark. The current experimental measurement on the rate of $B \to X_s\gamma$, where X_s corresponds to any hadronic system containing a strange particle, can be equaled to the rate of $b \to s\gamma$ due to small non-perturbative effects and the heavy quark-hadron duality [148, 149]. $BR(B \to X_s\gamma)$ is used to estimate the SM prediction and the corresponding SUSY contribution. The world average performed by the Heavy Flavor Averaging Group reads $BR(B \to X_s\gamma)_{EXP} = (3.43 \pm 0.21 \pm 0.7) \cdot 10^{-4}$ [99] and is in agreement with the current next-to-leading order calculations of $BR(B \to X_s\gamma)_{SM} = (3.15 \pm 0.23) \cdot 10^{-4}$ [100]. This decay is of interest in many studies since it is sensitive to new physics. Additional diagrams from charged Higgs bosons and charginos as shown in Fig. 5.18(b) can lead to a significant contribution to the SM prediction for $b \to s\gamma$. The experimental measurement and the predicted SM value are compatible within errors, so the SUSY contribution has to be small in order to agree with $BR(B \to X_s\gamma)_{EXP}$.
The two main SUSY contributions from charged Higgs bosons [150] and charginos [151] can be approximated for large tanβ [152]. The charged Higgs bosons will give a positive contribution of the order of

$$BR(B \to X_s\gamma)_{H^\pm} \propto \frac{m_b(h_t \cos\beta - \delta h_t \sin\beta)}{v \cos\beta(1 + \delta m_b)} g(m_{H^\pm}, m_t), \tag{5.7}$$

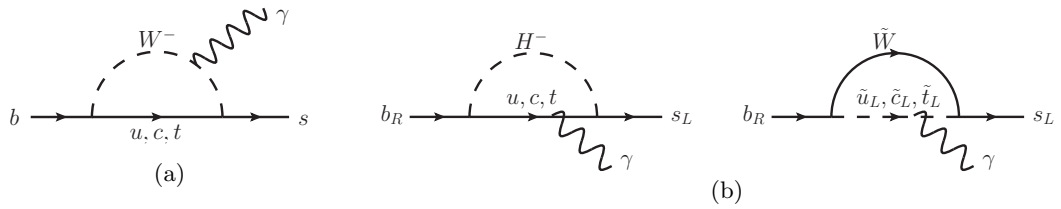

Figure 5.18.: (a): A sample leading order diagram to the electromagnetic radiative decay $B \to X_s\gamma$ within the SM. (b): Corresponding SUSY diagrams include charged Higgs bosons and charginos, which contribute additionally to the SM branching ratio.

where δh_t is an effective coupling and $g(m_{H^\pm}, m_t)$ represents the loop integral appearing at one loop level. All dominant higher order contributions are included by Δm_b. The chargino induced loops can have a positive or negative contribution to the SM BR depending on the sign of μ. For large tanβ the chargino contribution to $BR(B \to X_s\gamma)$ reads

$$BR(B \to X_s\gamma)_{\chi^\pm} \propto \mu A_t \tan\beta \; f(m_{\tilde{t}_1}, m_{\tilde{t}_2}, m_{\tilde{\chi}^\pm}) \frac{m_b}{v(1+\Delta m_b)}. \tag{5.8}$$

$f(m_{\tilde{t}_1}, m_{\tilde{t}_2}, m_{\tilde{\chi}^\pm})$ corresponds to the loop integral appearing at one loop level. The sign of A_t at low scale is negative, so the chargino contribution is positive(negative) for a negative(positive) sign of μ.

The $B \to X_s\gamma$ constraint can be fulfilled within the whole m_0-$m_{1/2}$ plane. In the CMSSM the sign of μ is taken to be positive, which leads to a negative contribution from the charginos depending on the value of A_0. The contribution is high(low) for large negative(positive) values of A_0 as shown by the dashed(dotted) line in Fig. 5.19(a). Here the dependence of $BR(B \to X_s\gamma)$ on tanβ for a fixed mass point $m_0 = 1000$ GeV $m_{1/2} = 510$ GeV and varying values of A_0 is shown. For large values of tanβ the negative contribution is compensated by the positive contribution from the charged Higgs, which becomes light for large tanβ. A small positive contribution from light stops can be observed for small values of tan$\beta \approx 5$. In case of light SUSY masses the required BR can be reached for small values of tanβ or large values of tanβabove 50. The SUSY contribution from charginos and charged Higgs bosons becomes small for high values of m_0 and $m_{1/2}$ indicating heavier sparticle masses in the loop. This is demonstrated by the light blue and dark red lines in Fig. 5.19(b), which shows the dependence of $BR(B \to X_s\gamma)$ on tanβ for different SUSY masses indicated by the corresponding m_0-$m_{1/2}$ values for $A_0 = 0$ GeV. The charged Higgs and chargino mass distribution for a light(heavy) mass point is shown in 5.19(c) indicated by the blue(light red) solid and dotted lines. The predicted branching ratio is close to the SM value for particle masses above 1 TeV. This leads to a small constant contribution to the overall χ^2 function of the order of 0.5σ. The charged Higgs mass decreases steeply for large values of tanβ compared to the flat mass distribution of the chargino, as shown by the solid and dotted lines in 5.19(c). This yields a remaining positive contribution from $H^\pm$ to $BR(B \to X_s\gamma)$, which leads to the required measured value. The slight dependence of the charged Higgs mass on A_0 is negligible for heavy SUSY masses. It simply leads to a small shift in the required tanβ value for a fixed mass point. This is indicated by the dotted and solid line in 5.19(b) which corresponds to $A_0 = 1.8 \cdot m_0$ and $A_0 = 0$ GeV, respectively.

The negative sign of μ, which is only relevant for the NMSSM, leads to a positive chargino contribution, so the required experimental value is already reached for small values of tan$\beta < 10$ as shown in Fig. 5.19(d). Here the dependence of $BR(B \to X_s\gamma)$ on tanβ is shown for a light(heavy) mass points indicated by the blue(light red) solid line for $A_0 =$

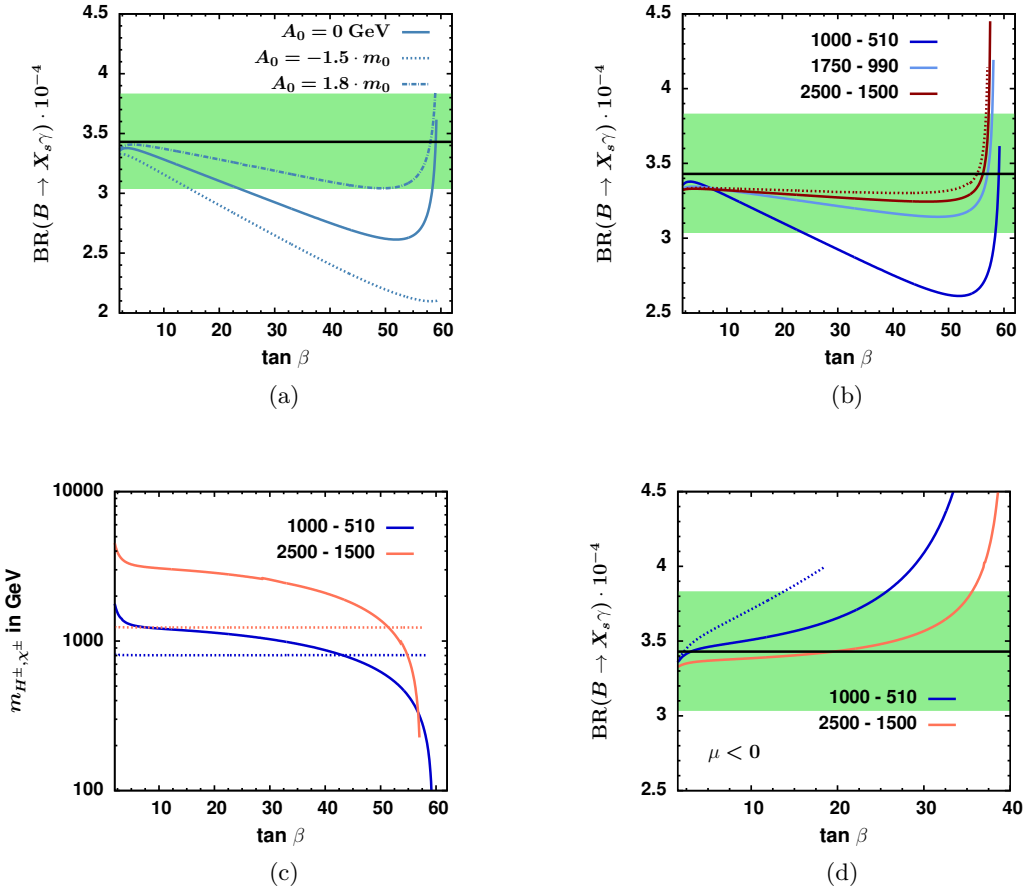

Figure 5.19.: (a): $BR(B \to X_s\gamma)$ plotted versus tanβ for a fixed mass point $m_0 = 1000$ GeV and $m_{1/2} = 510$ GeV. The lines correspond to different values of $A_0 = \{-1.5 \cdot m_0, 0 \text{ GeV}, 1.8 \cdot m_0\}$, which affect the negative chargino contribution. The horizontal line and the colored band represent the experimental measurement and its total error. (b): $BR(B \to X_s\gamma)$ plotted versus tanβ for different SUSY masses indicated by the m_0-$m_{1/2}$ values. $BR(B \to X_s\gamma)$ is close to the SM prediction within a wide range of tanβ for heavy SUSY masses except for large tan$\beta > 50$. Here the charged Higgs mass contribution dominates, due to the steep decreases of $m_{H^\pm}$ for large tanβ compared to the flat distribution of $m_{\chi^\pm}$. The dotted red line corresponds to a higher value of A_0 for the same mass point. (c): The dependence of the chargino (dotted line) and charged Higgs bosons (solid line) mass for a light (blue) and heavy (light red) SUSY mass is demonstrated. (d): $BR(B \to X_s\gamma)$ plotted versus tanβ for $\mu < 0$. The experimental value is reach for small values of tanβ due to the positive chargino contribution in addition to the charged Higgs contribution. The dotted blue line corresponds to a lower value of A_0 for the same mass point.

$3 \cdot m_0$. In case of $\mu < 0$, only low values of tanβ are compatible with the experimental measurement, since for large values of tanβ the combination of two positive contributions from charginos and charged Higgs bosons is too large. The alternate sign of μ leads to a opposite dependence of $BR(B \to X_s\gamma)$ on A_0. This is shown in Fig. 5.19(d) by the blue dotted line which corresponds to $A_0 = -m_0$. The SUSY contribution is small for heavy involved particles, so the sign of μ is only significant for SUSY masses below 1 TeV.

5.4. Mass Limits on Squarks and Gluinos

At the LHC strongly interacting supersymmetric particles can be produced in proton-proton collisions. So far no supersymmetric particles have been found at the LHC, which leads to upper limits on the hadronic cross section. The cross section can be translated

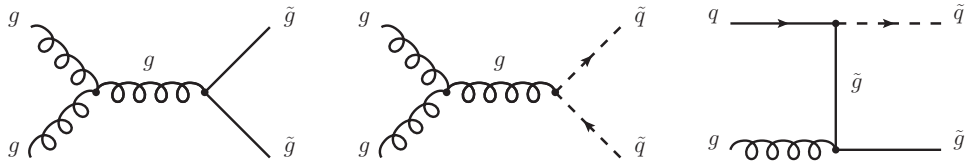

Figure 5.20.: Diagrams contributing to the strong production at the LHC. More diagrams can be found in the Appendix D.

into corresponding limits on the squark and gluino masses. Selected diagrams contributing to the hadronic cross section are shown in Fig. 5.20, while more diagrams can be found in the Appendix D. The corresponding cross section for a center-of-mass energy of 8 TeV in the m_0-$m_{1/2}$ plane is shown in Fig. 5.21(a)-5.21(c), while the figures are divided into the $\tilde{g}\tilde{g}$, $\tilde{q}\tilde{q}$ and $\tilde{g}\tilde{q}$ contribution. The cross section contributions have been calculated for fixed values of $\tan\beta = 30$ and $A_0 = -2 \cdot m_0$. Since the cross section is sensitive to the mass of the involved particles, the contribution is distributed according to the sparticle masses in the m_0-$m_{1/2}$ plane. The gluino mass is proportional to $m_{1/2}$, while the squark masses are sensitive to m_0 and $m_{1/2}$. The corresponding cross section is large for low masses, i.e. low values of m_0-$m_{1/2}$ are dominated by squark and squark-gluino production, while only low values of $m_{1/2}$ are needed for the gluino production. Therefore the gluino production dominates for large values of m_0[153].

The best limits on the cross section is given by the hadronic searches, while the results from ATLAS [108, 109], which have been translated into the m_0-$m_{1/2}$ plane, are used for this analysis. The total hadronic cross section $\sigma(pp \to \tilde{g}\tilde{g}, \tilde{g}\tilde{q}, \tilde{q}\tilde{q})$ along with the parameterized 95% C.L. exclusion contour from ATLAS are shown in Fig. 5.21(d). The excluded region below the solid line follows rather closely the total cross section indicated by the color shading. However, a small deviation can be observed which is coming due to variation in the efficiency of the combined searches.
The total cross section and the corresponding upper limit on the cross section has been calculated according to the fixed parameters $A_0 = -2m_0$ and $\tan\beta = 30$. The normalized upper limit on the cross section corresponds to a specific value of m_0 and $m_{1/2}$, which refers to a specific sparticle masses. The sparticle masses are largely independent of $\tan\beta$ and A_0, except for the stop mass. $\tilde{t}_1$ can become light for small values of $\tan\beta$ and large negative values of A_0, as shown in Fig. 5.22(a). The lines correspond to different values of A_0 given in GeV and indicated by the numbers for a fixed mass point $m_0 = 1400$ GeV $m_{1/2} = 800$ GeV. For a large splitting in the stop sector which corresponds to a large values of A_0, the stop $\tilde{t}_1$ becomes light and its associated cross section contribution dominates the hadronic cross section. This is shown in Fig. 5.22(b), where the cross section is plotted versus $\tan\beta$. The solid black line corresponds to the hadronic cross section without the cross section contribution from the stop $\sigma_{tot\ \mathrm{w/o}\ \tilde{t}}$. It is constant for varying $\tan\beta$ and A_0. The horizontal red line marks the 95% C.L. upper limit on the cross section. The blue lines correspond to the cross section of the stops $\sigma(pp) \to \tilde{t}\tilde{t}$ for the given parameter set in 5.22(a). The total cross section results from the combination of the black and one blue curve.

The stop cross section and therefore the total cross section is above the upper 95% C.L. limit for the parameter configuration indicated by the dashed-dotted blue line. Such small stop masses are only possible for small values of $\tan\beta$ combined with large values of A_0 as can be seen from Fig. 5.22(a). Large $\tan\beta$ are favored in the CMSSM, so the variation of A_0 and $\tan\beta$ has no impact on the exclusion limit from the hadronic searches. Small values of $\tan\beta$ are favored in the NMSSM so the impact of the stops can be significant. The determination of the χ^2 contribution has to be slightly modified in this case. The

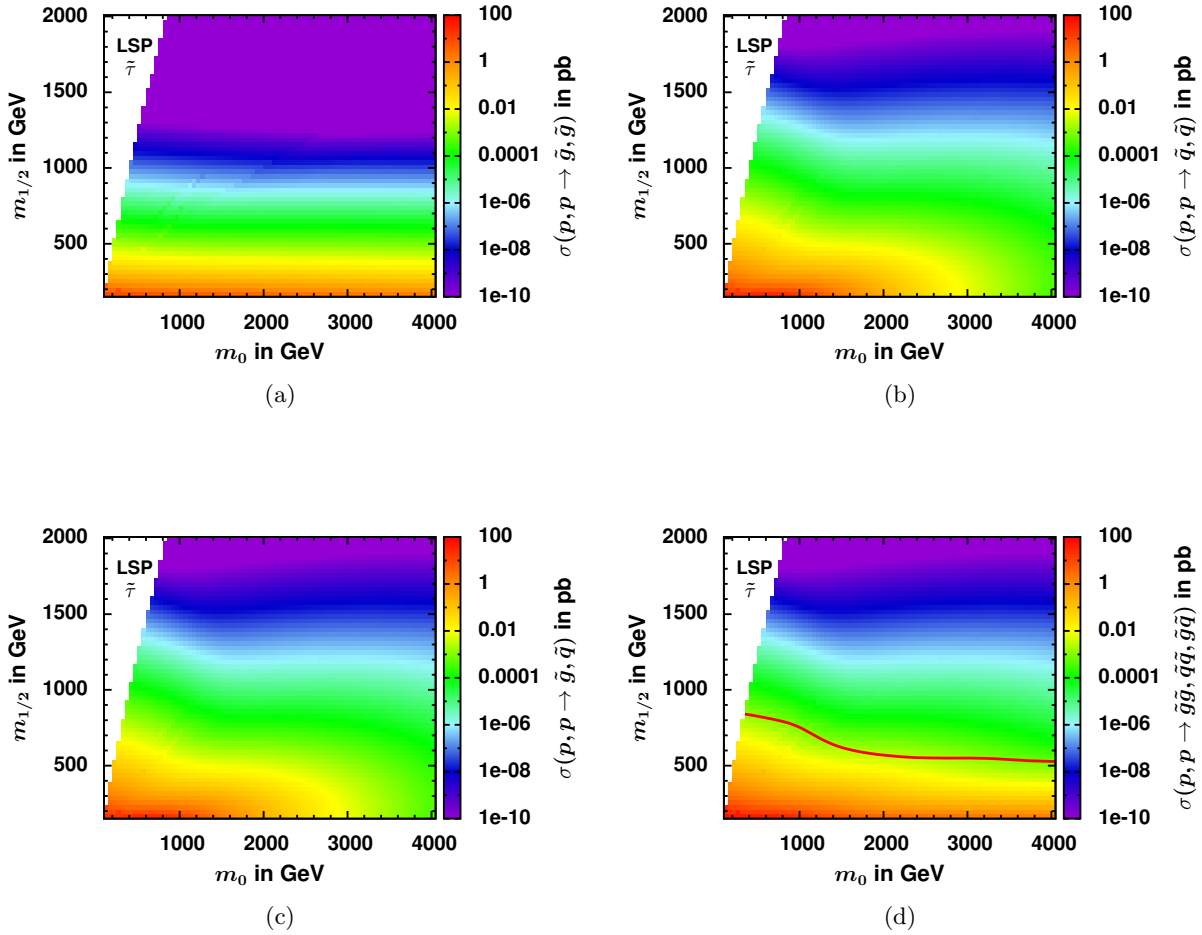

Figure 5.21.: Cross section distribution indicated by the color coding for the $\tilde{g}\tilde{g}$ (a), $\tilde{q}\tilde{q}$ (b), $\tilde{g}\tilde{q}$ (c) strong production at the LHC translated into the m_0-$m_{1/2}$ plane for fixed $\tan\beta = 30$ and $A_0 = -2 \cdot m_0$. The cross section follows the mass distribution. For small/mediate/large values of $\tan\beta$ the dominate contribution is coming from $\tilde{q}\tilde{q}/\tilde{g}\tilde{q}/\tilde{g}\tilde{g}$. (d): The total hadronic cross section $\sigma(pp \to \tilde{g}\tilde{g}, \tilde{g}\tilde{q}, \tilde{q}\tilde{q})$ plotted along with the parameterized 95% C.L. exclusion contour from ATLAS in the m_0-$m_{1/2}$ plane. The excluded region below the solid line follows rather closely the total cross section indicated by the color shading due to varying efficiencies. Within the white region the stau represents the LSP.

stop contribution is separated from the hadronic cross section and separately included. The separate upper limit on the stop cross section resulting from the contour line in Ref. [108, 109] with respect to the corresponding stop mass is given in the Appendix B.2 in Fig. B.4. The distribution follows a power law and can be parameterized with a corresponding estimated error of 15% such that $\Delta\chi^2_{\tilde{t}} = 5.99$ on the line. The stop contribution is combined with contribution from $\sigma_{tot\ \text{w/o}\ \tilde{t}}$ to get a total contribution from the ATLAS constraint taking the dependence on $\tan\beta$ and A_0 into account. In this way parameter sets leading to light stops are not misleadingly excluded. A separate stop mass dependent contribution respects the varying values of $\tan\beta$ and A_0, which has been checked for different combinations of $\tan\beta$ and A_0.

The limit on the squarks and gluinos from the ATLAS constraint can be fulfilled above the solid line in Fig. 5.21(d). The region below the solid line is associated with light gluinos and first and second generation squarks and is therefore excluded for all possible combinations of $\tan\beta$ and A_0.

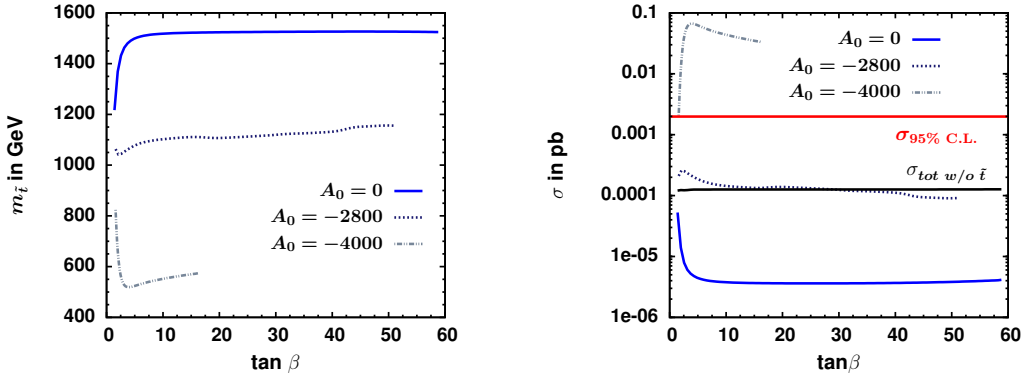

(a) (b)

Figure 5.22.: (a): Dependence of the stop mass on tanβ and A_0 for a fixed mass point $m_0 = 1400$ GeV $m_{1/2} = 800$ GeV. A_0 is given in GeV and indicated by the corresponding value. Large mixing and small tanβ leads to light stops, so the total hadronic cross section is dominated by the stop contribution. (b): The cross section contribution plotted versus tanβ using the A_0 values given in (a). The black solid line corresponds to the total hadronic cross section without the stop contribution $\sigma_{tot\ w/o\ tildet}$, while the red solid horizontal line represents the cross section referring to the 95% C.L. upper limit $\sigma_{95\%\ C.L.}$. The parameter configurations referring to the blue dashed-dotted would have been misleadingly excluded by the normalized upper limit on the cross section because of the large stop contribution. The separate stop contribution to the total χ^2 function respects the variations of tanβ and A_0.

5.5. Mass Limit on the pseudo-scalar Higgs Boson

After the discovery of the SM-like Higgs boson at the LHC, further searches for additional Higgs boson are still ongoing due to the enriched SUSY Higgs sector. The Higgs production cross section has been extensively studied both for the SM and MSSM, see e.g. [4, 67]. The dominant production mechanism for the SM Higgs boson is the gluon fusion process via a top quark loop as shown in Fig. 5.23(a). This process is also the main contribution to $pp \to \phi + X$ for the MSSM Higgs boson for small and moderate values of tanβ, where $\phi = h^0, H^0, A^0$. However, the Higgs coupling to down-type quarks is proportional to tanβ, so for large values of tanβ the b-quark associated production becomes the dominant contribution in the MSSM. The corresponding diagrams for the Higgs production in the MSSM are shown in Fig. 5.23(b).

The b-quark associated production is enhanced about 3 orders of magnitude for values of tan$\beta \approx 50$ compared to the gluon fusion process, see e.g. Ref. [133]. Thus the strongly enhanced production cross section becomes as large as the cross section for electroweak gauge bosons motivating the searches for the heavy Higgs boson at the LHC. Although the $b\bar{b}$ decay mode is enhanced as well, it suffers from an overwhelming QCD background. So the decay into tau pairs serves the current best experimental signature for this search. The best limit is given by the CMS experiment [107]. The results have been interpreted in terms of an upper limit on the cross section times branching fraction $\sigma \cdot BR(\phi \to \tau\tau)$ and additionally in the context of the MSSM for different benchmark scenarios, which refer to different mixing scenarios. The limits on the cross section are translated into the tan$\beta - m_A$ plane since those parameters describe the Higgs sector in the MSSM at tree level. If higher order corrections are taking into account, the parameter set defining the Higgs sector is extended and now include additional mass and mixing parameters. The stop mixing parameter $X_t = A_t - \mu/\tan\beta$ is crucial for the lightest Higgs boson as already discussed in section 5.2. The results can be interpreted for a specific X_t, e.g. it is chosen to get a lightest Higgs reaching its maximum. It turned out, that for this so-called

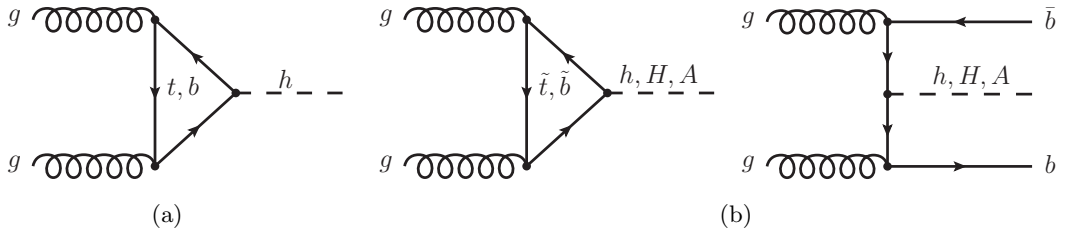

Figure 5.23.: The dominant diagrams contributing to the production of a Higgs boson at the LHC in the SM (a) and MSSM (b). The dominant production mechanism for the SM Higgs boson is the gluon fusion process, while in the MSSM the b-quark associated production is enhanced for large values of tanβ.

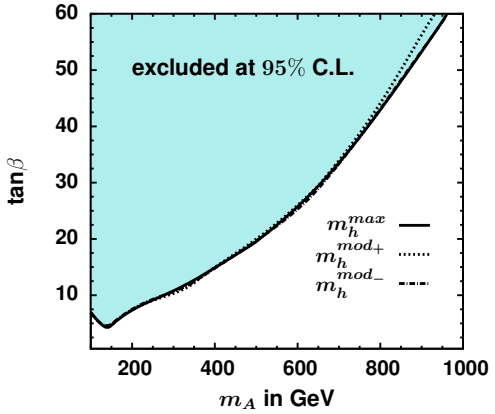

Figure 5.24.: Comparison of the 95% C.L. exclusion contours for the different benchmark scenarios m_h^{max}, m_h^{mod+} and of m_h^{mod-} given by CMS for the search of neutral Higgs bosons into tau pairs in pp collisions [107]. The limits are hardly affected by the mixing scenarios, only the remaining parameter space varies in terms of the compatibility with a 125 GeV Higgs.

m_h^{max} scenario a large part of allowed tanβ and m_A parameter space is excluded, if the discovered Higgs is associated to the lightest MSSM Higgs. The mass of the lightest Higgs is too heavy in most of the parameter space, which yields additional scenarios using only moderate mixing. Within this so-called m_h^{mod} scenario, the remaining parameter space in the tanβ-m_A plane is compatible with a 125 GeV Higgs. The scenarios affect mainly the mass of the lightest Higgs, while the exclusion curves in the tanβ-m_A plane persist, as shown in Fig. 5.24. Here the limits for three different scenarios used in Ref. [107] are shown. Since the lines resemble, the exclusion limit can be applied to the CMSSM parameter space independent on the mixing scenario.

The limit on the pseudo-scalar Higgs mass can be fulfilled within the whole m_0-$m_{1/2}$ plane for small values of tanβ. For large values of tanβ, the allowed region can slightly be modified by different values of A_0, which influences the heavy Higgs mass as already shown in Fig. 5.17(a). In the NMSSM small values of tanβ are favored, so the corresponding parameter space is hardly affected by the limit on the pseudo-scalar Higgs mass. Although in most of the parameter space, the heavy pseudo-scalar Higgs boson A_2 in the NMSSM corresponds to the pseudo-scalar MSSM Higgs A, the model independent limit on the cross section times branching fraction $\sigma \cdot BR(\phi \to \tau\tau)$ for gluon fusion has to be applied due to the modified Higgs sector.

5.6. Elastic WIMP-Nucleon Scattering

In section 5.1 experimental and theoretical evidence for the existence of DM has been summarized, which is known to make up roughly 85% of the matter in the universe. It is generally accepted that our galaxy consists of a barionic component, composed of a central bulge and spiral disk, which is embedded in a smooth spherical halo of DM particles. Since the earth is moving through the halo with given local WIMP density, an interaction between a DM particle and a nucleus should be detected at earth, which is the aim of so-called direct dark matter detection experiments. DM is detected in direct DM searches by measuring the recoil of a WIMP on a nucleus, while the scattering happens via elastic scattering. Several experiments try to measure theses rare events, but no DM particle has been detected so far. Only upper limits on the WIMP-nucleon cross section are given. These upper limits result from assumptions about the local DM density, which can be determined from the rotation curve of the Milky Way and take values between 0.3 and 1.3 GeV/cm^3, see e.g. [154]. Since the limits given by different experiments are consistent with a conservative local DM density, this normalization uncertainty will not further be discussed.
Since the elastic WIMP-nucleon scattering cross section determines the detection rate of DM detection experiments, the knowledge of the WIMP-quark interaction, the distribution of the quarks in the nucleon and the distribution of the nucleons in the nucleus is crucial. After the calculation of the interaction of WIMPs with quarks and gluons, which give the effective interactions of neutralinos at the microscopic level, the matrix elements of quarks and gluon operators in a nucleon state has to be determined to translate the microscopic interactions into a interaction with the nucleons. These matrix elements can be extracted from scattering data or lattice calculations. As a last step, using the nuclear wave function, the components must be added coherently to give the matrix element for the WIMP-nucleus cross section.
Since the elastic scattering of DM takes place in the non-relativistic limit, the calculations are simplified. Only two cases have to be considered [155], the spin-spin interaction, where the WIMP couples to the spin (spin-dependent (SD)) of the nucleus and the scalar (spin independent (SI)) interaction, where the WIMP couples to the mass of the nucleus. In the following subsection the SI and SD WIMP-nucleon cross section are discussed, which follows the discussion in Ref. [127]. Although it will be shown that the limits on the SD limits are much weaker compared to the SI cross section limits, both limits have to be fulfilled for a given parameter set in the supersymmetric parameters space to be consistent with the experimental data.

5.6.1. Spin-Dependent Cross Section

The axial-vector current becomes an interaction between the quark spin and the WIMP spin. The corresponding diagrams which give rise to this interaction are shown in Fig. 5.25 while the corresponding microscopic axial vector interaction is given by

$$\mathcal{L}_A = d_q \bar{\chi}\gamma^\mu\gamma_5\tilde{\chi}\bar{q}\gamma_\mu\gamma_5 q. \tag{5.9}$$

The coupling d_q, where q denotes the quark sector, includes the fundamental couplings of the theory, which are coming from Z^0 and squark exchange. Since the squarks are known to be much heavier than the Z^0 boson, the interaction is dominated by the Z^0 boson exchange. The matrix element of the quark axial vector current in a nucleon is proportional to the spin of the nucleon, while the corresponding coefficients can be extracted from data on polarized deep inelastic scattering [127]. Uncertainties in the experimental determination of theses coefficients lead to variation in the predicted rates for WIMP detection. As will

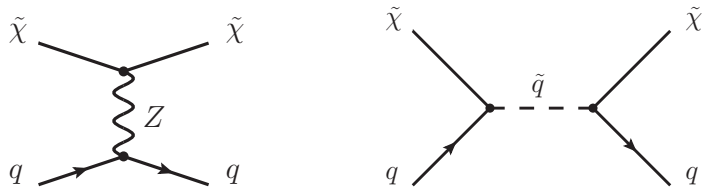

Figure 5.25.: Diagrams contributing to the spin dependent elastic scattering of neutralinos from quarks. The squarks are usually much heavier compared to the Z^0 boson, so the SD nucleon cross section is dominated by the Z^0 boson exchange.

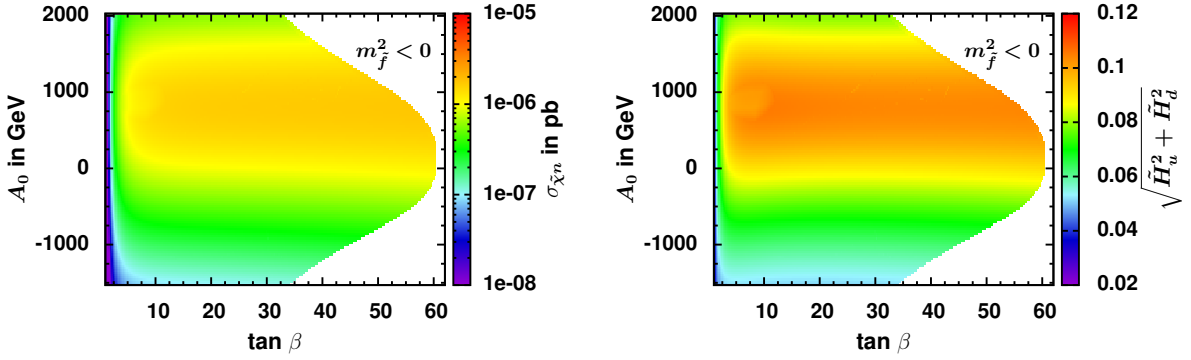

(a) (b)

Figure 5.26.: SD WIMP-neutron cross section (a) and the corresponding Higgsino component (b) within the tanβ-A_0 plane for a fixed mass point $m_0 = 500$ GeV $m_{1/2} = 500$ GeV. The plotted Higgsino component is defined as $\sqrt{\tilde{H}_u^2 + \tilde{H}_d^2}$. The SD cross section is dominated by the Z^0 exchange, so a large Higgsino component leads to an enhancement of the WIMP-nucleon cross section. The white region is not allowed due to negative sfermion and/or Higgs mass squared.

be shown in the next section, the limit on the spin-dependent cross section is about two orders of magnitude above the spin-independent limit, so this uncertainty can be currently neglected. The calculation of the nuclear matrix elements is at zero momentum transfer equivalent to the calculation of the average spins for neutrons and protons. The total cross section at zero momentum transfer reads accordingly

$$\sigma_{\text{spin}} = (32/\pi) G_F^2 m_\tau^2 \Lambda^2 J(J+1). \tag{5.10}$$

The reduced mass $m_\tau = \frac{m_N m_\chi}{m_N + m_\chi}$ includes the nucleon mass m_N. J is the total angular moment of the nucleus, while Λ includes the expectation value of the spin content of the proton and neutron group in the nucleus and the coefficients related to the quark spin content of the nucleons.

The current best limit on the SD cross section is given by XENON100 for the WIMP-neutron [112] and by COUPP for the WIMP-proton cross section [113]. The SD cross section is dominated by the Z^0 boson exchange, so it varies slightly due to varying neutralino masses within the m_0-$m_{1/2}$ plane. The maximal cross section is of the order of 10^{-4} pb and is reached for small values of m_0-$m_{1/2}$, where the neutralinos are light. Since the SD cross section is dominated by the Z^0 boson exchange it is enhanced is the Higgsino component is large. This is shown in Fig. 5.26(a) for a fixed mass point $m_0 = 500$ GeV $m_{1/2} = 500$ GeV in the tanβ-A_0 plane. The Higgsino component, which is defined as

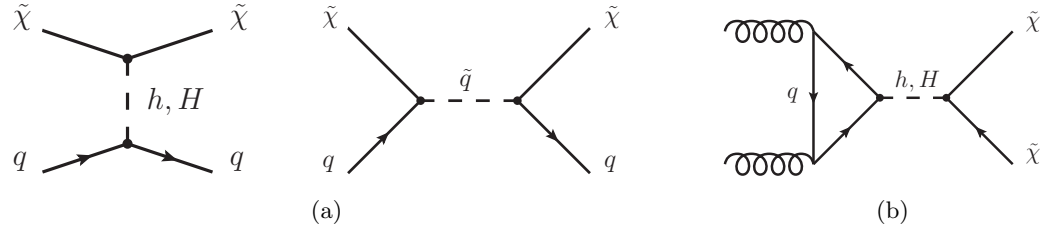

Figure 5.27.: (a): Diagrams contributing to the spin-independent WIMP-nucleon cross section. (b): In addition to the squark and Higgs exchange one-loop contributions for the interactions with gluons have to be considered for the SI WIMP-nucleon cross section.

$\sqrt{\tilde{H}_u^2 + \tilde{H}_d^2}$, is shown in Fig. 5.26(b). A clear correlation is shown between the Higgsino and the SD cross section. Such a enhancement is more significant in the focus point region, where the Higgsino component becomes large due to small values of μ. However, the cross section is largely below the current limits on the SD WIMP-nucleon cross section, so the corresponding constraints are easily fulfilled within the whole m_0-$m_{1/2}$ plane.

5.6.2. Spin-Independent Cross Section

WIMPs are Majorana particles, so they do not have a vector interactions. The calculation of the SI cross section therefore includes the scalar interactions and the tensor current. This interaction, where the WIMP couples to the mass of the nucleus, often dominates the axial-vector interaction for heavy nuclei. The contribution to the scalar neutralino-nucleon interaction arises from the coupling to quarks currents, as they are shown in Fig. 5.27(a). The interactions includes diagrams via squark and Higgs exchange but the one-loop contributions for the interactions with gluons, as shown in Fig. 5.27(b), has to be considered as well. The Higgs bosons are usually light compared to the squarks, so the Higgs exchange dominate the scalar interaction. The microscopic interactions are calculated from the effective Lagrangian including the scalar and tensor neutralino-quark and neutralino gluon interaction. A complete overview of the calculation is given in Ref. [156]. The nucleon matrix elements for quarks is defined by

$$\langle n|m_q \bar{q} q|n\rangle = m_n f_{T_q}^{(n)}. \tag{5.11}$$

It is determined from measurements of the pion-nucleon term. The same evaluation can be performed for the matrix element of the gluon operators in a nucleon state to determine the effective coupling of a neutralino to a proton and neutron f_p and f_n. In the limit of large squark masses they become

$$\frac{f_{p,n}}{m_{p,n}} \simeq \frac{f_{T_s} f_s}{m_s} + \frac{2}{27} \sum_{q=c,b,t} \frac{f_q}{m_q}, \tag{5.12}$$

where the small contributions form the light squarks has been neglected. The matrix elements of the nucleon operators have to be determined to calculate the effective interaction with the nuclei. For a scalar interaction the operators simply count for the nucleons, so the amplitude is proportional to the number of nucleons. At zero moment transfer, the cross section is therefore defined by

$$\sigma_{\text{scalar}} = \frac{4m_\tau^2}{\pi} \left[Z f_p + (A - Z) f_n \right]. \tag{5.13}$$

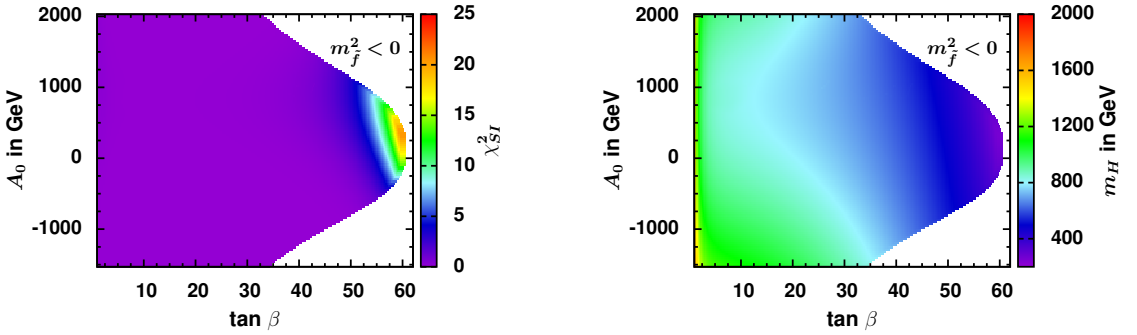

(a) (b)

Figure 5.28.: χ^2 contribution of the SI WIMP-nucleon cross section (a) and the corresponding mass distribution of the heavy scalar Higgs H (b) within the tanβ-A_0 plane for a fixed mass point $m_0 = 500$ GeV $m_{1/2} = 500$ GeV. The SI WIMP-nucleon cross section is dominated by the Higgs exchange, so it is enhanced if the Higgs boson becomes light. The white region is not allowed due to negative sfermion and/or Higgs mass squared.

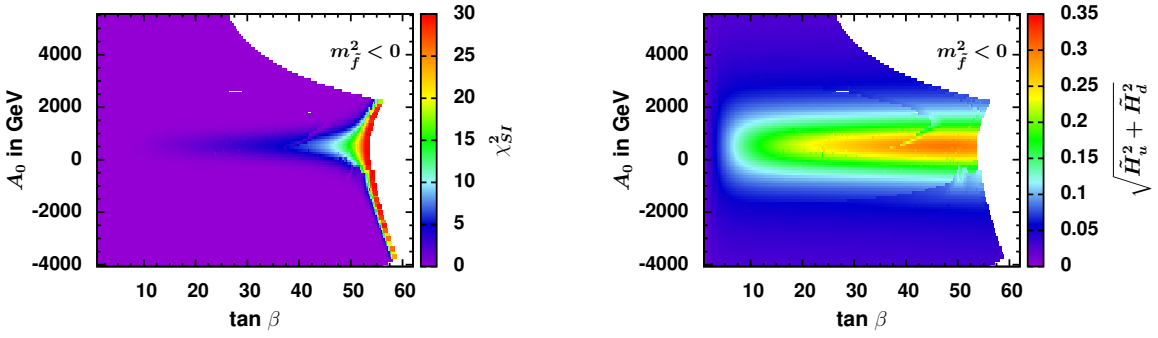

(a) (b)

Figure 5.29.: χ^2 contribution of the SI WIMP-nucleon cross section (a) and the corresponding Higgsino component (b) within the tanβ-A_0 plane for a fixed mass point $m_0 = 2000$ GeV $m_{1/2} = 400$ GeV within the focus point region. An additional enhancement to the WIMP-nucleon cross section is coming from a large Higgsino component. To obtain a small cross section large values of A_0 are preferred for low and moderate tanβ, which is correlated to large values of μ leading to a smaller Higgsino component. The Higgsino component is defined as $\sqrt{\tilde{H}_u^2 + \tilde{H}_d^2}$. The white region is excluded due to negative sfermion and/or Higgs mass squared.

As can be seen, from Eq. 5.13 for similar effective couplings for proton and neutron, the cross section is proportional to the mass of the nucleus squared, which leads to a substantial enhancement for heavy nuclei. The strange quark content within a nucleon is sufficient in the large squark limit as can be derived from Eq. 5.12. The cross section increases if the strange quark form-factor is increased. The quark form-factors suffer from large uncertainties from pion-nucleon scattering measurements. In addition, these measurements deviate from the form-factor resulting from lattice calculations. The default form-factors given in micrOMEGAs have been used to calculate the SI cross section. They represent the average of a variety of different measurements and lattice calculations [114].
The current best limit on the SI WIMP nucleon cross section is given by the LUX exper-

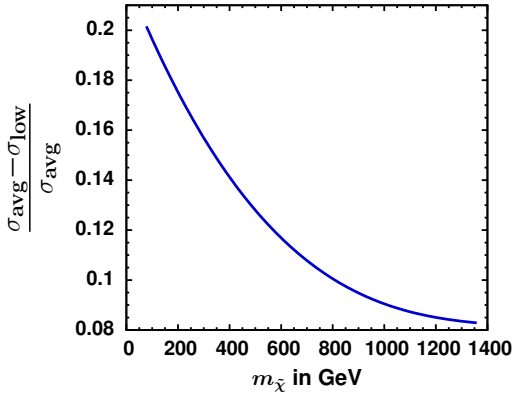

Figure 5.30.: Relative difference between the cross section using the averaged σ_{avg} and lowest form-factors σ_{low} as a function of the neutralino mass. The solid line indicates the maximal difference of the SI WIMP-nucleon cross section, referring to the same CMSSM parameter set. By slightly varying the CMSSM parameters for different sets of form-factors, the difference vanishes and similar exclusion contours in the m_0-$m_{1/2}$ plane are obtained.

iment [111]. They exclude discovery claims by DAMA/LIBRA [157] and CoGeNT [158]. The corresponding constraint can be fulfilled if the SI WIMP-nucleon cross section is below the upper limit. This is accomplished within the whole m_0-$m_{1/2}$ plane. The dominant diagram contributing to the SI cross section is coming from the Higgs exchange, so a sufficient small cross section is obtained by a large Higgs mass. An enhancement of the cross section is maintained if the heavier Higgs is getting small as well. This is demonstrated in Fig. 5.28(a), where the χ^2 contribution of the WIMP-nucleon cross section for a fixed mass point $m_0 = 500$ GeV and $m_{1/2} = 500$ GeV in the tanβ-A_0 plane is shown. The color coding indicates the χ^2 values while the red and yellow region are excluded at 95% C.L.. The corresponding mass distribution of the heavier scalar Higgs is shown in Fig. 5.28(b). The Higgs boson mass becomes small at large values of tanβ, which in turn leads to a large cross section. To obtain the limit on the WIMP-nucleon cross section limit small and moderate values of tanβ are preferred. The impact on A_0 is milder except for the focus point region. Here large values of A_0 are needed to obtain the required cross section. This is explained as follows: small values of μ lead to an enhanced Higgsino component for small and moderate values of tanβ. Thus the cross section of the Higgs exchange is enhanced. The WIMP nucleon cross section can become small, if the value of A_0 is changed. Large values of A_0 are correlated with large μ leading to a small Higgsino component and therefore to a reduction of the WIMP nucleon cross section. This is demonstrated in Fig. 5.29(a), which shows the χ^2 contribution from the WIMP-nucleon cross section in the tanβ-A_0 plane for a fixed mass point in the focus point region $m_0 = 2000$ GeV $m_{1/2} = 400$ GeV. The cross section is indicated by the color coding. For vanishing A_0 the cross section is enhanced, because of the large corresponding Higgsino component, which is shown in Fig. 5.29(b) and defined as $\sqrt{\tilde{H}_u^2 + \tilde{H}_d^2}$.

The cross section is sensitive to the chosen form-factors [153]. The scalar coefficients for the quark content in the nucleon are computed from the quark mass ratios $m_u/m_d = 0.56$, $m_s/m_d = 20.2$ as well as $\sigma_s = 42MeV$ and $\sigma_{\pi N} = 34MeV$, which are interpreted as the contribution of the strange and the light quarks to the nucleon mass. The resulting scalar form-factors are summarized in the Appendix E. These averaged values on the form-factors are applied for the calculation of the scalar cross section which suggest a similar content of the strangeness compared to the light quark content. The lowest possible form-factors result from a combination of the form-factors given in Refs. [159–161] and are summarized in Appendix E. If the lowest possible form-factors are applied for a fixed mass point, the

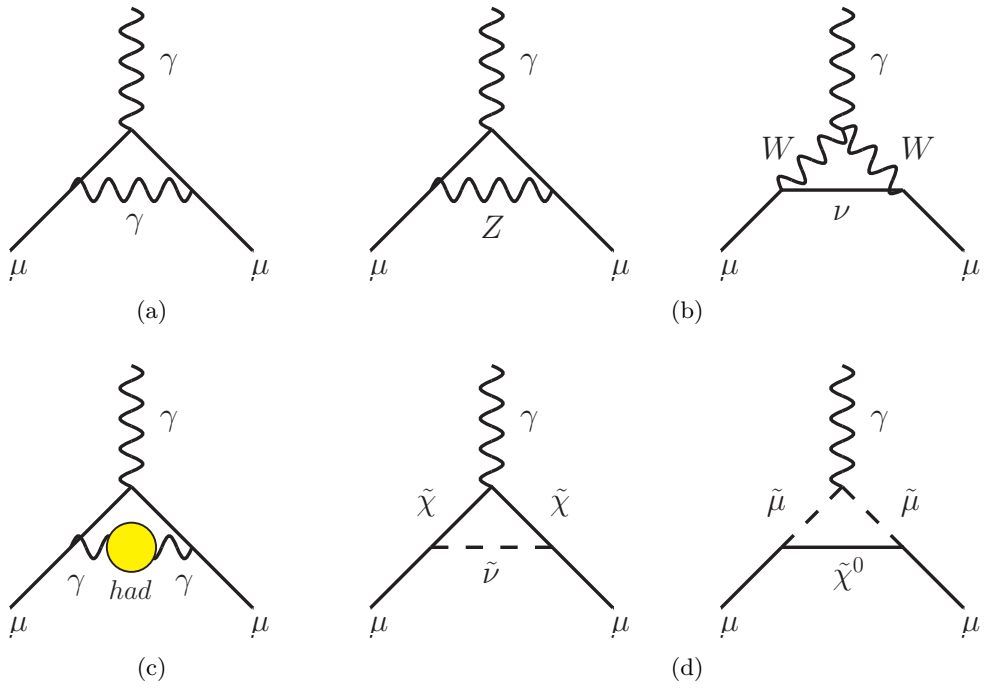

Figure 5.31.: Diagrams contributing to a_μ^{SM} from first order QED (a), weak (b) and lowest order hadronic (c) corrections. (b): Supersymmetric diagrams including charginos contribute to the anomalous magnetic moment of the muon.

SI cross section can vary between 8 to 20% depending on the neutralino mass. This is demonstrated in Fig. 5.30. The solid line indicates the relative difference between the cross section using the averaged σ_{avg} and lowest form-factors σ_{low} as a function of the neutralino mass. The enhancement refers to the same CMSSM parameters so by slightly changing them results in similar exclusion contours for different sets of form-factors.

5.7. Anomalous Magnetic Moment of the Muon

The muon, a spin 1/2 massive particle, is described by the Dirac equation, which predicts a magnetic moment of the muon proportional to its spin: $\vec{M} = g_\mu \frac{e}{2m_\mu}\vec{S}$. The Landé g-factor of $g_\mu = 2$ represents the proportionality constant that relates the spin to the magnetic moment. Due to quantum loop effects, the g-factor deviates slightly from 2. The deviation is parameterized by the anomalous magnetic moment $a_\mu \equiv \frac{g_\mu - 2}{2}$. This quantity, also known as g-2, is predicted precisely within the SM and can be generally divided into three main parts consisting of a QED, weak and hadronic part: $a_\mu^{SM} = a_\mu^{QED} + a_\mu^{EW} + a_\mu^{Had}$ [162]. The corresponding diagrams are shown in Figure 5.31. The QED part (Fig. 5.31(a)), which includes all photonic and leptonic loops, has been computed through 4 loops and estimated at the 5-loop level. The electroweak part (Fig. 5.31(b)) describes loops involving heavy $W^\pm, Z$ and Higgs particles, which are suppressed due to the heavy mass. The main uncertainties on the anomalous magnetic moment are coming from the hadronic loop contribution including quarks and gluons (Fig. 5.31(c)). The calculation of the LO and NLO hadronic contribution rely on a dispersion relation approach and on model-depended estimates of the light-by-light scattering contribution [163]. The combination of all contributions leads to a SM prediction of $a_\mu^{SM} = (116591802 \pm 2 \pm 42 \pm 26) \cdot 10^{-11}$ [104]. The first error corresponds to the electroweak corrections while the other two errors results from the LO hadronic and light-by-light scattering contribution.

The E821 experiment at the Brookhaven National Lab (BNL) measured the anomalous magnetic moment of the muon by studying the precession of muons in a constant external

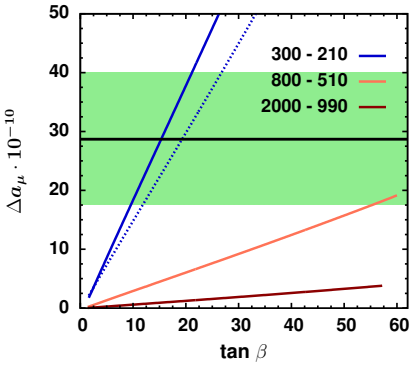

Figure 5.32.: Dependence of Δa_μ on tanβ for different mass points denoted by the corresponding m_0-$m_{1/2}$ values. For the light SUSY mass point (blue lines) the difference of a small (solid) and large (dashed) value of A_0 is shown. The horizontal line represents $\Delta a_\mu = a_\mu^{EXP} - a_\mu^{SM}$ while the colored band corresponds to the total error.

magnetic field [164], and found $a_\mu^{EXP} = (11659208.9 \pm 5.4 \pm 3.3) \cdot 10^{-10}$ [86, 103]. A clear discrepancy between the SM prediction and the experimental measurement exists and leads to $\Delta a_\mu = a_\mu^{EXP} - a_\mu^{SM} = (28.7 \pm 6.3 \pm 4.9) \cdot 10^{-11}$. If the theoretical and experimental errors are added in quadrature for the total error on Δa_μ the discrepancy is of the order of 3.6σ. To be conservative the theoretical and experimental errors are added linearly, as previously mentioned in section 4. The linear addition of the errors leads still to a deviation of 2.6σ.

Additional supersymmetric particles can be involved in the loops, as demonstrated by the diagrams in Fig. 5.31(d). They can supplemented the missing contribution to the SM prediction. The Yukawa coupling in the muon-sneutrino-Higgsino vertex is dominant [165] and leads to an additional SUSY contribution to a_μ^{SM} in the large tanβ limit of the order of

$$\left|a_\mu^{SUSY}\right| \simeq \frac{\alpha(M_Z)}{8\pi \sin^2\theta_W} \frac{m_\mu^2}{m_{SUSY}^2} \tan\beta \left(1 - \frac{4\alpha}{\pi} \ln \frac{m_{SUSY}}{m_\mu}\right), \tag{5.14}$$

with the typical supersymmetric mass m_{SUSY} in the loop. The leading 2-loop EW effects leads to a small suppression of about 7%. The sign of the SUSY contribution a_μ^{SUSY} resembles the sign of the μ parameter, while $\mu < 0$ is only relevant for the NMSSM. Numerically the SUSY contribution to a_μ^{SUSY} can be approximated by

$$\left|a_\mu^{SUSY}\right| \simeq 130 \cdot 10^{-11} \left(\frac{100\text{GeV}}{m_{SUSY}}\right)^2 \tan\beta. \tag{5.15}$$

The positive sign of μ leads to the required positive contribution to the SM prediction. But even for $\mu > 0$, the needed enhancement is only warrant for light SUSY particles of a few hundred GeV combined with the small and moderate values of tanβ as shown in Fig. 5.32. Here the dependence of Δa_μ on tanβ is shown by the solid lines for a low (blue), moderate (light red) and high (dark red) SUSY mass point denoted by the corresponding m_0-$m_{1/2}$ value for $A_0 = 0$ GeV. The distributions for negative μ can be obtained by mirroring the distributions. The horizontal line corresponds to $\Delta a_\mu = a_\mu^{EXP} - a_\mu^{SM}$, while the colored band represents the total error. Low SUSY masses require low values of tanβ, since large values of tanβ give a too large SUSY contribution. High values of tanβ are preferred for increasing m_{SUSY}, since m_{SUSY} determines the slope of the distribution. If $m_{SUSY} >> 100$GeV the distribution of Δa_μ is flat. a_μ^{SUSY} is close to the SM prediction,

so the impact of sgn(μ) is negligible. This is demonstrated by the light red and dark red line in Fig. 5.32. The distribution is sensitive to the trilinear coupling A_0, as shown for the light SUSY mass point. The solid and dashed red line correspond to $A_0 = 0$ GeV and $A_0 = -2 \cdot m_0$. The difference between the lines can be explained as follows: a large value of A_0 leads to strong mixing effects in the squark sector and therefore increases the Higgs masses and accordingly the Higgs mixing parameter μ. The mass of the lightest chargino is proportional to μ, so the mass in the loop becomes large for large values of A_0. The impact of A_0 is negligible for heavy SUSY masses due to the flat distribution of a_μ^{SUSY}.

6. Combination of All Constraints in the CMSSM and NMSSM

Each constraint has been discussed separately so far and its favored region in parameter space has been summarized. Some constraints are related to each other, so their combination is more challenging. In particular, the Higgs mass and the DM constraint are connected which can be explained as follows:
the DM annihilation cross section, which is depicted in Fig. 6.1(a), is fixed by the relic density. The amount of dark matter in the Universe requires an annihilation cross section of the order of $\sim$ 10 pb, which is associated with a weak interaction as expected. The elastic DM-nucleon scattering as shown in Fig. 6.1(b) is related to the annihilation of DM, since its diagram results from rotating Fig. 6.1(a). However, the associated cross section limit on the SI elastic scattering cross section is approximately $\sim 10^{-8}$ pb, so many orders of magnitude below the annihilation cross section. To explain the neutral and weak interactions only the Z^0 or the Higgs boson can be considered. The differences of 9 orders of magnitude can be most easily explained by the Higgs exchange, since the Higgs boson couples only weakly to light quarks in the proton. However, the coupling to the Z^0 boson has to be sufficiently suppressed. This is done by either a bino-like neutralino in the CMSSM or a singlino-like neutralino, which has reduced SM couplings. The latter case is provided in the NMSSM. If the diagram is rotated further, the direct production of DM at a collider is maintained, which is the third possibility of detecting DM. The connection of the Higgs and DM sector via the annihilation and scattering cross section leads to non-trivial constraints which are easily fulfilled in SUSY.

In the previous section it has been demonstrated that each constraint is fulfilled separately almost in the whole m_0-$m_{1/2}$ plane, but their combination is much more challenging since the favored region of the parameter space do not overlap for every observable. Instead they sometimes favor orthogonal parts of the parameter space. Their combination leads to a tension and thus to a high value for the total χ^2 function. The combination of all constraints will therefore exclude a larger region of parameter space.
This section starts with the discussion on the correlation of the free SUSY parameters and their determination, in particular the Higgs sector parameters. Afterwards the results of the combination of all constraints will be discussed and the impact of the dominant constraints are summarized for the CMSSM and NMSSM. In addition the difference of the Higgs and DM sector will be highlighted. The results of the global fits will be compared to other analyses. In the end, the prospects of the sensitivities for future searches at the LHC and for experiments for direct dark matter searches are estimated.

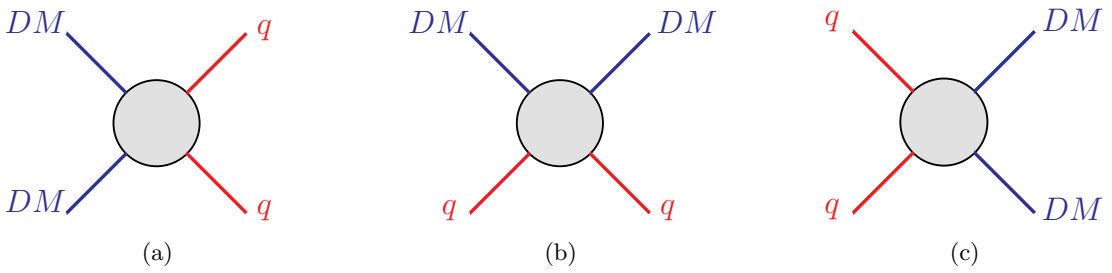

Figure 6.1.: Diagrams associated with the DM annihilation (a), DM-nucleon scattering (b) and DM production (c). The clockwise rotation of the first diagram yields the latter two. However, the associated cross section of (a) and (b) differ by several orders of magnitude. To bring these two cross sections in line, the interaction has to be mediated by a Higgs boson. In this way the DM and Higgs sector are connected. The required reduced couplings to the Z^0 boson is fulfilled within SUSY, either by a bino-like neutralino in the CMSSM or a singlino-like neutralino in the NMSSM.

6.1. Determination of the Allowed Parameter Space

The allowed parameter space has been determined by performing global fits to all available data listed in section 4.2 using the multi-step fitting technique, which has been discussed in section 4.3. In a first step the common masses for the spin 0 and spin 1/2 particles at the GUT scale (m_0 and $m_{1/2}$) are fixed. Then the fits are preformed for all possible pairs of m_0-$m_{1/2}$ in the range between 180(100) GeV and 3(5) TeV for $m_{1/2}(m_0)$ in the CMSSM and NMSSM. By minimizing the χ^2 function the remaining parameters, two in the CMSSM and seven in the NMSSM, are restricted. The allowed region in the CMSSM is determined by constraints which are very sensitive to the free parameters like the relic density constraint and $B_s^0 \to \mu^+\mu^-$, thus strong correlations of the free parameters are maintained. Fig. 6.2 exemplary shows this strong correlation. Here the relic density and BR($B_s^0 \to \mu^+\mu^-$), indicated by the solid lines, are plotted as a function of tanβ in the CMSSM for two different values of the trilinear coupling $A_0 = 0$ GeV (Fig. 6.2(a)) and $A_0 = 3090$ GeV (Fig. 6.2(b)). The blue line and right axis corresponds to the relic density, while the red line and left axis correspond to $B_s^0 \to \mu^+\mu^-$. The horizontal green line represents the experimental measured values. To fulfill both constraints simultaneously both parameters have to be varied at the same time. So only in Fig. 6.2(b) the constraints favor equal parameter sets. This situation becomes more challenging, if additional constraints are included. Close to the favored value of tanβ in Fig. 6.2(b) both distributions stop, since here the stau is the LSP. If such a scenario would be considered, the distributions smoothly continue. The steep increase of both distributions combined with the highly correlated parameters requires a careful fitting technique. The multi-step fitting approach described in section 4.3 is able to cope with such strong correlations. On a grid in the m_0-$m_{1/2}$ plane, the highly correlated parameters are fitted first by fixed other parameters. In this way, the minimization of the χ^2 function is fast and converges to the global minimum to not misleadingly excluded highly correlated regions as it can be the case for random sampling techniques.

6.1.1. Higgs Sector Parameters

The Higgs sector of the CMSSM is described by two parameters, the pseudo-scalar Higgs mass m_A and tanβ (see section 3.1.1). Those two parameters are determined by the relic density constraint. The dominant neutralino annihilation channel via the s-channel A-exchange requires a mass relation of $m_A \approx 1.5 - 2.5 m_{\tilde{\chi}}$ between the pseudo-scalar Higgs mass and the neutralino mass $m_{\tilde{\chi}}$. Such light m_A masses require large values of tanβ, as previously shown in Fig. 5.4. The pseudo-scalar Higgs mass is slightly sensitive to the

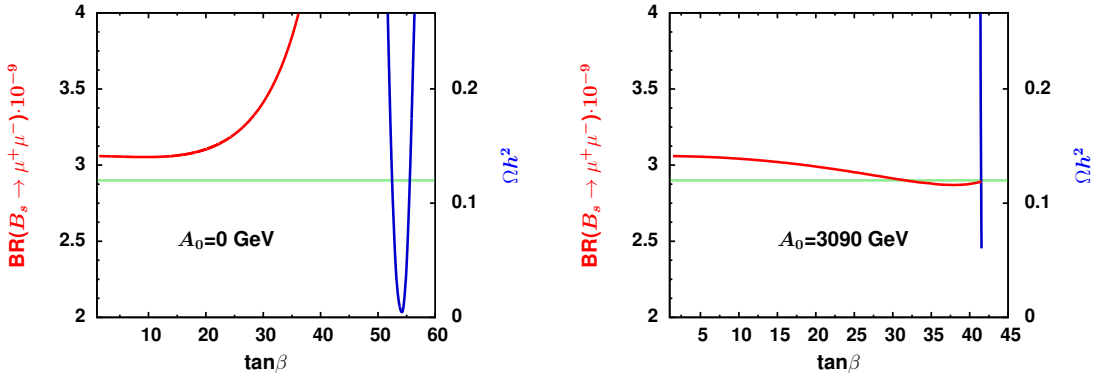

(a) (b)

Figure 6.2.: Ωh^2 (blue lines) and $B_s^0 \to \mu^+\mu^-$ (red lines) plotted versus tanβ for two different values of the trilinear coupling $A_0 = 0$ GeV (a) and $A_0 = 3090$ GeV (b) for a fixed mass point $m_0 = 1000$ GeV and $m_{1/2} = 630$ GeV. The horizontal green line refers to the measured value of $\Omega h^2(BR(B_s^0 \to \mu^+\mu^-))$, while the corresponding value is associated with the right blue(left red) axis. Both constraints can be fulfilled at the same time, i.e. they prefer the same parameter set, if A_0 and tanβ are simultaneously varied as demonstrated in (b). The multi-step fitting method allows to find solutions reliably in such highly correlated parameter regions. Close to the favored value of tanβ in (b) both distributions are discontinued, since for higher tanβ the stau becomes the LSP.

trilinear coupling, which modifies the required values of m_A and tanβ. This is helpful if the relic density is combined with other constraints, e.g. the Higgs mass and flavor constraints, to fulfill all constraints simultaneously.

The Higgs sector of the NMSSM is described by six parameters: λ, κ, A_κ, A_λ, tanβ and μ_{eff} (see section 3.2.1). Here the parameters are hardly determined by the applied constraints if all parameters are allowed to vary [166]. If four of the six parameters are fixed, the remaining parameters are well determined by the combination of the relic density and Higgs mass constraint, which is shown in Fig. 6.3. Here the χ^2 distribution indicated by the color coding is plotted in the $\lambda - \kappa$ plane for fixed other parameters for the Higgs constraint (Fig. 6.3(a)) and its combination with the relic density (Fig. 6.3(b)) constraint. If both constraints are combined the χ^2 function favors a small region in the $\lambda - \kappa$ plane as indicated by the purple region in Fig. 6.3(b). By changing the remaining parameters the favored values of λ and κ move to different values. However, there exist no constraints on the trilinear couplings and μ_{eff}, besides the argument of μ_{eff} to be of the order of the EW scale since it refers to a vev. If all parameters are left free, almost the whole $\lambda - \kappa$ plane is allowed. This is shown in the in Fig. 6.3(c) and 6.3(d), where again the χ^2 for the Higgs and its combination with the relic density is plotted in the $\lambda - \kappa$ plane.

6.2. Comparison of the Allowed Parameter Space

The results of the global fits are shown in Fig. 6.4(a)(Fig. 6.4(b)) for the CMSSM(NMSSM). The white region corresponds to the allowed region at 95% C.L., while the 68% C.L. regions are summarized in the Appendix F. The best-fit point is marked by the black cross for the CMSSM. In the NMSSM the χ^2 distribution is almost flat, so an exclusive best-fit point is not reasonable. The colored red region is excluded because of a combination of all constraints, while the gray region in the upper left corner of Fig. 6.4(a) is excluded since the stau is the LSP. The main contributions to the excluded regions are shown by separate white contour lines. The lines correspond to 95% C.L. contours and are drawn in the following way: $\Delta\chi_i^2 = \chi_i^2 - \chi_{min}^2 = 5.99$ is separately fulfilled for each constraint

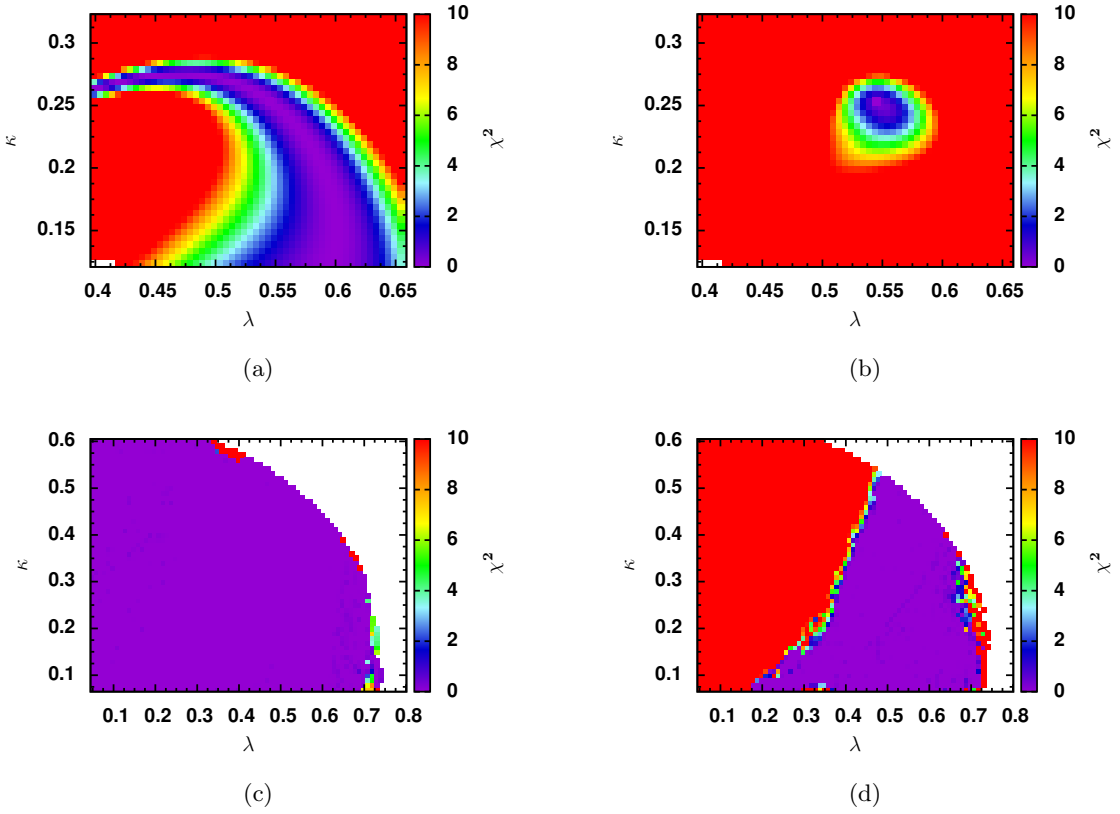

Figure 6.3.: The χ^2 distribution indicated by the color coding is plotted in the $\lambda - \kappa$ plane for a fixed mass point. The χ^2 function includes the Higgs mass constraint (a) and in addition the relic density constraint (b) for fixed remaining Higgs sector parameters ($\tan\beta$, A_λ, A_κ and μ_{eff}). The values of the couplings λ and κ are well determined if both constraints are combined. By changing the trilinear couplings and μ_{eff} the favored values of λ and κ move. If all remaining NMSSM Higgs parameters are allowed to vary, almost the whole $\lambda - \kappa$ plane is allowed for the Higgs mass constraint as shown in (c) and hardly constrained if combined with the relic density as shown in (d).

where χ^2_{min} is the χ^2 contribution of variable i at the best-fit point and χ^2_i is the χ^2 value of variable i at the contour.
The allowed region in the CMSSM and NMSSM can be translated into the gluino-squark mass plane, so the limits on the corresponding masses can be extracted. This has been performed for the CMSSM(NMSSM) in Fig. 6.5(a)(Fig. 6.5(b)). The squark mass on the y-axis corresponds to the average squark mass for the first and second generation squark. The colored red region again represents the excluded region, while the white region is allowed at 95% C.L.. The gray region is not allowed in the constrained models, since the squarks and gluinos couple to each other. The squarks have important contribution from the gluinos in the color field, so their mass cannot be considerable lighter than the gluino mass. The horizontal and vertical dotted lines indicate the lower limit on the squark and gluino mass. The detailed discussion of the main constraints is given separately for the NMSSM and CMSSM in the following subsections.

6.2.1. Discussion on the NMSSM Parameter Space

In the NMSSM, the dominant constraint corresponds to the limit on the squarks and gluino masses from the SUSY searches at the LHC as indicated by the white solid line

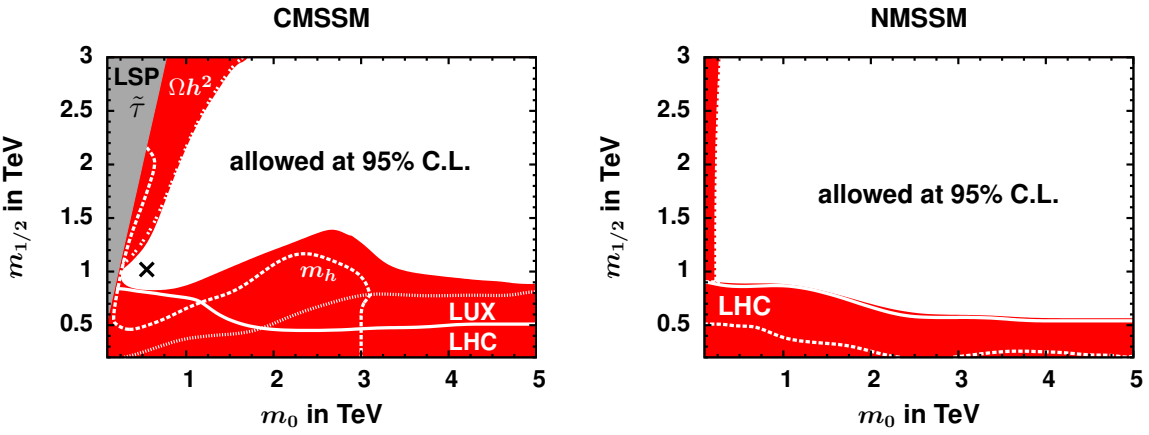

(a) (b)

Figure 6.4.: The allowed parameter space for the CMSSM (a) and NMSSM (b) in the m_0-$m_{1/2}$ plane. The white region corresponds to the allowed region at 95% C.L.. The best-fit point is marked by the black cross within the CMSSM. The χ^2 distribution within the NMSSM is flat, so a best-fit point is meaningless. The colored red region is excluded because of the combinations of all constraints. The stau is the LSP within the gray region. The white lines represent the main contributions to the excluded region. A contour line corresponds to a 95% C.L. contour, so each constraint separately fulfills $\Delta\chi^2 = 5.99$ on the line. Each contour line is denoted by the corresponding constraint. The main contributions to the excluded region in the CMSSM are coming from the direct searches for SUSY particles (LHC), the relic density (Ωh^2), the Higgs mass (m_h) and the direct searches for DM (LUX). The excluded region in the NMSSM results from a combination of the latter ones, which is anyhow excluded by the dominant LHC direct searches. In the CMSSM large tanβ are favored due to the relic density constraint, while in the NMSSM low values of tanβ are required to obtain a 125 GeV Higgs boson (see Appendix G). The LSP is typically singlino-like with a Higgsino fraction in the NMSSM, so the DM constraints can be easily fulfilled.

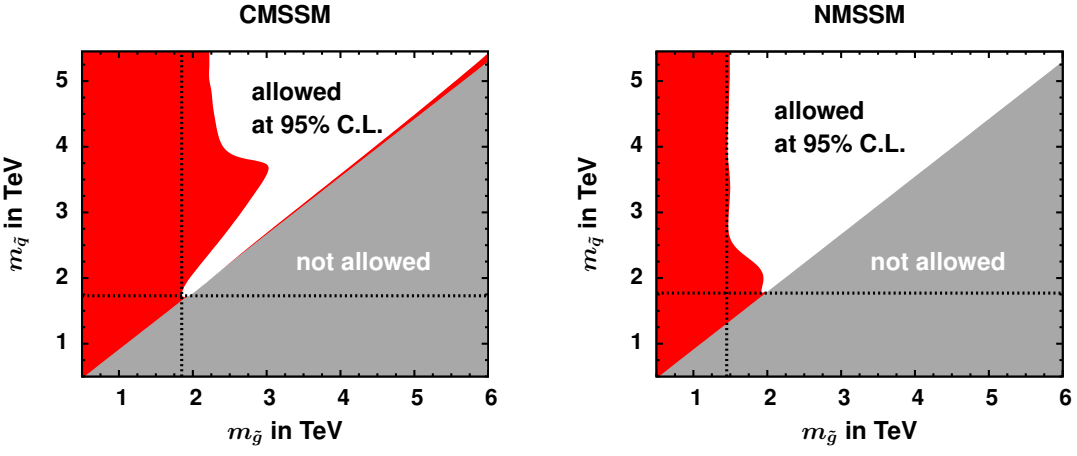

(a) (b)

Figure 6.5.: The allowed parameter space for the CMSSM (a) and NMSSM (b) from Fig. 6.4 translated into the gluino-squark mass plane. The colored red region again corresponds to the excluded region, while the white region is allowed at 95% C.L.. The horizontal and vertical dotted lines indicate the lower limit on the squark and gluino mass. The gray region is not allowed within the constrained models due to radiative corrections.

in Fig. 6.4(b). This leads to a restriction on the first and second generation squarks and the gluinos, which is represented by the red region in Fig. 6.5(b). The mass limits can be obtained by the dotted lines in Fig. 6.5(b). Here the gluino can be as light as 1.45 TeV, while the limit on the squarks is about 1.75 TeV. The given limits on the squark masses correspond to the first and second generation. The SM Higgs mass constraint determines the mixing with the singlet. The Higgs masses are determined by the additional Higgs parameter of the NMSSM, which are largely independent of m_0 and $m_{1/2}$. Therefore, the Higgs mass constraint in the NMSSM can be obtained for all points in the m_0-$m_{1/2}$ plane for similar parameter sets. Small values of $\tan\beta$ are preferred as shown in the Appendix G, so the B-physics constraints are automatically fulfilled. The LSP obtains a large Higgsino and singlino fraction, so the required DM amount can be easily fulfilled. Only a small excluded region is obtained from the combination of several constraints, indicated by the white dashed line in Fig. 6.4(b), which is anyhow below the dominant exclusion of the LHC constraint. The χ^2 distribution is flat for all scenarios in the NMSSM so no best-fit point is specified in Fig. 6.4(b). The flatness of the distributions can be extracted by the slight difference of the 68% (see Appendix F) and 95% C.L. region. The Higgs and DM sector of the allowed parameter space for the NMSSM will be discussed in more detail in section 6.2.4 and 6.2.5

6.2.2. Discussion on the CMSSM Parameter Space

In the CMSSM, a large contribution to the excluded region is coming from the LHC direct searches as indicated by the solid white line denoted as LHC in Fig. 6.4(a). Here light gluinos and first and second generation squarks are excluded due to their large hadronic cross section. The contour line follows rather close the exclusion contour shown in section 5.4. Small deviations to the published curve are observed due to the stop contributions. The direct dark matter searches, indicated by the white dotted line denoted as LUX, are complementary to the direct searches at the LHC. They dominate the region for large values of m_0. Here the Higgsino component of the LSP is enhanced which leads to a large WIMP-nucleon cross section. The region next to the stau LSP region is excluded due the relic density constraint Ωh^2 as indicated by the double-dotted line. Here the required mass of the pseudo-scalar mass is only obtained for the parameter space, where the stau is the LSP. Since this parameter space is excluded, the annihilation cross section is too small leading to a large relic density, as previously shown in section 5.1.
The dominant exclusion is coming from the Higgs mass constraint, as shown by the white dashed line in Fig. 6.4(a). It results from the combination of m_h, Ωh^2 and $BR(B_s^0 \to \mu^+\mu^-)$. All constraints are separately fulfilled within almost the whole m_0-$m_{1/2}$ plane, as already discussed in section 5. Even the combination of only two out of these three constraints is compatible in the m_0-$m_{1/2}$ plane, which was checked by a separate minimization of two constraints. However, their combination and the difficulty to fulfill all constraints simultaneously excludes masses up to $m_{1/2} = 1.4$ TeV. This can be explained as follows: the relic density prefers large values of $\tan\beta$, but the exact value of the favored $\tan\beta$ value varies with A_0 as already explained in section 5.1. Only specific combinations of the two parameters are possible to fulfill the relic density which restricts the parameter space. The Higgs mass constraint can be easily fulfilled for large splitting in the stop sector and moderate $\tan\beta$. If the mixing in the stop sector is sufficient, large values of $\tan\beta$ are possible as well, since the Higgs mass starts to saturate for values of $\tan\beta$ above 10. However, the $B_s^0 \to \mu^+\mu^-$ constraint prefers a minimal mixing in the stop sector to compensate the large preferred values of $\tan\beta$ from Ωh^2 leading to a tension with the required Higgs mass. The χ^2 distribution of Ωh^2 and $B_s^0 \to \mu^+\mu^-$ are both very steep in contrast to the Higgs mass constraint. So the minimal χ^2 value in the excluded region is obtained, if Ωh^2 and $B_s^0 \to \mu^+\mu^-$ are fulfilled accepting the less significant χ^2 contribution from the Higgs mass constraint. This tension becomes smaller for large SUSY masses

Table 6.1.: The first parameter set corresponds to the best-fit point in the CMSSM. There are two additional low χ^2 regions in the m_0-$m_{1/2}$ plane, so two points denoted as II and II have been added. In Addition to the parameter set, the masses of the pseudo-scalar Higgs A, the lightest neutralino, selected squarks and the gluino are listed as well. The common SUSY mass parameters, the trilinear coupling and sparticle masses are given in GeV. The sign of μ is positive.

	m_0	$m_{1/2}$	tanβ	A_0	A	χ_1^0	$\tilde{u}_R$	$\tilde{t}_1$	$\tilde{g}$
CMSSM Best-Fit	550	1020	19.16	-2878	1860.13	440.2	2017.1	1145.3	2234.3
CMSSM II	1550	2790	45.00	-1598	2524.84	1256.0	5098.0	4053.3	5710.0
CMSSM III	5000	2430	50.12	1557	2203.09	1095.3	6506.4	4793.7	5252.7

because the SUSY contribution to $B_s^0 \to \mu^+\mu^-$ becomes small and the Higgs boson is getting heavier at the same time. At 68% C.L. the allowed region is reduced and three additional allowed regions are found, as shown in the Appendix F. However only a small region refers to the light SUSY mass range, which includes the best-fit point at $m_0 = 550$ GeV and $m_{1/2} = 1020$ GeV. Two region are associated to large SUSY masses. The separation of these regions result from balancing the main contributions from the m_h, Ωh^2 and $B_s^0 \to \mu^+\mu^-$ constraint in order to get a low χ^2 value. The limit of the combination of all constraints is slightly shifted compared to the contour of m_h, since the χ^2 distribution of the Higgs mass constraint is broad.

The excluded region for the CMSSM is translated into the gluino-squark mass plane in Fig.6.5(a). The dotted black lines indicate the limits on the corresponding masses, so squark(gluino) masses above 1.73(1.85) TeV are required in the CMSSM. The neutralino mass is related to $m_{1/2}$ in the CMSSM. So considering the relation $m_{\tilde{g}} = 2.7 m_{1/2}$, the limit on the gluino mass translates automatically in a limit on the neutralino and pseudo-scalar Higgs mass of about 360 GeV and 940 GeV, respectively. The given limits on the squark masses correspond to the first and second generation. The third generation is typically lighter depending on the splitting, which is determined by the Higgs mass constraint and at the same time restricted by $B_s^0 \to \mu^+\mu^-$ to compensated the large values of tanβ. In most of the parameter space of the CMSSM the splitting is adjusted since $B_s^0 \to \mu^+\mu^-$ is proportional to $\tan^6\beta$, so a rather small mass splitting is preferred. Therefore the third generation squarks are usually 30% lighter compared to the first and second generation squarks.

The Higgs mas constraint is one of the main constraints which determines the allowed parameter space within the CMSSM and NMSSM. This leads to a dependence on the chosen theoretical error, which can be doubled to account for the MSSM Higgs boson mass calculations. A larger theoretical error only slightly enlarges the allowed 95% C.L. region, which is discussed in more detail in the Appendix H.

6.2.2.1. Best-Fit Point in the CMSSM

The best-fit point for the CMSSM has been marked in Fig. 6.4(a) by the black cross. The corresponding parameter set and some sparticle masses are given in Table 6.1. There exist two additional 68% C.L. regions, which refer to higher values of m_0 and $m_{1/2}$ but yield a similar χ^2 value. Therefore two additional points denoted as II and II are summarized in Table 6.1. The separate χ^2 contributions and the complete mass spectra for the best-fit point and the CMSSM points II/III are summarized in Appendix I. Fig. 6.6 and 6.7 demonstrates the running of the soft masses from the high to the low scale for the best-fit point in the CMSSM. The running of the masses for the additional points II and III are plotted in Appendix J. Fig. 6.6(a) and 6.6(b) show the scale dependence of the gaugino and squark/slepton masses. In the CMSSM, M_1 and M_3 correspond approximately to the neutralino and gluino mass. For the best fit point a large splitting in the stop and the stau

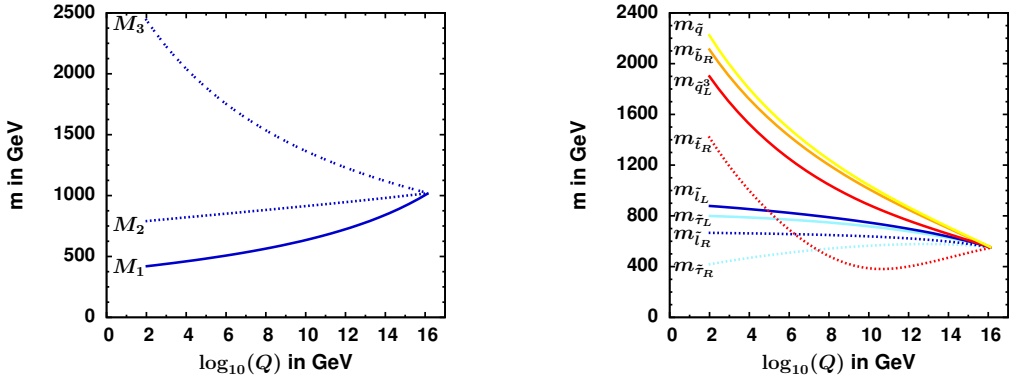

Figure 6.6.: The running of the soft masses from the high to the low scale for the best-fit point in the CMSSM is shown. The soft masses are divided into the gaugino (a) and slepton/squark (b) masses. In the CMSSM the neutralino and gluino masses correspond approximately to M_1 and M_3. Since the stau annihilation contribute to the relic density, the stau is slightly above the neutralino mass, so $M_1 \approx \tilde{\tau}_R$.

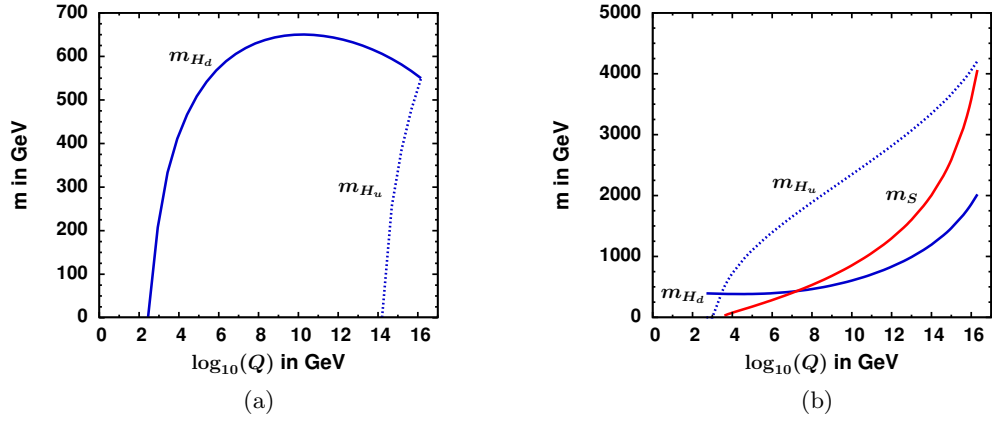

Figure 6.7.: The scale dependence for squarks/sleptons and gauginos is similar in the NMSSM except for the running of the Higgs soft masses. A comparison of the running of the Higgs soft masses of the CMSSM best-fit point (a) and the corresponding mass point in the NMSSM (b) is shown. Unlike the CMSSM, the Higgs soft masses are not unified at the GUT scale in the NMSSM.

sector can be observed which results from the large negative trilinear coupling as listed in Table 6.1. The stau annihilation diagram starts to contribute to the relic density as previously discussed in section 5.1. Therefore the stau mass is slightly above the neutralino mass, so $M_1 \approx \tilde{\tau}_R$. The scale dependence is similar in the NMSSM except for the running of the Higgs soft masses, which is demonstrated in Fig. 6.7(a) and 6.7(b) for the CMSSM and NMSSM, respectively, for same mass point. Unlike the CMSSM, the soft masses are not unified at the GUT scale. The steep decrease of m_{H_u} in the CMSSM results from the large negative trilinear coupling. For small values of A_0 the squared Higgs soft masses get negative for smaller values of Q, see Fig. 5.4.

The best-fit point is slightly above the limit of the LHC searches and is associated with first and second generation squarks of about 2 TeV and gluinos of 2.2 TeV. These masses are in reach of the next run of the LHC. The lightest stop mass is about 1.1 TeV so it will be covered by the direct stop searches. The neutralino mass is of about 440 GeV with a corresponding WIMP-nucleon cross section of about $8.5 \cdot 10^{-12}$ pb, which will be

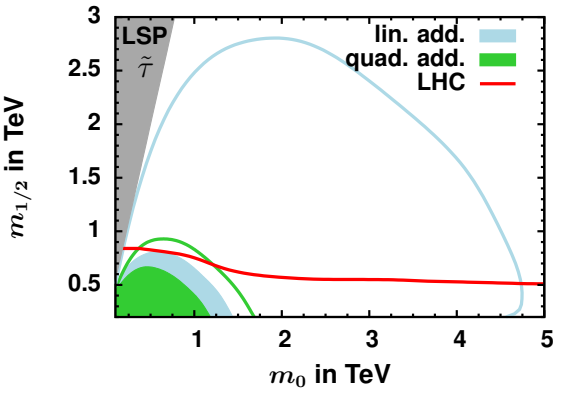

Figure 6.8.: Favored region of Δa_μ for quadratic (green) and linear (light blue) addition of the experimental and theoretical error in the m_0-$m_{1/2}$ plane. The colored regions correspond to the 68% C.L. regions. The lines correspond to the 95% C.L. contours. The LHC direct searches from squarks and gluinos exclude the region below the red line at 95% C.L.. The favored 68% C.L. region is already excluded by the LHC direct searches independent of the error addition, so only a light preference for light SUSY masses is given by the favored 95% C.L. region.

challenging for the direct dark matter searches as it is close to the limit of the coherent neutrino scattering. The value of tanβ is rather small, so the bino-like neutralino decays predominately into tau (51%) and top (30%) pairs. The heavier Higgs boson is of about 1860 GeV which leads to a low production cross section. The remaining 68% C.L. region II and III are associated with multi-TeV squarks, sleptons and gluinos and a lightest neutralino above 1 TeV as can be seen in the Appendix I. Not only their detection will be challenging but also their indirect effect within loops will be negligible.
Fig. 6.6(a) demonstrates that a relatively heavy gluino of a about 2 TeV is in line with a light gaugino mass of about several hundred GeV. The fact that no SUSY particles could be found in the hadronic searches should not questioning the existence of SUSY. The gauginos have same couplings as gauge bosons but their mass is at least two to three times heavier. So, only a fraction of events could have been detected by the LHC so far if the mass suppression is considered for the di-boson events. So a higher luminosity is required to state the status of SUSY.

6.2.3. Influence of g-2

Other constraints like $B \to X_s\gamma$ and $B \to \tau\nu_\tau$ are less important, since they are close to the SM value in the CMSSM and NMSSM, so they are not included as a separate contour line in Fig. 6.4. a_μ^{SUSY} is close to the SM prediction as well for large SUSY masses, which leads to a constant contribution to the total χ^2 function of about $\chi^2_{\Delta a_\mu} = \left(\frac{\Delta a_\mu - \Delta a_\mu^{SUSY}}{\sigma}\right)^2 \sim \left(\frac{\Delta a_\mu^{EXP} - \Delta a_\mu^{SM}}{\sigma}\right)^2 = (2.6)^2$ for the linear addition of the errors for SUSY masses above 1 TeV as discussed in section 5.7. This resembles the deviation of the experimental to the predicted SM value, which varies within $2.6 - 3.6\sigma$ depending on the error addition. The resulting offset of the total χ^2 function vanishes if the confidence regions are calculated by using the χ^2 difference with respect to χ^2_{min}. So the g-2 constraint therefore hardly contributes to the total χ^2 except for the light preference for light SUSY masses. The reason for the constant contribution results from the fact, that the g-2 constraint cannot be fulfilled within the whole m_0-$m_{1/2}$ plane, since it requires low SUSY masses. Fig. 6.8 shows the favored region of Δa_μ translated into the m_0-$m_{1/2}$ plane indicated by the

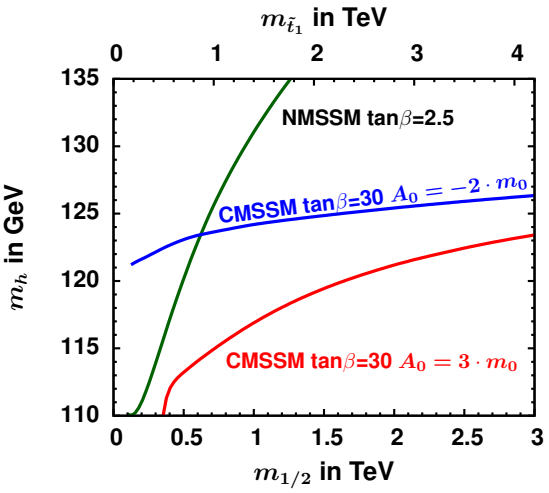

Figure 6.9.: The Higgs boson mass within the CMSSM and NMSSM are compared by plotting m_h as a function of $m_{1/2}$ for fixed values of all other parameters [166]. The stop mass is indicated at the top. Within the NMSSM a 125 GeV Higgs boson can be easily fulfilled for light stop masses as indicated by the green line. Whereas the CMSSM requires multi-TeV stops if all constraints are considered. The blue(red) solid line corresponds to a trilinear coupling of $A_0 = -2 \cdot m_0 (3 \cdot m_0)$ for $\tan\beta = 30$.

colored region. The two colors corresponds to the linear (light blue) and quadratic (green) addition of the theoretical and experimental errors. The colored region indicates the 68% C.L. region, while the region below the colored lines represents the allowed 95% C.L. region. The region below the solid red line is excluded by the LHC SUSY searches. As derived from Fig. 6.8, the favored region of Δa_μ at 68% C.L. is already excluded by the LHC SUSY searches independent of the error addition [106]. Only a slight preference for light SUSY masses is given by the 2σ contour of Δa_μ. The deviation between the experimental measurement and the theoretical prediction may either be a statistical fluctuation or the theoretical and experimental errors have been underestimated.

6.2.4. Higgs Sector

The comparison of the allowed regions in the CMSSM and NMSSM in Fig. 6.4 clearly shows a larger allowed region in the NMSSM due the various possibilities of the combination of the free parameters. However, the reason which motivates the additional study of the NMSSM is the allowed low SUSY mass region which includes in particular light stops. Light SUSY masses are generally preferred, since they lead to less fine-tuning. The CMSSM favors mostly large values of the SUSY masses and therefor large values of the stop, see e.g. [166]. This is demonstrated in Fig. 6.9, where the Higgs boson mass plotted as function of $m_{1/2}$ for fixed values of all other parameters for the CMSSM and NMSSM. Increasing $m_{1/2}$ increases the stop mass, as indicated on the scale at the top of the figure. One notice the steep increase in the Higgs boson mass of the NMSSM, which reaches 125 GeV for significantly lower stop masses as indicated by the green solid line than in the CMSSM. The blue(red) solid line corresponds to a trilinear couplings of $A_0 = -2 \cdot m_0 (3 \cdot m_0)$ for $\tan\beta = 30$. Within the NMSSM a 125 GeV Higgs boson can be easily fulfilled for light stop masses since the mixing with the singlet enhances the mass of the lightest Higgs boson, whereas the CMSSM requires multi-TeV stops if all constraints are considered.

Since there is no constraint on the vev of the singlet nor on the trilinear couplings as discussed in section 6.2.4, they can be chosen to be rather small or large. Furthermore in the NMSSM there exist three Higgs bosons, so a choice is given to define which Higgs

Table 6.2.: Parameter set for the benchmark points in the NMSSM referring to different Higgs boson scenarios [166]. BMP II and III distinguish themselves by the fact, that for BMP II the second lightest Higgs has a mass of 125 GeV, while in BMP III the lightest Higgs boson mass is 125 GeV. The third Higgs boson H_3 is light for BMP I while for BMP II and III H_3 is heavy. A fixed mass point for $m_0 = 2400$ GeV and $m_{1/2} = 600$ GeV is chosen to be outside the LHC direct searches. For the CMSSM a different value of $m_{1/2} = 2100$ GeV is used to be within the 95% C.L. region. The trilinear coupling and μ_{eff} are given in GeV.

	$\tan\beta$	A_0	$\mathrm{sgn}(\mu)/\mu_{eff}$	λ	κ	A_λ	A_κ
BMP I	2.72	-975	119.94	0.648	0.379	-510	-848
BMP II	2.67	-142	383.21	0.642	0.1388	2666	2589
BMP III	2.59	-2359	385.37	0.627	0.1352	894	1413
CMSSM IV	50.11	-4585	1	-	-	-	-

Table 6.3.: Reduced couplings from the Higgs boson to up-/down-type fermions and gauge boson and the corresponding Higgs mixing elements for the benchmark points in the NMSSM [166]. The reduced couplings are in units of the SM couplings. The couplings and mixing matrix elements of BMP II and I are similar, so only the couplings for BMP II are shown.

		H_d	H_u	S	κ_u	κ_d	$\kappa_{W/Z}$
BMP II $\sim$ BMP I	H_1	0.06	-0.07	0.99	-0.07	0.16	-0.04
	H_2	0.35	0.93	0.04	0.99	1.01	0.99
	H_3	0.93	-0.35	-0.07	-0.37	2.67	-0.001
	A_1	-0.07	-0.03	0.99	-0.03	-0.21	0.00
	A_2	0.93	0.35	0.08	0.37	2.67	0.00
BMP III	H_1	0.36	0.93	0.02	0.99	1.00	0.99
	H_2	0.06	-0.05	0.99	-0.05	0.17	-0.02
	H_3	0.93	-0.36	-0.07	-0.39	2.58	-0.0009
	A_1	-0.07	-0.03	0.99	-0.03	-0.19	0.00
	A_2	0.93	0.36	0.07	0.39	2.58	0.00

boson should have a mass of 125 GeV, the lightest one or second lightest one. Three different scenarios have been defined for a fixed mass point in the m_0-$m_{1/2}$ plane denoted as benchmark point (BMP) I, II and III [166]. The three different benchmark scenarios are given in Table 6.2. Their mass spectra at low scale are summarized in Appendix K. To compare these different scenarios to the CMSSM, a CMSSM BMP IV has been included for the same m_0 but different $m_{1/2}$ value, which had to be shifted to higher masses to be within the 95% C.L. region.

In the NMSSM the mass of the Higgs bosons and in particular the heavy Higgs H_3 can be varied by μ_{eff} and the trilinear coupling. Since they are an input, they are chosen to be either relatively light (BMP I) or heavy (BMP II and III). The latter two distinguish themselves by the fact, that for BMP II the second lightest Higgs has a mass of 125 GeV, while in BMP III the lightest Higgs boson mass is 125 GeV. The mass of the heaviest Higgs is largely determined by the mass of the pseudo-scalar Higgs boson m_A as can be derived from the Higgs mass matrix in Eq. 3.25. In the CMSSM m_A is proportional to $m_{1/2}$, while in the NMSSM it is independent of m_0 and $m_{1/2}$. The m_A dependence of the three eigenvalues of the Higgs mass matrix is shown in Fig. 6.10(a)-6.10(c). The second lightest Higgs boson can have a mass close to 125 GeV for pseudo-scalar Higgs boson masses in the range of 300 GeV, see Fig. 6.10(a). The allowed range of m_A is limited by the requirement that all Higgs boson values have to be positive. But they can be shifted by different values of μ_{eff}, A_λ, $\tan\beta$ and κ, as shown in Fig. 6.10(b) and 6.10(c), where large values of A_λ

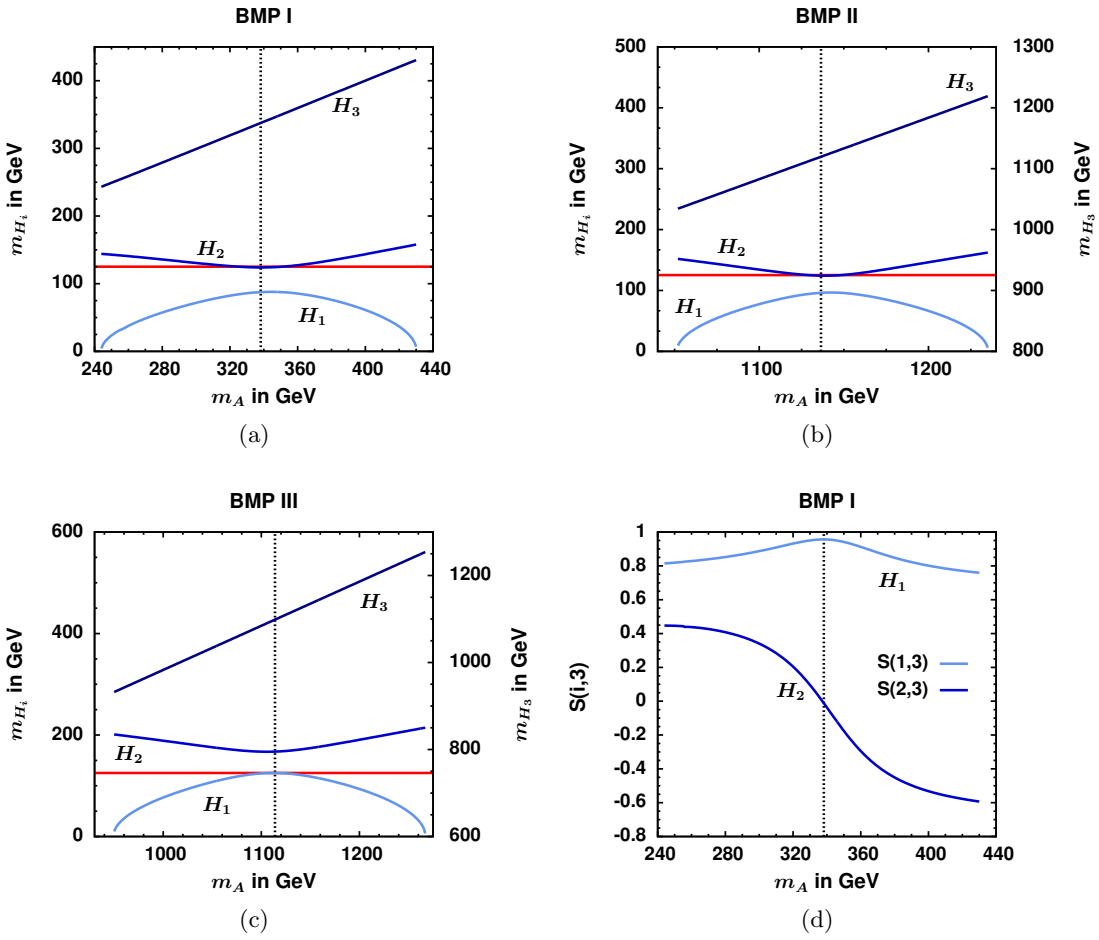

Figure 6.10.: The scalar Higgs boson masses plotted versus the pseudo-scalar Higgs mass m_A for the three benchmark points in the NMSSM (a-c) [166]. The mass of the third Higgs H_3 is indicated on the right axis for BMP II and III. To get a significant contribution from the mixing the masses have to be rather close. In this minimum/maximum of H_2/H_1 the mixing is minimal and the singlet component of H_i denoted as $S(i,3)$ where $i = 1,2$ is minimal/maximal as shown in (d). Away from these extremes the mixing increases, thus lowering one Higgs mass and increasing the other one.

have been used.

To get a significant contribution to the Higgs boson mass at tree level from mixing, thus preventing multi-TeV stops, the masses have to be rather close so in the NMSSM a second Higgs boson is either below or above 125 GeV, as it is apparent from Fig. 6.10. In this minimum/maximum of H_2/H_1 the mixing is minimal and the corresponding singlet component is close to 0/1 as demonstrated in Fig. 6.10(d). Here the singlet component $S(i,3)$ is plotted for the lightest and second lightest Higgs bosons H_i where $i = 1,2$ for BMP I. Away from these extremes the mixing increases, thus lowering one Higgs mass and increasing the other. The large singlet component for the lightest Higgs results in reduced couplings to SM particles which are summarized in Table 6.3 for each Higgs boson. If one of the two light Higgs bosons should have SM-like couplings, the other one has automatically reduced couplings to SM particles as it becomes apparent from Table 6.3. The negligible gauge bosons couplings could explain why the singlet-like Higgs boson has not been seen at LEP. The heaviest Higgs couples similar to the heavy CMSSM Higgs boson, so it couples preferentially to down-type fermions and has negligible couplings to W and Z bosons. The corresponding branching ratios, which depend on the mixing and masses, are given in Table 6.4 for BMP I and CMSSM IV. The branching ratios for BMP II and III are

Table 6.4.: Summary of the branching ratios for the Higgs boson into SM particles, neutralinos and charginos for the CMSSM IV and BMP I in the NMSSM [166]. The cross section in the last line represents the Higgs production cross section at 8 TeV for the dominant gluon-gluon fusion process. The branching ratios for BMP II and III are summarized in the Appendix L.

Branching Ratios in %								
	CMSSM IV			NMSSM BMP I				
Mass [GeV]	h 125.82	H 2025.87	A 2025.97	H_1 87.59	H_2 124.03	H_3 337.57	A_1 207.21	A_2 326.72
$b\bar{b}$	67.21	84.68	84.77	90.26	64.71	2.86	0.18	1.85
W^+W^-	17.76	1.65e-5	-	6.47e-7	17.63	0.17	-	-
$\tau\tau$	5.16	15.03	15.06	9.23	6.96	0.37	0.02	0.24
hh	-	8.56e-5	-	-	-	-	-	-
H_1H_2	-	-	-	-	-	44.59	-	-
A_1H_1	-	-	-	-	-	-	-	4.62
Zh	-	-	1.64e-5	-	-	-	-	-
ZH_1	-	-	-	-	-	-	0.22	27.44
$\chi_1^0\chi_1^0$	-	8.89e-5	7.11e-4	-	-	6.68	99.57	37.64
$\chi_1^0\chi_3^0$	-	-	-	-	-	19.31	-	4.92
$\chi_1^+\chi_1^-$	-	-	-	-	-	19.23	-	16.47
σ_{prod} [pb]	19.13	1.18e-6	1.96e-6	1.85	19.51	0.55	4.2e-2	1.44

summarized in the Appendix L.

The heavy Higgs boson in the CMSSM preferentially decays into b quarks and tau leptons. If the heavy Higgs mass in the NMSSM is of the order of several 100 GeV (BMP I) it prefers to decay into two Higgs bosons. This is due to the relatively large values of λ and κ parameters of the Higgs self couplings which allow for large branching ratios of the heaviest Higgs into two lightest Higgs bosons. This double Higgs boson production, is negligible in the CMSSM not only due to the heavy Higgs mass, but such couplings are absent, so a trilinear coupling can only be obtained from the derivatives of the scalar potential of the form $\lambda_{ijk} = \frac{\partial V_H}{\partial H_i \partial H_j \partial H_k}|_{min}$ evaluated at its minimum [67]. With this sizable double Higgs production the singlet Higgs boson can be discovered despite of the small couplings. In addition, the LSP has a large Higgsino component in the NMSSM, which leads to sizable decays into gauginos including LSPs in the NMSSM. Such invisible decays are shown for BMP I. Theses decay modes are practically absent in the CMSSM. The decay properties of the heavier Higgs bosons depend on their mass. For heavy Higgs masses new channels open up, which are obtained if the trilinear couplings are large. Large values of the trilinear couplings require opposite signs of A_0 and A_λ, A_κ due to their correlation via the RGEs. In case of heavy Higgs scenarios the $t\bar{t}$ decay modes are allowed and the branching ratios into lighter Higgs bosons or LSPs decrease. The heaviest Higgs boson mass depends on the chosen trilinear couplings, so no upper limit on H_3 can be found. Only a lower limit around 200 GeV is obtained from the lower limit on the chargino mass which limits μ.

If scenarios are considered, where the second lightest Higgs boson represents the SM-like Higgs boson, a lower limit for the lightest singlet-like Higgs boson can be found from the relic density constraint for moderate values of the trilinear couplings between 0 and -1.5 TeV. Assuming that DM consists only of neutralinos, the lower limit of about 60 GeV for the lightest Higgs boson is obtained from the relic density, since else the relic density becomes too small. This is demonstrated in Fig. 6.11. Here the Higgs mass dependence is plotted as function of A_κ at the low scale. For small values of the trilinear coupling the Higgs mass becomes small, since it enters the mixing matrix in Eq. 3.25. The relic density is plotted for the corresponding range for A_κ indicated by the color coding. The different lines correspond to different values of the A_λ varying between 0 and -1.5 TeV.

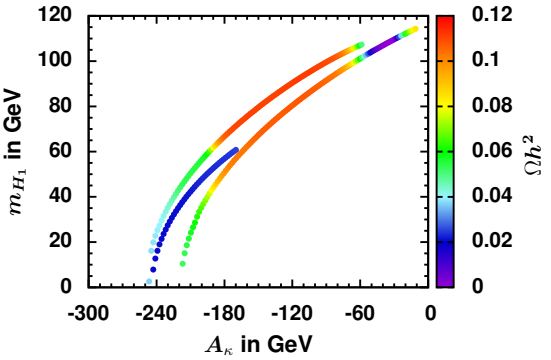

Figure 6.11.: Relic density and the lightest Higgs mass plotted as a function of A_κ at the low scale [166]. By varying A_κ the Higgs can become light, but for light Higgs boson masses the relic density, indicated by the color coding, is too small due to additional kinematically allowed annihilation channels. So the relic density can be used to give a lower limit on the lightest Higgs mass of about 60 GeV. The different lines corresponds to different values of the A_λ for a fixed mass point varying between 0 and -1.5 TeV.

For m_{H_1} below 60 GeV the LSP annihilation into two lightest Higgs boson or a Higgs and a Z^0 boson becomes kinematically allowed, thus leading to a too low relic density. Such low values of the lightest Higgs mass requires low values of the trilinear couplings A_κ at the GUT scale.

Not only A_λ and A_κ but all parameters associated to the Higgs singlet enters the Higgs mass matrix in Eq. 3.25 in addition to tanβ. The Higgs boson masses are therefore determined by the parameters independent of the common SUSY masses, so a similar Higgs spectrum can be obtained within the whole m_0-$m_{1/2}$ for a similar parameter set. Thus the limit from the gluinos do not affect the Higgs boson mass. The mass limit on the lightest Higgs boson shown in Fig. 6.11 is obtained by using moderate values of the trilinear couplings between 0 and -1.5 TeV and μ_{eff} of the order of the EW scale, which is a natural NMSSM scenario. However, this limit can vary for different NMSSM Higgs parameters.

6.2.5. Neutralino Sector

The neutralino is determined by the corresponding mixing matrix in Eq. 3.35. Usually the diagonal terms dominate over the off-diagonal terms, so the neutralino masses are approximately of the order of M_1, M_2, μ in the CMSSM and in case of the NMSSM of the order of M_1, M_2, μ_{eff} and $\sqrt{2}\kappa v_s$. The mass spectrum at the low scale is calculated via the RGEs, so the masses are correlated. The gaugino masses satisfy Eq. 3.29. In the CMSSM the values of the Higgs mixing parameter μ is given by electroweak symmetry breaking, which leads to $\mu > m_{1/2}$, so typically $M_1 < \mu$, which implies that in the CMSSM the lightest neutralino is usually bino-like, with a mass of approximately $0.4 m_{1/2}$. The 125 GeV Higgs requires large stop masses, which can be obtained for large values of m_0 and/or $m_{1/2}$ implying a large neutralino mass. As already been discussed in section 6.2, the combination of all constraints leads to a lower limit of about 360 GeV on the lightest neutralino mass in the CMSSM. In case of the NMSSM, the vacuum expectation value of the Higgs singlet and therefore μ_{eff} is usually taken to be of the order of the electroweak scale, so the element $(5,5)$ from the mixing matrix in Eq. 3.35 is the lightest element. In this case the lightest neutralino is singlino-like with a mass independent of $m_{1/2}$, so neither the LHC SUSY searches nor the Higgs mass affect the WIMP mass. The neutralino mass eigenstates are obtained by the diagonalization of the mass matrix $\mathcal{M}_{\tilde{\chi}^0}$ and are linear combinations of the gaugino and Higgsino states

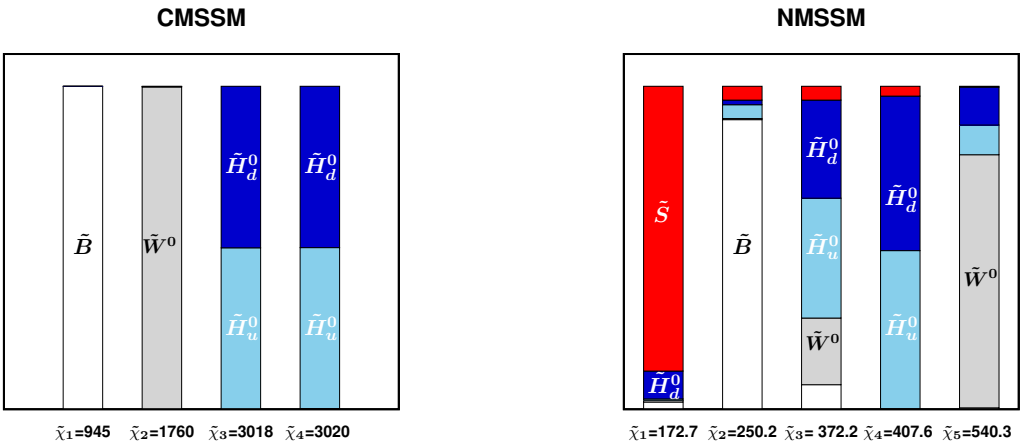

(a) (b)

Figure 6.12.: The neutralino mass matrix elements squared for the CMSSM IV (a) and NMSSM BMP II (b) point [167]. The elements are indicated by the different colors going from white, gray, light blue, dark blue and red for the $\tilde{B}, \tilde{W}^0, \tilde{H}_u^0, \tilde{H}_d^0$ and $\tilde{S}$, respectively. The mass of the neutralino is given by the numbers below the bars in GeV. In the CMSSM the lightest neutralino is almost bino-like, while in the NMSSM the singlino-like lightest neutralino has also a small Higgsino fraction.

$$\tilde{\chi}_i^0 = \mathcal{M}_{\tilde{\chi}^0}(i,1)\left|\tilde{B}\right\rangle + \mathcal{M}_{\tilde{\chi}^0}(i,2)\left|\tilde{W}^0\right\rangle + \mathcal{M}_{\tilde{\chi}^0}(i,3)\left|\tilde{H}_d^0\right\rangle + \mathcal{M}_{\tilde{\chi}^0}(i,4)\left|\tilde{H}_u^0\right\rangle + \mathcal{M}_{\tilde{\chi}^0}(i,5)\left|\tilde{S}\right\rangle . \tag{6.1}$$

The coefficients $\mathcal{M}_{\tilde{\chi}^0}(i,j)^2$ of the neutralino mixing matrix are plotted in Fig. 6.12 for each of the four CMSSM neutralinos for point CMSSM IV (Fig. 6.12(a)) and for the five neutralinos of the NMSSM in BMP II (Fig. 6.12(b)). The neutralino mixing matrix elements for BMP I and III are summarized in the Appendix M. The main difference between the BMPs in the NMSSM is the relatively large Higgsino component for the lightest neutralino, which will be significant for the elastic scattering cross section. In the CMSSM/NMSSM the lightest neutralino is largely a bino/singlino and rather heavy/light.

Since there is no constraint on the vev of the singlet, one can choose it to be heavy as well. In this case, if it is chosen to be above M_1 in the mass matrix, the lightest neutralino is not a singlino anymore, but it becomes bino-like like in the CMSSM. However this is only allowed in the NMSSM in a very restricted region of parameter space, namely if the lightest Higgs has SM couplings. In most of the cases the second lightest Higgs boson has SM couplings as already discussed in section 6.2.4. So to obtain the reserve this requires a strong fine tuning of the rather large trilinear couplings. So almost in all region of the NMSSM parameter space the LSP is singlino-like.

The impact on the DM searches can be investigated for the neutralino sector by translating allowed points into the WIMP-nucleon cross section versus WIMP mass plane [167]. The spin-independent WIMP nucleon cross section and the corresponding neutralino mass for allowed points in the parameter space, both for the CMSSM and NMSSM, are calculated and shown in Fig. 6.13 by the shaded colored region. Since the lightest neutralino is independent of m_0 and $m_{1/2}$, the allowed regions generated for the NMSSM in Fig. 6.13(b) are given for a fixed combination for m_0 and $m_{1/2}$. This point has been chosen to be outside the LHC limit, otherwise all combinations would be excluded because of too light squark and gluino masses. Both scenarios, where the lightest or the second lightest Higgs boson corresponds to the SM Higgs boson have been taken into account. For the allowed region

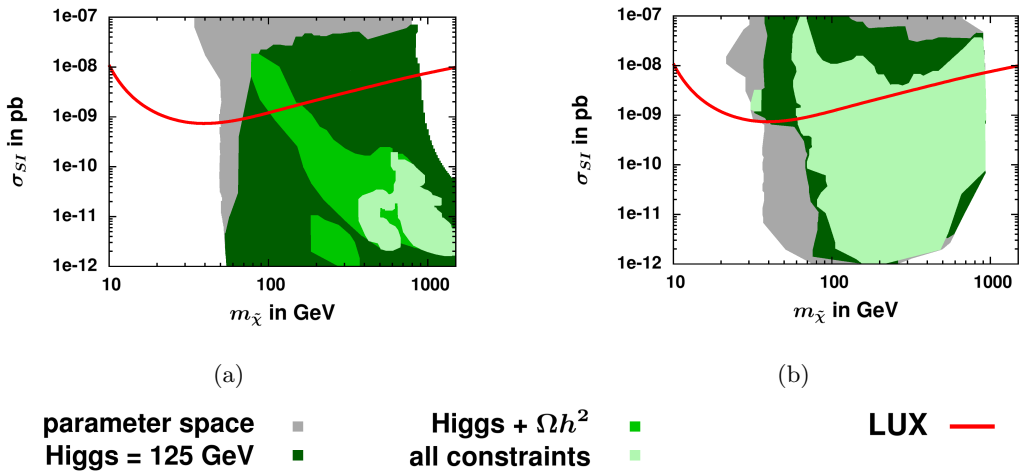

Figure 6.13.: The allowed parameter space within the SI WIMP-nucleon cross section versus WIMP mass plane for points in the CMSSM (a) and NMSSM (b). The different colored regions correspond to regions which fulfill certain constraints specified in the legend below. Since the WIMP mass is independent of the SUSY masses in the NMSSM, the allowed regions are generated for a fixed mass point outside the LHC limit, while in the CMSSM a scan over all mass points has been preformed [167].

in the CMSSM shown in Fig. 6.13(a), the points are generated in the applied mass range of the common SUSY masses. The allowed regions are further divided into regions which fulfill

- the Higgs mass m_h constraint
- the Higgs mass m_h and the relic density Ωh^2 constraint
- the Higgs mass m_h, the relic density Ωh^2 and all other constraints from Table 4.3 and 4.4 except for the direct dark matter searches.

The colored regions correspond all to 95% C.L. regions. The region above the solid line, which corresponds to the current LUX limit, is excluded by the direct dark matter searches. In the CMSSM the WIMP mass can reach large values since $w_{\tilde{\chi}} \propto m_{1/2}$. The lower limit on the WIMP mass in the CMSSM is given by the LEP limit on the chargino mass. If this constraint is neglected even smaller allowed values are possible. The Higgs mass reduces the allowed parameter space slightly as shown by the dark green region. If the relic density is added, this narrows the allowed region, since only certain values of σ_{SI} are allowed (light green region). If all constraints are added, only heavy SUSY masses are allowed due to $B_s^0 \to \mu^+\mu^-$, which needed a suppression by heavy SUSY masses, as already discussed. The lower limit on the WIMP mass is of about 360 GeV within the CMSSM. In the NMSSM the singlino like neutralino ranges from 20-1000 GeV. The lower limit is combining from the fact, that μ_{eff} cannot be arbitrary small, otherwise the lightest Higgs mass squared is getting negative. High WIMP values can be obtained if all diagonal elements in Eq. 3.35 are large, which requires a large values of the singlet vev. The whole WIMP mass range is compatible with the combination of all constraints, while the LUX limit determines the allowed region in the SI cross section.

The analysis in this thesis has been performed under the assumption that all the DM in the universe consists of neutralinos. There exist other WIMP candidates, so DM could have in principle more then one component. This would soften the constraint on the relic density, since then only an upper limit on the relic density would be valid.
The effect of a bound on the relic density is negligible for the CMSSM. Usually the relic density is too high in the excluded regions as shown in Fig. 6.4(a) since a small value of

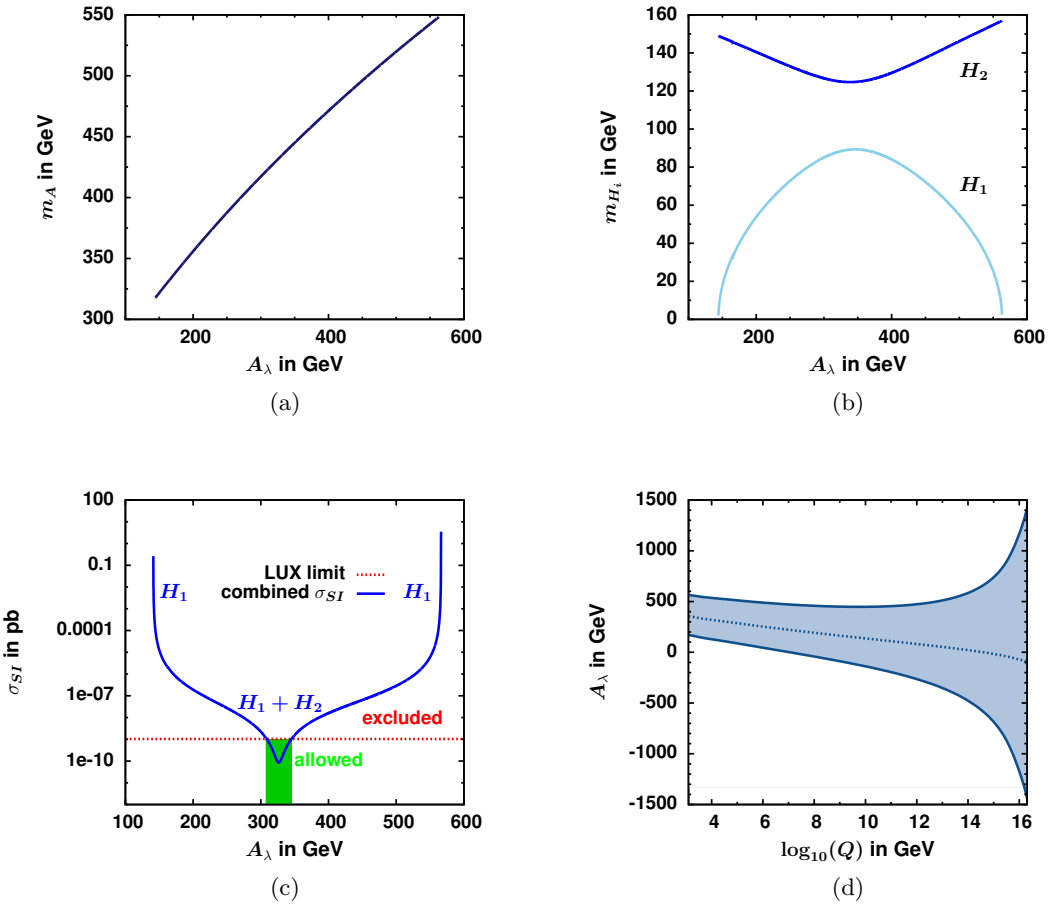

Figure 6.14.: The Higgs masses m_A (a) and $m_{H_{1(2)}}$ (b) plotted as a function of the trilinear couplings A_λ at the low scale [167]. If the masses of the lightest and second lightest Higgs are getting close, the SI WIMP-nucleon cross section can get zero. But this does not happen simultaneously for neutron and proton, so the average cross section stays finite as indicated by the solid blue line in (c). The cancellation is within the quasi-fixed point solution for A_λ as indicated in (d) where the running of A_λ from the GUT to the low scale is shown.

Ωh^2 is only obtained at the narrow m_A resonance, see Fig. 5.5. Thus a limit on Ωh^2 does not effect the allowed region in the CMSSM.
In the NMSSM the allowed region is neither effected by a bound on the the relic density, since the dominant exclusion is coming from the SUSY searches at the LHC. However, a limit affects the limit on the lightest Higgs mass H_1. It was shown in section 6.2.4 that the relic density constraint restricts the lightest Higgs mass in the NMSSM. A limit on the relic density, allows for lighter Higgs bosons, so the limit on the H_1 mass is not valid anymore.

6.2.6. Elastic Scattering Cross Section

The main contribution to the scalar elastic scattering amplitude of the neutralino scattering on quarks comes form the scalar Higgs boson t-channel exchange. The pseudo-scalar Higgs boson exchange is suppressed because of parity, whereas the heavy squark exchange as well as the heavy Higgs boson exchange are suppressed by their mass. So the scattering via the lightest and in case of the NMSSM the second lightest Higgs boson is dominant. These diagrams have a negative interference in the NMSSM, which can lead to very small cross sections, especially if the masses of H_1 and H_2 are similar. H_1 and H_2 depend both on

the pseudo-scalar Higgs mass m_A, which in turn is a function of A_λ at low energy SUSY scale.

The dependence of m_A and the other Higgs bosons on A_λ at the SUSY scale is shown in Fig. 6.14(a) and 6.14(b). m_{H_1} can become zero for small and large values of A_λ and the SI cross section becomes correspondingly large as shown in Fig. 6.14(c). For A_λ values in between the values of H_1 and H_2 masses become similar and σ_{SI} becomes small as indicated by the solid blue line in Fig. 6.14(c). The cross section can actually become zero for either a proton or a neutron but this does not happen for equal regions in parameter space [167]. Therefore the average cross section stays finite. The horizontal red dotted line corresponds to the LUX limit, which excludes a wide range of A_λ. The allowed values of A_λ are indicated by the green region in Fig. 6.14(c) and are in the range of the quasi-fixed point solutions of the RGEs as indicated by Fig. 6.14(d). However, the elastic scattering also consist of a SD part. In the CMSSM, the corresponding excluded parameter space is negligible but for the NMSSM this contribution can be significant. The SD cross section is dominated by the Z^0 boson exchange, so the Higgsino component should be small to fulfill the limit on the SD WIMP-nucleon cross section. A resonance like it happens for the SI is not obtained, so by varying A_λ the SD cross section stays rather constant. The mass point only benefits from the negative interference, if the corresponding SD cross section is compatible with the limit. Many other analyses do not include the SD cross section, since the SI limits are more stringent. This applies only for the CMSSM, where the masses are correlated but is not necessarily true for the NMSSM. So many scenarios, which favor a large Higgsino component for the lightest neutralino could be ruled out by the limit on the SD cross section.

6.3. Comparison to Other Analyses

Many different groups pursued similar combinations of experimental constraints to determine the allowed supersymmetric parameter space using either a frequentist approach by maximizing a likelihood or using random sampling techniques. Many of such scans have been performed within the CMSSM as well as in the NMSSM. The sampling techniques depend on the prior, which leads to an additional, non-quantifiable uncertainty in the excluded or allowed region. This uncertainty is due to the high correlations between three of the four CMSSM parameters: m_0 is highly correlated with $\tan\beta$ because of the relic density constraint, which requires large $\tan\beta$ in most of the parameter space except for the narrow co-annihilation regions at low and large m_0 as shown in section 5.1. The trilinear coupling is highly correlated with $\tan\beta$ because of the B-physics constraints, namely $B_s^0 \to \mu^+\mu^-$. Since $BR(B_s^0 \to \mu^+\mu^-)$ is proportional to $\tan^6\beta$, it can become large and even be above the present experimental measurement for large $\tan\beta$ as shown in section 5.3.1. But it can be strongly reduced by the appropriate mixing in the stop sector which is determined by the trilinear coupling A_0. Such strong correlations lead to likelihood spikes in the parameter region, where three of the four parameters have to have specific values. Although the likelihood of such narrow regions is high, they are either not found in methods based on stepping techniques or their probability is given a different weight because of its low posterior mass. To cope with the strong correlations a multi-step fitting technique is used by fitting the highly correlated parameters first for fixed other parameters, e.g. first $\tan\beta$ and A_0 are fitted for each pair of the mass parameters m_0 and $m_{1/2}$ in the CMSSM. In this way such likelihood spikes can be easily identified. The multi-step fitting technique is fast, since initially two parameters are fitted for each point in the m_0-$m_{1/2}$ grid in the CMSSM and NMSSM. The most probable region of the parameter space is determined by the minimum of the χ^2 value.

Our results are close to the ones of Ref. [168]. They estimate confidence intervals within the frequentist approach in a similar way, although they use a sampling technique based on a Bayesian interpretation approach. They sample the parameter space with the MultiNest algorithm [169, 170], a multi-modal nested sampling algorithm. The blue line in Fig. 6.15 corresponds to the 95% C.L. contour and is compared to the 95% C.L. allowed region resulting from this analysis. The allowed region is indicated by the green line which equals the allowed region in Fig. 6.4(a). The comparison of the 68% C.L. contours is summarized in Appendix N. As can be derived from Fig. 6.15, their allowed region associated to light SUSY masses is compatible, but they are not sensitive to the left top corner of the parameter space. In this region, the allowed parameter space requires a careful fitting method. The sampling techniques seems to miss the nodes of high likelihood. In addition their best-fit point, is outside the applied m_0 range. However they added best-fit points for low mass points, since their distribution is rather flat. This point agrees with the given best-fit point in this analyses indicated by the black cross. The 95% C.L. contour of Ref. [168] allows for a parameter space in the bottom right corner. This is due to different form-factors for the SI WIMP-nucleon cross section calculation and an additional applied error due to the uncertainty on the scalar form-factors.
The results differ significantly from results using Markov Chain Monte Carlo sampling techniques. MCMC or other scanning techniques usually find smaller allowed regions, since the parameters are strongly correlated, unless a correlation matrix is used during the scanning which tells if the parameter i moves to a certain value, all other correlated parameter should move to specific values as well. Fig. 6.16(a) shows the comparison of the allowed 95% C.L. region from Ref. [171] indicated by the blue solid line and the allowed 95% C.L. contour from this analysis indicated by the green solid line which resembles the allowed region from Fig. 6.4(a). The comparison of the 68% C.L. contours is again summarized in Appendix N. These sampling techniques exclude the parameter region

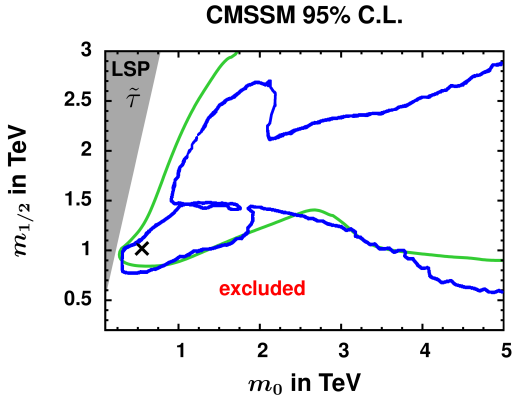

Figure 6.15.: Comparison of the 95% C.L. contour of Ref. [168], indicated by the solid blue line, and the allowed 95% C.L. region resulting from this analysis which is represented by the green line. The line corresponds to the allowed region showed in Fig. 6.4(a). The comparison of the 68% C.L. contours is summarized in Appendix N. The results of the 95% C.L. contours are rather similar. However, the lines of Ref. [168] exclude the parameter space for large $m_{1/2}$, where the parameters are highly correlated. Their best-fit point is outside the given m_0 range.

for intermediate m_0, which corresponds to the region of large tanβ. Here tanβ and A_0 are highly correlated and finding the correct minimum depends strongly on the stepping algorithm, e.g. stepping in the logarithm of a parameter is different from stepping in the parameter prior dependence. If all values of tanβ are equally sampled, the highly correlated, intermediate regions of the masses m_0 and $m_{1/2}$ are excluded, since they need large values of tanβ, so the sampling in the low tanβ range is inefficient. An additional allowed region for large m_0 is given, since the limit on the elastic WIMP-nucleon scattering cross section is not included. In Ref. [172] logarithmic priors are used. The light blue solid line in Fig. 6.16(b) corresponds to their 95% C.L. contour. Logarithmic priors sample preferentially low tanβ, but almost in the whole m_0-$m_{1/2}$ plane large tanβ are favored, so the careful sampling at high tanβ is needed. This is not possible if the logarithmic sampling of tanβ is used. As a result, they exclude the highly correlated parameter space for large values of $m_{1/2}$. In addition, the 68% C.L. regions do not match at all, as demonstrated in the Appendix N.
In the NMSSM the resulting allowed region is similar to Ref. [173] as showed in Fig. 6.17. The green line corresponds to the 95% C.L. region from Fig. 6.4(b). Similar constraints and the same constrained model is applied. The dominant exclusion corresponds to the SUSY direct searches for both analyses. Since the parameter space has been randomly scanned in Ref. [173], the allowed points are not equally spread within the m_0-$m_{1/2}$ plane and stop above $m_0 = 4000$ GeV. Slight deviations between the contour lines result from different applications of the constraints. In Ref. [173] the constraints are applied as a step-function, while in this analysis a smooth χ^2 distribution is defined. In addition, the stops are rather light in the NMSSM, which modifies their contribution to the total hadronic cross section.

Many another analyses have been performed in the NMSSM, e.g. see Refs. [93, 174–180], by using EW input and/or focusing on the Higgs phenomenology. However, GUT scale relations are not applied within theses analyses. Such general SUSY models include all soft masses and couplings as free parameters, which are independently defined at the TeV scale. In this case, the radiative corrections are only integrated between the low scale and the actual mass, which in practice means the masses are close to the tree level masses, thus efficiently eliminating radiative corrections. In addition low scale definitions ignore the

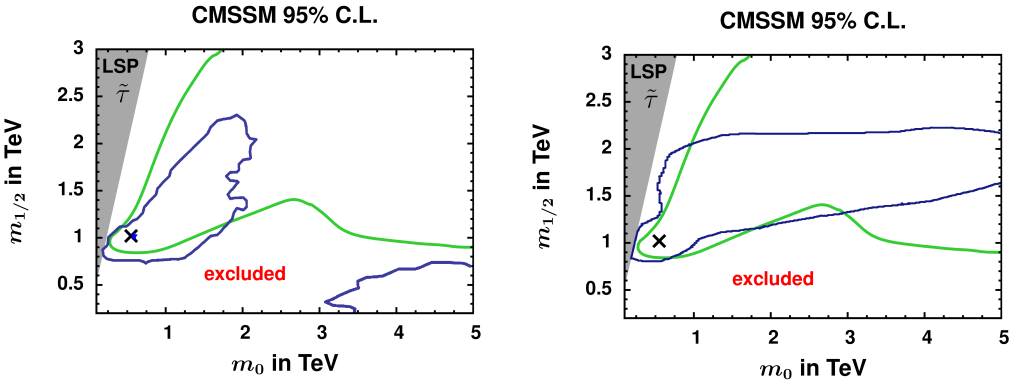

(a) (b)

Figure 6.16.: Comparison of the 95% C.L. contour resulting from this analysis indicated by the green line and the corresponding contours of Ref. [171] (a) and Ref. [172](b). The green line resembles the allowed region in Fig. 6.4(a). The allowed region of Ref. [171] indicated by the solid blue line in (a), overlaps with the allowed region of this analysis. However, the random sampling technique excludes most of the parameter space since they equally sample the highly correlated parameters. The second allowed region for large values of m_0 is allowed, since in Ref. [171] the DDMS constraint is not applied. The 95% C.L. region of Ref. [172] indicated by the blue line in (b) is mostly in line with the green contour. The region for large $m_{1/2}$ is again excluded due to the highly correlated parameters which is missed by the random sampling techniques. The comparison of the 68% C.L. contours is summarized in Appendix N.

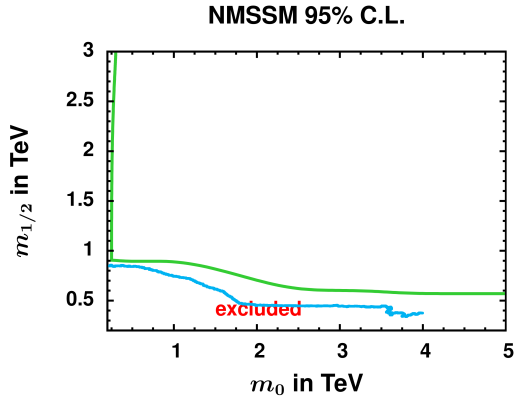

(a)

Figure 6.17.: Comparison of the exclusion contour of Ref. [173] and the allowed 95% C.L. region resulting from this analysis indicated by the green solid line, which resembles the allowed region in Fig. 6.4(b). Since a random scan in the m_0-$m_{1/2}$ plane is performed in Ref. [173], the allowed points are not equally distributed. However, the dominant exclusion is also coming from the LHC SUSY searches. The upper limit from the scan preformed by Ref. [173] is indicated by the solid blue line.

fixed point solution of the couplings, which restrict the minimal/maximal mixing scenarios in the stop sector. In this analysis GUT scale relations are applied to use the full radiative corrections to the SUSY masses and couplings. The resulting allowed region is therefore a part of the more general parameter space of the other analyses.

6.4. Prospects of Future Searches Including Extrapolated Sensitivities for SUSY

Since no SUSY or dark matter particles have been found so far, future searches are needed to probe the remaining allowed parameter space. In this section, the discovery prospects are given by extrapolating the current sensitivities for the future dark matter experiment XENON1T and LHC at 14 TeV. Furthermore, possibilities to discriminate the two SUSY models are introduced.

The sensitivity for the future direct dark matter experiment is determined by extrapolating the limit given by XENON100 [181] to the XENON1T limit. XENON1T is expected to reach a sensitivity two orders of magnitude better than XENON100. The corresponding parametrization is given in the Appendix O. For the future prospects of an energy of 14 TeV at the LHC with an integrated luminosity of 3000 fb^{-1} (LHC-14) the current cross section limits of the SUSY searches at the LHC for squarks and gluinos are extrapolated. The searches excluded low SUSY masses and accordingly large cross sections. The 95% C.L. exclusion in the m_0-$m_{1/2}$ plane determines the limit on the hadronic cross section, as already discussed in section 5. Since the χ^2 contribution is proportional to the total cross section which in turn is depending on the luminosity L by $\sigma_{tot} = \frac{N}{\epsilon L}$, for a given number of events N and the efficiency ϵ, the limit on the cross section at higher luminosity L is obtained by scaling the limit with $1/L^2$ and than check for each point in the m_0-$m_{1/2}$ plane, where the limit is reached for 14 TeV. This method is tested to work if the early low luminosity results at 7 TeV have been extrapolated to high luminosity results at 8 TeV. The LHC running at a center-of-mass energy of 14 TeV including $3000 fb^{-1}$ will be sensitive to the 95% C.L. low mass region in the CMSSM, as can be derived from Fig. 6.18(a). Here the extrapolated limit of the LHC direct searches has been included as a solid red line into the 95% C.L. allowed parameter space shown in Fig. 6.4(a), indicated by the red dotted line. The red region corresponds to the excluded region from the LHC direct searches at 8 TeV. The best-fit point will be in reach of the next run of the LHC. A large region of parameter space will be covered by the LHC which corresponds to a large squark and gluino mass range. This can be extracted from the translated limits into the gluino-squark mass plane, which is shown in Fig. 6.18(b). The red region corresponds to the excluded region from the current limit of the LHC SUSY searches at 8 TeV, while the solid red line demonstrates the extrapolated sensitivity. The 95% C.L. contour of all constraints from Fig. 6.4(a) is represented by the dotted red line. The LHC will be able to cover squark and gluino masses of about 3.6 and 3.0 TeV, respectively, as indicated by the horizontal and vertical black dotted line in Fig. 6.18(b).

To compare this sensitivity with the direct searches, Fig. 6.13 is repeated and the expected limits from XENON1T is added [167]. The regions above theses contours are excluded. In addition, the blue area corresponds to the region, which will escape the sensitivity from the LHC at 14 TeV. In the CMSSM the non-accessible region occurs for large WIMP masses, since the LHC SUSY searches are sensitive to gluino masses up to 3.0 TeV. This implies sensitivities to WIMPs around 600 GeV, since $m_{\tilde{g}}/m_{WIMP} \approx M_3/M_1 \approx 5 - 6.75$ in the CMSSM. If the LHC SUSY searches are combined with all constraints, the lower limit increases slightly to 680 GeV. In the NMSSM for a singlino-like WIMP such a relation to the gluino mass does not exist and light singlino-like WIMPs can only be probed efficiently by the direct dark matter searches. Light WIMPs, as claimed in Ref. [182] would only be allowed in the NMSSM and exclude the CMSSM.

Other searches at the LHC for SUSY particles, e.g. in multilepton searches, or for DM in monojets and invisible Higgs decays are ongoing and discussed in more detail in the Appendix P. Theses searches are less sensitive compared to the current hadronic searches and the limit on the elastic scattering cross section and thus not included into this analysis.

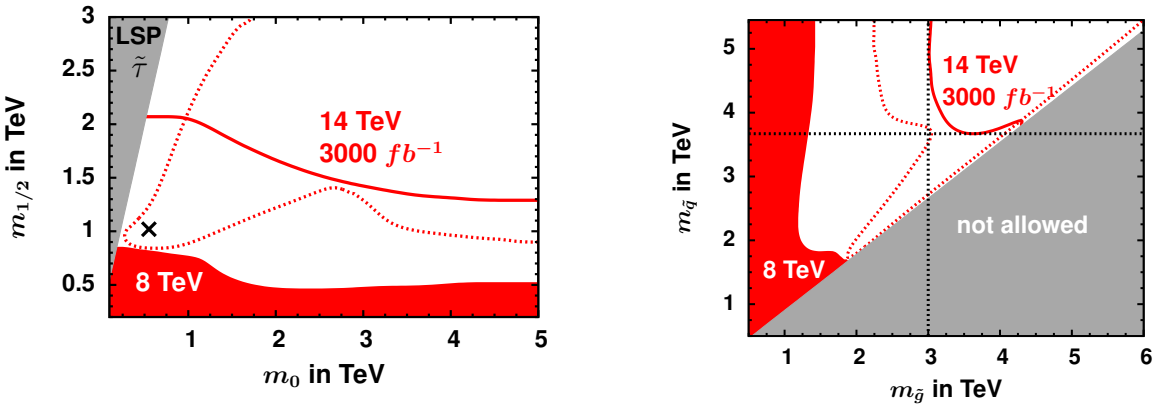

(a) (b)

Figure 6.18.: (a): The extrapolated sensitivity of LHC at 14 TeV and 3000fb^{-1}, indicated by the solid red line, within the allowed 95% allowed parameter region from Fig. 6.4(a), which corresponds to the red dotted line. The contribution from the LHC searches at 8 TeV is represented by the red colored region. LHC-14 will be able to cover a large region of parameter space including the best-fit point so a large mass range of squarks and gluinos is covered as well. (b): The extrapolated sensitivity translated into the gluino-squark mass plane. The colored red region corresponds to the current limit from the LHC SUSY searches at 8 TeV, while the solid line represents the extrapolation for LHC-14. The dotted red line corresponds to the combination of all constraints at 95% C.L. from Fig. 6.4(a). The dotted vertical and horizontal line corresponds to the expected limits on the squark and gluino masses. The gray region is not allowed in constrained models.

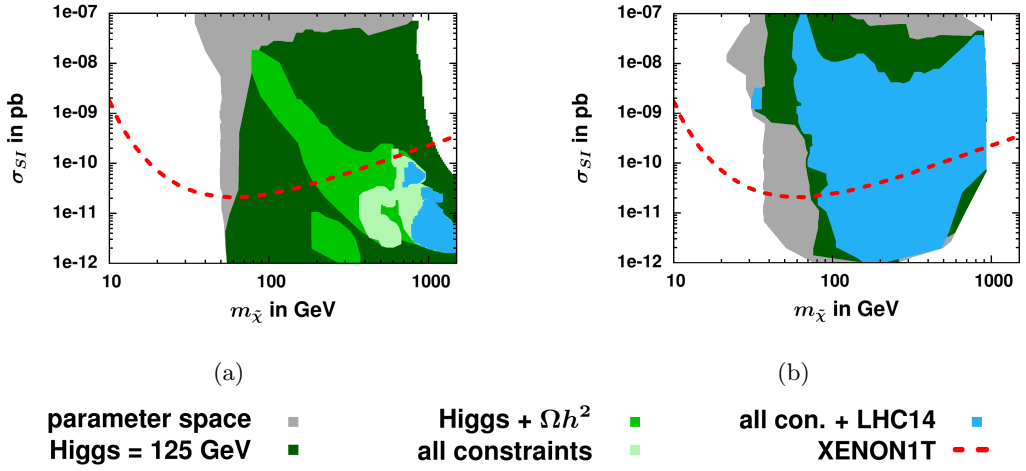

(a) (b)

Figure 6.19.: Same allowed parameter space as in Fig. 6.13 but including the expected sensitivities for LHC-14 and XENON1T for the CMSSM (a) and NMSSM (b). The regions above the red dashed line are sensitive to XENON1T. The blue region will not be accessible to the LHC SUSY searches at 14 TeV and 3000fb^{-1} [167].

Finding additional Higgs bosons and DM would be the key to prove physics beyond the SM. The properties of the additional Higgs boson and the DM particle could be used to distinguish the two models.

If a additional Higgs boson would be discovered its mass could distinguish between the CMSSM and NMSSM. A lower limit of 940 GeV on the pseudo-scalar Higgs is determined in the CMSSM from the combination of all constraints, so a Higgs boson of several hundred GeV, would disfavor the CMSSM but can obtained in the NMSSM. A further Higgs boson

below 125 GeV would be clearly favored in the NMSSM. Since the additional light Higgs boson has a large singlet component, it is hard to discover at the LHC because of its reduced couplings. It may be discovered in the decay mode of the heavier Higgs boson. The relatively large values of the Higgs self couplings parameters allow for large branching ratios of the heaviest Higgs into two lightest Higgs bosons. Such couplings are strongly suppressed in the CMSSM. Another interesting signature is given by the lightest pseudo-scalar Higgs. The LSP in the NMSSM has rather large Higgsino component, so the lightest pseudo-scalar Higgs boson decays almost exclusively to two LSP, i.e. invisible decays, if kinematically allowed. The unique NMSSM search signatures are therefore the double Higgs boson production, i.e. two Higgs bosons in a single event, one of them having a mass of 125 GeV and a second Higgs boson below or above 125 GeV, and Higgs boson decays into LSPs can be appreciable, thus leading to invisible Higgs decays. Another key signature for the NMSSM with respect to the DM sector would be a light WIMP. The large singlino component of the lightest neutralino leads to small values of the LSP mass independent of the other SUSY masses in contrast to the rather heavy bino-like neutralino in the CMSSM.

7. Summary and Outlook

Supersymmetry (SUSY) is a well-motivated theory beyond the SM, which has been searched for for many years. SUSY solves many problems of the SM simultaneously like the fine-tuning problem, the unification of the couplings, electroweak symmetry breaking via radiative corrections and it provides a perfect dark matter (DM) candidate. In addition, it predicts a light Higgs boson below 135 GeV, so the discovery of a Higgs boson at 125 GeV is a major triumph for SUSY. But the predicted supersymmetric partners of the SM particles have not been found yet.
Within the simplest supersymmetric model, the constrained minimal supersymmetric SM (CMSSM), the Born term for the lightest Higgs boson is below the Z^0 boson mass. However, the radiative corrections from the stop loops can increase the mass to 125 GeV, although this requires stop masses in the multi-TeV range, at least if constraints from cosmology and flavor physics are required to be fulfilled (see section 6.2). In the next-to-minimal CMSSM (NMSSM) the Higgs mass can be above the Z^0 boson mass, because of the mixing with the additional Higgs singlet, which distinguishes the NMSSM from the CMSSM. Such a singlet also solves the μ-problem, i.e. the Higgs mixing parameter μ becomes naturally of the order of the electroweak scale, because it is assumed to be proportional to the vev of the Higgs singlet. The Higgs sector of the NMSSM is described by six (see section 3.2.1) instead of two free parameters in the CMSSM.

There are two major topics in this thesis, which have been published in Refs. [106, 153, 166, 167]. The first topic is the determination of the parameter space allowed by current experimental data from accelerators and cosmology. These allowed regions have been identified, both in the CMSSM and NMSSM, by using a χ^2 minimization, where the χ^2 function includes all applied constraints summarized in Table 4.3 and 4.4. The free parameters are highly correlated (see section 6.1), which requires a careful fitting technique. To cope with these strong correlations the multi-step fitting technique is applied, where the highly correlated parameters are fitted first for fixed values of all other parameters. In this way regions of high likelihood are identified and not misleadingly missed like it can be the case when using random sampling techniques. For both models the GUT boundary conditions, which imply unified SUSY masses and couplings at the GUT scale, have been applied to include all radiative corrections from the GUT to the low scale. Both models satisfy the experimental constraints, which has been demonstrated in Fig. 6.4, except for the anomalous magnetic moment of the muon. The g-2 favored region in the parameter space is already excluded by the LHC SUSY direct searches, so the 2-3σ has either another origin or is simply a statistical fluctuation. The major constraints are the Higgs sector

(m_h=125 GeV), the DM sector (Ωh^2, $\sigma_{\chi N}$) and for the CMSSM the heavy flavor sector, since in the CMSSM the relic density constraint can only be fulfilled for high tanβ values. In this case $B_s^0 \to \mu^+\mu^-$ SUSY contributions tend to become large, since its branching ratio is $\propto \tan^6\beta$, but its measured value is close to the SM value. The SUSY contributions can only be tempered by nearly equal values of the $\tilde{t}_1$ and $\tilde{t}_2$ masses, which requires small mixing in the stop sector.
The second main topic is the comparison of the Higgs and DM sectors of the CMSSM and NMSSM, which are connected via the neutralino annihilation and scattering cross section. The constraints from the Higgs and DM sector are shortly summarized and followed by an outlook including the reach for new physics at the LHC in comparison with the reach in direct DM search experiments.

7.1. Higgs Sector

In the CMSSM the lightest Higgs boson is associated with the SM-like Higgs boson. The tree level mass of the lightest Higgs boson is below the Z^0 boson mass, so large radiative corrections are needed to obtain a mass of 125 GeV. These radiative corrections require heavy SUSY particles and in particular stops in the multi-TeV range if all constraints are combined, as indicated in Fig. 6.9.
Furthermore, Fig. 6.9 demonstrates that a 125 GeV Higgs boson can be obtained for significant smaller stop masses in the NMSSM due to the mixing with the additional Higgs singlet. Since small values of tanβ are favored to obtain a 125 GeV Higgs boson the SUSY contribution to the heavy flavor constraints is small, so the corresponding constraints are automatically fulfilled. In the NMSSM either the lightest or the second lightest Higgs can have a mass of 125 GeV and SM couplings. Since one of the lightest Higgs boson has SM couplings, the other Higgs boson is almost a pure singlet and has reduced couplings to SM particles (see Fig. 6.10(d) and Table 6.3). These small couplings are challenging for the production at the LHC, but the singlet-like Higgs boson can be found in the decay of the heavier Higgs into two light Higgs bosons, which has a large branching fraction due to the large triple Higgs coupling compared to the CMSSM as shown in Table 6.4.

7.2. Dark Matter Sector

In the CMSSM, the neutralino annihilation is dominated by the s-channel pseudo-scalar Higgs boson exchange. The neutralino is almost a pure bino, as shown in Fig. 6.12(a), so its mass $m_{\tilde{\chi}}$ is related to $m_{1/2}$. The correct relic density is obtained for $m_A = 1.5-2.5\cdot m_{\tilde{\chi}}$. Thus the pseudo-scalar Higgs masses is proportional to $m_{1/2}$ as well and has to be of the order of $m_{1/2}$. Such small pseudo-scalar Higgs masses are obtained for large values of tanβ, as shown in Fig. 5.4. The fact that the neutralino and pseudo-scalar Higgs are proportional to $m_{1/2}$ yield a limit on their masses from the limit on the gluino mass from the direct SUSY searches at the LHC. This is not the case for the NMSSM. Here the lightest neutralino is almost a pure singlino, see Fig. 6.12(b), with a significant Higgsino contribution, so the limits of the LHC SUSY searches have no impact on the neutralino mass nor on the pseudo-scalar Higgs mass. Furthermore, the elastic neutralino-nucleon scattering cross section is modified in the NMSSM. Since two light Higgs bosons exist, which both can contribute to the dominant Higgs exchange for the spin-independent cross section, negative interferences occur, which lead to a small cross section. The cross section can even become zero for both, the WIMP-proton and WIMP-neutron cross section. Since this does not happen simultaneously, the nucleon cross section stays finite as shown in Fig. 6.14(c). The spin-dependent searches are often neglected, since the spin-independent cross sections are larger because of the coherence of the scattering on the whole nucleus, which gives an enhancement proportional to the nucleon mass squared. This is true for

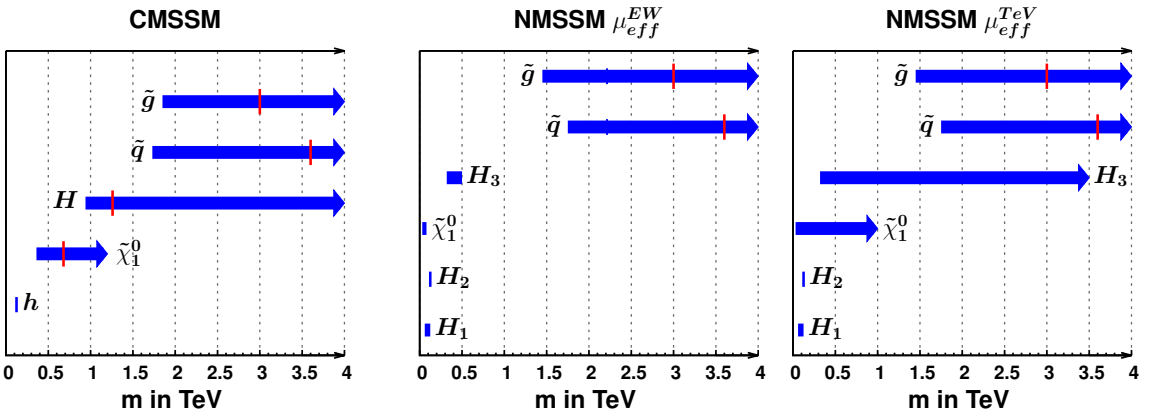

(a) (b) (c)

Figure 7.1.: Mass limits for the gluino ($\tilde{g}$), first and second generation squarks ($\tilde{q}$), the Higgs bosons (H, h, H_3, H_2 and H_1) and the lightest neutralino ($\tilde{\chi}_1^0$) resulting from the global fits for the CMSSM (a) and NMSSM (b)(c). In the CMSSM the gluino and neutralino are related, so the lower mass limits on $\tilde{g}$ from the LHC SUSY direct searches translates into a lower limit on $\tilde{\chi}_1^0$ and heavy Higgs mass. In the NMSSM such a relation is not given, so the limits on the Higgs boson and neutralino masses are independent of the limit on the gluino and squarks from the LHC SUSY direct searches. However, the masses depend on the NMSSM Higgs parameter, so the limits are given for μ_{eff} at the EW (b) and up to the TeV scale (c). The trilinear couplings are chosen accordingly to be below or above ± 1 TeV. The arrows indicate no upper limit on the corresponding mass limit, while the vertical red lines correspond to the expected sensitivity of LHC14.

the CMSSM. Here, the contribution from the spin-dependent cross section is negligible. However, a large Higgsino component of the lightest neutralino in the NMSSM can lead to a large spin-dependent cross section, since the Z^0 exchange is the dominant contribution. This constraint on the spin-dependent neutralino-nucleon scattering cross section excludes a large part of the NMSSM parameter space.

7.3. Outlook

So far no SUSY particles have been discovered, but the combination of all constraints and the model specific correlations lead to mass limits, which are listed in section 6.2 and summarized in Fig. 7.1(a) and 7.1(b)/7.1(c) for the CMSSM and NMSSM, respectively. In the NMSSM, the trilinear couplings and μ_{eff} can be chosen to be either of the order of the EW or TeV scale, which determines the mass limits on the third Higgs and the neutralino mass as indicated by Fig. 7.1(b) and 7.1(c). For the μ_{eff}^{EW} scenario, the masses are rather well determined, while for the TeV scenario no upper limit can be given. Note that μ_{eff} is $\lambda\langle s\rangle$. Since the couplings λ is smaller than 1 and the vev of the singlet is expected to be of the order of the EW scale, the μ_{eff}^{EW} scenario is the most natural one.

Future searches, like the LHC at 14 TeV and 3000 fb^{-1} (LHC14) and XENON1T, will provide a higher luminosity and sensitivity, which are needed to further constrain the parameter space. In the CMSSM a large part of parameter space will be covered by the LHC14 (see Fig. 6.18(a)). These searches will access the multi-TeV range for squarks and gluinos (see Fig. 6.18(b)) as indicated by red vertical bars in Fig. 7.1. The direct searches will restrict the range of the elastic cross section which is demonstrated in see Fig. 6.19(a). However, the part of parameter space which will escape the LHC will not be covered by the direct dark matter searches. Within the NMSSM, the same mass range for squarks and gluinos can be covered, but the Higgs and neutralino masses are independent of the SUSY masses, so the mass range on the neutralino is not affected by the LHC direct

searches (see Fig. 6.19(b)).
An additional Higgs boson or a WIMP would be the key to prove physics beyond the SM. The mass of this additional Higgs boson and its decays mode will be able to distinguish the CMSSM and NMSSM. An indication for a light WIMP would also distinguish the two models, since a light neutralino is only possible in the NMSSM and would exclude the CMSSM. Such light WIMPs and the corresponding spin-independent cross section down to 10^{-11} pb will be probed by future direct dark matter searches. The complementary searches at the LHC and at experiments for the direct dark matter search are both needed to further cover the supersymmetric parameter space in the future.

Bibliography

[1] G. Ekspong and Nobelstiftelsen, "Nobel Lectures, Physics, 1996-2000". Nobel Lectures in Physics. World Scientific, 2002.

[2] ATLAS Collaboration, "Measurement of the Higgs boson mass from the $H \to \gamma\gamma$ and $H \to ZZ^* \to 4\ell$ channels with the ATLAS detector using 25 fb^{-1} of pp collision data", arXiv:1406.3827.

[3] CMS Collaboration, "Precise determination of the mass of the Higgs boson and studies of the compatibility of its couplings with the standard model", Technical Report CMS-PAS-HIG-14-009, CERN, Geneva, 2014.

[4] A. Djouadi, "The Anatomy of electro-weak symmetry breaking. I: The Higgs boson in the standard model", *Phys.Rept.* **457** (2008) 1–216, arXiv:hep-ph/0503172.

[5] M. Veltman, "The Infrared - Ultraviolet Connection", *Acta Phys.Polon.* **B12** (1981) 437.

[6] Planck Collaboration, "Planck 2013 results. XVI. Cosmological parameters", arXiv:1303.5076.

[7] P. Fayet and S. Ferrara, "Supersymmetry", *Physics Reports* **32** (1977), no. 5, 249 – 334.

[8] H. Nilles, "Supersymmetry, supergravity and particle physics", *Physics Reports* **110** (1984), no. 1, 1 – 162.

[9] H. Haber and G. Kane, "The search for supersymmetry: Probing physics beyond the standard model", *Physics Reports* **117** (1985), no. 2, 75 – 263.

[10] S. P. Martin, "A Supersymmetry primer", arXiv:hep-ph/9709356.

[11] D. Kazakov, "Beyond the standard model: In search of supersymmetry", arXiv:hep-ph/0012288.

[12] I. J. R. Aitchison, "Supersymmetry in particle physics : an elementary introduction". Cambridge University Press, Cambridge, 2007. Includes bibliographical references and index. - Formerly CIP.

[13] G. R. Farrar and P. Fayet, "Phenomenology of the Production, Decay, and Detection of New Hadronic States Associated with Supersymmetry", *Phys.Lett.* **B76** (1978) 575–579.

[14] S. Novaes, "Standard model: An Introduction", arXiv:hep-ph/0001283.

[15] P. Langacker, "Introduction to the Standard Model and Electroweak Physics", arXiv:0901.0241.

[16] J. Iliopoulos, "Introduction to the STANDARD MODEL of the Electro-Weak Interactions", *2012 CERN Summer School of Particle Physics, Angers :* **France** (2012) arXiv:1305.6779.

[17] C. P. Burgess and G. D. Moore, "The standard model: a primer". Cambridge Univ. Press, Cambridge [u.a.], 2007. Includes bibliographical references and index.

[18] D. J. Griffiths, "Introduction to elementary particles". Physics textbook. Wiley-VCH, Weinheim, 2., rev. ed. edition, 2008.

[19] "Elementary particle physics", volume 1: Quantum field theory and particles. Wiley-VCH, Weinheim, 2010.

[20] Y. Nagashima, "Elementary particle physics", volume 2: Foundations of the standard model. Wiley-VCH, Weinheim, 2013.

[21] B. R. Martin, "Particle physics". The Manchester physics series. Wiley, Chichester [u.a.], 3. ed. edition, 2008. Includes bibliographical references and index. - Previous ed.: Chichester: Wiley, 1997.

[22] S. L. Glashow, "Partial-symmetries of weak interactions", *Nuclear Physics* **22** (1961), no. 4, 579 – 588.

[23] P. W. Higgs, "Broken Symmetries and the Masses of Gauge Bosons", *Phys. Rev. Lett.* **13** (Oct, 1964) 508–509.

[24] S. Weinberg, "A Model of Leptons", *Phys. Rev. Lett.* **19** (Nov, 1967) 1264–1266.

[25] A. Salam, "Elementary Particle Theory", *ed. N. Svartholm, Almqvist and Wiksells, Stockholm* (1969) 367.

[26] G. 'tHooft, "Renormalization of massless Yang-Mills fields", *Nuclear Physics B* **33** (1971), no. 1, 173 – 199.

[27] G. Hooft, "Renormalizable Lagrangians for massive Yang-Mills fields", *Nuclear Physics B* **35** (1971), no. 1, 167 – 188.

[28] O. W. Greenberg, "Spin and Unitary-Spin Independence in a Paraquark Model of Baryons and Mesons", *Phys. Rev. Lett.* **13** (Nov, 1964) 598–602.

[29] M. Y. Han and Y. Nambu, "Three-Triplet Model with Double SU(3) Symmetry", *Phys. Rev.* **139** (Aug, 1965) B1006–B1010.

[30] D. J. Gross and F. Wilczek, "Ultraviolet Behavior of Non-Abelian Gauge Theories", *Phys. Rev. Lett.* **30** (Jun, 1973) 1343–1346.

[31] D. J. Gross and F. Wilczek, "Asymptotically Free Gauge Theories. I", *Phys. Rev. D* **8** (Nov, 1973) 3633–3652.

[32] H. D. Politzer, "Reliable Perturbative Results for Strong Interactions?", *Phys. Rev. Lett.* **30** (Jun, 1973) 1346–1349.

[33] U. Amaldi, W. de Boer, and H. Furstenau, "Comparison of grand unified theories with electroweak and strong coupling constants measured at LEP", *Phys.Lett.* **B260** (1991) 447–455.

[34] S. L. Adler and W. A. Bardeen, "Absence of Higher-Order Corrections in the Anomalous Axial-Vector Divergence Equation", *Phys. Rev.* **182** (Jun, 1969) 1517–1536.

[35] S. Treiman, R. Jackiw, and D. Gross, "Lectures on current algebra and its application". 1977.

[36] C. Bouchiat, J. Iliopoulos, and P. Meyer, "An anomaly-free version of Weinberg's model", *Physics Letters B* **38** (1972), no. 7, 519 – 523.

[37] F. Englert and R. Brout, "Broken Symmetry and the Mass of Gauge Vector Mesons", *Phys. Rev. Lett.* **13** (Aug, 1964) 321–323.

[38] G. S. Guralnik, C. R. Hagen, and T. W. B. Kibble, "Global Conservation Laws and Massless Particles", *Phys. Rev. Lett.* **13** (Nov, 1964) 585–587.

[39] N. Cabibbo, "Unitary Symmetry and Leptonic Decays", *Phys. Rev. Lett.* **10** (Jun, 1963) 531–533.

[40] M. Kobayashi and T. Maskawa, "CP Violation in the Renormalizable Theory of Weak Interaction", *Prog.Theor.Phys.* **49** (1973) 652–657.

[41] J. F. Gunion, H. E. Haber, G. L. Kane et al., "The Higgs Hunter's Guide", *Front.Phys.* **80** (2000) 1–448.

[42] L. Evans and P. Bryant, "LHC Machine", *JINST* **3** (2008) S08001.

[43] CMS collaboration, "Public CMS Lumionsity Information",. https://twiki.cern.ch/twiki/bin/view/CMSPublic/LumiPublicResults.

[44] CMS Collaboration, "The CMS experiment at the CERN LHC", *JINST* **3** (2008) S08004.

[45] ATLAS Collaboration, "The ATLAS Experiment at the CERN Large Hadron Collider", *JINST* **3** (2008) S08003.

[46] LHCb Collaboration, "The LHCb Detector at the LHC", *JINST* **3** (2008) S08005.

[47] CMS collaboration, "CMS Muon Results",. https://twiki.cern.ch/twiki/bin/view/CMSPublic/PhysicsResultsMUO.

[48] CMS collaboration, "Summaries of CMS cross section measurements",. https://twiki.cern.ch/twiki/bin/view/CMSPublic/PhysicsResultsCombined.

[49] P. Binetruy, "Supersymmetry : theory, experiment, and cosmology". Oxford graduate texts. Oxford Univ. Press, Oxford, 1. publ. edition, 2006.

[50] ALEPH and CDF and D0 and DELPHI and L3 and OPAL and SLD and LEP Electroweak Working Group and Tevatron Electroweak Working Group and SLD Electroweak Working Group and Heavy Flavour Group Collaboration, "Precision Electroweak Measurements and Constraints on the Standard Model", `arXiv:0811.4682`.

[51] P. Ramond, "Dual Theory for Free Fermions", *Phys.Rev.* **D3** (1971) 2415–2418.

[52] A. Neveu and J. Schwarz, "Factorizable dual model of pions", *Nucl.Phys.* **B31** (1971) 86–112.

[53] J.-L. Gervais and B. Sakita, "Field Theory Interpretation of Supergauges in Dual Models", *Nucl.Phys.* **B34** (1971) 632–639.

[54] J. Wess and B. Zumino, "A Lagrangian Model Invariant Under Supergauge Transformations", *Phys.Lett.* **B49** (1974) 52.

[55] J. Wess and B. Zumino, "Supergauge Transformations in Four-Dimensions", *Nucl.Phys.* **B70** (1974) 39–50.

[56] J. Wess and B. Zumino, "Supergauge Invariant Extension of Quantum Electrodynamics", *Nucl.Phys.* **B78** (1974) 1.

[57] P. Fayet, "Supergauge Invariant Extension of the Higgs Mechanism and a Model for the electron and Its Neutrino", *Nucl.Phys.* **B90** (1975) 104–124.

[58] P. Fayet, "Supersymmetry and Weak, Electromagnetic and Strong Interactions", *Phys.Lett.* **B64** (1976) 159.

[59] P. Fayet, "Spontaneously Broken Supersymmetric Theories of Weak, Electromagnetic and Strong Interactions", *Phys.Lett.* **B69** (1977) 489.

[60] W. de Boer, "Grand unified theories and supersymmetry in particle physics and cosmology", *Prog.Part.Nucl.Phys.* **33** (1994) 201–302, arXiv:hep-ph/9402266.

[61] H. Baer, "Weak scale supersymmetry : from superfields to scattering events". Cambridge Univ. Press, Cambridge, 2006. hbk.. - : Â£45.00 : CIP entry (Feb.).

[62] N. Polonsky, "Supersymmetry: structure and phenomena : extensions of the standard model". Lecture notes in physics : New series M, monographs ; 68. Springer, Berlin, 2001. Pp. : DM 74.00.

[63] H. Kalka and G. Soff, "Supersymmetrie". Teubner Studienbücher : Physik. Teubner, Stuttgart, 1997.

[64] G. Bhattacharyya, "R-parity violating supersymmetric Yukawa couplings: A Minireview", *Nucl.Phys.Proc.Suppl.* **52A** (1997) 83–88, arXiv:hep-ph/9608415.

[65] M. Chemtob, "Phenomenological constraints on broken R parity symmetry in supersymmetry models", *Prog.Part.Nucl.Phys.* **54** (2005) 71–191, arXiv:hep-ph/0406029.

[66] K. Inoue, A. Kakuto, H. Komatsu et al., "Aspects of Grand Unified Models with Softly Broken Supersymmetry", *Prog.Theor.Phys.* **68** (1982) 927.

[67] A. Djouadi, "The Anatomy of electro-weak symmetry breaking. II. The Higgs bosons in the minimal supersymmetric model", *Phys.Rept.* **459** (2008) 1–241, arXiv:hep-ph/0503173.

[68] S. P. Martin, "Complete two loop effective potential approximation to the lightest Higgs scalar boson mass in supersymmetry", *Phys.Rev.* **D67** (2003) 095012, arXiv:hep-ph/0211366.

[69] M. S. Carena, H. Haber, S. Heinemeyer et al., "Reconciling the two loop diagrammatic and effective field theory computations of the mass of the lightest CP - even Higgs boson in the MSSM", *Nucl.Phys.* **B580** (2000) 29–57, arXiv:hep-ph/0001002.

[70] A. Brignole, G. Degrassi, P. Slavich et al., "On the two loop sbottom corrections to the neutral Higgs boson masses in the MSSM", *Nucl.Phys.* **B643** (2002) 79–92, arXiv:hep-ph/0206101.

[71] S. Heinemeyer, W. Hollik, and G. Weiglein, "QCD corrections to the masses of the neutral CP - even Higgs bosons in the MSSM", *Phys.Rev.* **D58** (1998) 091701, arXiv:hep-ph/9803277.

[72] J. E. Kim and H. P. Nilles, "The mu Problem and the Strong CP Problem", *Phys.Lett.* **B138** (1984) 150.

[73] D. Miller, R. Nevzorov, and P. Zerwas, "The Higgs sector of the next-to-minimal supersymmetric standard model", *Nucl.Phys.* **B681** (2004) 3–30, `arXiv:hep-ph/0304049`.

[74] U. Ellwanger, C. Hugonie, and A. M. Teixeira, "The Next-to-Minimal Supersymmetric Standard Model", *Phys.Rept.* **496** (2010) 1–77, `arXiv:0910.1785`.

[75] J. R. Ellis, J. Gunion, H. E. Haber et al., "Higgs Bosons in a Nonminimal Supersymmetric Model", *Phys.Rev.* **D39** (1989) 844.

[76] H. P. Nilles, M. Srednicki, and D. Wyler, "Weak Interaction Breakdown Induced by Supergravity", *Phys.Lett.* **B120** (1983) 346.

[77] C. Panagiotakopoulos and A. Pilaftsis, "Higgs scalars in the minimal nonminimal supersymmetric standard model", *Phys.Rev.* **D63** (2001) 055003, `arXiv:hep-ph/0008268`.

[78] A. Dedes, C. Hugonie, S. Moretti et al., "Phenomenology of a new minimal supersymmetric extension of the standard model", *Phys.Rev.* **D63** (2001) 055009, `arXiv:hep-ph/0009125`.

[79] R. Peccei and H. R. Quinn, "CP Conservation in the Presence of Instantons", *Phys.Rev.Lett.* **38** (1977) 1440–1443.

[80] S. Weinberg, "A New Light Boson?", *Phys.Rev.Lett.* **40** (1978) 223–226.

[81] F. Wilczek, "Problem of Strong p and t Invariance in the Presence of Instantons", *Phys.Rev.Lett.* **40** (1978) 279–282.

[82] S. Abel, S. Sarkar, and P. White, "On the cosmological domain wall problem for the minimally extended supersymmetric standard model", *Nucl.Phys.* **B454** (1995) 663–684, `arXiv:hep-ph/9506359`.

[83] A. Vilenkin, "Cosmic Strings and Domain Walls", *Phys.Rept.* **121** (1985) 263–315.

[84] S. Abel, "Destabilizing divergences in the NMSSM", *Nucl.Phys.* **B480** (1996) 55–72, `arXiv:hep-ph/9609323`.

[85] S. Dimopoulos and D. W. Sutter, "The Supersymmetric flavor problem", *Nucl.Phys.* **B452** (1995) 496–512, `arXiv:hep-ph/9504415`.

[86] Particle Data Group Collaboration, "Review of Particle Physics", *Phys. Rev. D* **86** (2012) 010001. updated results from 2013 at http://pdg.lbl.gov/.

[87] H. P. Nilles, "Dynamically Broken Supergravity and the Hierarchy Problem", *Phys.Lett.* **B115** (1982) 193.

[88] A. H. Chamseddine, R. L. Arnowitt, and P. Nath, "Locally Supersymmetric Grand Unification", *Phys.Rev.Lett.* **49** (1982) 970.

[89] M. Dine and A. E. Nelson, "Dynamical supersymmetry breaking at low-energies", *Phys.Rev.* **D48** (1993) 1277–1287, `arXiv:hep-ph/9303230`.

[90] A. Djouadi, U. Ellwanger, and A. Teixeira, "The Constrained next-to-minimal supersymmetric standard model", *Phys.Rev.Lett.* **101** (2008) 101802, arXiv:0803.0253.

[91] J. F. Gunion, Y. Jiang, and S. Kraml, "The Constrained NMSSM and Higgs near 125 GeV", *Phys.Lett.* **B710** (2012) 454–459, arXiv:1201.0982.

[92] U. Ellwanger and C. Hugonie, "Higgs bosons near 125 GeV in the NMSSM with constraints at the GUT scale", *Adv.High Energy Phys.* **2012** (2012) 625389, arXiv:1203.5048.

[93] S. King, M. Mühlleitner, R. Nevzorov et al., "Natural NMSSM Higgs Bosons", *Nucl.Phys.* **B870** (2013) 323–352, arXiv:1211.5074.

[94] G. Cowan, "Statistical Data Analysis". Clarendon Press, 1998.

[95] J. L. Feng, P. Kant, S. Profumo et al., "Three-Loop Corrections to the Higgs Boson Mass and Implications for Supersymmetry at the LHC", *Phys.Rev.Lett.* **111** (2013) 131802, arXiv:1306.2318.

[96] LHCb Collaboration, "Measurement of the $B_s^0 \to \mu^+\mu^-$ branching fraction and search for $B^0 \to \mu^+\mu^-$ decays at the LHCb experiment", *Phys.Rev.Lett.* **111** (2013) 101805, arXiv:1307.5024.

[97] CMS Collaboration, "Measurement of the B(s) to mu+ mu- branching fraction and search for B0 to mu+ mu- with the CMS Experiment", *Phys.Rev.Lett.* **111** (2013) 101804, arXiv:1307.5025.

[98] C. Bobeth, M. Gorbahn, T. Hermann et al., "$B_{s,d} \leftarrow l + l-$ in the Standard Model with Reduced Theoretical Uncertainty", *Phys.Rev.Lett.* **112** (2014) 101801, arXiv:1311.0903.

[99] Heavy Flavor Averaging Group Collaboration, "Averages of B-Hadron, C-Hadron, and tau-lepton properties as of early 2012", arXiv:1207.1158. updated results taken from //www.slac.stanford.edu/xorg/hfag/rare/2013/radll/OUTPUT/TABLES/radll.pdf.

[100] M. Misiak, H. Asatrian, K. Bieri et al., "Estimate of B(anti-B to X(s) gamma) at O(alpha(s)**2)", *Phys.Rev.Lett.* **98** (2007) 022002, arXiv:hep-ph/0609232.

[101] Belle Collaboration, "Evidence for $B^- \to \tau^- \bar{\nu}_\tau$ with a Hadronic Tagging Method Using the Full Data Sample of Belle", *Phys.Rev.Lett.* **110** (2013), no. 13, 131801, arXiv:1208.4678.

[102] CKMfitter Group Collaboration, "CP violation and the CKM matrix: Assessing the impact of the asymmetric B factories", *Eur.Phys.J.* **C41** (2005) 1–131, arXiv:hep-ph/0406184. updated results from 2013 at http://ckmfitter.in2p3.fr/.

[103] Muon G-2 Collaboration, "Final Report of the Muon E821 Anomalous Magnetic Moment Measurement at BNL", *Phys.Rev.* **D73** (2006) 072003, arXiv:hep-ex/0602035.

[104] M. Davier, A. Hoecker, B. Malaescu et al., "Reevaluation of the Hadronic Contributions to the Muon g-2 and to alpha(MZ)", *Eur.Phys.J.* **C71** (2011) 1515, arXiv:1010.4180.

[105] B. Allanach, G. Belanger, F. Boudjema et al., "Uncertainties in relic density calculations in mSUGRA", arXiv:hep-ph/0402161.

[106] C. Beskidt, W. de Boer, D. Kazakov et al., "Constraints on Supersymmetry from LHC data on SUSY searches and Higgs bosons combined with cosmology and direct dark matter searches", *Eur.Phys.J.* **C72** (2012) 2166, arXiv:1207.3185.

[107] CMS Collaboration, "Search for neutral MSSM Higgs bosons decaying to a pair of tau leptons in pp collisions", arXiv:1408.3316.

[108] "Search for squarks and gluinos with the ATLAS detector in final states with jets and missing transverse momentum and 20.3 fb^{-1} of $\sqrt{s} = 8$ TeV proton-proton collision data", Technical Report ATLAS-CONF-2013-047, CERN, Geneva, May, 2013.

[109] "Search for strong production of supersymmetric particles in final states with missing transverse momentum and at least three b-jets using 20.1 fb^{-1} of pp collisions at sqrt(s) = 8 TeV with the ATLAS Detector.", Technical Report ATLAS-CONF-2013-061, CERN, Geneva, Jun, 2013.

[110] LEP Working Group for Higgs boson searches, ALEPH, DELPHI, L3, OPAL Collaboration, "Search for the standard model Higgs boson at LEP", *Phys.Lett.* **B565** (2003) 61–75, arXiv:hep-ex/0306033.

[111] LUX Collaboration, "First results from the LUX dark matter experiment at the Sanford Underground Research Facility", arXiv:1310.8214.

[112] XENON100 Collaboration, "Limits on spin-dependent WIMP-nucleon cross sections from 225 live days of XENON100 data", *Phys.Rev.Lett.* **111** (2013), no. 2, 021301, arXiv:1301.6620.

[113] COUPP Collaboration, "First Dark Matter Search Results from a 4-kg CF_3I Bubble Chamber Operated in a Deep Underground Site", *Phys.Rev.* **D86** (2012) 052001, arXiv:1204.3094.

[114] G. Belanger, F. Boudjema, A. Pukhov et al., "micrOMEGAs: A program for calculating dark matter observables", *Comput.Phys.Commun.* **185** (2014) 960–985, arXiv:1305.0237.

[115] A. Djouadi, J.-L. Kneur, and G. Moultaka, "SuSpect: A Fortran code for the supersymmetric and Higgs particle spectrum in the MSSM", *Comput.Phys.Commun.* **176** (2007) 426–455, arXiv:hep-ph/0211331.

[116] D. Das, U. Ellwanger, and A. M. Teixeira, "NMSDECAY: A Fortran Code for Supersymmetric Particle Decays in the Next-to-Minimal Supersymmetric Standard Model", *Comput.Phys.Commun.* **183** (2012) 774–779, arXiv:1106.5633.

[117] U. Ellwanger and C. Hugonie, "NMSPEC: A Fortran code for the sparticle and Higgs masses in the NMSSM with GUT scale boundary conditions", *Comput.Phys.Commun.* **177** (2007) 399–407, arXiv:hep-ph/0612134.

[118] M. Mühlleitner, A. Djouadi, and Y. Mambrini, "SDECAY: A Fortran code for the decays of the supersymmetric particles in the MSSM", *Comput.Phys.Commun.* **168** (2005) 46–70, arXiv:hep-ph/0311167.

[119] F. James, "MINUIT Function Minimization and Error Analysis: Reference Manual Version 94.1",.

[120] F. Zwicky, "Die Rotverschiebung von extragalaktischen Nebeln", *Helv.Phys.Acta* **6** (1933) 110–127.

[121] V. C. Rubin and J. Ford, W. Kent, "Rotation of the Andromeda Nebula from a Spectroscopic Survey of Emission Regions", *Astrophys.J.* **159** (1970) 379–403.

[122] K. Begeman, A. Broeils, and R. Sanders, "Extended rotation curves of spiral galaxies: Dark haloes and modified dynamics", *Mon.Not.Roy.Astron.Soc.* **249** (1991) 523.

[123] D. Walsh, R. Carswell, and R. Weymann, "0957 + 561 A, B - Twin quasistellar objects or gravitational lens", *Nature* **279** (1979) 381–384.

[124] D. Clowe, M. Bradac, A. H. Gonzalez et al., "A direct empirical proof of the existence of dark matter", *Astrophys.J.* **648** (2006) L109–L113, arXiv:astro-ph/0608407.

[125] E. W. Kolb and M. S. Turner, "THE EARLY UNIVERSE. REPRINTS",.

[126] V. Springel, S. D. White, A. Jenkins et al., "Simulating the joint evolution of quasars, galaxies and their large-scale distribution", *Nature* **435** (2005) 629–636, arXiv:astro-ph/0504097.

[127] G. Jungman, M. Kamionkowski, and K. Griest, "Supersymmetric dark matter", *Phys.Rept.* **267** (1996) 195–373, arXiv:hep-ph/9506380.

[128] G. Bertone, D. Hooper, and J. Silk, "Particle dark matter: Evidence, candidates and constraints", *Phys.Rept.* **405** (2005) 279–390, arXiv:hep-ph/0404175.

[129] J. Gunn, B. Lee, I. Lerche et al., "Some Astrophysical Consequences of the Existence of a Heavy Stable Neutral Lepton", *Astrophys.J.* **223** (1978) 1015–1031.

[130] J. R. Ellis, J. Hagelin, D. V. Nanopoulos et al., "Supersymmetric Relics from the Big Bang", *Nucl.Phys.* **B238** (1984) 453–476.

[131] K. Griest and D. Seckel, "Three exceptions in the calculation of relic abundances", *Phys.Rev.* **D43** (1991) 3191–3203.

[132] P. Gondolo and G. Gelmini, "Cosmic abundances of stable particles: Improved analysis", *Nucl.Phys.* **B360** (1991) 145–179.

[133] C. Beskidt, W. de Boer, T. Hanisch et al., "Constraints on Supersymmetry from Relic Density compared with future Higgs Searches at the LHC", *Phys.Lett.* **B695** (2011) 143–148, arXiv:1008.2150.

[134] H. E. Haber, R. Hempfling, and A. H. Hoang, "Approximating the radiatively corrected Higgs mass in the minimal supersymmetric model", *Z.Phys.* **C75** (1997) 539–554, arXiv:hep-ph/9609331.

[135] B. Allanach, "SOFTSUSY: a program for calculating supersymmetric spectra", *Comput.Phys.Commun.* **143** (2002) 305–331, arXiv:hep-ph/0104145.

[136] A. Arbey and F. Mahmoudi, "SuperIso Relic: A Program for calculating relic density and flavor physics observables in Supersymmetry", *Comput.Phys.Commun.* **181** (2010) 1277–1292, arXiv:0906.0369.

[137] C. T. Hill, "Quark and Lepton Masses from Renormalization Group Fixed Points", *Phys.Rev.* **D24** (1981) 691.

[138] A. Arbey, M. Battaglia, A. Djouadi et al., "An update on the constraints on the phenomenological MSSM from the new LHC Higgs results", *Phys.Lett.* **B720** (2013) 153–160, arXiv:1211.4004.

[139] P. Bechtle, S. Heinemeyer, O. Stal et al., "MSSM Interpretations of the LHC Discovery: Light or Heavy Higgs?", *Eur.Phys.J.* **C73** (2013) 2354, arXiv:1211.1955.

[140] M. Carena, S. Heinemeyer, O. Stål et al., "MSSM Higgs Boson Searches at the LHC: Benchmark Scenarios after the Discovery of a Higgs-like Particle", *Eur.Phys.J.* **C73** (2013) 2552, arXiv:1302.7033.

[141] CMS and LHCb Collaboration, "Combination of results on the rare decays $B^0_{(s)} \to \mu^+\mu^-$ from the CMS and LHCb experiments", Technical Report CMS-PAS-BPH-13-007. CERN-LHCb-CONF-2013-012, CERN, Geneva, Jun, 2014.

[142] C. Bobeth, T. Ewerth, F. Kruger et al., "Analysis of neutral Higgs boson contributions to the decays $\bar{B}(\ s) \to \ell^+\ell^-$ and $\bar{B} \to K\ell^+\ell^-$", *Phys.Rev.* **D64** (2001) 074014, arXiv:hep-ph/0104284.

[143] R. L. Arnowitt, B. Dutta, T. Kamon et al., "Detection of $B_s \to \mu^+\mu^-$ at the Tevatron run II and constraints on the SUSY parameter space", *Phys.Lett.* **B538** (2002) 121–129, arXiv:hep-ph/0203069.

[144] C. Beskidt, W. de Boer, D. Kazakov et al., "Constraints from the decay $B^0_s \to \mu^+\mu^-$ and LHC limits on Supersymmetry", *Phys.Lett.* **B705** (2011) 493–497, arXiv:1109.6775.

[145] T. Banks, "Supersymmetry and the Quark Mass Matrix", *Nucl.Phys.* **B303** (1988) 172.

[146] L. J. Hall, R. Rattazzi, and U. Sarid, "The Top quark mass in supersymmetric SO(10) unification", *Phys.Rev.* **D50** (1994) 7048–7065, arXiv:hep-ph/9306309.

[147] A. Akeroyd, C. H. Chen, and S. Recksiegel, "Measuring $B^\pm \to \tau^\pm\nu$ and $B_c^\pm \to \tau^\pm\nu$ at the Z peak", *Phys.Rev.* **D77** (2008) 115018, arXiv:0803.3517.

[148] I. I. Bigi, N. Uraltsev, and A. Vainshtein, "Nonperturbative corrections to inclusive beauty and charm decays: QCD versus phenomenological models", *Phys.Lett.* **B293** (1992) 430–436, arXiv:hep-ph/9207214.

[149] M. A. Shifman, "Quark hadron duality", arXiv:hep-ph/0009131.

[150] J. L. Hewett, "Can $b \to s\gamma$ close the supersymmetric Higgs production window?", *Phys.Rev.Lett.* **70** (1993) 1045–1048, arXiv:hep-ph/9211256.

[151] R. Garisto and J. Ng, "Supersymmetric $b \to s\gamma$ with large chargino contributions", *Phys.Lett.* **B315** (1993) 372–378, arXiv:hep-ph/9307301.

[152] M. S. Carena, D. Garcia, U. Nierste et al., "$b \to s\gamma$ and supersymmetry with large tan Beta", *Phys.Lett.* **B499** (2001) 141–146, arXiv:hep-ph/0010003.

[153] C. Beskidt, W. de Boer, D. Kazakov et al., "Where is SUSY?", *JHEP* **1205** (2012) 094, arXiv:1202.3366.

[154] M. Weber and W. de Boer, "Determination of the Local Dark Matter Density in our Galaxy", *Astron.Astrophys.* **509** (2010) A25, arXiv:0910.4272.

[155] M. W. Goodman and E. Witten, "Detectability of Certain Dark Matter Candidates", *Phys.Rev.* **D31** (1985) 3059.

[156] M. Drees and M. Nojiri, "Neutralino - nucleon scattering revisited", *Phys.Rev.* **D48** (1993) 3483–3501, arXiv:hep-ph/9307208.

[157] DAMA, LIBRA Collaboration, "New results from DAMA/LIBRA", *Eur.Phys.J.* **C67** (2010) 39–49, arXiv:1002.1028.

[158] CoGeNT Collaboration, "CoGeNT: A Search for Low-Mass Dark Matter using p-type Point Contact Germanium Detectors", *Phys.Rev.* **D88** (2013) 012002, arXiv:1208.5737.

[159] D. Majumdar, "Detection rates for Kaluza-Klein dark matter", *Phys.Rev.* **D67** (2003) 095010, arXiv:hep-ph/0209277.

[160] H. Ohki, H. Fukaya, S. Hashimoto et al., "Nucleon sigma term and strange quark content from lattice QCD with exact chiral symmetry", *Phys.Rev.* **D78** (2008) 054502, arXiv:0806.4744.

[161] J. Cao, K.-i. Hikasa, W. Wang et al., "Constraints of dark matter direct detection experiments on the MSSM and implications on LHC Higgs search", *Phys.Rev.* **D82** (2010) 051701, arXiv:1006.4811.

[162] F. Jegerlehner and A. Nyffeler, "The Muon g-2", *Phys.Rept.* **477** (2009) 1–110, arXiv:0902.3360.

[163] J. Prades, E. de Rafael, and A. Vainshtein, "Hadronic Light-by-Light Scattering Contribution to the Muon Anomalous Magnetic Moment", arXiv:0901.0306.

[164] J. P. Miller, E. de Rafael, and B. L. Roberts, "Muon (g-2): Experiment and theory", *Rept.Prog.Phys.* **70** (2007) 795, arXiv:hep-ph/0703049.

[165] A. Czarnecki and W. J. Marciano, "The Muon anomalous magnetic moment: A Harbinger for 'new physics'", *Phys.Rev.* **D64** (2001) 013014, arXiv:hep-ph/0102122.

[166] C. Beskidt, W. de Boer, and D. Kazakov, "A comparison of the Higgs sectors of the CMSSM and NMSSM for a 126 GeV Higgs boson", *Phys.Lett.* **B726** (2013) 758–766, arXiv:1308.1333.

[167] C. Beskidt, W. de Boer, and D. Kazakov, "The impact of a 126 GeV Higgs on the neutralino mass", *Phys.Lett.* **B** (2014) arXiv:1402.4650.

[168] O. Buchmueller, R. Cavanaugh, A. De Roeck et al., "The CMSSM and NUHM1 after LHC Run 1", arXiv:1312.5250.

[169] F. Feroz, K. Cranmer, M. Hobson et al., "Challenges of Profile Likelihood Evaluation in Multi-Dimensional SUSY Scans", *JHEP* **1106** (2011) 042, arXiv:1101.3296.

[170] F. Feroz, M. Hobson, and M. Bridges, "MultiNest: an efficient and robust Bayesian inference tool for cosmology and particle physics", *Mon.Not.Roy.Astron.Soc.* **398** (2009) 1601–1614, arXiv:0809.3437.

[171] P. Bechtle, K. Desch, H. K. Dreiner et al., "Constrained Supersymmetry after the Higgs Boson Discovery: A global analysis with Fittino", arXiv:1310.3045.

[172] L. Roszkowski, E. M. Sessolo, and A. J. Williams, "What next for the CMSSM and the NUHM: Improved prospects for superpartner and dark matter detection", *JHEP* **1408** (2014) 067, arXiv:1405.4289.

[173] U. Ellwanger and C. Hugonie, "The semi-constrained NMSSM satisfying bounds from the LHC, LUX and Planck", arXiv:1405.6647.

[174] J.-J. Cao, Z.-X. Heng, J. M. Yang et al., "A SM-like Higgs near 125 GeV in low energy SUSY: a comparative study for MSSM and NMSSM", *JHEP* **1203** (2012) 086, arXiv:1202.5821.

[175] T. Gherghetta, B. von Harling, A. D. Medina et al., "The Scale-Invariant NMSSM and the 126 GeV Higgs Boson", *JHEP* **1302** (2013) 032, arXiv:1212.5243.

[176] K. Agashe, Y. Cui, and R. Franceschini, "Natural Islands for a 125 GeV Higgs in the scale-invariant NMSSM", *JHEP* **1302** (2013) 031, arXiv:1209.2115.

[177] D. A. Vasquez, G. Belanger, C. Boehm et al., "The 125 GeV Higgs in the NMSSM in light of LHC results and astrophysics constraints", *Phys.Rev.* **D86** (2012) 035023, arXiv:1203.3446.

[178] S. King, M. Mühlleitner, and R. Nevzorov, "NMSSM Higgs Benchmarks Near 125 GeV", *Nucl.Phys.* **B860** (2012) 207–244, arXiv:1201.2671.

[179] M. Badziak, M. Olechowski, and S. Pokorski, "New Regions in the NMSSM with a 125 GeV Higgs", *JHEP* **1306** (2013) 043, arXiv:1304.5437.

[180] S. King, M. Mühlleitner, R. Nevzorov et al., "Discovery Prospects for NMSSM Higgs Bosons at the High-Energy Large Hadron Collider", arXiv:1408.1120.

[181] XENON100 Collaboration, "Dark Matter Results from 225 Live Days of XENON100 Data", *Phys.Rev.Lett.* **109** (2012) 181301, arXiv:1207.5988.

[182] T. Daylan, D. P. Finkbeiner, D. Hooper et al., "The Characterization of the Gamma-Ray Signal from the Central Milky Way: A Compelling Case for Annihilating Dark Matter", arXiv:1402.6703.

[183] Thomas Williams and Colin Kelley and many others, "Gnuplot 4.4: an interactive plotting program",. http://gnuplot.sourceforge.net/.

[184] CMS Collaboration, "Higgs to tau tau (MSSM)", Technical Report CMS-PAS-HIG-13-021, CERN, Geneva, 2013.

[185] P. Z. Skands, B. Allanach, H. Baer et al., "SUSY Les Houches accord: Interfacing SUSY spectrum calculators, decay packages, and event generators", *JHEP* **0407** (2004) 036, arXiv:hep-ph/0311123.

[186] A. Belyaev, N. D. Christensen, and A. Pukhov, "CalcHEP 3.4 for collider physics within and beyond the Standard Model", *Comput.Phys.Commun.* **184** (2013) 1729–1769, arXiv:1207.6082.

[187] G. Degrassi, S. Heinemeyer, W. Hollik et al., "Towards high precision predictions for the MSSM Higgs sector", *Eur.Phys.J.* **C28** (2003) 133–143, arXiv:hep-ph/0212020.

[188] CMS Collaboration, "Searches for electroweak production of charginos, neutralinos, and sleptons decaying to leptons and W, Z, and Higgs bosons in pp collisions at 8 TeV", arXiv:1405.7570.

[189] CMS Collaboration, "Search for new physics in monojet events in pp collisions at sqrt(s)= 8 TeV", Technical Report CMS-PAS-EXO-12-048, CERN, Geneva, 2013.

[190] CMS Collaboration, "Search for invisible decays of Higgs bosons in the vector boson fusion and associated ZH production modes", arXiv:1404.1344.

Appendix

A. Probability Density Function

The probability to observe a value of a variable x within a infinitesimal interval $[x, x+dx]$ is given by the probability density function $f(x)$, which is normalized such that the total probability is one for the entire sample space S

$$\int_S f(x)dx = 1. \tag{7.1}$$

The probability for a random variable to take a value less than or equal to x is defined by the cumulative distribution $F(x)$ which is related to the pdf via

$$F(x) = \int_{-\infty}^{x} f(x')dx'. \tag{7.2}$$

The expectation value $E[x]$, also known as the mean, of a random variable which is distributed according to the pdf $f(x)$ is defined by

$$E[x] = \int_{-\infty}^{\infty} xf(x)dx = \mu. \tag{7.3}$$

A measure of how widely x is spread around its mean is given by its variance $V[x]$, whereas the square root of the variance is called the standard deviation σ of x

$$E[(x - E[x])^2] = \int_{-\infty}^{\infty} (x-\mu)^2 f(x)dx = \sigma^2 = V[x]. \tag{7.4}$$

A.1. χ^2 distribution

The χ^2 distribution for a continuous variable z where $0 \leq z < \infty$ and n degrees of freedom is defined by

$$f(z;n) = \frac{1}{2^{n/2}\Gamma(n/2)} z^{n/2-1} e^{-z/2}, \tag{7.5}$$

where $\Gamma(x)$ represents the gamma function

$$\Gamma(x) = \int_0^{\infty} e^{-t} t^{x-1} dt. \tag{7.6}$$

The mean and variance of z read

$$\begin{aligned} E[x] &= \int_0^\infty z \ \frac{1}{2^{n/2}\Gamma(n/2)} z^{n/2-1} e^{-z/2} dz = n, \\ V[x] &= \int_0^\infty (z-n)^2 \ \frac{1}{2^{n/2}\Gamma(n/2)} z^{n/2-1} e^{-z/2} dz = 2n. \end{aligned} \tag{7.7}$$

B. Parametrization of the Experimental Limits

In chapter 4 the experimental constraints have been introduced and their implementation to the χ^2 function has been discussed. The χ^2 contribution which refers to the experimental limit is defined by

$$\chi^2 = \begin{cases} \left(\frac{x_{theo}-x^X_{exp}}{\sigma}\right)^2, \text{if } x_{theo} \geq x^X_{exp} \\ 0, \qquad\qquad \text{if } x_{theo} < x^X_{exp} \end{cases}$$

for an upper limit. The lower limit is reversely defined, while X stands either for a 95% or 90% C.L. limit. The χ^2 contribution is zero if the theoretical prediction if below/above the evaluated minimum for the upper/lower limit marked x^X_{exp}. Those values can be derived from the corresponding published exclusion contour. The detailed parameterization of the published 95% and 90% C.L. exclusion contour as well as the 1σ band are summarized in the following subsections.

B.1. Limit on the Pseudo-Scalar Higgs Boson Mass

The parameterization of $\tan\beta^{95}(m_A)$ given in $\chi^2_{m_A}$ is determined by the requirement that $\Delta\chi^2_{m_A}$ is 5.99 on the contour line:

$$\begin{aligned} \Delta\chi^2 &= 5.99 \\ &= \left(\frac{\tan\beta^{obs}(m_A) - \tan\beta^{95}(m_A)}{\sigma_{\tan\beta^{95}}(m_A)}\right)^2 \\ \rightarrow \tan\beta^{95}(m_A) &= \tan\beta^{obs}(m_A) - \sqrt{5.99}\cdot\sigma_{\tan\beta^{95}}(m_A). \end{aligned} \tag{7.8}$$

The 95% C.L. contour line is parameterized by fitting piecewise a polynomial using GNUPLOT [183]. Outside the published mass range, the exclusion contour is approximated to be linear with a fixed error. The parametrization for $\tan\beta^{obs}(m_A)$ reads

$$\tan\beta^{obs}(m_A) = \begin{cases} m_A < 90, & 7.2 \\ 90 \leq m_A < 134.5, & a_1 + a_2\cdot m_A + a_3\cdot m_A^2 + a_4\cdot m_A^3 + a_5\cdot m_A^4 \\ 134.5 \leq m_A < 900, & b_1 + b_2\cdot m_A + b_3\cdot m_A^2 + b_4\cdot m_A^3 \\ 900 \leq m_A, & c_1 + c_2\cdot m_A \end{cases} \tag{7.9}$$

with

$$\begin{aligned} a_1 &= -462.45, & b_1 &= -3.18\ , & c_1 &= -57.05, \\ a_2 &= 15.55\ , & b_2 &= 6.14\cdot 10^{-2}\ , & c_2 &= 1.28\cdot 10^{-1}, \\ a_3 &= -1.89\cdot 10^{-1}\ , & b_3 &= -6.10\cdot 10^{-5}\ , & & \\ a_4 &= 9.96\cdot 10^{-4}\ , & b_4 &= 7.53\cdot 10^{-8}\ , & & \\ a_5 &= -1.94\cdot 10^{-6}\ . & & & & \end{aligned}$$

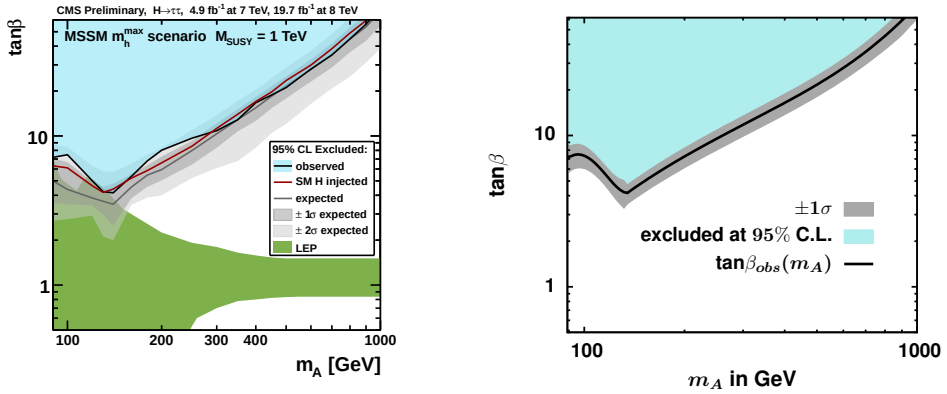

(a) (b)

Figure B.1.: Comparison of the published 95% C.L. contour taken from Ref. [184] (a) and their parametrization needed for the χ^2 contribution (b). The blue area is excluded at 95%C.L.. The solid black line corresponds to the observed limit while the dark gray band represents the 1σ error band.

The mass m_A is given in GeV. A similar parameterization can be used for the 1σ error band which corresponds to $\sigma_{\tan\beta^{95}}(m_A)$:

$$\sigma_{\tan\beta^{95}}(m_A) = \begin{cases} m_A < 90, & 1.6 \\ 90 \leq m_A < 134.5, & A_1 + A_2 \cdot m_A + A_3 \cdot m_A^2 + A_4 \cdot m_A^3 + A_5 \cdot m_A^4 \\ 134.5 \leq m_A < 900, & B_1 + B_2 \cdot m_A + B_3 \cdot m_A^2 + B_4 \cdot m_A^3 + B_5 \cdot m_A^4 \\ 900 \leq m_A, & 11.6 \end{cases} \quad (7.10)$$

with

$$\begin{aligned} A_1 &= -131.39\ , & B_1 &= -0.39, \\ A_2 &= 4.64\ , & B_2 &= 7.38 \cdot 10^{-3}, \\ A_3 &= -5.96 \cdot 10^{-2}\ , & B_3 &= 3.92 \cdot 10^{-6}, \\ A_4 &= 3.33 \cdot 10^{-4}, & B_4 &= -1.60 \cdot 10^{-8}, \\ A_5 &= -6.84 \cdot 10^{-7}\ , & B_5 &= 2.11 \cdot 10^{-11}. \end{aligned}$$

Fig. B.1 shows the comparison of the published data from Ref. [184] and the parameterization used for the global fit. The blue areas are excluded at 95% C.L.. The green area in Fig. B.1(a) is excluded by the LEP constraint. The LEP constraint is taken into account separately by an additional χ^2 contribution. Therefore, only $\tan\beta^{obs}(m_A)$ (solid black line) and the corresponding error $\sigma_{\tan\beta^{95}}(m_A)$ (gray band) is shown in Fig. B.1(b). The parameterization is based on the preliminary results from CMS in Ref. [184]. It has been checked that the limit is similar to the updated limit given in Ref. [107] and leads to the same exclusion contour in the m_0-$m_{1/2}$ plane.

The Higgs sector is modified in the NMSSM. Therefore, the model independent upper limit on the cross section times branching fraction $\sigma \cdot BR(\phi \to \tau\tau)$ for the gluon fusion is used to include the constraint on the pseudo-scalar Higgs mass. To get the corresponding χ^2 contribution $\tan\beta(m_A)$ is replaced by $(\sigma \cdot BR)(m_\phi)$. The parameterization $(\sigma \cdot BR)^{95}(m_\phi)$ given in $\chi^2_{m_\phi}$ is determined by the requirement that $\Delta\chi^2_{m_\phi}$ is 5.99 on the contour line from Ref. [107]:

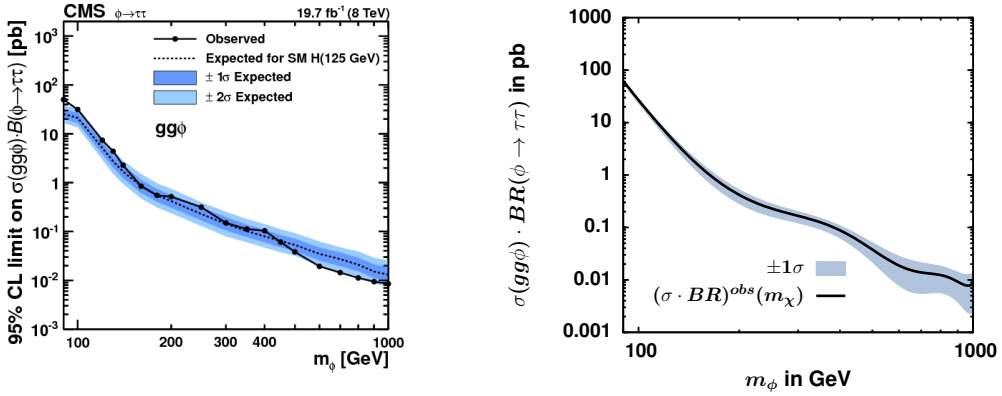

(a) (b)

Figure B.2.: Comparison of the published model independent 95% C.L. contour taken from Ref. [107] (a) and the parametrization for the corresponding χ^2 contribution (b). The contour line corresponds to an 95%C.L. upper limit exclusion contour on the cross section times branching fraction, while the blue band represents the 1σ error band.

$$\begin{aligned} \Delta\chi^2 &= 5.99 \\ &= \left(\frac{(\sigma \cdot BR)^{obs}(m_\phi) - (\sigma \cdot BR)^{95}(m_\phi)}{\sigma_{(\sigma \cdot BR)^{95}}(m_\phi)} \right)^2 \\ \rightarrow (\sigma \cdot BR)^{95}(m_\phi) &= (\sigma \cdot BR)^{obs}(m_\phi) - \sqrt{5.99} \cdot \sigma_{(\sigma \cdot BR)^{95}}(m_\phi). \end{aligned} \tag{7.11}$$

The 95% C.L. contour line is parameterized by fitting a polynomial using GNUPLOT. Outside the published mass range, the exclusion contour is approximated to be linear with a fixed error. The parametrization for $(\sigma \cdot BR)^{obs}(m_\phi)$ reads

$$(\sigma \cdot BR)^{obs}(m_\phi) = \begin{cases} m_\phi < 90, & d_1 + d_2 \cdot m_\phi \\ 90 \leq m_\phi < 1000, & 10^{e_1 + e_2 \cdot m_\phi + e_3 \cdot m_\phi^2 + e_4 \cdot m_\phi^3 + e_5 \cdot m_\phi^4 + e_6 \cdot m_\phi^5 + e_7 \cdot m_\phi^6} \\ 1000 \leq m_\phi, & f_1 + f_2 \cdot m_\phi \end{cases} \tag{7.12}$$

with

$e_1 = 7.96,$ $e_6 = -1.37 \cdot 10^{-12}$, $d_1 = 217.69,$
$e_2 = -1.07 \cdot 10^{-1}$, $e_7 = 3.79 \cdot 10^{-16}$, $d_2 = -1.86,$
$e_3 = 5.46 \cdot 10^{-4}$, $f_1 = 2.22 \cdot 10^{-2},$
$e_4 = -1.43 \cdot 10^{-6}$, $f_2 = -1.39 \cdot 10^{-5},$
$e_5 = 1.98 \cdot 10^{-9}$.

The mass m_ϕ is given in GeV. A similar parameterization can be used for the 1σ error band which corresponds to $\sigma_{(\sigma \cdot BR)^{95}}(m_\phi)$:

$$\sigma_{(\sigma \cdot BR)^{95}}(m_\phi) = \begin{cases} m_\phi < 90, & 3.87 \\ 90 \leq m_\phi < 1000, & 10^{E_1 + E_2 \cdot m_\phi + E_3 \cdot m_\phi^2 + E_4 \cdot m_\phi^3 + E_5 \cdot m_\phi^4 + E_6 \cdot m_\phi^5 + E_7 \cdot m_\phi^6} \\ 1000 \leq m_\phi, & 6.10 \cdot 10^{-3} \end{cases} \tag{7.13}$$

with

Table B.1.: The hadronic cross section $\sigma_{tot}(pp \to \tilde{g}\tilde{g}, \tilde{g}\tilde{q}, \tilde{q}\tilde{q})$ given on the published 95% C.L. contour line in Ref. [108, 109]. The cross sections in the last row shows vary due to varying efficiencies along the exclusion contour.

m_0 in GeV	$m_{1/2}$ in GeV	$\sigma_{tot} \cdot 10^{-3}$ in pb
400	843.11	1.513613
800	798.26	1.155236
1200	705.35	1.271251
1600	602.82	2.814515
2000	572.71	3.352062
2400	556.69	2.996126
2800	554.77	1.997814
3200	548.36	1.350165
3600	545.15	0.9181249
4000	535.54	0.7640308
4400	521.44	0.7729961
4800	519.52	0.6964154
5200	516.32	0.6665289
5600	514.40	0.6335210

$E_1 = 4.33$, $E_5 = 7.97 \cdot 10^{-10}$,
$E_2 = -5.84513 \cdot 10^{-2}$, $E_6 = -5.39 \cdot 10^{-13}$,
$E_3 = 2.56 \cdot 10^{-4}$, $E_7 = 1.48 \cdot 10^{-16}$,
$E_4 = -6.09 \cdot 10^{-7}$.

The comparison of the published data and the parameterization used for the global fit is shown in Fig. B.2. The solid black line in Fig. B.2(a) corresponds to the exclusion contour at 95% C.L. on the cross section times branching fraction from Ref. [107], while the blue band represents the 1σ error band. Fig. B.2(b) shows $(\sigma \cdot BR)^{obs}(m_\phi)$ (solid black line) and the corresponding error $\sigma_{(\sigma \cdot BR)^{95}}(m_\phi)$ (blue band).

B.2. Mass Limits on Squarks and Gluinos

The implementation of the ATLAS contribution requires the parametrization of $\sigma_{ATLAS}(m_0)$, which takes the varying efficiencies into account. The hadronic cross section $\sigma_{tot}(pp \to \tilde{g}\tilde{g}, \tilde{g}\tilde{q}, \tilde{q}\tilde{q})$ on the published 95% C.L. contour line in Ref. [108, 109] has been calculated with micrOMEGAs. Table B.1 summarize the excluded hadronic cross sections, which vary due to varying efficiencies. σ_{ATLAS} can be parameterized as a function of m_0 to compensate the variation of the hadronic cross section. By using the requirement

$$\begin{aligned} \chi^2 &= 5.99 \\ &= \sigma_{tot}^2/\sigma_{ATLAS}^2 \\ \to \sigma_{ATLAS} &= \frac{\sigma_{tot}}{\sqrt{5.99}}, \end{aligned} \tag{7.14}$$

$\Delta\chi^2 = 5.99$ is fulfilled on the contour line. The 95% C.L. exclusion contour line has been parameterized by piecewise fitting a polynomial using GNUPLOT. The parametrization for $\sigma_{ATLAS}(m_0)$ reads

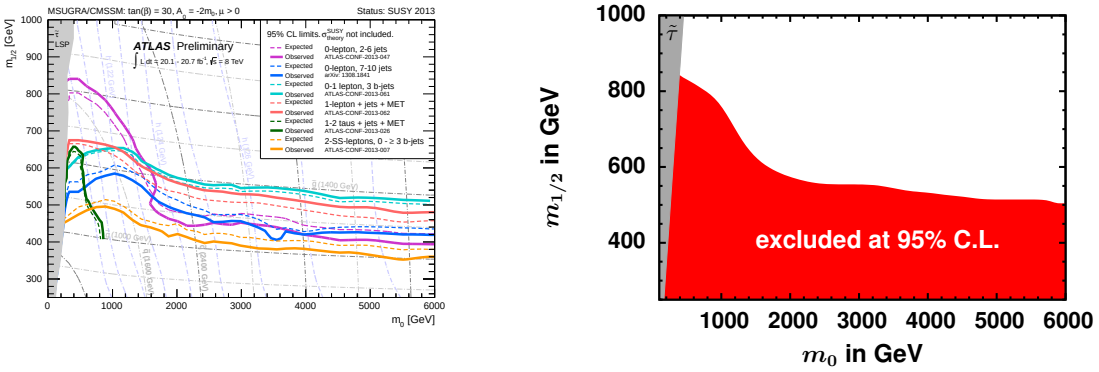

(a) (b)

Figure B.3.: Comparison of the published 95% C.L. contour taken from Ref. [108, 109] (a) and their corresponding excluded region which results from the parametrization of $\sigma_{ATLAS}(m_0)$ (b). The region below the lower 95% exclusion C.L. contours in (a) resemble the red region in (b).

$$\sigma_{ATLAS}(m_0) = \begin{cases} m_0 < 400, & 1.48 \cdot 10^{-3} \\ 400 \leq m_0 < 992, & a_1 + a_2/m_0 + a_3 \cdot m_0 + a_4 \cdot m_0^2 + a_5 \cdot m_0^3 + a_6 \cdot m_0^4 \\ 992 \leq m_0 < 3966, & b_1 + b_2 \cdot m_0 + b_3 \cdot m_0^2 + b_4 \cdot m_0^3 + b_5 \cdot m_0^4 + b_6 \cdot m_0^5 \\ 3966 \leq m_0 < 5800, & a_1 + a_2/m_0 + a_3 \cdot m_0 + a_4 \cdot m_0^2 + a_5 \cdot m_0^3 + a_6 \cdot m_0^4 \\ 5800 \leq m_0, & 6.65 \cdot 10^{-4} \end{cases} \quad (7.15)$$

with

$$\begin{aligned} a_1 &= 4.59 \cdot 10^{-3}, & b_1 &= 2.07 \cdot 10^{-2}, \\ a_2 &= -5.77 \cdot 10^{-1}, & b_2 &= -5.81 \cdot 10^{-5}, \\ a_3 &= -4.84 \cdot 10^{-6}, & b_3 &= 6.08 \cdot 10^{-8}, \\ a_4 &= 2.11 \cdot 10^{-9}, & b_4 &= -2.78 \cdot 10^{-11}, \\ a_5 &= -3.80 \cdot 10^{-13}, & b_5 &= 5.76 \cdot 10^{-15}, \\ a_6 &= 2.41 \cdot 10^{-17}, & b_6 &= -4.46 \cdot 10^{-19}. \end{aligned}$$

The mass m_0 is given in GeV. The published exclusion curve from Ref. [108, 109] is shown in Fig. B.3(a) along with the corresponding excluded region at 95% C.L. in Fig. B.3(b) indicated by the red region. The red region results from the parametrization from Eq. 7.16.

In the NMSSM, a large stop splitting and therefore light stops can arise, while the remaining particles stays unaffected. This leads to an enhancement of the total hadronic cross section due to the light stops. In this case the stop contribution has to be separated from the total hadronic cross section and an additional χ^2 contribution is calculated from the stop with respect to the stop mass. First the remaining hadronic cross section has to be determined. For this, the stop contribution is calculated and subtracted from the total hadronic contribution. The remaining hadronic cross section $\sigma_{tot}^{(w/o)}(pp \to \tilde{g}\tilde{g}, \tilde{g}\tilde{q}, \tilde{q}\tilde{q})$ on the published 95% C.L. contour line is given in Table B.2.

The χ^2 contribution coming from the total cross section without the stop contribution can be obtained by the requirement in Eq. 7.14. The parametrization of the 95% C.L. exclusion contour for $\sigma_{ATLAS}^{(w/o)}(m_0)$ reads

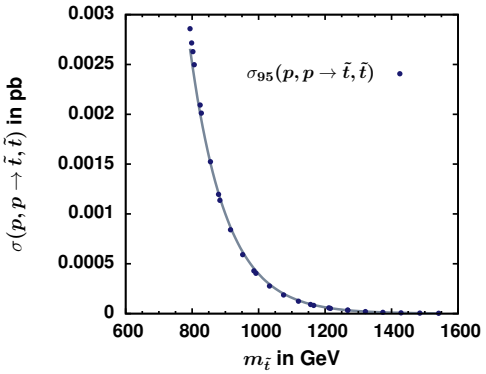

Figure B.4.: Upper limit on the cross section of the stop contribution with respect to the stop mass.

Table B.2.: The hadronic cross section $\sigma_{tot}^{(w/o)}(pp \to \tilde{g}\tilde{g}, \tilde{g}\tilde{q}, \tilde{q}\tilde{q})$ without the stop contribution given on the published 95% C.L. contour line from Ref. [108, 109]. The last row corresponds to the stop contribution $\sigma_{\tilde{t}}(pp \to \tilde{t}\tilde{t})$.

m_0 in GeV	$m_{1/2}$ in GeV	$\sigma_{tot}^{(w/o)} \cdot 10^{-3}$ in pb	$\sigma_{\tilde{t}} \cdot 10^{-3}$ in pb
400	843.11	1.47842	0.035196
800	798.26	1.06343	0.091803
1200	705.35	0.842563	0.428687
1600	602.82	0.721977	2.092538
2000	572.71	0.493441	2.858621
2400	556.69	0.498709	2.497417
2800	554.77	0.473849	1.523965
3200	548.36	0.509381	0.840784
3600	545.15	0.513310	0.404814
4000	535.54	0.577234	0.186797
4400	521.44	0.690872	0.082123
4800	519.52	0.663571	0.032844
5200	516.32	0.653581	0.012947
5600	514.40	0.628648	0.004872

$$\sigma_{ATLAS}^{(w/o)}(m_0) = \begin{cases} m_0 < 400, & 1.52 \cdot 10^{-3} \\ 400 \leq m_0 < 992, & c_1 + c_2 \cdot m_0 + c_3 \cdot m_0^2 + c_4 \cdot m_0^3 + c_5 \cdot m_0^4 + c_6 \cdot m_0^5 \\ 5800 \leq m_0, & 6.66 \cdot 10^{-4} \end{cases} \quad (7.16)$$

with

$$c_1 = 1.86 \cdot 10^{-3}, \qquad c_4 = 9.84 \cdot 10^{-14},$$
$$c_2 = -1.00 \cdot 10^{-6}, \qquad c_5 = -2.35 \cdot 10^{-17},$$
$$c_3 = 5.45 \cdot 10^{-11}, \qquad c_6 = 1.54 \cdot 10^{-21}.$$

The mass m_0 is given in GeV. The stop contribution given in the las row of Table B.2 is associated with a separate χ^2 contribution $\chi^2_{stop}(m_{\tilde{t}})$. This contribution includes the stop cross section $\sigma_{\tilde{t}}(pp \to \tilde{t}\tilde{t})$ which is a function of the stop mass. By calculating for each m_0-$m_{1/2}$ point on the contour line the stop mass and the corresponding stop cross section $\sigma(pp \to \tilde{t}\tilde{t})$, the 95% C.L. contour can be derived. The contour is shown in Fig. B.4. The requirement $\Delta\chi^2 = 5.99$ has to be fulfilled on the contour line in Fig. B.4 for $\sigma_{stop}(m_{\tilde{t}})$, which leads to the parameterization of $\sigma_{\tilde{t}}^{95}(m_{\tilde{t}})$

$$\begin{aligned} \Delta\chi^2 &= 5.99 \\ &= \left(\frac{\sigma_{\tilde{t}}^{obs}(m_{\tilde{t}}) - \sigma_{\tilde{t}}^{95}(m_{\tilde{t}})}{\sigma} \right)^2 \\ \rightarrow \sigma_{\tilde{t}}^{95}(m_{\tilde{t}}) &= \sigma_{\tilde{t}}^{obs}(m_{\tilde{t}}) - \sqrt{5.99} \cdot \sigma, \end{aligned} \tag{7.17}$$

with an estimated error σ of 15% on the cross section. The 95% C.L. contour line is parameterized by piecewise fitting a polynomial using GNUPLOT. Outside the published mass range, the exclusion contour is approximated to be fixed with a fixed error. The parametrization for $\sigma^{obs}(m_{\tilde{t}})$ reads

$$\sigma^{obs}(m_{\tilde{t}}) = 10^{d_1 + d_2 \cdot m_{\tilde{t}}} \tag{7.18}$$

with

$$d_1 = 5.95164 \cdot 10^{-1}, \qquad d_2 = -3.99 \cdot 10^{-3}.$$

The mass $m_{\tilde{t}}$ is given in GeV. χ^2_{ATLAS} and χ^2_{stop} are added to get the total χ^2 contribution from the ATLAS constraint for a parameter set in the NMSSM.

B.3. Standard Model-like Higgs Boson

The LEP collaboration put a constraint on a SM Higgs bosons of about 114.4 GeV. The 95% C.L. exclusion contour in [110] refers to the ratio $\xi^2 = (g_{HZZ}/g^{SM}_{HZZ})^2$, so a light Higgs with reduced couplings below the upper limit is still allowed. The limit is only significant for the NMSSM, which provides two light Higgs bosons with possibly non-SM couplings. In the MSSM the light Higgs boson h has SM couplings in the decoupling limit $M_A >> M_Z$, which is true for the considered parameter space. So the lower limit of 114.4 GeV is already fulfilled by the Higgs mass constraint of about 125 GeV and the corresponding χ^2 contribution $\chi^2_{m_h}$. The requirement $\Delta\chi^2 = 5.99$ is fulfilled on the 95% C.L. contour line, which leads to the parameterization

$$\begin{aligned} \Delta\chi^2 &= 5.99 \\ &= \left(\frac{\xi^2_{obs}(m_h) - \xi^2_{95}(m_h)}{\sigma_{\xi^2_{95}}(m_A)} \right)^2 \\ \rightarrow \xi^2_{95}(m_h) &= \xi^2_{obs}(m_h) - \sqrt{5.99} \cdot \sigma_{\xi^2_{95}}(m_h), \end{aligned} \tag{7.19}$$

where the mass of m_h is given in GeV. The published 95% C.L. contour is already implemented as a table within the software package NMSSMTools, so $\xi^2_{obs}(m_h)$ is extracted from this table. The parametrization of the 1σ error band arises from the fit of a polynomial function on a logarithmic scale using GNUPLOT

$$\sigma_{\xi^2_{95}}(m_h) = \begin{cases} m_h < 15, & 3.15 \cdot 10^{-3} \\ 15 \leq m_h < 115, & 10^{A_1 + A_2 \cdot m_h + A_3 \cdot m_h^2 + A_4 \cdot m_h^3 + A_5 \cdot m_h^4 + A_6 \cdot m_h^5 + A_7 \cdot m_h^6} \\ 115 \leq m_h, & 4.31 \cdot 10^{-1} \end{cases} \tag{7.20}$$

where

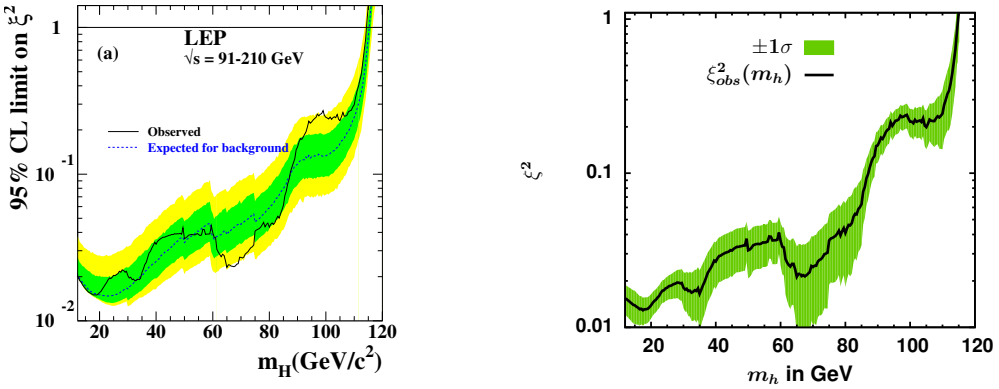

(a) (b)

Figure B.5.: Comparison between the published 95% C.L. contour (a) from Ref. [110] and the parametrization of $\xi^2_{obs}(m_h)$ (b). The solid black line corresponds to the observed limit whereas the dark green band represents the 1σ error band. The area above the solid black line is excluded at 95%C.L..

$$
\begin{aligned}
A_1 &= 2.38421, & A_5 &= 1.35 \cdot 10^{-5},\\
A_2 &= -7.35 \cdot 10^{-1}\ , & A_6 &= -8.85 \cdot 10^{-8},\\
A_3 &= 3.99 \cdot 10^{-2}, & A_7 &= 2.29 \cdot 10^{-10}\ ,\\
A_4 &= -1.02 \cdot 10^{-3}.
\end{aligned}
$$

The comparison between the published data taken from Ref. [110] and the parameterization for the χ^2 contribution is shown in Fig. B.5. The area below the solid black line in Fig. B.5 is excluded at 95% C.L.. The green band corresponds to the 1σ error band.

B.4. Elastic Scattering Cross Section

In direct dark matter experiments no dark matter particles have been found so far, which results in 90% C.L. upper exclusion limit on the WIMP-nucleon cross section as a function of the WIMP mass. The corresponding χ^2 contribution fulfills $\Delta\chi^2 = 4.91$ on the contour line, which leads to

$$
\begin{aligned}
\Delta\chi^2 &= 4.91 \\
&= \left(\frac{\sigma^{obs}_{\chi N}(m_\chi) - \sigma^{90}_{\chi N}(m_\chi)}{\sigma_{\sigma^{90}_{\chi N}}(m_\chi)} \right)^2 \\
\rightarrow \sigma^{90}_{\chi N}(m_\chi) &= \sigma^{obs}_{\chi N}(m_\chi) - \sqrt{4.91} \cdot \sigma_{\sigma^{90}_{\chi N}}(m_\chi). \qquad (7.21)
\end{aligned}
$$

The observed 90% C.L. contour and the corresponding 1σ error band can be parametrized by fitting a polynomial on a double logarithmic scale using GNUPLOT. The procedure can be performed for the SD and SI cross section limits. The parametrized limit on the SI cross section $\sigma^{obs}_{\chi N}(m_\chi)$, which corresponds to χ^2_{LUX}, reads

$$
\sigma^{obs}_{\chi N}(x) = 10^{a_1 + a_2 \cdot x + a_3 \cdot x^2 + a_4 \cdot x^3 + a_5 \cdot x^4 + a_6 \cdot x^5 + a_7 \cdot x^6 + a_8 * \cdot x^7 + a_9 \cdot x^8 + a_1 0 \cdot x^9}, \qquad (7.22)
$$

where $x = \log_{10}(m_\chi)$ with a neutralino mass m_χ given in GeV. The parameters read

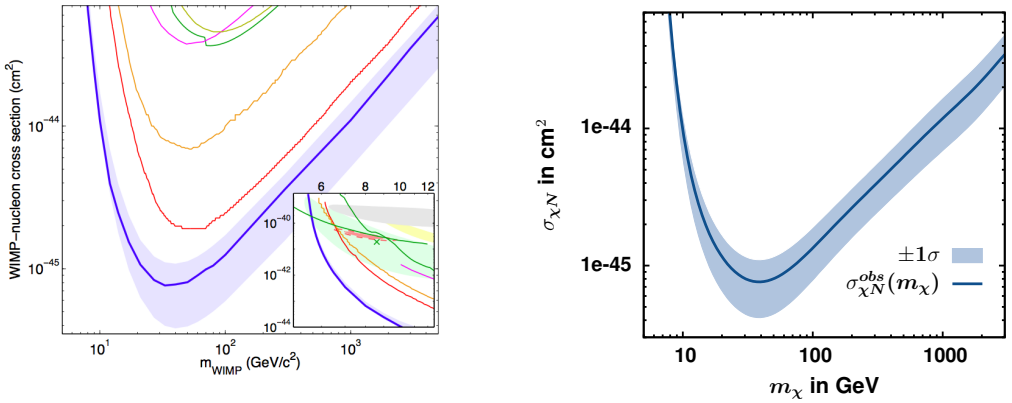

(a) (b)

Figure B.6.: Comparison of the published (a) and parameterized (b) 90% C.L. contour on the WIMP-nucleon cross section from the SI elastic scattering cross section. The published curve has been taken from Ref. [111].

$a_1 = 206.84$, $a_5 = 1708.90$, $a_8 = -45.56$,
$a_2 = -1107.32$, $a_6 = -790.71$, $a_9 = 4.97$,
$a_3 = 2154.06$, $a_7 = 239.06$, $a_{10} = 2.37 \cdot 10^{-1}$,
$a_4 = -2414.01$.

The fit to the corresponding error band shows the same polynomial function like Eq. 7.22 but with slightly different parameters:

$A_1 = 142.25$, $A_5 = 1245.74$, $A_8 = -33.25$,
$A_2 = -815.32$, $A_6 = -576.52$, $A_9 = 3.63$,
$A_3 = 1575.96$, $A_7 = 174.40$, $A_{10} = -1.73 \cdot 10^{-1}$,
$A_4 = -1761.15$.

Fig. B.6(a) shows the published 90% C.L. contour taken from Ref. [111] for the upper limit on the SI WIMP-nucleon cross section. The parameterized 90% C.L. contour, which enters the χ^2 function, is shown in Fig. B.6(b). The blue band corresponds to the 1σ error band.

The limit on the SD elastic scattering cross section is separated into a limit on the WIMP-neutron and on the WIMP-proton cross section. The distribution is similar, so the parameterization from Eq. 7.22 is taken for the WIMP-proton, WIMP-neutron and the corresponding 1σ error band. The associated parameters for parameterization of the WIMP-proton cross section read

$b_1 = 7.92$, $b_5 = 224.58$, $b_8 = -5.01$,
$b_2 = -178.19$, $b_6 = -98.37$, $b_9 = 5.10 \cdot 10^{-1}$,
$b_3 = 317.75$, $b_7 = 28.03$, $b_{10} = -2.26 \cdot 10^{-2}$,
$b_4 = -334.78$.

The following parameters are associated with the error band:

$B_1 = 27.26$, $B_5 = 300.13$, $B_8 = -5.39$,
$B_2 = -253.23$, $B_6 = -124.12$, $B_9 = 4.98 \cdot 10^{-1}$,
$B_3 = 450.55$, $B_7 = 32.89$, $B_{10} = -1.97 \cdot 10^{-2}$,
$B_4 = -465.505$,

The comparison between the published 90% C.L. contour from Ref. [113] and the parametrization for the contribution χ^2_{COUPP} is shown in Fig. B.7. The blue bands refer to the 1σ error band.

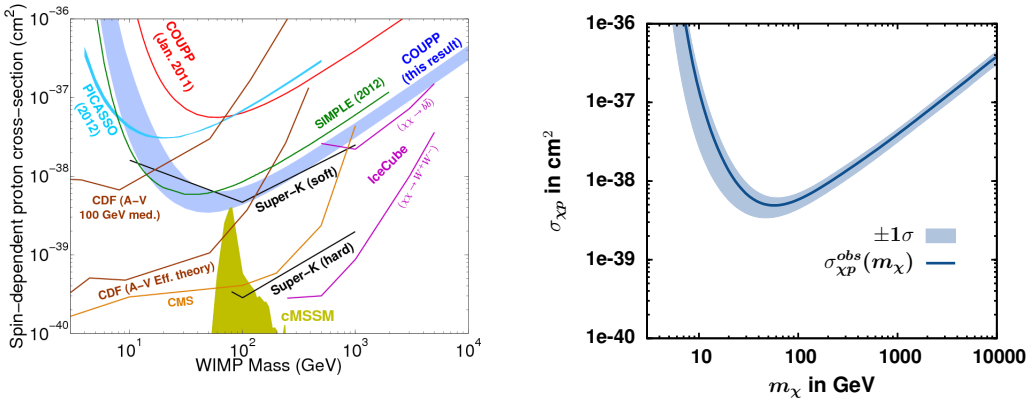

(a) (b)

Figure B.7.: The published limit on the SD WIMP-proton cross section (a) taken from Ref. [113] compared to the parametrized 90% C.L. limit (b) for the corresponding contribution χ^2_{COUPP}.

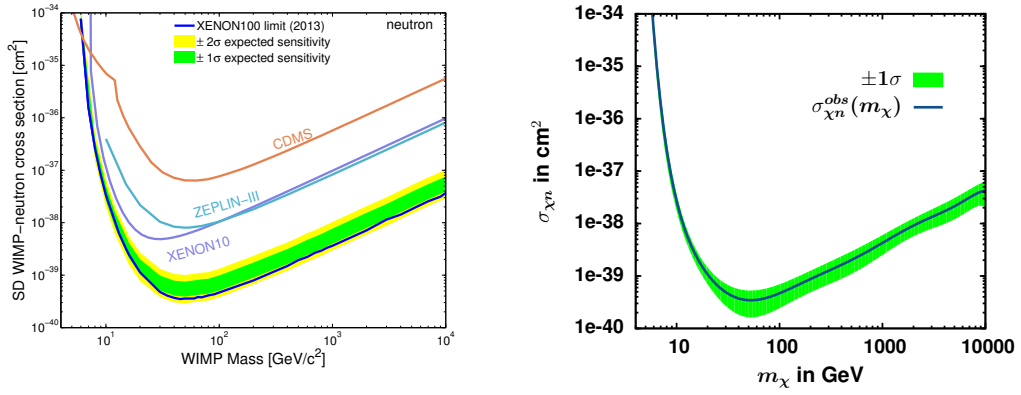

(a) (b)

Figure B.8.: Comparison of the published (a) and parameterized (b) 90% C.L. contour for the χ^2 contribution resulting from the spin-dependent WIMP-neutron cross section. The published 90% C.L. contour has been taken from Ref. [112].

For the limit on the SD WIMP-neutron cross section, the following parameter are used:

$$
\begin{aligned}
c_1 &= 164.42\ , & c_5 &= 1149.37, & c_8 &= -25.97\ ,\\
c_2 &= -849.15\ , & c_6 &= -506.08, & c_9 &= 2.65,\\
c_3 &= 1580.61\ , & c_7 &= 144.79, & c_{10} &= -1.18 \cdot 10^{-1},\\
c_4 &= -1698.10\ . & & & &
\end{aligned}
$$

The parameters for the corresponding error $\sigma_{\sigma^{90}_{\chi N}}$ read

$$
\begin{aligned}
C_1 &= 68.98, & C_5 &= 221.64, & C_8 &= -1.54,\\
C_2 &= -360.97\ , & C_6 &= -71.13, & C_9 &= 7.25 \cdot 10^{-2},\\
C_3 &= 525.24, & C_7 &= 13.99, & C_{10} &= 2.82 \cdot 10^{-5},\\
C_4 &= -434.31\ . & & & &
\end{aligned}
$$

The published 90% C.L. contour from Ref. [112] and the parametrization, which is used to evaluate the contribution $\chi^2_{XENON100}$ are shown in Fig. B.8. The 1σ error band is represented by the green band.

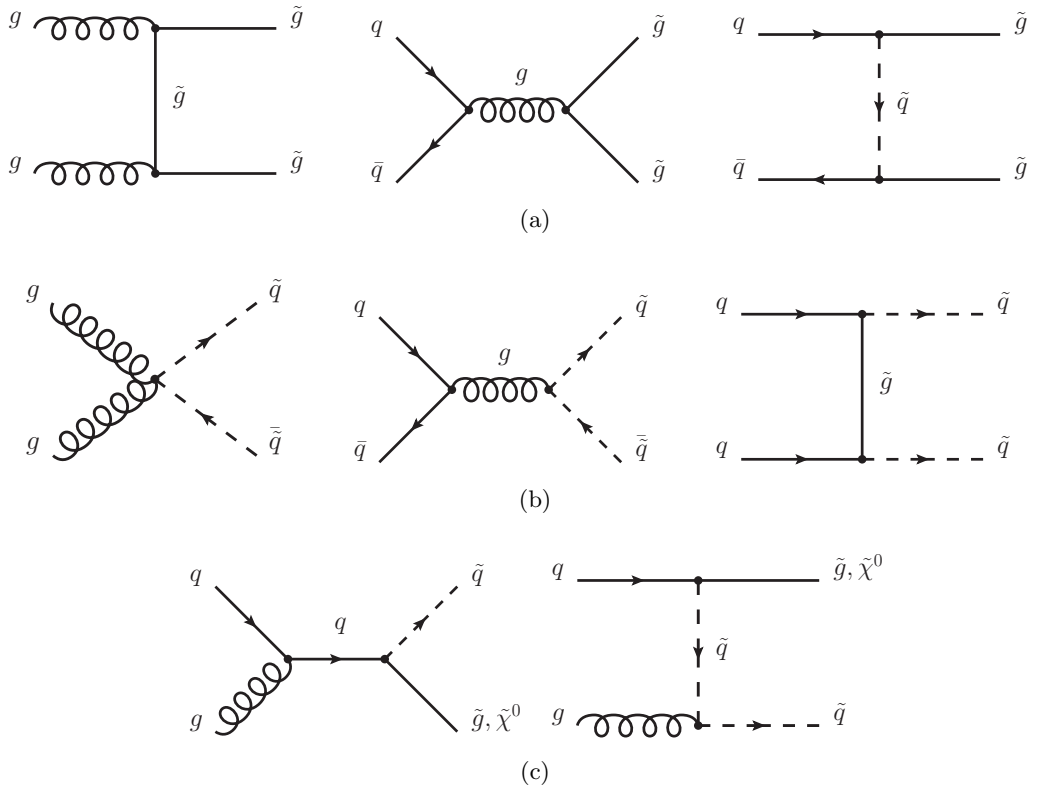

Figure B.9.: Additional diagrams contributing to strong production at the LHC.

C. Implementation of the χ^2 function

The implementation of the χ^2 function for the NMSSM and MSSM is similar, except for the calculation of the mass spectrum and the observables, so the following discussion will mainly refer to the NMSSM SUSY model. The NMSSMTools/micrOMEGAs software package is used for the calculations of the mass spectra and observables, which correspond to a parameter set of a NMSSM/MSSM model. NMSSMTools is written in Fortran while micrOMEGAs is written in Fortran and C. The mass spectrum in the NMSSM is calculated inside NMSSMTools using the Routine `NMSPEC`. MicrOMEGAs is linked to SuSpect to calculate the supersymmetric spectrum. Both program packages use masses and mixing matrices as specified in the SUSY Les Houches Accord [185]. NMSSMTools is linked to micrOMEGAs to calculate the dark matter observables. The evaluated cross sections are extracted from CalcHEP [186], a software package which is designed for effective evaluation and simulation of high energy physics collider processes at parton level.

After the calculation of the mass spectra, the parameter configurations have to be checked first, which is done in the subroutine `CHECK_ERR_SCAN`, since a parameter set can give a non-physical solution or correspond to a excluded region in parameter space e.g. the stau being the lightest supersymmetric particle. In case, the point in parameter space refers to such a forbidden region, the corresponding χ^2 function is set to the maximal `DOUBLE` value. In this way the non-physical regions are absorbed into a large χ^2 value, forcing the minimization tool to move to another region in parameter space. From numerical point of view a smooth steep function is more suitable for the minimization since a step function sometimes causes convergence problems. However there exist no intermediate transition region, i.e. either a region is physical or non-physical. Therefore, the step function is reasonable to describe the physical solutions. After the parameter set is checked to be relevant, the mass spectra and observables for the χ^2 function are calculated. These values are passed to the subroutine `CHI`. It contains all separate χ^2 contribution, which are

calculated and finally added to the total χ^2 value. Whether or not a specific χ^2 contribution is included into the fit is specified in the corresponding input file. It includes an additional `BLOCK LISTCON` summarizing all constraints. The entry 1/0 includes/excluded the constraint from the total χ^2 function for the minimization. Additionally the subroutine `OUTPUT_SCAN` has been added to print all resulting masses, couplings and branching ratios for the chosen mass point into a corresponding output file. The total χ^2 value is passed to the minimization software package Minuit. The minimization input file includes all parameters and the fitting strategy. Furthermore it contains information about the parameters, e.g. if they are fixed or varied within a certain range. Using theses informations Minuit starts the minimization until the chosen convergence criteria is fulfilled. Minuit stops the minimization after it has converged. The χ^2 value and the corresponding parameter configuration is written into an output file. This is repeated for each mass point in the parameter space for the chosen range. A fast calculation is maintained if the calculation for each mass point is separately submitted to several nodes on a computing cluster to parallelized the calculation.

D. Strong and Electroweak Diagrams

Additional diagrams contributing to the strong production at the LHC are shown in Fig. B.9. The first row represents the $\tilde{g}\tilde{g}$, the second the $\tilde{g}\tilde{q}$ and the last row the $\tilde{q}\tilde{q}$ production.

E. Scalar Form-Factors

A summary of the applied default scalar form-factors and the lowest possible form-factors with respect to the strange quark content, which result from a combination of Refs. [159–161], are given in Table E.3.

Table E.3.: Summary of the default and the lowest scalar form-factors.

Quark	Default Form-Factor	Lowest Form-Factors
	proton	
u	$1.5323 \cdot 10^{-2}$	$1.4 \cdot 10^{-2}$
d	$1.9093 \cdot 10^{-2}$	$3.6 \cdot 10^{-2}$
s	$4.4762 \cdot 10^{-2}$	$2.0 \cdot 10^{-2}$
	neutron	
u	$1.0677 \cdot 10^{-2}$	$2.0 \cdot 10^{-2}$
d	$2.7325 \cdot 10^{-2}$	$2.6 \cdot 10^{-2}$
s	$4.4700 \cdot 10^{-2}$	$2.0 \cdot 10^{-2}$

F. Allowed 68% C.L. Regions

The allowed region at 95% C.L. within the m_0-$m_{1/2}$ plane for the CMSSM and NMSSM are shown in chapter 6. The corresponding 68% C.L. regions are summarized in Fig. F.10(a) and Fig. F.10(b). For each confidence region a separate region is plotted in the m_0-$m_{1/2}$ plane, indicated by a green colored region. The green region in Fig. F.10(a)(Fig. F.11(a)) and Fig. F.10(b)(Fig. F.11(b)) is allowed at 68% and 95% C.L. for the CMSSM (NMSSM), respectively. The white region is excluded.

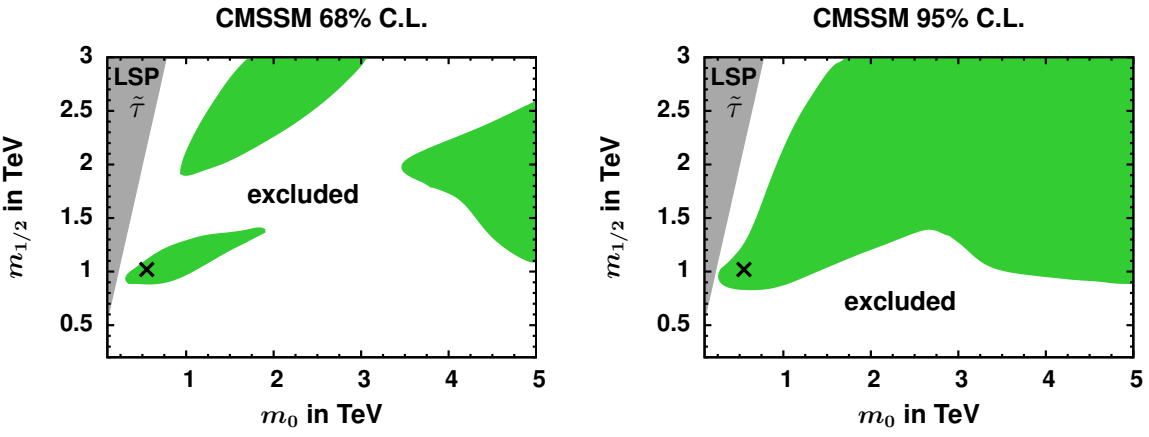

(a) (b)

Figure F.10.: The allowed 68%(a) and 95% C.L. (b) regions for the CMSSM within the m_0-$m_{1/2}$ plane indicated by the colored green region. The white region is accordingly excluded, while the gray region is not allowed due to the stau being the LSP. The black cross marks the best-fit point.

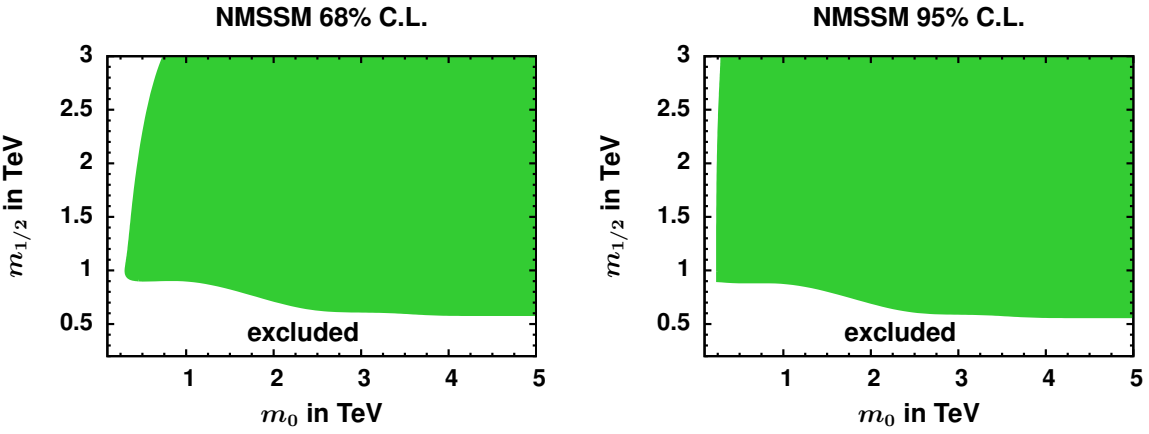

(a) (b)

Figure F.11.: The allowed 68%(a) and 95% C.L. (b) regions for the NMSSM within the m_0-$m_{1/2}$ plane indicated by the colored green region. The white region is excluded. The distribution is very flat, which can be derived from the similar allowed colored regions for the different confidence regions.

G. Optimized $\tan\beta$ values in the m_0-$m_{1/2}$ plane

The allowed region at 95% C.L. within the m_0-$m_{1/2}$ plane for the CMSSM and NMSSM are shown in chapter 6. The corresponding optimized values of $\tan\beta$ for the CMSSM and NMSSM are summarized in Fig. G.12a and G.12, respectively. Large values of $\tan\beta$ are preferred by the global fit in the CMSSM, since the free parameters are mainly determined by the relic density constraint, as discussed in section 6.1. In the NMSSM, the Higgs mass constraint favors low values of $\tan\beta$ to obtain a significant enhancement of the tree level mass due to the mixing with the Higgs singlet.

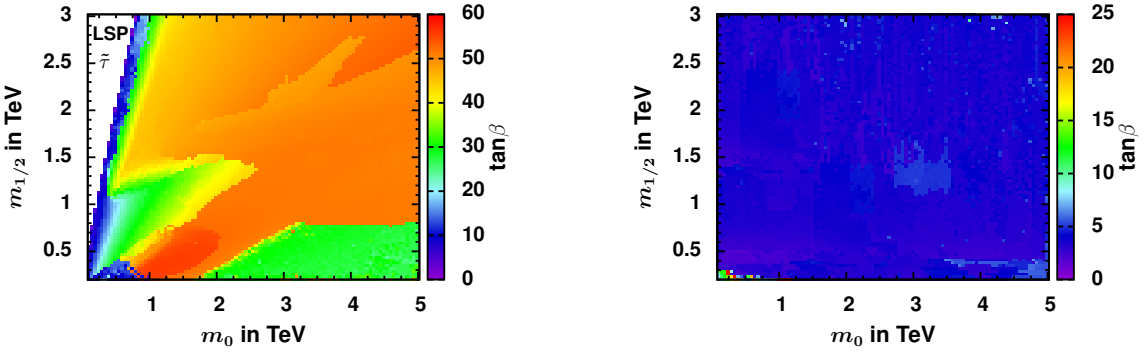

Figure G.12.: The optimized tanβ values for the CMSSM (b) and NMSSM (b) within the m_0-$m_{1/2}$ plane. Within the CMSSM large values of tanβ are favored due to the relic density constraint, while in the NMSSM low values of tanβ are required to obtain the Higgs boson mass of 125 GeV.

H. Impact of the Theoretical Error on the Higgs mass

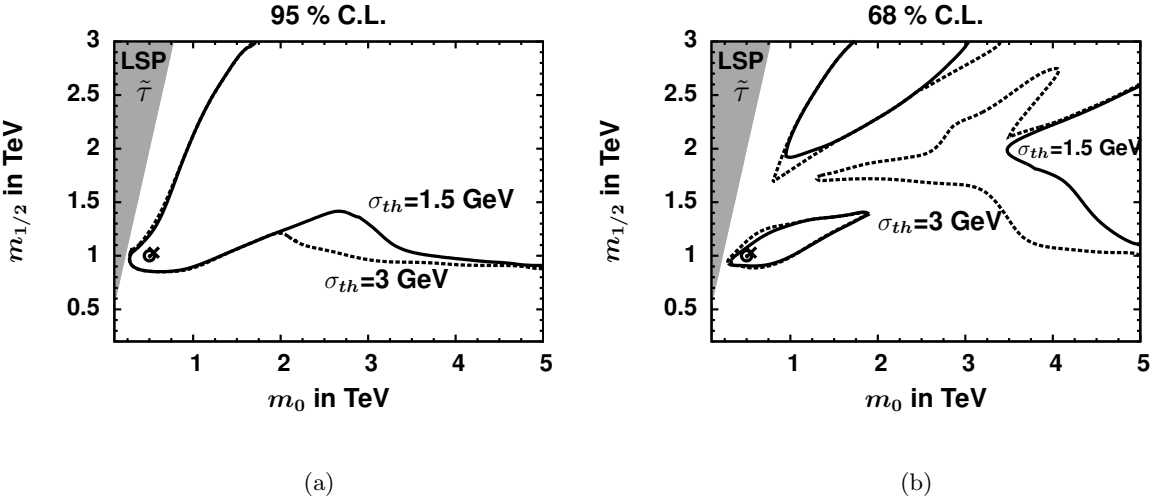

Figure H.13.: Impact of the theoretical error of the Higgs mass constraint on the allowed 95% (a) and 68% C.L.(b) regions within the CMSSM. The solid line corresponds to the applied theory error of $\sigma_{th} = 1.5$ GeV, while the dashed line represents the allowed region using a theory error of 3 GeV. A doubled theory error on the Higgs mass slightly changes the 95% C.L. region. The 68% C.L. regions are enlarged, so the different regions merge together. The best-fit points indicated by the black cross ($\sigma_{th} = 1.5$ GeV) and the empty circle ($\sigma_{th} = 3$ GeV) are hardly affected. The stau is the LSP in the gray region.

The excluded region in the CMSSM is sensitive to the m_h constraint and therefore to the chosen error of the Higgs mass, see e.g. Ref. [106]. A theoretical error of 1.5 GeV for the Higgs mass as suggested in [95] has been applied but the theory error can be as well of the order of 3 GeV to account for the theoretical uncertainties of the MSSM Higgs boson mass calculations [187]. The impact of the theory error on the allowed region in the CMSSM is demonstrated in Fig. H.13. Here the allowed 95% (Fig. H.13(a)) and 68% C.L. (Fig. H.13(b)) contours are shown for two theoretical errors indicated by the solid and dashed lines. The larger theory error $\sigma_{th} = 3$ GeV has been applied on the results including the optimized tanβ and A_0 values for $\sigma_{th} = 1.5$ GeV. The two errors can be regarded as the minimal and maximal theoretical error, so taking a theoretical error within this interval,

leads to an exclusion contour in between the solid and dashed lines in Fig. H.13. The 95% C.L. exclusion contour for the doubled theoretical error is slightly shifted as expected. The 68% C.L. excluded region for $\sigma_{th} = 3$ GeV is enlarged, so the three allowed regions merge together. The best fit point, which is associated with the larger theory error, is indicated by the empty circle, overlaps with the black cross. Unlike the CMSSM, within the NMSSM the Higgs mass constraint is easily fulfilled, so changing the theoretical error on the Higgs mass will not affect the allowed region because the excluded region is dominated by the LHC direct searches.

I. Mass spectrum and χ^2 contributions for the CMSSM benchmark points

The theortical prediction of the constraints from Table 4.3 and the χ^2 contribution are given in Table I.4 and I.5 for the three benchmark points are summarized for the CMSSM in Table 6.1. The mass spectrum at low scale is summarized in Table I.6.

Table I.4.: Summary of the predicted values of the constraints from Table 4.3 for the three benchmark points in the CMSSM.

	CMSSM Best-Fit	CMSSM II	CMSSM III
m_h	124.45	125.02	123.97
$BR(B_s^0 \to \mu^+\mu^-) \cdot 10^{-9}$	3.18	3.46	3.20
$BR(B \to X_s\gamma) \cdot 10^{-9}$	3.14	3.28	3.31
$R_{BR(B\to\tau\nu_\tau)} \cdot 10^{-1}$	9.95	9.85	9.73
$\Delta a_\mu \cdot 10^{-11}$	29.30	9.59	5.99
$\Omega h^2 \cdot 10^{-1}$	1.21	1.21	1.20

Table I.5.: χ^2 contributions to the total χ^2 value for each constraint given for the parameter points in Table 6.1. The contributions $\chi^2_{m_A}$, χ^2_{LUX}, $\chi^2_{XENON100}$ and χ^2_{COUPP} are negligible, so they are not specified.

	CMSSM Best-Fit	CMSSM II	CMSSM III
$\chi^2_{m_h}$	0.16	0.01	0.42
$\chi^2_{BR(B_s^0\to\mu^+\mu^-)}$	0.09	0.36	0.10
$\chi^2_{BR(B\to X_s\gamma)}$	0.42	0.11	0.07
$\chi^2_{R_{BR(B\to\tau\nu_\tau)}}$	0.47	0.50	0.54
$\chi^2_{\Delta a_\mu}$	5.23	6.06	6.22
$\chi^2_{\Omega h^2}$	0.00	0.01	0.00
χ^2_{ATLAS}	0.05	0.00	0.00
χ^2_{tot}	6.42	7.05	7.35

Table I.6.: Mass spectrum at low scale for the parameter points in Table 6.1 given in GeV.

	CMSSM Best-Fit	CMSSM II	CMSSM III
h	124.45	125.02	123.97
H	1859.73	2524.82	2203.12
A	1860.13	2524.84	2203.09
$H^{\pm}$	1862.02	2526.23	2204.73
χ_1^0	440.2	1256.0	1095.3
χ_2^0	833.5	2313.1	1607.7
χ_3^0	1826.4	3005.9	1614.0
χ_4^0	1829.2	3010.2	2045.9
$\chi_1^{\pm}$	833.5	2313.1	1606.5
$\chi_2^{\pm}$	1829.4	3010.2	2045.9
$\tilde{e}_L$	865.7	2357.2	5213.3
$\tilde{e}_R$	666.0	1848.8	5068.1
$\tilde{\mu}_L$	865.7	2357.2	5213.3
$\tilde{\mu}_R$	666.0	1848.8	5068.1
$\tilde{\tau}_1$	440.2	1256.0	3710.0
$\tilde{\tau}_2$	800.8	2165.1	4612.7
$\tilde{\nu}_e$	862.2	2356.0	5212.7
$\tilde{\nu}_\mu$	862.2	2356.0	5212.7
$\tilde{\nu}_\tau$	790.5	2159.0	4611.7
$\tilde{u}_L$	2093.2	5312.7	6621.2
$\tilde{u}_R$	2017.1	5098.0	6506.4
$\tilde{d}_L$	2094.7	5313.3	6621.6
$\tilde{d}_R$	2008.3	5070.1	6492.2
$\tilde{c}_L$	2093.2	5312.7	6621.2
$\tilde{c}_R$	2017.1	5098.0	6506.4
$\tilde{s}_L$	2094.7	5313.3	6621.6
$\tilde{s}_R$	2008.3	5070.1	6492.2
$\tilde{b}_1$	1711.7	4583.8	5361.4
$\tilde{b}_2$	1918.2	4661.3	5513.7
$\tilde{t}_1$	1145.3	4053.3	4793.7
$\tilde{t}_2$	1738.6	4631.3	5342.2
$\tilde{g}$	2234.3	5710.0	5252.7

J. Running of the masses in the CMSSM

The running of the masses for the additional CMSSM points II and III are plotted in Fig. J.14. Since theses points refer to the two 68% C.L. regions in the m_0-$m_{1/2}$ plane for high SUSY masses, the corresponding low energy soft masses are heavy as well.

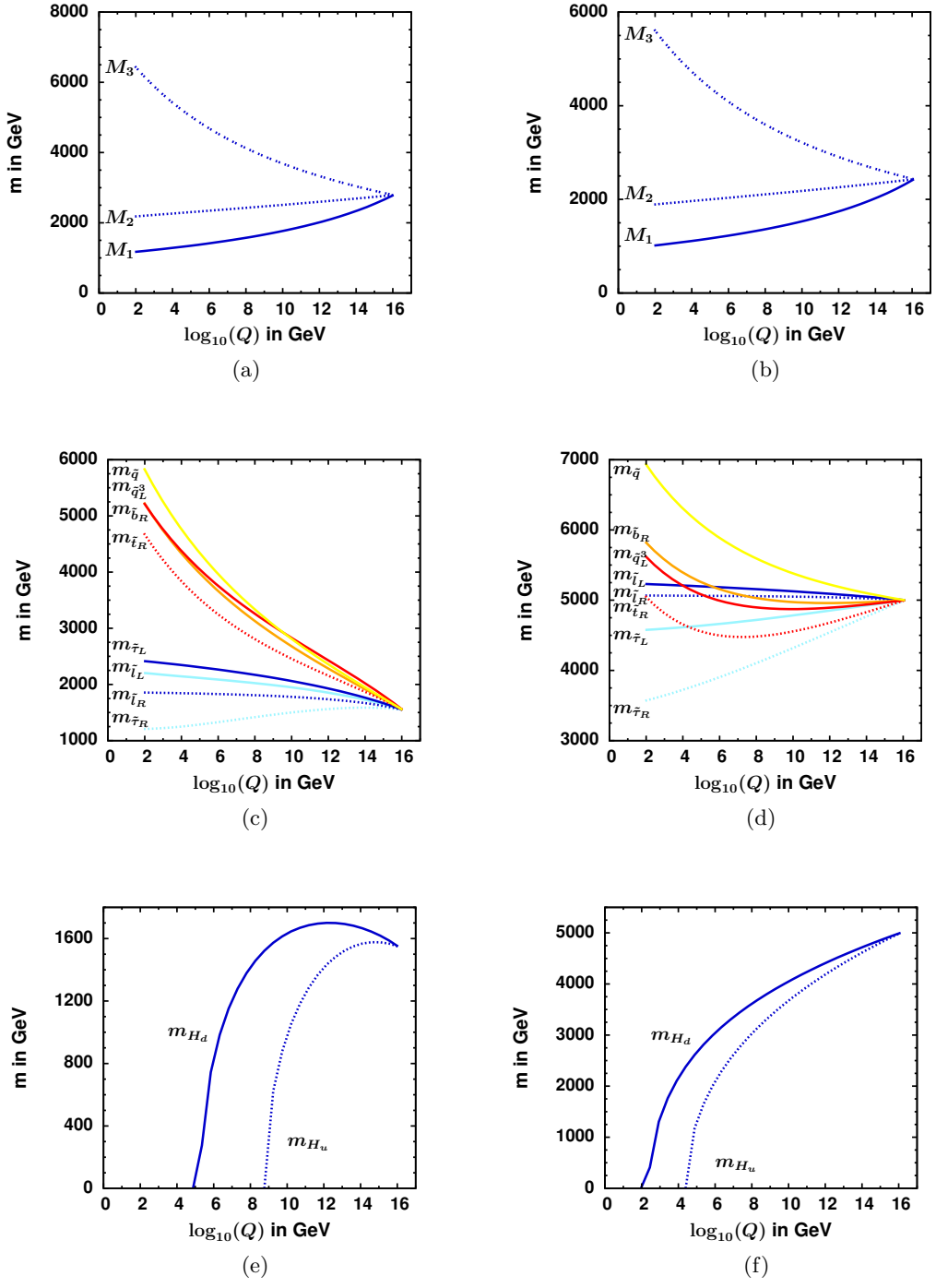

Figure J.14.: The running of the soft masses from the high to the low scale for the CMSSM point II and III is shown. The soft masses are divided into the gaugino (a)((b)), slepton/squark (c)((d)) and Higgs masses (e)((f)) for CMSSM point II(III).

K. Mass spectrum for the NMSSM Benchmark Points

In section 6.2.4 three benchmark points for the NMSSM are summarized. The corresponding mass spectrum at low scale is given in Table L.8.

Table K.7.: Mass spectrum at low scale for the parameter points in Table 6.2 given in GeV.

	BMP I	BMP II	BMP III	CMSSM IV
H_1	87.59	96.07	125.21	-
H_2	124.03	124.35	167.40	125.82
H_3	337.57	1119.61	1098.69	2025.87
A_1	207.21	306.25	191.19	-
A_2	326.72	1119.95	1098.84	2025.97
$H^\pm$	316.61	1114.27	1093.71	2027.72
χ_1^0	78.3	172.7	172.7	945.5
χ_2^0	159.9	250.2	251.9	1760.4
χ_3^0	199.1	372.2	372.3	3018.1
χ_4^0	268.1	407.6	406.6	3020.3
χ_5^0	516.2	540.3	544.7	-
$\chi_1^\pm$	110.6	353.3	353.7	1760.4
$\chi_2^\pm$	516.0	538.5	543.1	3020.4
$\tilde{e}_L$	2471.5	2464.8	2472.8	2746.5
$\tilde{e}_R$	2300.8	2313.8	2298.0	2515.6
$\tilde{\mu}_L$	2471.5	2464.8	2472.8	2746.5
$\tilde{\mu}_R$	2300.8	2313.8	2298.0	2515.6
$\tilde{\tau}_1$	2299.4	2312.4	2295.9	945.5
$\tilde{\tau}_2$	2470.9	2464.1	2471.9	2216.0
$\tilde{\nu}_e$	2470.6	2463.8	2471.9	2745.5
$\tilde{\nu}_\mu$	2470.6	2463.8	2471.9	2745.5
$\tilde{\nu}_\tau$	2469.9	2463.2	2470.9	2210.0
$\tilde{u}_L$	2636.0	2635.9	2638.5	4576.9
$\tilde{u}_R$	2701.3	2692.3	2705.9	4439.5
$\tilde{d}_L$	2636.8	2636.7	2639.3	4577.6
$\tilde{d}_R$	2606.6	2608.9	2608.8	4422.4
$\tilde{c}_L$	2636.0	2635.9	2638.5	4576.9
$\tilde{c}_R$	2701.3	2692.3	2705.9	4439.5
$\tilde{s}_L$	2636.8	2636.7	2639.3	4577.6
$\tilde{s}_R$	2606.6	2608.9	2608.8	4422.4
$\tilde{b}_1$	1964.3	1984.7	1860.3	3542.3
$\tilde{b}_2$	2590.7	2594.0	2583.9	3663.9
$\tilde{t}_1$	1050.9	1105.9	5371.5	2956.3
$\tilde{t}_2$	1971.7	1992.6	18703.4	3550.1
$\tilde{g}$	1492.5	1491.1	1491.2	4447.5

L. Branching Ratios for the NMSSM Benchmark Points II and III

In section 6.2.4 the branching ratios of CMSSM IV and BMP I are summarized. The remaining branching ratios for BMP II and III are given in Table K.7.

Table L.8.: Branching ratios for BMP II and III in the NMSSM. The cross section in the last line represents the Higgs production cross section at 8 TeV for the dominant gluon-gluon fusion process.

Branching Ratios [%]										
	NMSSM (BMP II)					NMSSM (BMP III)				
Mass [GeV]	H_1 96.07	H_2 124.35	H_3 1119.61	A_1 306.25	A_2 1119.95	H_1 125.21	H_2 167.40	H_3 1098.69	A_1 191.19	A_2 1098.84
$b\bar{b}$	88.21	63.50	0.40	50.67	0.39	61.92	30.25	0.39	88.09	0.39
$t\bar{t}$	0.00	0.00	26.35	0.00	27.70	0.00	0.00	28.74	0.00	30.62
$\tau\tau$	9.23	6.83	0.06	6.50	0.06	6.67	3.49	0.06	10.40	0.06
W^+W^-	0.02	18.61	4.58e-3	-	-	20.12	63.73	0.14e-3	-	-
$\chi_1^0\chi_1^0$	-	-	4.19	-	4.65	-	-	3.79	-	4.25
$\chi_1^0\chi_3^0$	-	-	7.51	-	3.67	-	-	7.67	-	3.48
$\chi_1^0\chi_4^0$	-	-	5.33	-	11.01	-	-	4.99	-	10.93
$\chi_1^+\chi_1^-$	-	-	1.92	-	9.53	-	-	1.77	-	9.34
H_1H_2	-	-	10.50	-	-	-	-	9.76	-	-
A_1H_2	-	-	-	-	8.99	-	-	-	-	0.37
ZA_1	-	-	8.18	-	-	-	-	8.28	-	-
ZH_1	-	-	-	39.33	9.60	-	-	-	-	0.01
A_1H_1	-	-	-	-	0.43	-	-	-	-	9.16
ZH_2	-	-	-	0.11	0.04	-	-	-	-	9.02
σ_{prod} [pb]	0.27	19.5	2.4e-3	8.4e-3	3.2e-3	19.35	4.5e-2	2.8e-3	1.2e-2	3.5e-3

M. Neutralino Mixing Matrix for BMP I and III

The neutralino mixing matrix elements for BMP I and III are given in Fig. M.15(a) and M.15(b), respectively. The large Higgsino component for BMP I is excluded by limits of the SD WIMP-nucleon cross section.

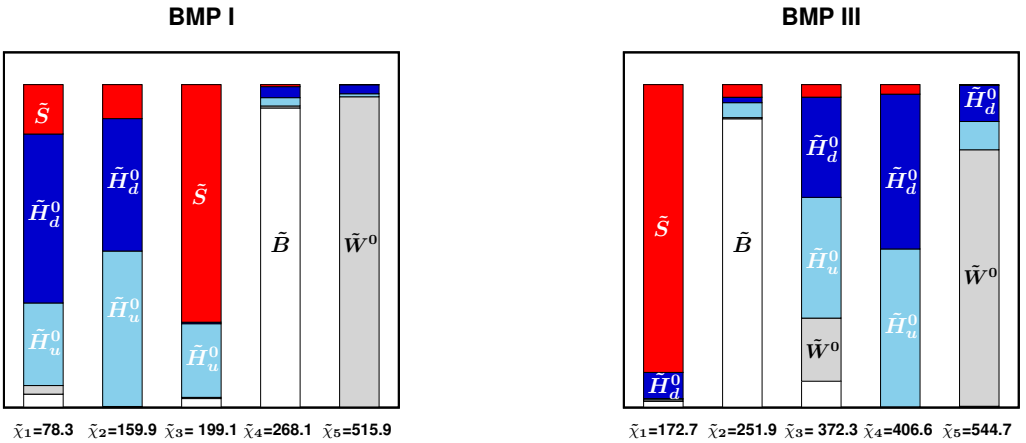

(a) (b)

Figure M.15.: The neutralino mass matrix elements squared for the BMP I (a) and BMP III (b) in the NMSSM. The elements are indicated by the different colors going from white, gray, light blue, dark blue and red for the $\tilde{B}, \tilde{W}^0, \tilde{H}_u^0, \tilde{H}_d^0$ and $\tilde{S}$, respectively. The mass of the neutralino is given by the numbers below the bars in GeV.

N. Comparison of Allowed 68% C.L. Regions

The comparison of the allowed contours at 95% C.L. within the m_0-$m_{1/2}$ plane for the CMSSM and NMSSM with other analyses are summarized in chapter 6. The corresponding

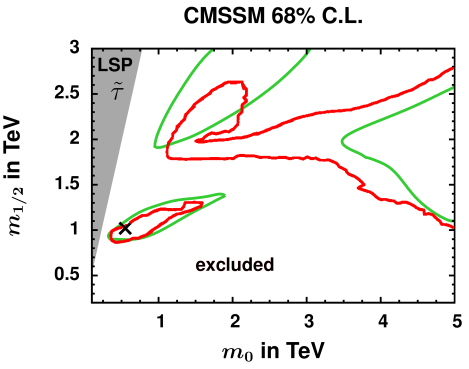

Figure N.16.: Comparison of the 68% C.L. contour of Ref. [168] indicated by the solid red line and the allowed 68% C.L. contour resulting from this analysis represented by the solid green line from Fig. F.10(a). The χ^2 distribution from Ref. [168] is rather flat, so the 68% C.L. contour is close to the 95% C.L.. Since the best-fit point has a lower minimum, the 68% C.L. regions are smaller compared to the contour of Ref. [168].

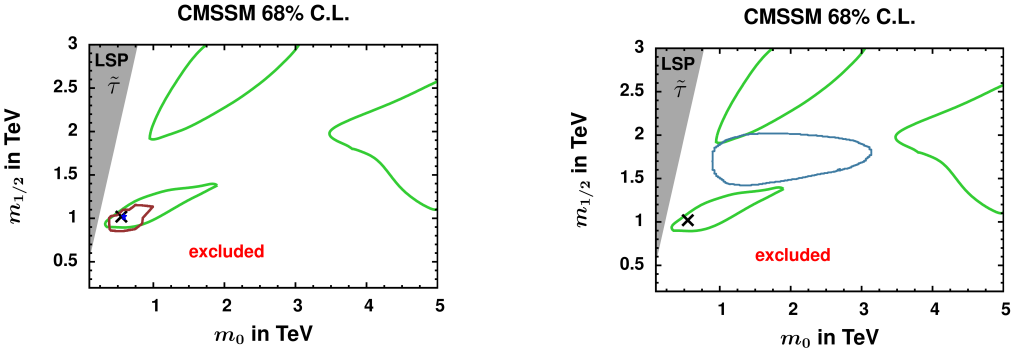

(a) (b)

Figure N.17.: Comparison of the 68% C.L. contour of Ref. [171] (a) and Ref. [172](b) with the allowed region of this analysis indicated by the green solid line from Fig. F.10(a). The 68% C.L. regions in (a) match, but the random sampling technique excludes a large part of the parameter space. The 68% C.L. contour in (b) do not match at all, due to the logarithmic priors.

68% C.L. regions are given in Fig. N.16 for Ref. [168] indicated by the solid red line. The resulting 68% C.L. contour from Fig. F.10(a) is represented by the solid green line. The χ^2 distribution from Ref. [168] is flat, which is derived from the similar 68% and 95% C.L. contours. The best-fit point marked by a cross has a lower minimum compared to Ref. [168], so the 68% C.L. regions are smaller. The comparison of the 68% C.L. region for Ref. [171]([172]) is showed in Fig. N.17(a)(Fig. N.17(b)), indicated by the solid red(blue) line. The resulting 68% C.L. allowed region from this analysis. is again represented by the solid green line, which resembles the allowed region in Fig. F.10. The 68% C.L. contours in Fig. N.17(a) match, but the random sampling technique used in Ref. [171] excludes a large part of the parameter space. The 68% C.L. contour in Fig. N.17(b) do not match at all because in Ref. [172] logarithmic priors are applied.

O. Extrapolation of XENON100

In section 6.4 the sensitivities for future DDMS searches has been estimated by using the limit of XENON1T. This limit has been extracted from the published 90% C.L. contour given by the XENON100 experiment in Ref. [181]. The parameterization of the limit has been obtained by a polynomial on a double logarithmic scale using GNUPLOT. The exclusion curve for the SI WIMP-nucleon cross section given in pb reads

$$\sigma_{\chi N}^{XENON100}(x) = 10^{d_1+d_2\cdot x^{-1}+d_3\cdot x^{-2}+d_4\cdot x^{-4}+d_5\cdot x^{-6}}, \tag{7.23}$$

where $x = \log_{10}(m_\chi)$ with a neutralino mass m_χ given in GeV. The corresponding parameters read

$d_1 = -0.86$, $d_3 = 35.42$, $d_5 = 3.43209$,
$d_2 = -31.70$, $d_4 = -13.05$.

The XENON1T is expected to be two orders of magnitude better than XENON100, so $\sigma_{\chi N}^{XENON100}(x)$ has been scaled accordingly to obtain the XENON1T limit, which reads

$$\sigma_{\chi N}^{XENON1T}(x) = \sigma_{\chi N}^{XENON100}(x) \cdot 10^{-2}. \tag{7.24}$$

P. Additional SUSY Searches at the LHC

Further searches for SUSY in multilepton events from electroweak production are ongoing at the LHC. Diagrams for the electroweak production of charginos and neutralinos at the LHC are shown in Fig. P.18. The comparatively light chargino and neutralino masses lead to higher cross sections compared to the strong production, as shown in Fig. P.19. Here the electroweak production cross section, indicated by the color coding, is plotted within the m_0-$m_{1/2}$ plane. This figure can be compared with Fig. 5.21(d), which includes the total hadronic cross section. However, the full cascade of such processes has to be taken into account. The strong production cross sections are characterized by a large jet activity from the long decay chains and large missing energy from the escaping neutralino. This characteristic decay products can be used to efficiently suppress the background. Compared to the electroweak production the number of jets and the missing transverse energy is rather low [188]. Leptonic decays are needed to reduce the background, so these signatures suffer from the luminosity. With increase luminosity in the next run of the LHC at 14 TeV, the sensitivity will compete with the strong production of squarks and gluinos. So these limits can also be included to be sensitive to large values of m_0, which cannot be covered by the hadronic searches.

In addition to the searches for SUSY particles at the LHC, there exist also searches for DM particles at the LHC in monojets [189] and in searches for invisible decays of the Higgs boson [190], which can currently cover WIMP-nucleon cross sections down to 10^{-8} pb. However these searches have not been included into the current and extrapolated sensitivities, since these limits are still above the limit reached by the direct dark matter searches. In addition those searches are not fully compatible with the limits from the elastic scattering cross section. The searches for monojets give limits for an effective cross section, which includes only specific interactions corresponding to specific effective operators, like the axial-vector interaction between neutralino and quarks. The calculation of the SI elastic scattering cross section inside micrOMEGAs includes the whole nuclei. Here not only one but several effective operators at the microscopic level are summarized

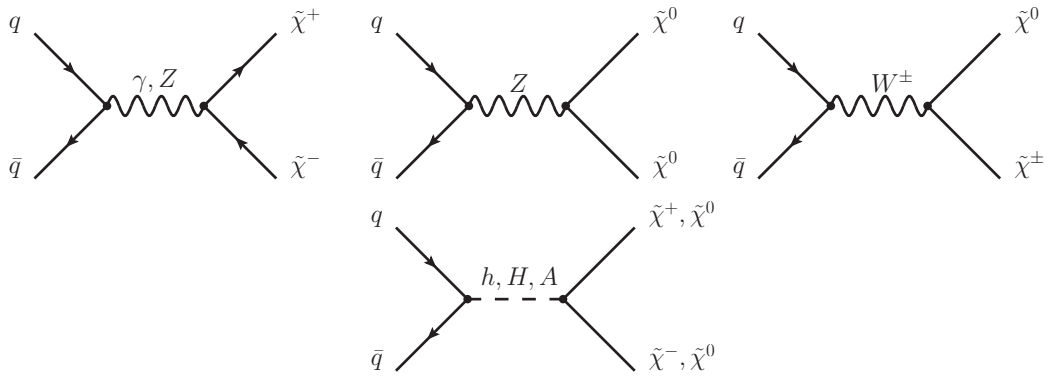

Figure P.18.: Additional diagrams contributing to the electroweak production at the LHC.

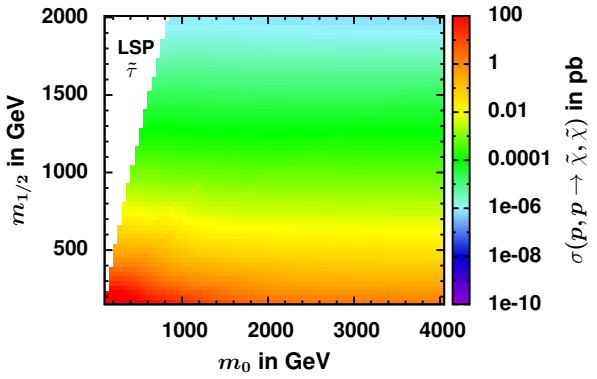

(a)

Figure P.19.: Cross section distribution indicated by the color coding for the electroweak production at the LHC translated into the m_0-$m_{1/2}$ plane for fixed $\tan\beta = 30$ and $A_0 = -2 \cdot m_0$.

and extended to the whole nuclei. The limits from the monojet searches can only be applied if the corresponding observable is calculated.
The limit on the WIMP-nucleon cross section from the limit on the invisible branching ratio covers WIMP masses up to 0.5 m_h. For light singlino-like neutralinos in the NMSSM this mass region is relevant but it is not significant for the CMSSM because the limit on the neutralino is far above 0.5 m_h due to the SUSY searches at the LHC.

Danksagung

An dieser Stelle möchte ich mich bei Allen bedanken, die zum Gelingen dieser Arbeit beigetragen haben und mich in dieser Zeit unterschützt haben.
Mein besonderer Dank gilt Prof. Wim de Boer für die Möglichkeit meine Doktorarbeit am Institut für Experimentelle Kernphysik anzufertigen, der sehr guten Betreuung und das Vertrauen in meine Arbeit während der gesamten Zeit meiner Promotion.
Prof. Günter Quast danke ich für die Übernahme des Korreferats und den wertvollen Ratschlägen.
Prof. Dmitri Kazakov möchte ich für die konstruktiven Diskussionen und der Unterstützung bei der theoretischen Ausarbeitung der Arbeit danken.
Ebenso geht mein Dank an meine Kollegen, die mich in den vergangenen Jahren mit bereichernden Tipps und Diskussionsbeiträgen unterstützt haben.
Stefan Wayand, Yasmin Anstruther und Felix Frensch bin ich im bosonderen für das Lesen dieser Arbeit und den damit verbundenden Korrektur- und Verbesserungsvorschlägen dankbar.
Eine herausragende Stellung in jeglicher Hinsicht nimmt mein Familie ein. Gerade die letzte Phase meiner Arbeit war eine nicht minder aufreibende Zeit für Simon, meine Mutter, Elli und Roman. Für Ihre liebevolle und bedingunslose Fürsorge sowie mentale und moralische Unterstützung möchte ich mich von Herzen bedanken.